Analysis of additional regulators necessary for autophagy in *Drosophila* muscle tissue

by

Yungui Guo

B.S., Dalian Medical University, 2016
M.S., Emporia State University, 2019

AN ABSTRACT OF A DISSERTATION

submitted in partial fulfillment of the requirements for the degree

DOCTOR OF PHILOSOPHY

Department of Biochemistry and Molecular Biophysics
College of Arts and Sciences

KANSAS STATE UNIVERSITY
Manhattan, Kansas

2024

Abstract

Our lab uses *Drosophila* as a model organism to study the role of Bcl-2-associated athanogene 3 (BAG3)-mediated chaperone-assisted selective autophagy (CASA) in skeletal muscle. We previously showed that the serine/threonine protein kinase (NUAK) biochemically and genetically interacts with *Drosophila* Starvin (Stv), the ortholog of mammalian BAG3. While this NUAK-Stv complex plays a role in the autophagic clearance of proteins, the discovery of novel autophagy regulators will facilitate a better understanding of tissue and/or stress-specific responses.

To this end, we have employed a sensitized genetic assay using an RNA interference (RNAi) approach and found *NUAK* and *stv* genetically interacts with genes that encode for Striatin-interacting phosphatase and kinase (STRIPAK) complex proteins, including Striatin-interacting protein (Strip), MOB kinase activator 4 (Mob4), and Connector of kinase to AP-1 (Cka). These data indicate that both *NUAK* and *stv* function in the same biological process with genes that encode for STRIPAK complex proteins. To confirm these results biochemically, we performed affinity purification-mass spectrometry (AP-MS) with Strip as a bait protein. Indeed, we found that STRIPAK complex members can be co-purified from *Drosophila* larval muscle tissue with Stv and NUAK. Knockdown of Strip in muscle tissue using RNAi resulted in the buildup of ubiquitinated cargo, p62, and Autophagy-related 8a (Atg8a), indicating alternations in the autophagy pathway. In fact, autophagic flux was reduced in muscles with *Strip RNAi*, but lysosome biogenesis and activity remained unchanged. Our findings suggest a model in which the STRIPAK-NUAK-Stv complex collaboratively regulates autophagy in muscle tissue.

We also utilized p62 immunostaining to test microtubule-related candidates as another approach to further our understanding of autophagy regulation in muscle tissue. Pavarotti (Pav)/kinesin family member 23 (KIF23) emerged as one of the strongest candidates using this

approach. Pav and its binding partner Tumbleweed (Tum)/RacGAP1 are well known for their role in MT-dependent movements during cytokinesis. We found that Ubiquitin and p62 are recruited to damaged mitochondria and formed autophagosome clusters with Atg8a upon muscle-specific RNAi knockdown of Pav or Tum in larval muscles. This Pav-Tum complex is also enriched in the nucleus, counterintuitive for a direct role in MT-mediated transport throughout the muscle cell. However, these observations are consistent with a recent report describing the roles of Pav and Tum in nuclear envelope budding (NEB), an alternative pathway for the export of cargo that is too big to traverse through nuclear pores. In *Drosophila* larval muscles, mRNAs necessary for mitochondrial integrity, such as *Marf mRNA*, is one of the cargos of the NEB pathway. As expected, *Marf mRNA* levels were reduced in the myoplasm of *pav RNAi* or *tum RNAi* muscles. We also observed that the knockdown of Marf or other NEB components, such as Wash or Torsin, resulted in autophagosome clustering. Together, these findings suggest a model in which blocking NEB decreases mitochondrial activity, subsequently leading to the recruitment of p62 and autophagosome components for lysosomal degradation.

Our research demonstrated that the STRIPAK complex collaborates with the NUAK-Stv complex in the autophagic clearance of proteins. This finding enhances our understanding of the BAG3-mediated CASA in protein quality control. Additionally, we are the first group to report abnormal mitophagy resulting from defects in NEB formation. Autophagosome clusters represent a unique phenotype that can be readily examined through immunostaining and microscopy techniques. Consequently, we propose that our research provides a rapid and straightforward method for detecting defects in NEB development.

Analysis of additional regulators necessary for autophagy in *Drosophila* muscle tissue

by

Yungui Guo

B.S., Dalian Medical University, 2016
M.S., Emporia State University, 2019

A DISSERTATION

submitted in partial fulfillment of the requirements for the degree

DOCTOR OF PHILOSOPHY

Department of Biochemistry and Molecular Biophysics
College of Arts and Sciences

KANSAS STATE UNIVERSITY
Manhattan, Kansas

2024

Approved by:

Major Professor
Erika R. Geisbrecht

Copyright

© Yungui Guo 2024.

Abstract

Our lab uses *Drosophila* as a model organism to study the role of Bcl-2-associated athanogene 3 (BAG3)-mediated chaperone-assisted selective autophagy (CASA) in skeletal muscle. We previously showed that the serine/threonine protein kinase (NUAK) biochemically and genetically interacts with *Drosophila* Starvin (Stv), the ortholog of mammalian BAG3. While this NUAK-Stv complex plays a role in the autophagic clearance of proteins, the discovery of novel autophagy regulators will facilitate a better understanding of tissue and/or stress-specific responses.

To this end, we have employed a sensitized genetic assay using an RNA interference (RNAi) approach and found *NUAK* and *stv* genetically interacts with genes that encode for Striatin-interacting phosphatase and kinase (STRIPAK) complex proteins, including Striatin-interacting protein (Strip), MOB kinase activator 4 (Mob4), and Connector of kinase to AP-1 (Cka). These data indicate that both *NUAK* and *stv* function in the same biological process with genes that encode for STRIPAK complex proteins. To confirm these results biochemically, we performed affinity purification-mass spectrometry (AP-MS) with Strip as a bait protein. Indeed, we found that STRIPAK complex members can be co-purified from *Drosophila* larval muscle tissue with Stv and NUAK. Knockdown of Strip in muscle tissue using RNAi resulted in the buildup of ubiquitinated cargo, p62, and Autophagy-related 8a (Atg8a), indicating alternations in the autophagy pathway. In fact, autophagic flux was reduced in muscles with *Strip RNAi*, but lysosome biogenesis and activity remained unchanged. Our findings suggest a model in which the STRIPAK-NUAK-Stv complex collaboratively regulates autophagy in muscle tissue.

We also utilized p62 immunostaining to test microtubule-related candidates as another approach to further our understanding of autophagy regulation in muscle tissue. Pavarotti (Pav)/kinesin family member 23 (KIF23) emerged as one of the strongest candidates using this

approach. Pav and its binding partner Tumbleweed (Tum)/RacGAP1 are well known for their role in MT-dependent movements during cytokinesis. We found that Ubiquitin and p62 are recruited to damaged mitochondria and formed autophagosome clusters with Atg8a upon muscle-specific RNAi knockdown of Pav or Tum in larval muscles. This Pav-Tum complex is also enriched in the nucleus, counterintuitive for a direct role in MT-mediated transport throughout the muscle cell. However, these observations are consistent with a recent report describing the roles of Pav and Tum in nuclear envelope budding (NEB), an alternative pathway for the export of cargo that is too big to traverse through nuclear pores. In *Drosophila* larval muscles, mRNAs necessary for mitochondrial integrity, such as *Marf mRNA*, is one of the cargos of the NEB pathway. As expected, *Marf mRNA* levels were reduced in the myoplasm of *pav RNAi* or *tum RNAi* muscles. We also observed that the knockdown of Marf or other NEB components, such as Wash or Torsin, resulted in autophagosome clustering. Together, these findings suggest a model in which blocking NEB decreases mitochondrial activity, subsequently leading to the recruitment of p62 and autophagosome components for lysosomal degradation.

Our research demonstrated that the STRIPAK complex collaborates with the NUAK-Stv complex in the autophagic clearance of proteins. This finding enhances our understanding of the BAG3-mediated CASA in protein quality control. Additionally, we are the first group to report abnormal mitophagy resulting from defects in NEB formation. Autophagosome clusters represent a unique phenotype that can be readily examined through immunostaining and microscopy techniques. Consequently, we propose that our research provides a rapid and straightforward method for detecting defects in NEB development.

Table of Contents

List of Figures x
List of Tables xi
Acknowledgements xii
Dedication xiii
Chapter 1 - Autophagy and *Drosophila* 1
1.1, Major milestones in autophagy research 1
1.1, A brief overview of autophagy 4
1.3, BAG3 and Chaperone-Assisted Selective Autophagy (CASA) 8
1.4, General overview of mitochondrial dynamics and mitophagy 10
1.5, *Drosophila* as a model of skeletal muscle autophagy and diseases 14
References 18
Chapter 2 - A conserved STRIPAK complex is required for autophagy in muscle tissue 26
Abstract 27
Introduction 27
Results 30
Discussion 50
Materials and methods 54
Reference 63
Chapter 3 - Orchestration of autophagosome fusion by STRIPAK complex components in muscle tissue 69
Abstract 69
Summary 70
Reference 74
Chapter 4 - Protocol for affinity purification-mass spectrometry interactome profiling in larvae of *Drosophila melanogaster* 75
Graphical abstract 76
Epitope-tagging, creation of transgenic flies, and validation of bait solubility 77
Fly crosses 80
Materials and equipment setup 84
Solutions to be prepared in advance 84
Solutions to be prepared on the day of the experiment 84
Step-by-step method details 85
Larval lysate preparation 85
Affinity purification 87
Elution and digestion of antibody-bound protein complexes 89
Mass Spectrometry 90
MaxQuant peptide assignments 92
Recompilation of data using LFQ Analyst 94
Expected outcomes 96
Limitations 101
Troubleshooting 101
Problem 1: 101
Potential solution: 102

Problem 2: 102
Potential solution: 102
Problem 3: 102
Potential solution: 102
Problem 4: 102
Potential solution: 102
Problem 5: 103
Potential solution: 103
Resource availability 103
Reference 104
Chapter 5 - Pavarotti and Tumbleweed function in mitophagy initiation via blockage of nuclear envelope bud formation 106
Abstract 106
Introduction 107
Results 109
Discussion 122
Materials and Methods 124
References 131
Chapter 6 - NUAK function in maintain normal muscle function 134
6.1, Introduction 134
6.2, Independent pathways control muscle tissue size and sarcomere remodeling 134
6.3, Identification of CryAB as a target of NUAK kinase activity in *Drosophila* muscle tissue. 136
References 139
Chapter 7 - Conclusions and Future Directions 140
Conclusions 140
Future Directions 141
References 146
Appendix A - Copyright Permissions 148
Appendix B - Chapter 2 Supplemental Materials 152
Appendix C - Chapter 4 Method C4.1 162
Appendix D - Chapter 5 Supplemental Materials 167

List of Figures

Figure 1.1. Number of autophagy-related publications each year from 1940 to 2023. 4
Figure 1.2. Three main types of autophagy. 5
Figure 1.3. Schematic of Chaperone-Assisted Selective Autophagy (CASA) and Bcl2-associated athanogene 3 (BAG3) domain or motif. 9
Figure 1.4. Schematic of mitochondria dynamics, PINK1-Parkin-dependent mitophagy and PINK1-Parkin-independent mitophagy. 12
Figure 1.5. The *Drosophila* life cycle and Model for NUAK function. 15
Figure 2.1. Network analysis uncovers interacting genes in *T.castaneum*. 31
Figure 2.2. Induction of Strip RNAi in muscle tissue compromises muscle structure and function. 33
Figure 2.3. Co-purification of STRIPAK complex proteins from larval muscle tissue. 35
Figure 2.4. Functional interactions between NUAK and stv with STRIPAK complex members. 39
Figure 2.5. p62-Ub and p62-Atg8a complexes accumulate in Strip RNAi muscles. 41
Figure 2.6. Knockdown of Strip impedes autophagic flux. 45
Figure 2.7. Endosome morphology is altered upon loss of Strip. 48
Figure 2.8. Lysosomal fusion appears partially blocked upon a reduction of Strip in muscles. . 50
Figure 3.1. Model depicting possible degradation routes for Strip-mediated autophagosome turnover during autophagy in *D. melanogaster* muscles. 74
Figure 4.1. Strategy to determine the solubility of a tagged bait protein. 78
Figure 4.2. LFQ-Analyst interface. 95
Figure 4.3. A sample of the quality control and analysis output available using LFQ-Analyst. .. 99
Figure 5.1. Genetic screen reveals Pav as new regulator of autophagic activity. 110
Figure 5.2. p62-Ubi and p62-Atg8a complexes accumulate in pav and tum RNAi muscles. 114
Figure 5.3. Knockdown of Pav or Tum decreases the formation of NE buds resulting in p62 clusters that overlap with faint ATP5α signal. 117
Figure 5.4. FISH and qPCR experiments demonstrate a reduction in Marf mRNA export and transcript levels in pav RNAi muscles. 121
Figure 6.1. New protein synthesis is not altered in NUAK mutant muscles. 138
Figure 6.2. human NUAK1 and fly NUAK have similar functions in muscle structure maintenance. 138
Figure 7.1. Strip protein schematics. 144
Figure 7.2. Schematic of Strip mutations that will disrupt the interaction between Strip and other STRIPAK members. 145

List of Tables

Table 4.1. *Drosophila* media. 80
Table 4.2. Key resources table. 81
Table 4.3. FLAG lysis buffer. 84
Table 4.4. FLAG lysis buffer plus inhibitors. 84
Table 4.5. Wash buffers. 85
Table 4.6. Required columns for the LFQ_Analyst_MaxQuant.txt file. 93
Table 7.1. Experimental design. 144

Acknowledgements

I am profoundly grateful to **Dr. Erika Geisbrecht**, my Ph.D. advisor, for your unwavering support over the past five years. I appreciate your role as my mentor, teacher, and friend. You have been an exceptional mentor. You astutely balanced granting me the autonomy to pursue my own research interests and explore novel areas, while simultaneously providing invaluable feedback, guidance, and encouragement. Your mentorship has been instrumental in fostering my growth as an independent researcher. As an exemplary educator, you have been instrumental in honing my academic skills. Your assistance in preparing presentations for student seminars and scientific conferences, as well as your guidance in crafting my articles and dissertation, has been indispensable. Beyond your academic roles, you have also been a trusted friend, offering sage advice that extends beyond the realm of academia.

A special thanks to **Dr. Brian Geisbrecht**, **Dr. Timothy Durrett**, and **Dr. Jocelyn McDonald**, for serving on my advisory committee, and for your advice, recommendations, and comments over the years. Thanks**, Dr. Om Prakash** for serving as interim member of the committee. Thank **Dr. Michal Zolkiewski**, for his expeditious approval of various administrative documents and his assistance in resolving payroll discrepancies with Human Resources. I am deeply appreciative of **Mr. Dave Manning's** technical support over the years, particularly for his expertise in recovering data from a compromised laptop. Last but not least, I want to acknowledge my lab colleagues: **David**, thank you for your assistance and valuable suggestions throughout my research, you helped me adjust to the lab swiftly. **Ziwei**, thank you for the help in some experiments. **Jared** and **Prabhat**, thanks for the suggestions for my preliminary exam. To undergraduate students, **Qiling**, and **Erica** for being supportive.

Dedication

This thesis is dedicated to my family. I extend my deepest gratitude to my parents, ***Shuxiang Guo*** *and* ***Shouying Zhao****, as well as my wife,* ***Ying Zhang****, for their unwavering moral support and constant encouragement. I am profoundly appreciative of my mother-in-law,* ***Cuiping Wang****, for her devoted care of my son,* ***Ethan (Zhangyi) Guo****. Your unconditional love has been invaluable; this work would not have been possible without your steadfast faith in my abilities.*

Chapter 1 - Autophagy and *Drosophila*

1.1, Major milestones in autophagy research

Benefiting from the development of electron microscopy in the 1950s, Christian de Duve found the existence of various hydrolases, which subsequently led to the identification of lysosomes as cellular organelles [1]. The word "autophagy," which means "self-eating," was created by Christian de Duve in 1963 during a lysosome conference to characterize this phenomenon by which the lysosome breaks down components of cells [2]. Christian de Duve, Albert Claude, and George E. Palade were awarded the Nobel Prize in Physiology or Medicine in 1974 for their discoveries related to the structural and functional organization of the cell. Around the same time, Mortimore's group was diligently investigating the control of autophagy by nutrition. In 1977, they found that autophagy could be induced by amino acid deprivation in perfused rat liver [3]. One year later, Pfeifer and colleagues discovered that insulin inhibited the formation of autophagic vacuoles in rat liver, which was consistent with the known control function of insulin in anabolism [4]. During the 1980s, Seglen and Gordon conducted research on the screening of organic compounds that block autophagy. In 1982, they reported that 3-methyladenine inhibited autophagic/lysosomal protein degradation, marking it as the first recognized autophagy inhibitor [5].

However, it wasn't until Yoshinori Ohsumi's work using *Saccharomyces cerevisiae* (*S. cerevisiae)* (baker's yeast) in the early 1990s that the mechanism of autophagy became evident. Ohsumi is renowned for being the first scientist to see the process of autophagy under a microscope. He utilized yeast cells with mutant vacuoles and observed the accumulation of spherical entities (autophagosomes) during cellular starvation [6]. For a long time, autophagy proved challenging to

investigate until the identification of autophagy-related genes (ATG genes) in yeast. Miki Tsukada, and Ohsumi used ethyl methanesulfonate (EMS) mutagenesis to induce mutations in *S. cerevisiae* and screen for mutants defective in autophagy. They successfully isolated 15 autophagy-defective yeast mutants, leading to the discovery of the ATG genes [7]. Ohsumi was awarded the 2016 Nobel Prize in Physiology or Medicine for his discoveries of mechanisms for autophagy. Also in the early 1990s, Blommaart *et al's*. work using rat hepatocytes demonstrated that rapamycin reduces the phosphorylation of ribosomal protein S6 (RPS6). Since RPS6 phosphorylation suppresses autophagy, thus rapamycin can initiate the autophagic process [8].

After the identification of the ATG genes, autophagy research sped up like a rocket. By the end of the 1990s, several groundbreaking discoveries were published. In 1998, Mizushima's team used Western blot analysis to discover the Atg12 conjugation system, a crucial step essential for the generation of autophagosomes. They found that the high molecular weight band corresponding to the predicted molecular weight of Atg12 was absent in *atg5*, *atg7*, or *atg10* mutants [9]. One year later, Liang *et al*. found that *beclin 1* is a mammalian autophagy gene. Beclin 1's ability to promote autophagy is linked to the reduction of MCF7 (a human breast cancer cell line) in cellular proliferation, in vitro clonigenicity, and tumorigenesis in nude mice [10]. At the beginning of the 20th century, Ichimura and colleagues determined that Atg8 in yeast is the homologue of mammalian microtubule-associated protein 1A/1B-light chain 3 (LC3). In the same year, Kabeya's team found Atg8/LC3 was present inside and outside of autophagosome membranes using immunoelectron microscopy. Since this discovery, LC3 has been used as the main autophagosomal marker [11, 12].

Since the 20th century, numerous studies have shown the connection between autophagy and organism health. For instance, Ravikumar *et al.* discovered that autophagy has a

neuroprotective effect [13]. Melendez's team demonstrated the anti-aging effect of autophagy [14]. In the meantime, Kuma and colleagues showed that at birth, neonates adapt to the nutritional shortage between the trans-placental nutrient supply interruption and the supply of milk by inducing autophagy [15]. Soon after, Komatsu's lab proved that autophagy deficiency within the central nervous system contributes to neurodegeneration in mouse models [16]. Furthermore, Hara *et al.* identified that a lack of basal autophagy in neural cells is associated with the development of neurodegenerative disorders in mice [17]. Hampe and Rioux's team employed a genome-wide association study (GWAS) to determine ATG16L1 as a multifunctional susceptibility factor in Crohn's disease [18, 19]. Identifying the role of ATG16L1 in Crohn's disease promotes further investigation into the diverse functions and interactions of ATG proteins, thereby facilitating the development of novel interventions and deepening our understanding of complex disease mechanisms. For example, Narendra's research group illustrated that Parkinson protein 2 (Parkin) enhances the autophagic process of damaged mitochondria, suggesting that the failure to eliminate dysfunctional mitochondria may contribute to the pathogenesis of Parkinson's disease [20]. Insights into the function of Parkin encouraged research into autophagy-modulating drugs, which could prove beneficial not only for Parkinson's disease treatment but also for other illnesses associated with impaired autophagy. Haack's lab and Saitsu's lab concurrently uncovered that mutations in the human autophagy gene WD repeat domain 45 (WDR45) are responsible for static encephalopathy of childhood with neurodegeneration in adulthood (SENDA) disease [21, 22]. Their findings demonstrated that autophagy serves a protective role against neurodegenerative and neurodevelopmental disorders. According to PubMed, since 1940, there has been a substantial rise in the number of publications related to autophagy every year, from 1 publication in 1940 to 10040

publications in 2023 (**Figure 1.1**). The above overview presents significant findings in the autophagy field. However, it does not encompass all essential discoveries due to space limitations.

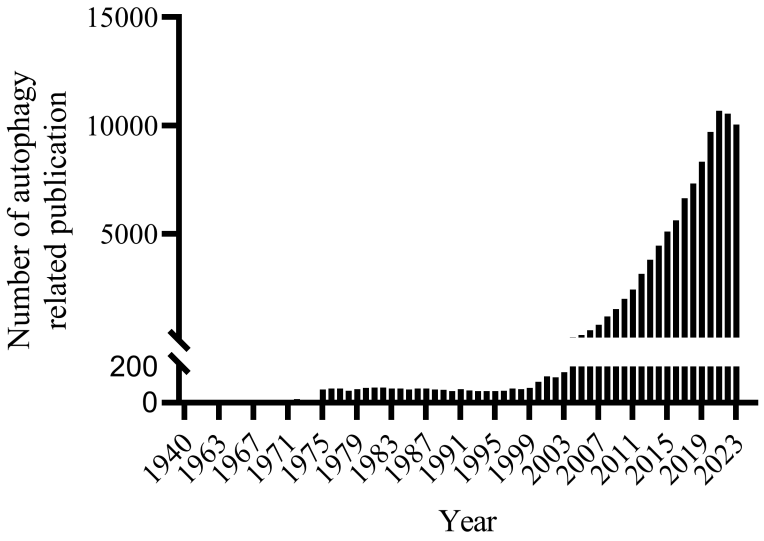


Figure 1.1. Number of autophagy-related publications each year from 1940 to 2023.
The data was acquired from PubMed by searching the term "autophag*", the asterisk ensuring that all words beginning with “autophag” were included in the result.

1.1, A brief overview of autophagy

Autophagy is a universal, evolutionarily conserved mechanism that exists in all eukaryotic cells [23]. Organisms undergo autophagy in response to a variety of stimuli, such as hypoxia, reduced insulin levels, decreased ATP levels, and amino acid starvation [24]. Depending on the nature of the cargo and the unique molecular mechanisms that direct these cargo into the lysosome, autophagy can be categorized as macroautophagy, microautophagy, or chaperone-mediated autophagy (CMA) [25-28], as shown in **Figure 1.2** [29, 30].

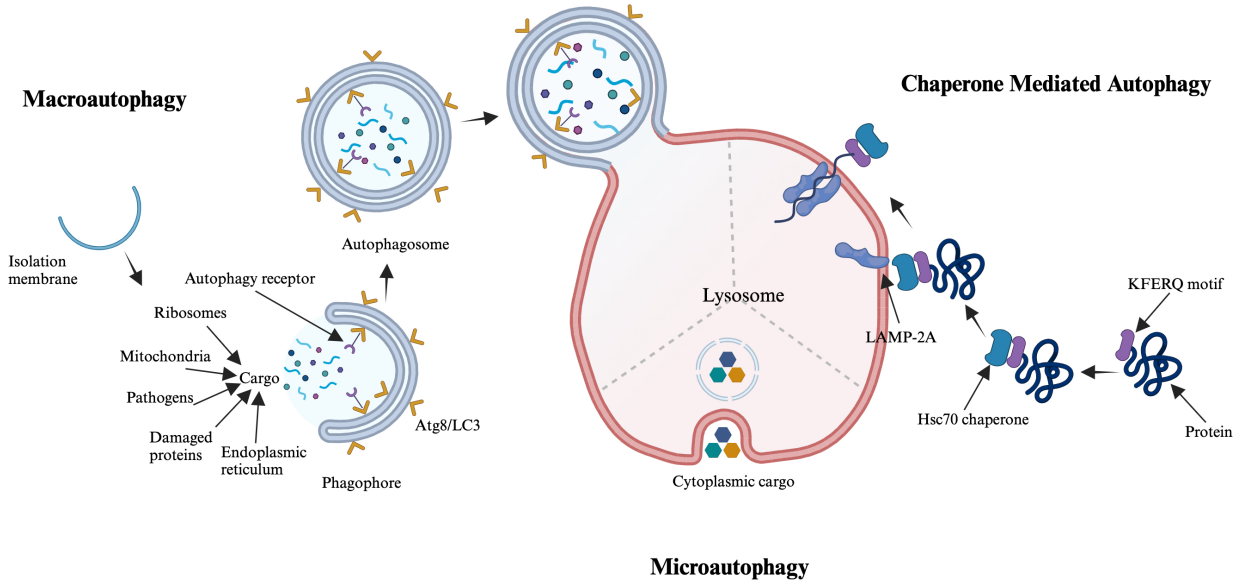


Figure 1.2. Three main types of autophagy.

Autophagy can be classified into three main types, macroautophagy, microautophagy, or chaperone-mediated autophagy (CMA) (29-30). Macroautophagy involves the double-membrane structure autophagosome formation. Microautophagy is the process of the direct absorption of cellular constituents into lysosomes. CMA requires chaperones to recognize the KFERQ-like motifs for protein degradation. (Created using BioRender.com).

Macroautophagy, hereafter referred to as autophagy, is a multi-step process progressing from initiation, phagophore nucleation, phagophore elongation, autophagosome formation, and fusion of the autophagosome with lysosome for cargo degradation. Some of these steps are under the control of distinct evolutionarily conserved Atg protein complexes. For instance, the Atg1 complex, consisting of Atg11, Atg13, Atg 17, Atg 29, and Atg 31, functions in the initiation step. Autophagosome formation requires the Atg12 conjugation system, including Atg5, Atg7, Atg 10, 12 and Atg 16, while the Atg8 conjugation system contains Atg 3 and Atg 7 [9, 29]. Autophagy is associated with lifespan extension as it can function at a basal level for the degradation of damaged proteins and pathogens and for the removal of extra or damaged organelles. Autophagy

is also inducible by various stress conditions, such as nutrient limitation, and oxidative stress, therefore contributing to cellular homeostasis [31].

Depending on the cellular conditions and signaling events, autophagy can be either non-selective or selective. Non-selective autophagy occurs under stress conditions, such as starvation and hypoxia. As a nutritional sensor, AMP-activated protein kinase (AMPK) is activated when nutrients are lacking. This causes AMPK to phosphorylate and activate the unc-51-like kinase 1 (ULK1)/Atg1 (yeast). The activation of ULK1/Atg1 drives the formation of the phagophore, promoting autophagosome production across the cell and nonselectively breaking down the cytoplasm [32-34]. In contrast to non-selective autophagy, selective autophagy specifically targets damaged proteins, or organelles, such as mitochondria, ribosomes, and endoplasmic reticulum (ER), as well as invasive pathogens for degradation [34]. Although the Atg family proteins involved in different subtypes of selective autophagy are conserved, they necessitate distinct autophagy receptors. For example, p62/SQSTM1 is an autophagy receptor identifying damaged mitochondria, whereas FAM134B is a significant autophagy receptor detecting the ER [34-37].

Several types of selective autophagy have unique names based on the specific cargo for degradation - degradation of mitochondria (mitophagy) [38-41], ribosomes (ribophagy) [42], endoplasmic reticulum (ERphagy) [37], aggregated/damaged proteins (aggrephagy) [43-46] or pathogens (xenophagy) [47-50] (Figure 1.2). Selective autophagy is crucial for organisms' health for various reasons: it is essential for maintaining cellular homeostasis and serves as a cell-autonomous defensive mechanism against viruses [51, 52]. Also, impairments in selective autophagy are linked to neurodegenerative disorders, including Parkinson's disease, Amyotrophic lateral sclerosis (ALS), and Frontotemporal dementia (FTD) [53].

Microautophagy is a mechanism that entails the direct absorption of cellular constituents into lysosomes for degradation. This process is defined by the invagination of the lysosomal membrane, resulting in the formation of tubules that detach into the lysosome [54, 55] (Figure 1.2). The primary roles of microautophagy include the preservation of organellar size, membrane homeostasis, and cell survival under nitrogen limitation [56, 57]. In mammalian cells, microautophagy is often regarded as a non-selective process, which means that it absorbs and degrads cytoplasmic material without specific cargo receptors. However, three types of selective microautophagy are observed in yeast, including piecemeal microautophagy of the nucleus (PMN) for the degradation of the non-essential components, micropexophagy, which specifically engulfs damaged or excess peroxisomes, and micromitophagy, which breaks down the mitochondria [58].

Unlike macroautophagy and microautophagy, CMA involves the transport of soluble cytoplasmic proteins across the lysosomal membrane, as opposed to their sequestration and delivery via membrane fusion (Figure 1.2). Another way that CMA differs from other types of autophagy is that it is extremely selective, only breaking down proteins that have a certain amino acid sequence (KFERQ-like motifs) [59, 60]. Proteins that contain KFERQ-like motifs bind to the heat shock-cognate protein of 70 KDa (Hsc70) chaperone. This complex then interacts with the cytosolic tail of the monomer form of lysosome-associated membrane protein type 2A (LAMP-2A19) on the surface of the lysosomes [61]. Subsequently, LAMP-2A forms a complex to transform into a multimer. The protein must unfold to pass through the lysosomal membrane, even though it can attach to the receptor while remaining folded [62]. The unfolding process happens before the LAMP-2A complex is completely built, and it is most likely mediated by Hsc70 and a few of its cochaperones found at the lysosomal membrane [63].

1.3, BAG3 and Chaperone-Assisted Selective Autophagy (CASA)

CASA is a biological mechanism that selectively degrades damaged and/or misfolded proteins through chaperone and ubiquitin-dependent pathways [64]. However, in contrast to CMA, CASA necessitates the fusion of the autophagosome with the lysosome (**Figure 1.3A**). The CASA complex is composed of three main proteins, heat shock protein family A (HSPA)/Hsc70, heat shock protein family B member 8 (HSPB8), and Bcl2-associated athanogene 3 (BAG3). The chaperones HSPA/HSC70 and HSPB8 recognize damaged and/or /misfolded client protein under regulation of the cochaperone BAG3 [64-66]. BAG3 also stimulates the binding of the STIP1 homology and U-box containing protein 1 (STUB1)/carboxyl terminus of Hsc70-interacting protein (CHIP) to the HSPA complex [67]. STUB1 is an E3 ubiquitin ligase that ubiquitinates the HSPA-HSPB8-BAG3 complex-bound client protein [68, 69]. The autophagic ubiquitin adaptor or autophagy receptor p62/SQSTM1 is recruited to ubiquitinated client proteins. This adapter protein then binds to Atg8/LC3 to coordinate autophagosome formation. The autophagosome contains client proteins that are delivered to the lysosome for client protein degradation [67].

BAG3 and CASA play a key role in protein quality control and maintenance of post-mitotic cells, including neurons and muscle cells [70-72]. BAG3 proteins contains multiple domains or motifs, including one WW domain (around 40 amino acids with two conserved tryptophan residues), two isoleucine–proline–valine (IPV) motifs, two 14-3-3 binding motifs, one proline-rich (PXXP) region, and a BAG domain (**Figure 1.3B**). Each type of domain or motif can engage with various proteins, hence implicating BAG3 in several biological processes (**Figure 1.3B**) [73, 74]. For instance, BAG3 interacts with synaptopodin-2 (SYNPO2) through its WW domain to facilitate autophagosome production during CASA [64, 75, 76]. BAG3 also mediates CASA complex assembly through the binding of IPV motifs to small heat shock

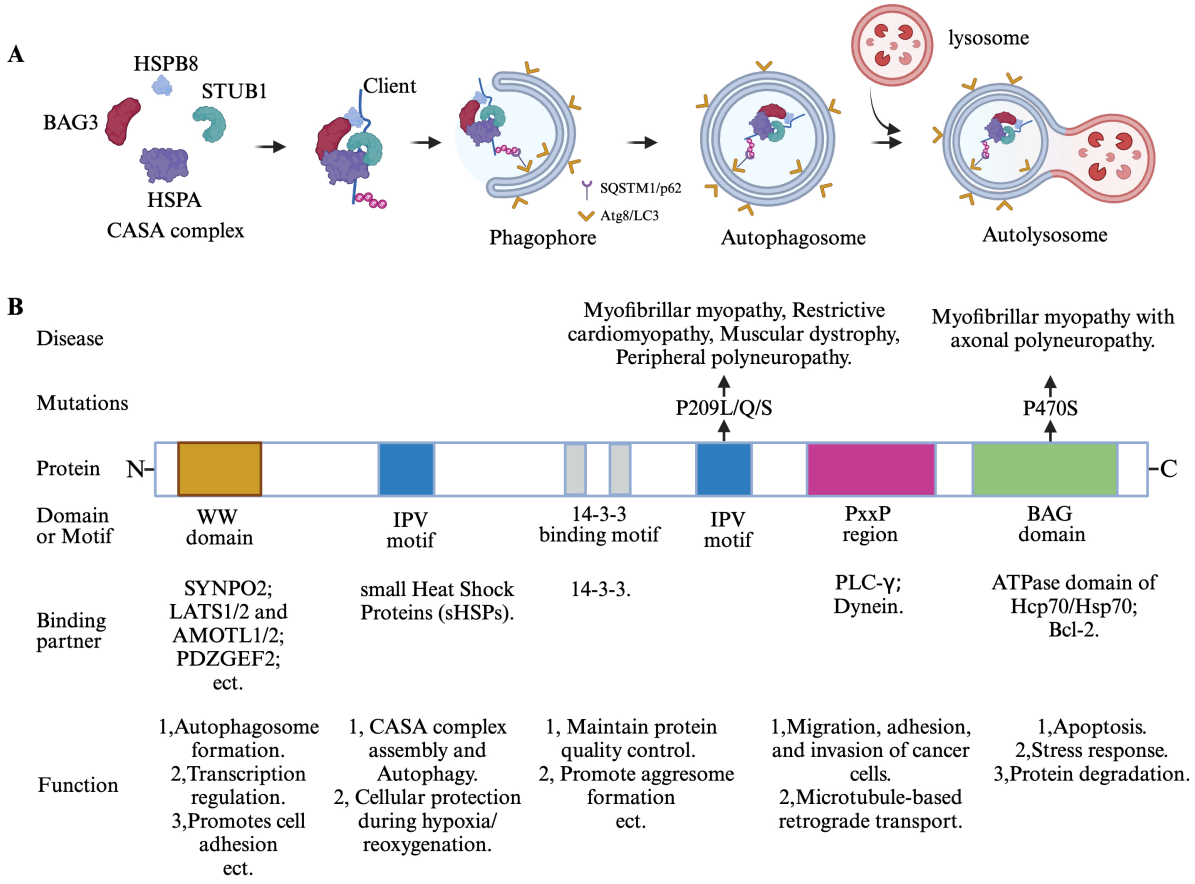


Figure 1.3. Schematic of Chaperone-Assisted Selective Autophagy (CASA) and Bcl2-associated athanogene 3 (BAG3) domain or motif.

A, The CASA complex contains three main proteins, BAG3, HSPB8 and HSPA(HSP70). The HSPA-HSPB8-BAG3 complex recognizes and binds to the client protein, and the STUB1 is recruited to the complex and ubiquitinated the client protein. The ubiquitinated client protein is recognized by the autophagy receptor and forms autophagosome, then autophagosome fuses with lysosome for protein degradation. B, BAG3 is a multi-domain/motif/binding region protein. It contains one WW domain, two IPV motifs, one 14-3-3 binding motif, one PxxP region, and one BAG domain. Different domain or motifs has different binding partners, thus BAG3 has multiple functions. BAG3 mutations are associated with myofibrillar myopathy, restrictive cardiomyopathy, muscular dystrophy, and peripheral polyneuropathy. (Created using BioRender.com).

proteins (sHSPs) such as HSPB8 [66, 77]. BAG3 functions in transcription regulation, and cell growth regulation through binding with large tumor suppressor 1/2 (LATS1/2) and angiomotin-like protein 1/2 (AMOTL1/2) via the WW domain. This binding prevents the LATS1/2 and AMOTL1/2 from binding to their transcription coactivators yes-associated protein (YAP) and the

transcriptional coactivator with PDZ-binding motif (TAZ)[64, 78]. Moreover, BAG3 enhances cell adhesion via its WW domain, which interacts with the PDZ domain containing guanine nucleotide exchange factor 2 (PDZGEF2). This binding activates the small GTPase Rap1, which regulates integrin-mediated cell adhesion [79].

BAG3 is a multi-functional protein required for maintaining normal muscle cell function and mutations in BAG3 are associated with myopathy. BAG3-related myopathy, also known as myofibrillar myopathy (MFM), was first identified in 2009 in three children and is caused by the Pro209Leu (P209L) mutation within the second IPV motif (**Figure 1.3B**) [80]. Additional BAG3 mutations have been identified to cause myopathy as well as other diseases. For example, the BAG3 Pro209Gln (P209Q), Pro209Ser (P209S), or Pro470Ser (P470S) mutations can cause myofibrillar myopathy, restrictive cardiomyopathy, muscular dystrophy, or peripheral polyneuropathy [79, 81-84]. While BAG3 is known for its involvement in protein quality control and MFM, further research is necessary to elucidate BAG3 interactors and the signaling pathways it modulates [84].

1.4, General overview of mitochondrial dynamics and mitophagy

Mitochondria are membrane-enclosed organelles located within the cells of most eukaryotes and are known as the "powerhouse of the cell" due to their role in producing adenosine triphosphate (ATP) as the cells' main energy source via oxidative phosphorylation [85]. Mitochondria are dynamic organelles that undergo changes in shape, number, and position within a cell. These changes result from a cycle of fission and fusion, which helps maintain the size and integrity of mitochondria [86]. Mitochondrial fusion is a process that amalgamates the membranes of two mitochondria, whereas fission is the converse, wherein one mitochondrion divides into two.

The mitochondrial assembly regulatory factor (Marf)/Mitofusin (MFN) encodes a dynamin-family GTPase that promotes the fusion of the outer mitochondrial membrane (OMM), whereas Dynamin-related protein 1 (Drp1) encodes a dynamin-like GTPase that governs mitochondrial fission (**Figure 1.4A**) [87-92]. Mitochondrial fission can generate impaired daughter units that will be degraded by mitophagy. Conversely, mitochondrial fusion might function in diluting impaired daughter mitochondria and thereby prevent their removal [92, 93].

Mitophagy is a type of selective autophagy that serves as a mitochondria quality control mechanism by specifically degrading dysfunctional or excess mitochondria [20, 94, 95]. In mammals, mitophagy can be classified as PINK1-Parkin-dependent mitophagy or PINK1-Parkin-independent mitophagy [20, 94, 96-98]. For PINK1-Parkin-dependent mitophagy (**Figure 1.4B**), under normal conditions, PINK1 is synthesized in the cytoplasm and transported into the mitochondria through the translocase of the outer membrane 20 (TOM20) complex and the translocase of the inner membrane (Tim) complex [99]. Under stress circumstances such as reactive oxygen species (ROS), mitochondrial depolarization, irradiation, or chemotherapeutic drugs, the mitochondrial membrane potential ($\Delta\Psi m$) is diminished or abolished, leading to the obstruction of PINK1 import and its accumulation on the outer mitochondrial membrane (OMM) [99, 100]. The accumulation of PINK1 on OMM recruits the cytoplasmic Parkin protein to mitochondria. Upon recruitment, PINK1 phosphorylates Parkin, hence activating its E3 ubiquitin ligase function. However, how Parkin interacts with PINK1 is still not clear (**Figure 1.4B**)[101]. One possibility is that PINK1 physically interacts with Parkin, which is suggested by in vitro co-immunoprecipitation [102, 103]. A second possibility is that PINK1 directly phosphorylates Parkin for activation. Evidence for this is provided by in vitro kinase assays [96]. Once Parkin is recruited to mitochondria and activated, it ubiquitinates substrates on the OMM, such as

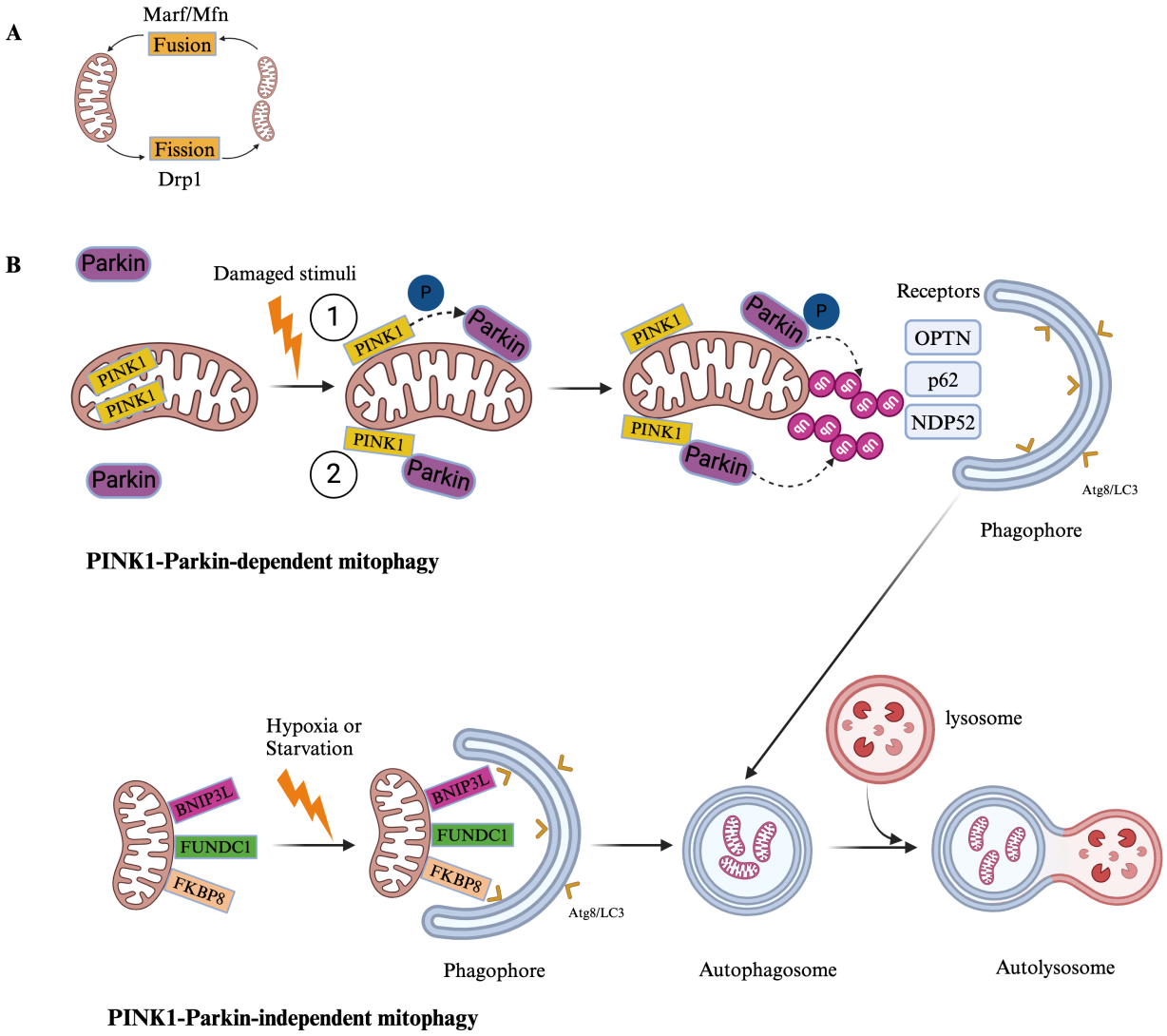


Figure 1.4. Schematic of mitochondria dynamics, PINK1-Parkin-dependent mitophagy and PINK1-Parkin-independent mitophagy.

A, mitochondria are considered as "dynamic" organelles, which undergo Marf/Mfn mediate fusion and Drp1 mediate fission. B, PINK1-Parkin-dependent mitophagy usually happens when mitochondria get damaged. The resulting mitochondrial membrane potential ($\Delta\Psi m$) drops or disappears making the PINK1 accumulate on the outer mitochondria membrane (OMM), then PINK1 recruits Parkin and activates it. The activated Parkin ubiquitinates the protein on the OMM. Then autophagy receptors recognize the ubiquitinated proteins, form autophagosome for degradation. PINK1-Parkin-independent mitophagy relies on the direct interaction between the receptor protein located on the outer mitochondrial membrane (OMM), such as BNIP3L, FUNDC1 or FKBP8, and Atg8/LC3 to form autophagosome for mitochondria turnover. (Created using BioRender.com).

MFN1/2, TOM20, and the voltage-dependent anion-selective channel 1/2/3 (VDAC1/2/3) (38). Autophagy receptors, including optineurin (OPTN), p62/SQSTM1, and nuclear dot protein 52 kDa (NDP52), will bind to polyubiquitin chains on OMM substrates and recruit Atg8/LC3 to form autophagosomes, eventually fusing with the lysosome for the mitochondria degradation [38, 67, 96, 98-103].

In contrast with PINK1-Parkin-dependent mitophagy, PINK1-Parkin-independent mitophagy does not require ubiquitin-p62 recognition. Instead, it relies on mitophagy receptors on the OMM directly binding with Atg8/LC3 to form the autophagosome for mitochondria turnover [97, 104] (**Figure 1.4B**). Several proteins on the surface of OMM have been identified as receptors during PINK1-Parkin-independent mitophagy. Under normal conditions, BCL2 interacting protein 3 like (BNIP3L)/NIX exits on the OMM in an inactive monomer form. Upon negative stimuli, usually hypoxia or starvation, the BNIP3L/NIX receptor is dephosphorylated to form the active dimer form, thus enhancing the binding with Atg8/LC3 to induce mitophagy [104, 105]. FUN14 domain containing 1 (FUNDC1) is a receptor for hypoxia-induced mitophagy and under hypoxic conditions, FUNDC1 is dephosphorylated at Tyr 18, increasing its binding to Atg8/LC3 [104, 106]. FK506-binding protein 8 (FKBP8) is anchored in the OMM and has a cytosolic N-terminus. The N-terminal LIR motif of FKBP8 increased the affinity for Atg8/LC3 binding under stress conditions (hypoxia or starvation), thus inducing mitophagy [104, 107].

In skeletal muscle tissue where energy demands are very high, the maintenance of efficient mitochondrial function is critical for preserving muscle health. Numerous research groups have demonstrated that mitophagy plays a vital role in sustaining muscle function by facilitating the removal of damaged mitochondria. For instance, a recent study revealed that impaired mitophagy in muscle cells resulted in locomotor defects in *Drosophila* larvae [108]. Mitophagy also promotes

muscle regeneration (through myogenesis) following exercise-induced damage as it can facilitate the rapid turnover of dysfunctional mitochondria, which enables the synthesis of more efficient, functional mitochondria [109]. Enhancing mitophagy might be a potential therapeutic strategy for addressing muscle mitochondrial dysfunction. Urolithin A, a mitophagy activator, has demonstrated the potential to improve muscle function in models of Duchenne muscular dystrophy (DMD) [110].

1.5, *Drosophila* as a model of skeletal muscle autophagy and diseases

Drosophila melanogaster, commonly referred to as the fruit fly, exhibits a significantly different morphology compared to humans. Despite this difference, the fundamental cellular and developmental processes, including signaling and autophagy pathways, remain evolutionarily conserved in *Drosophila*. Nearly every human organ has a corresponding structure in flies. Moreover, the *Drosophila* genome shares 60% homology with the human genome and it is estimated that approximately 75% of the genes associated with human disorders have homologs in *Drosophila* [111]. Additional advantages in using *Drosophila* for human disease research include less genetic redundancy, a vast genetic toolkit to overexpress or decrease gene function, a rapid life cycle, and lower maintenance costs [111-113].

Since the life cycle of *Drosophila* consists of four distinguishable stages: embryo, larva, pupa, and adult, each of these stages can be utilized to investigate different aspects of development, genetics, or environmental influences, thereby rendering *Drosophila* a valuable model organism for a diverse array of biological research (**Figure 1.5A**). For instance, the embryo stage may be employed to examine gene expression patterns throughout early development, aiding in the identification of genes essential for body plan formation. Also, researchers can investigate

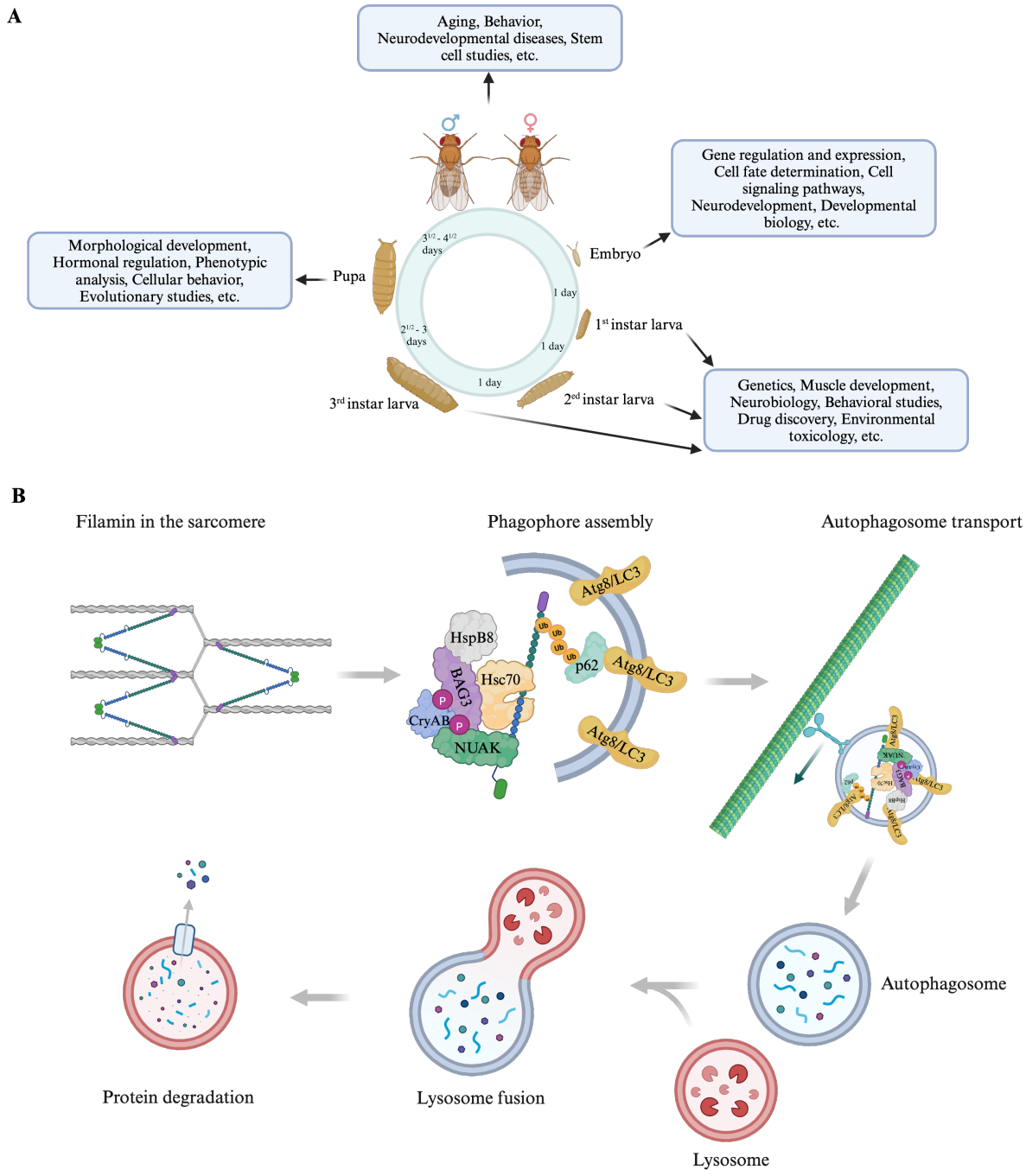


Figure 1.5. The *Drosophila* life cycle and Model for NUAK function.

A, The *Drosophila* life cycle is characterized by four distinct stages: embryo, larva, pupa, and adult. Different stages of *Drosophila* can be used to investigate different biological questions. B, NUAK phosphorylated damaged Filamin protein, CryAB is normally bound to Filamin. CASA complex detects and binds with damaged Filamin protein with the help of NUAK. The addition of the polyubiquitin chain on Filamin recruits p62 and Atg8a to form autophagosomes, then autophagosomes are transported to the site of the lysosome, and fused with lysosome for protein degradation. (Created using BioRender.com).

signaling pathways that control cell differentiation and organogenesis or the influence of environmental variables during embryogenesis [114-116]. In larval stages, different tissues can be employed to address specific biological questions. For example, the imaginal discs of the *Drosophila* larvae serve as a model for investigating the coordination of cell growth and division[117]. Additionally, the fat body, analogous to mammalian adipose tissue, facilitates the examination of mechanisms regulating fat metabolism[118]. Larval muscle tissue can be induced to undergo contraction and relaxation, thereby simulating exercise and offering a model for studying the effects of physical activity[119]. Furthermore, the larval stage is particularly suitable for exploring the impact of different diets on development and growth, helping researchers gain valuable insights into nutrient metabolism [120]. The pupa stage is crucial for the transformation from larva to adult. These immobile and transparent pupae are ideal for live imaging and studying metamorphosis. Another characteristic of the pupa stage is that it is very sensitive to hypoxia, making it suitable for the identification of novel hypoxia-related mechanisms involved in cell and tissue growth [117, 121-123]. Adult flies exhibit behaviors such as mating, feeding, and learning, which allow the investigation of the genetic underpinnings of behavior. Furthermore, the adult stage serves as a valuable model for examining aging processes and identifying genes associated with longevity.

More importantly, *Drosophila* can be utilized to study human diseases, including neurodegenerative disorders and muscle diseases [124-126]. Human MFM is associated with gene mutations, these genes include *desmin* (DES), *myotilin* (MYOT), *αB-crystallin* (CRYAB), *BAG3*, and *filamin-C* (FLNC). MFM is characterized by the breakdown of myofibrils and the abnormal accumulation of degradation products within the muscle tissue [80, 127, 128]. Multiple research teams have determined which proteins preferentially accumulate in biopsies of human MFM

patients using a combination of laser microdissection and mass spectrometry. Surprisingly, they found Desmin, Filamin C, and αB-crystallin proteins are always over-represented in protein aggregates from patients with myotilinopathy (*myotilin* gene mutation associated MFM), filaminopathy (*filamin-C* gene mutation associated MFM), and desminopathy (*desmin* gene mutation associated MFM) patients [127-130].

As mentioned in Chapter 1.3, BAG3 mutations result in MFM. To determine whether *Drosophila* could be used to study BAG3-related MFM, our lab examined loss-of-function of *Drosophila* Starvin (Stv), the ortholog of BAG3, using either RNA interference (RNAi) or mutant alleles [131] followed by immunostaining with anti-Filamin/FLNC antibody and phalloidin (F-actin, marker for muscle cells). We found the Filamin/FLNC abnormally accumulated within regions that lacked the typical F-actin sarcomere structure in *stv RNAi* or mutant muscles [131]. This result is consistent with the conclusion that FLNC serves as an important cargo for CASA [67]. We also found that the non-specific serine/threonine protein kinase NUAK physically and genetically interacts with the Stv-Hsc70 complex and plays a role in Filamin degradation through CASA (**Figure 1.5B**). While many proteins associated with the canonical autophagy pathway have been identified, discovering new regulators might improve our comprehension of tissue- and stress-specific responses.

References

1. DE DUVE C, PRESSMAN BC, GIANETTO R, WATTIAUX R, APPELMANS F. Tissue fractionation studies. 6. Intracellular distribution patterns of enzymes in rat-liver tissue. Biochem J. 1955 Aug;60(4):604-17. PMID: 13249955. doi: 10.1042/bj0600604.
2. Focusing on autophagy. Nat Cell Biol. 2010 Sep;12(9):813. PMID: 20811352. doi: 10.1038/ncb0910-813.
3. Mortimore GE, Schworer CM. Induction of autophagy by amino-acid deprivation in perfused rat liver. Nature. 1977 Nov 10;270(5633):174-6. PMID: 927529. doi: 10.1038/270174a0.
4. Pfeifer U. Inhibition by insulin of the formation of autophagic vacuoles in rat liver. A morphometric approach to the kinetics of intracellular degradation by autophagy. J Cell Biol. 1978 Jul;78(1):152-67. PMID: 670291. doi: 10.1083/jcb.78.1.152.
5. Seglen PO, Gordon PB. 3-Methyladenine: specific inhibitor of autophagic/lysosomal protein degradation in isolated rat hepatocytes. Proceedings of the National Academy of Sciences. 1982;79(6):1889-92.
6. Takeshige K, Baba M, Tsuboi S, Noda T, Ohsumi Y. Autophagy in yeast demonstrated with proteinase-deficient mutants and conditions for its induction. J Cell Biol. 1992 Oct;119(2):301-11. PMID: 1400575. doi: 10.1083/jcb.119.2.301.
7. Tsukada M, Ohsumi Y. Isolation and characterization of autophagy-defective mutants of Saccharomyces cerevisiae. FEBS Lett. 1993 Oct 25;333(1-2):169-74. PMID: 8224160. doi: 10.1016/0014-5793(93)80398-e.
8. Blommaart EF, Luiken JJ, Blommaart PJ, van Woerkom GM, Meijer AJ. Phosphorylation of ribosomal protein S6 is inhibitory for autophagy in isolated rat hepatocytes. J Biol Chem. 1995 Feb 03;270(5):2320-6. PMID: 7836465. doi: 10.1074/jbc.270.5.2320.
9. Mizushima N, Noda T, Yoshimori T, Tanaka Y, Ishii T, George MD, et al. A protein conjugation system essential for autophagy. Nature. 1998 Sep 24;395(6700):395-8. PMID: 9759731. doi: 10.1038/26506.
10. Liang XH, Jackson S, Seaman M, Brown K, Kempkes B, Hibshoosh H, et al. Induction of autophagy and inhibition of tumorigenesis by beclin 1. Nature. 1999 Dec 09;402(6762):672-6. PMID: 10604474. doi: 10.1038/45257.
11. Ichimura Y, Kirisako T, Takao T, Satomi Y, Shimonishi Y, Ishihara N, et al. A ubiquitin-like system mediates protein lipidation. Nature. 2000 Nov 23;408(6811):488-92. PMID: 11100732. doi: 10.1038/35044114.
12. Kabeya Y, Mizushima N, Ueno T, Yamamoto A, Kirisako T, Noda T, et al. LC3, a mammalian homologue of yeast Apg8p, is localized in autophagosome membranes after processing. EMBO J. 2000 Nov 01;19(21):5720-8. PMID: 11060023. doi: 10.1093/emboj/19.21.5720.
13. Ravikumar B, Duden R, Rubinsztein DC. Aggregate-prone proteins with polyglutamine and polyalanine expansions are degraded by autophagy. Human molecular genetics. 2002;11(9):1107-17.
14. Meléndez A, Tallóczy Z, Seaman M, Eskelinen EL, Hall DH, Levine B. Autophagy genes are essential for dauer development and life-span extension in C. elegans. Science. 2003 Sep 05;301(5638):1387-91. PMID: 12958363. doi: 10.1126/science.1087782.
15. Kuma A, Hatano M, Matsui M, Yamamoto A, Nakaya H, Yoshimori T, et al. The role of autophagy during the early neonatal starvation period. Nature. 2004 Dec 23;432(7020):1032-6. PMID: 15525940. doi: 10.1038/nature03029.

16. Komatsu M, Waguri S, Chiba T, Murata S, Iwata J-i, Tanida I, et al. Loss of autophagy in the central nervous system causes neurodegeneration in mice. Nature. 2006;441(7095):880-4.
17. Hara T, Nakamura K, Matsui M, Yamamoto A, Nakahara Y, Suzuki-Migishima R, et al. Suppression of basal autophagy in neural cells causes neurodegenerative disease in mice. Nature. 2006 Jun 15;441(7095):885-9. PMID: 16625204. doi: 10.1038/nature04724.
18. Hampe J, Franke A, Rosenstiel P, Till A, Teuber M, Huse K, et al. A genome-wide association scan of nonsynonymous SNPs identifies a susceptibility variant for Crohn disease in ATG16L1. Nat Genet. 2007 Feb;39(2):207-11. PMID: 17200669. doi: 10.1038/ng1954.
19. Rioux JD, Xavier RJ, Taylor KD, Silverberg MS, Goyette P, Huett A, et al. Genome-wide association study identifies new susceptibility loci for Crohn disease and implicates autophagy in disease pathogenesis. Nature genetics. 2007;39(5):596-604.
20. Narendra D, Tanaka A, Suen DF, Youle RJ. Parkin is recruited selectively to impaired mitochondria and promotes their autophagy. J Cell Biol. 2008 Dec 01;183(5):795-803. PMID: 19029340. doi: 10.1083/jcb.200809125.
21. Haack TB, Hogarth P, Kruer MC, Gregory A, Wieland T, Schwarzmayr T, et al. Exome sequencing reveals de novo WDR45 mutations causing a phenotypically distinct, X-linked dominant form of NBIA. Am J Hum Genet. 2012 Dec 07;91(6):1144-9. PMID: 23176820. doi: 10.1016/j.ajhg.2012.10.019.
22. Saitsu H, Nishimura T, Muramatsu K, Kodera H, Kumada S, Sugai K, et al. De novo mutations in the autophagy gene WDR45 cause static encephalopathy of childhood with neurodegeneration in adulthood. Nat Genet. 2013 Apr;45(4):445-9, 9e1. PMID: 23435086. doi: 10.1038/ng.2562.
23. Reggiori F, Klionsky DJ. Autophagy in the eukaryotic cell. Eukaryotic cell. 2002;1(1):11-21.
24. Ichimiya T, Yamakawa T, Hirano T, Yokoyama Y, Hayashi Y, Hirayama D, et al. Autophagy and Autophagy-Related Diseases: A Review. Int J Mol Sci. 2020 Nov 26;21(23). PMID: 33255983. doi: 10.3390/ijms21238974.
25. Yang Z, Klionsky DJ. Mammalian autophagy: core molecular machinery and signaling regulation. Curr Opin Cell Biol. 2010 Apr;22(2):124-31. PMID: 20034776. doi: 10.1016/j.ceb.2009.11.014.
26. Huber LA, Teis D. Lysosomal signaling in control of degradation pathways. Curr Opin Cell Biol. 2016 Apr;39:8-14. PMID: 26827287. doi: 10.1016/j.ceb.2016.01.006.
27. Yoshii SR, Mizushima N. Monitoring and Measuring Autophagy. Int J Mol Sci. 2017 Aug 28;18(9). PMID: 28846632. doi: 10.3390/ijms18091865.
28. Fukuda T, Kanki T. Mechanisms and Physiological Roles of Mitophagy in Yeast. Mol Cells. 2018 Jan 31;41(1):35-44. PMID: 29370687. doi: 10.14348/molcells.2018.2214.
29. Parzych KR, Klionsky DJ. An overview of autophagy: morphology, mechanism, and regulation. Antioxid Redox Signal. 2014 Jan 20;20(3):460-73. PMID: 23725295. doi: 10.1089/ars.2013.5371.
30. Stolz A, Ernst A, Dikic I. Cargo recognition and trafficking in selective autophagy. Nat Cell Biol. 2014 Jun;16(6):495-501. PMID: 24875736. doi: 10.1038/ncb2979.
31. Yang Z, Klionsky DJ. An overview of the molecular mechanism of autophagy. Autophagy in infection and immunity. 2009:1-32.
32. Kim J, Kundu M, Viollet B, Guan KL. AMPK and mTOR regulate autophagy through direct phosphorylation of Ulk1. Nat Cell Biol. 2011 Feb;13(2):132-41. PMID: 21258367. doi: 10.1038/ncb2152.

33. Alers S, Löffler AS, Wesselborg S, Stork B. Role of AMPK-mTOR-Ulk1/2 in the regulation of autophagy: cross talk, shortcuts, and feedbacks. Molecular and cellular biology. 2012;32(1):2-11.
34. Feng Y, He D, Yao Z, Klionsky DJ. The machinery of macroautophagy. Cell Res. 2014 Jan;24(1):24-41. PMID: 24366339. doi: 10.1038/cr.2013.168.
35. Ke P-Y. The multifaceted roles of autophagy in flavivirus-host interactions. International journal of molecular sciences. 2018;19(12):3940.
36. Kumar AV, Mills J, Lapierre LR. Selective Autophagy Receptor p62/SQSTM1, a Pivotal Player in Stress and Aging. Front Cell Dev Biol. 2022;10:793328. PMID: 35237597. doi: 10.3389/fcell.2022.793328.
37. Khaminets A, Heinrich T, Mari M, Grumati P, Huebner AK, Akutsu M, et al. Regulation of endoplasmic reticulum turnover by selective autophagy. Nature. 2015 Jun 18;522(7556):354-8. PMID: 26040720. doi: 10.1038/nature14498.
38. Sarraf SA, Raman M, Guarani-Pereira V, Sowa ME, Huttlin EL, Gygi SP, et al. Landscape of the PARKIN-dependent ubiquitylome in response to mitochondrial depolarization. Nature. 2013 Apr 18;496(7445):372-6. PMID: 23503661. doi: 10.1038/nature12043.
39. Lazarou M, Sliter DA, Kane LA, Sarraf SA, Wang C, Burman JL, et al. The ubiquitin kinase PINK1 recruits autophagy receptors to induce mitophagy. Nature. 2015 Aug 20;524(7565):309-14. PMID: 26266977. doi: 10.1038/nature14893.
40. Wong YC, Holzbaur EL. Optineurin is an autophagy receptor for damaged mitochondria in parkin-mediated mitophagy that is disrupted by an ALS-linked mutation. Proceedings of the National Academy of Sciences. 2014;111(42):E4439-E48.
41. Novak I, Kirkin V, McEwan DG, Zhang J, Wild P, Rozenknop A, et al. Nix is a selective autophagy receptor for mitochondrial clearance. EMBO Rep. 2010 Jan;11(1):45-51. PMID: 20010802. doi: 10.1038/embor.2009.256.
42. Kraft C, Deplazes A, Sohrmann M, Peter M. Mature ribosomes are selectively degraded upon starvation by an autophagy pathway requiring the Ubp3p/Bre5p ubiquitin protease. Nat Cell Biol. 2008 May;10(5):602-10. PMID: 18391941. doi: 10.1038/ncb1723.
43. Pankiv S, Clausen TH, Lamark T, Brech A, Bruun JA, Outzen H, et al. p62/SQSTM1 binds directly to Atg8/LC3 to facilitate degradation of ubiquitinated protein aggregates by autophagy. J Biol Chem. 2007 Aug 17;282(33):24131-45. PMID: 17580304. doi: 10.1074/jbc.M702824200.
44. Kirkin V, Lamark T, Sou Y-S, Bjørkøy G, Nunn JL, Bruun J-A, et al. A role for NBR1 in autophagosomal degradation of ubiquitinated substrates. Molecular cell. 2009;33(4):505-16.
45. Korac J, Schaeffer V, Kovacevic I, Clement AM, Jungblut B, Behl C, et al. Ubiquitin-independent function of optineurin in autophagic clearance of protein aggregates. J Cell Sci. 2013 Jan 15;126(Pt 2):580-92. PMID: 23178947. doi: 10.1242/jcs.114926.
46. Lu K, Psakhye I, Jentsch S. Autophagic clearance of polyQ proteins mediated by ubiquitin-Atg8 adaptors of the conserved CUET protein family. Cell. 2014;158(3):549-63.
47. Zheng YT, Shahnazari S, Brech A, Lamark T, Johansen T, Brumell JH. The adaptor protein p62/SQSTM1 targets invading bacteria to the autophagy pathway. J Immunol. 2009 Nov 01;183(9):5909-16. PMID: 19812211. doi: 10.4049/jimmunol.0900441.
48. Thurston TL, Ryzhakov G, Bloor S, von Muhlinen N, Randow F. The TBK1 adaptor and autophagy receptor NDP52 restricts the proliferation of ubiquitin-coated bacteria. Nat Immunol. 2009 Nov;10(11):1215-21. PMID: 19820708. doi: 10.1038/ni.1800.

49. Wild P, Farhan H, McEwan DG, Wagner S, Rogov VV, Brady NR, et al. Phosphorylation of the autophagy receptor optineurin restricts Salmonella growth. Science. 2011 Jul 08;333(6039):228-33. PMID: 21617041. doi: 10.1126/science.1205405.
50. Thurston TL, Wandel MP, von Muhlinen N, Foeglein A, Randow F. Galectin 8 targets damaged vesicles for autophagy to defend cells against bacterial invasion. Nature. 2012 Jan 15;482(7385):414-8. PMID: 22246324. doi: 10.1038/nature10744.
51. Turco E, Fracchiolla D, Martens S. Recruitment and Activation of the ULK1/Atg1 Kinase Complex in Selective Autophagy. J Mol Biol. 2020 Jan 03;432(1):123-34. PMID: 31351898. doi: 10.1016/j.jmb.2019.07.027.
52. Viret C, Duclaux-Loras R, Nancey S, Rozières A, Faure M. Selective Autophagy Receptors in Antiviral Defense. Trends Microbiol. 2021 Sep;29(9):798-810. PMID: 33678557. doi: 10.1016/j.tim.2021.02.006.
53. Adriaenssens E, Ferrari L, Martens S. Orchestration of selective autophagy by cargo receptors. Curr Biol. 2022 Dec 19;32(24):R1357-R71. PMID: 36538890. doi: 10.1016/j.cub.2022.11.002.
54. De Duve C, Wattiaux R. Functions of lysosomes. Annu Rev Physiol. 1966;28:435-92. PMID: 5322983. doi: 10.1146/annurev.ph.28.030166.002251.
55. Sieńko K, Poormassalehgoo A, Yamada K, Goto-Yamada S. Microautophagy in plants: consideration of its molecular mechanism. Cells. 2020;9(4):887.
56. Todde V, Veenhuis M, van Der Klei IJ. Autophagy: principles and significance in health and disease. Biochimica et Biophysica Acta (BBA)-Molecular Basis of Disease. 2009;1792(1):3-13.
57. Müller O, Sattler T, Flötenmeyer M, Schwarz H, Plattner H, Mayer A. Autophagic tubes: vacuolar invaginations involved in lateral membrane sorting and inverse vesicle budding. J Cell Biol. 2000 Oct 30;151(3):519-28. PMID: 11062254. doi: 10.1083/jcb.151.3.519.
58. Li WW, Li J, Bao JK. Microautophagy: lesser-known self-eating. Cell Mol Life Sci. 2012 Apr;69(7):1125-36. PMID: 22080117. doi: 10.1007/s00018-011-0865-5.
59. Dice JF. Peptide sequences that target cytosolic proteins for lysosomal proteolysis. Trends Biochem Sci. 1990 Aug;15(8):305-9. PMID: 2204156. doi: 10.1016/0968-0004(90)90019-8.
60. Bejarano E, Cuervo AM. Chaperone-mediated autophagy. Proceedings of the American thoracic society. 2010;7(1):29-39.
61. Cuervo AM, Dice JF. A receptor for the selective uptake and degradation of proteins by lysosomes. Science. 1996 Jul 26;273(5274):501-3. PMID: 8662539. doi: 10.1126/science.273.5274.501.
62. Salvador N, Aguado C, Horst M, Knecht E. Import of a cytosolic protein into lysosomes by chaperone-mediated autophagy depends on its folding state. J Biol Chem. 2000 Sep 01;275(35):27447-56. PMID: 10862611. doi: 10.1074/jbc.M001394200.
63. Cuervo AM, Wong E. Chaperone-mediated autophagy: roles in disease and aging. Cell Res. 2014 Jan;24(1):92-104. PMID: 24281265. doi: 10.1038/cr.2013.153.
64. Ulbricht A, Eppler FJ, Tapia VE, van der Ven PF, Hampe N, Hersch N, et al. Cellular mechanotransduction relies on tension-induced and chaperone-assisted autophagy. Curr Biol. 2013 Mar;23(5):430-5. PMID: 23434281. doi: 10.1016/j.cub.2013.01.064.
65. Ganassi M, Mateju D, Bigi I, Mediani L, Poser I, Lee HO, et al. A Surveillance Function of the HSPB8-BAG3-HSP70 Chaperone Complex Ensures Stress Granule Integrity and Dynamism. Mol Cell. 2016 Sep 01;63(5):796-810. PMID: 27570075. doi: 10.1016/j.molcel.2016.07.021.

66. Fuchs M, Poirier DJ, Seguin SJ, Lambert H, Carra S, Charette SJ, et al. Identification of the key structural motifs involved in HspB8/HspB6–Bag3 interaction. Biochemical Journal. 2010;425(1):245-57.
67. Arndt V, Dick N, Tawo R, Dreiseidler M, Wenzel D, Hesse M, et al. Chaperone-assisted selective autophagy is essential for muscle maintenance. Curr Biol. 2010 Jan;20(2):143-8. PMID: 20060297. doi: 10.1016/j.cub.2009.11.022.
68. Jiang J, Ballinger CA, Wu Y, Dai Q, Cyr DM, Höhfeld Jr, et al. CHIP is a U-box-dependent E3 ubiquitin ligase: identification of Hsc70 as a target for ubiquitylation. Journal of Biological Chemistry. 2001;276(46):42938-44.
69. Ballinger CA, Connell P, Wu Y, Hu Z, Thompson LJ, Yin L-Y, et al. Identification of CHIP, a novel tetratricopeptide repeat-containing protein that interacts with heat shock proteins and negatively regulates chaperone functions. Molecular and cellular biology. 1999;19(6):4535-45.
70. Cristofani R, Crippa V, Cicardi ME, Tedesco B, Ferrari V, Chierichetti M, et al. A Crucial Role for the Protein Quality Control System in Motor Neuron Diseases. Front Aging Neurosci. 2020;12:191. PMID: 32792938. doi: 10.3389/fnagi.2020.00191.
71. Mizushima W, Sadoshima J. BAG3 plays a central role in proteostasis in the heart. J Clin Invest. 2017 Aug 01;127(8):2900-3. PMID: 28737514. doi: 10.1172/JCI95839.
72. Stürner E, Behl C. The Role of the Multifunctional BAG3 Protein in Cellular Protein Quality Control and in Disease. Front Mol Neurosci. 2017;10:177. PMID: 28680391. doi: 10.3389/fnmol.2017.00177.
73. McCollum AK, Casagrande G, Kohn EC. Caught in the middle: the role of Bag3 in disease. Biochem J. 2009 Dec 14;425(1):e1-3. PMID: 20001957. doi: 10.1042/BJ20091739.
74. Rosati A, Graziano V, De Laurenzi V, Pascale M, Turco MC. BAG3: a multifaceted protein that regulates major cell pathways. Cell Death Dis. 2011 Apr;2:e141. PMID: 21472004. doi: 10.1038/cddis.2011.24.
75. Lohanadan K, Molt S, Dierck F, van der Ven PFM, Frey N, Höhfeld J, et al. Isoform-specific functions of synaptopodin-2 variants in cytoskeleton stabilization and autophagy regulation in muscle under mechanical stress. Exp Cell Res. 2021 Nov 15;408(2):112865. PMID: 34637763. doi: 10.1016/j.yexcr.2021.112865.
76. Ji C, Tang M, Zeidler C, Höhfeld J, Johnson GV. BAG3 and SYNPO (synaptopodin) facilitate phospho-MAPT/Tau degradation via autophagy in neuronal processes. Autophagy. 2019;15(7):1199-213.
77. Meister-Broekema M, Freilich R, Jagadeesan C, Rauch JN, Bengoechea R, Motley WW, et al. Myopathy associated BAG3 mutations lead to protein aggregation by stalling Hsp70 networks. Nature communications. 2018;9(1):5342.
78. Marzullo L, Turco MC, De Marco M. The multiple activities of BAG3 protein: Mechanisms. Biochimica et Biophysica Acta (BBA)-General Subjects. 2020;1864(8):129628.
79. Iwasaki M, Tanaka R, Hishiya A, Homma S, Reed JC, Takayama S. BAG3 directly associates with guanine nucleotide exchange factor of Rap1, PDZGEF2, and regulates cell adhesion. Biochem Biophys Res Commun. 2010 Sep 24;400(3):413-8. PMID: 20800573. doi: 10.1016/j.bbrc.2010.08.092.
80. Selcen D, Muntoni F, Burton BK, Pegoraro E, Sewry C, Bite AV, et al. Mutation in BAG3 causes severe dominant childhood muscular dystrophy. Ann Neurol. 2009 Jan;65(1):83-9. PMID: 19085932. doi: 10.1002/ana.21553.

81. Robertson R, Conte TC, Dicaire MJ, Rymar VV, Sadikot AF, Bryson-Richardson RJ, et al. BAG3. Am J Pathol. 2020 Mar;190(3):554-62. PMID: 31953038. doi: 10.1016/j.ajpath.2019.11.005.
82. Kimura K, Ooms A, Graf-Riesen K, Kuppusamy M, Unger A, Schuld J, et al. Overexpression of human BAG3P209L in mice causes restrictive cardiomyopathy. Nature communications. 2021;12(1):3575.
83. Semmler A-L, Sacconi S, Bach JE, Liebe C, Bürmann J, Kley RA, et al. Unusual multisystemic involvement and a novel BAG3 mutation revealed by NGS screening in a large cohort of myofibrillar myopathies. Orphanet journal of rare diseases. 2014;9:1-13.
84. Lin H, Koren SA, Cvetojevic G, Girardi P, Johnson GV. The role of BAG3 in health and disease: A "Magic BAG of Tricks". Journal of cellular biochemistry. 2022;123(1):4-21.
85. McBride HM, Neuspiel M, Wasiak S. Mitochondria: more than just a powerhouse. Current biology. 2006;16(14):R551-R60.
86. Tilokani L, Nagashima S, Paupe V, Prudent J. Mitochondrial dynamics: overview of molecular mechanisms. Essays in biochemistry. 2018;62(3):341-60.
87. Rapaport D, Brunner M, Neupert W, Westermann B. Fzo1p is a mitochondrial outer membrane protein essential for the biogenesis of functional mitochondria in Saccharomyces cerevisiae. Journal of Biological Chemistry. 1998;273(32):20150-5.
88. Hermann GJ, Thatcher JW, Mills JP, Hales KG, Fuller MT, Nunnari J, et al. Mitochondrial fusion in yeast requires the transmembrane GTPase Fzo1p. The Journal of cell biology. 1998;143(2):359-73.
89. Santel A, Fuller MT. Control of mitochondrial morphology by a human mitofusin. Journal of cell science. 2001;114(5):867-74.
90. Dorn GW, Clark CF, Eschenbacher WH, Kang M-Y, Engelhard JT, Warner SJ, et al. MARF and Opa1 control mitochondrial and cardiac function in Drosophila. Circulation research. 2011;108(1):12-7.
91. Smirnova E, Shurland D-L, Ryazantsev SN, van der Bliek AM. A human dynamin-related protein controls the distribution of mitochondria. The Journal of cell biology. 1998;143(2):351-8.
92. Twig G, Shirihai OS. The interplay between mitochondrial dynamics and mitophagy. Antioxid Redox Signal. 2011 May;14(10):1939-51. PMID: 21128700. doi: 10.1089/ars.2010.3779.
93. Twig G, Elorza A, Molina AJ, Mohamed H, Wikstrom JD, Walzer G, et al. Fission and selective fusion govern mitochondrial segregation and elimination by autophagy. The EMBO journal. 2008;27(2):433-46.
94. Youle RJ, Narendra DP. Mechanisms of mitophagy. Nature reviews Molecular cell biology. 2011;12(1):9-14.
95. Ashrafi G, Schwarz T. The pathways of mitophagy for quality control and clearance of mitochondria. Cell Death & Differentiation. 2013;20(1):31-42.
96. Kim Y, Park J, Kim S, Song S, Kwon S-K, Lee S-H, et al. PINK1 controls mitochondrial localization of Parkin through direct phosphorylation. Biochemical and biophysical research communications. 2008;377(3):975-80.
97. Zhang J, Randall MS, Loyd MR, Dorsey FC, Kundu M, Cleveland JL, et al. Mitochondrial clearance is regulated by Atg7-dependent and-independent mechanisms during reticulocyte maturation. Blood, The Journal of the American Society of Hematology. 2009;114(1):157-64.
98. Bayne AN, Trempe J-F. Mechanisms of PINK1, ubiquitin and Parkin interactions in mitochondrial quality control and beyond. Cellular and Molecular Life Sciences. 2019;76:4589-611.

99. Sekine S, Youle RJ. PINK1 import regulation; a fine system to convey mitochondrial stress to the cytosol. BMC biology. 2018;16:1-12.
100. Xiao B, Goh J-Y, Xiao L, Xian H, Lim K-L, Liou Y-C. Reactive oxygen species trigger Parkin/PINK1 pathway–dependent mitophagy by inducing mitochondrial recruitment of Parkin. Journal of Biological Chemistry. 2017;292(40):16697-708.
101. Jin SM, Youle RJ. PINK1-and Parkin-mediated mitophagy at a glance. Journal of cell science. 2012;125(4):795-9.
102. Xiong H, Wang D, Chen L, Choo YS, Ma H, Tang C, et al. Parkin, PINK1, and DJ-1 form a ubiquitin E3 ligase complex promoting unfolded protein degradation. The Journal of clinical investigation. 2009;119(3):650-60.
103. Sha D, Chin L-S, Li L. Phosphorylation of parkin by Parkinson disease-linked kinase PINK1 activates parkin E3 ligase function and NF-κB signaling. Human molecular genetics. 2010;19(2):352-63.
104. Li Y, Zheng W, Lu Y, Zheng Y, Pan L, Wu X, et al. BNIP3L/NIX-mediated mitophagy: molecular mechanisms and implications for human disease. Cell Death & Disease. 2021;13(1):14.
105. Marinković M, Novak I. A brief overview of BNIP3L/NIX receptor-mediated mitophagy. FEBS open bio. 2021;11(12):3230-6.
106. Liu L, Feng D, Chen G, Chen M, Zheng Q, Song P, et al. Mitochondrial outer-membrane protein FUNDC1 mediates hypoxia-induced mitophagy in mammalian cells. Nature cell biology. 2012;14(2):177-85.
107. Bhujabal Z, Birgisdottir ÅB, Sjøttem E, Brenne HB, Øvervatn A, Habisov S, et al. FKBP8 recruits LC3A to mediate Parkin-independent mitophagy. EMBO reports. 2017;18(6):947-61.
108. Wang ZH, Clark C, Geisbrecht ER. Drosophila Clueless is involved in Parkin-dependent mitophagy by promoting VCP-mediated Marf degradation. Hum Mol Genet. 2016 Feb. PMID: 26931463. doi: 10.1093/hmg/ddw067.
109. F AR, Quadrilatero J. Emerging role of mitophagy in myoblast differentiation and skeletal muscle remodeling. Semin Cell Dev Biol. 2023 Jul 15;143:54-65. PMID: 34924331. doi: 10.1016/j.semcdb.2021.11.026.
110. Luan P, D'Amico D, Andreux PA, Laurila PP, Wohlwend M, Li H, et al. Urolithin A improves muscle function by inducing mitophagy in muscular dystrophy. Sci Transl Med. 2021 Apr 07;13(588). PMID: 33827972. doi: 10.1126/scitranslmed.abb0319.
111. Ugur B, Chen K, Bellen HJ. Drosophila tools and assays for the study of human diseases. Disease models & mechanisms. 2016;9(3):235-44.
112. Baenas N, Wagner AE. Drosophila melanogaster as an alternative model organism in nutrigenomics. Genes & nutrition. 2019;14(1):14.
113. Verheyen EM. The power of Drosophila in modeling human disease mechanisms. The Company of Biologists Ltd; 2022. p. dmm049549.
114. Wieschaus E. Positional information and cell fate determination in the early Drosophila embryo. Current topics in developmental biology. 2016;117:567-79.
115. Alberts B, Johnson A, Lewis J, Raff M, Roberts K, Walter P. Drosophila and the molecular genetics of pattern formation: Genesis of the body plan. Molecular Biology of the Cell 4th edition: Garland Science; 2002.
116. Tennessen JM, Thummel CS. Coordinating growth and maturation—insights from Drosophila. Current Biology. 2011;21(18):R750-R7.
117. Bainbridge SP, Bownes M. Staging the metamorphosis of Drosophila melanogaster. Development. 1981;66(1):57-80.

118. Musselman LP, Kühnlein RP. Drosophila as a model to study obesity and metabolic disease. Journal of Experimental Biology. 2018;221(Suppl_1):jeb163881.
119. Ghosh AC, Hu Y, Tattikota SG, Liu Y, Comjean A, Perrimon N. Modeling exercise using optogenetically contractible Drosophila larvae. BMC Genomics. 2022 Aug 30;23(1):623. PMID: 36042416. doi: 10.1186/s12864-022-08845-6.
120. Martelli F, Quig A, Mele S, Lin J, Fulton TL, Wansbrough M, et al. A defined diet for pre-adult Drosophila melanogaster. Scientific Reports. 2024;14(1):6974.
121. Keroles MB, Dusseault SK, Liu C, Mohammed MR, Vadakkan CM, Amiel JH, et al. Imaging through the pupal case of Drosophila melanogaster. JoVE (Journal of Visualized Experiments). 2014 (83):e51239.
122. Stobdan T, Wen NJ, Lu-Bo Y, Zhou D, Haddad GG. The Pupa Stage Is the Most Sensitive to Hypoxia in Drosophila melanogaster. International Journal of Molecular Sciences. 2024;25(2):710.
123. Athilingam T, Tiwari P, Toyama Y, Saunders TE, editors. Mechanics of epidermal morphogenesis in the Drosophila pupa. Seminars in Cell & Developmental Biology; 2021: Elsevier.
124. Mollá-Albaladejo R, Sánchez-Alcañiz JA. Behavior individuality: a focus on Drosophila melanogaster. Frontiers in physiology. 2021;12:719038.
125. Piper MD, Partridge L. Drosophila as a model for ageing. Biochimica et Biophysica Acta (BBA)-Molecular Basis of Disease. 2018;1864(9):2707-17.
126. Jeibmann A, Paulus W. Drosophila melanogaster as a model organism of brain diseases. International journal of molecular sciences. 2009;10(2):407-40.
127. Olivé M, Kley RA, Goldfarb LG. Myofibrillar myopathies: new developments. Curr Opin Neurol. 2013 Oct;26(5):527-35. PMID: 23995273. doi: 10.1097/WCO.0b013e328364d6b1.
128. Maerkens A, Olivé M, Schreiner A, Feldkirchner S, Schessl J, Uszkoreit J, et al. New insights into the protein aggregation pathology in myotilinopathy by combined proteomic and immunolocalization analyses. Acta Neuropathol Commun. 2016 Feb;4:8. PMID: 26842778. doi: 10.1186/s40478-016-0280-0.
129. Kley RA, Maerkens A, Leber Y, Theis V, Schreiner A, van der Ven PF, et al. A combined laser microdissection and mass spectrometry approach reveals new disease relevant proteins accumulating in aggregates of filaminopathy patients. Mol Cell Proteomics. 2013 Jan;12(1):215-27. PMID: 23115302. doi: 10.1074/mcp.M112.023176.
130. Maerkens A, Kley RA, Olivé M, Theis V, van der Ven PF, Reimann J, et al. Differential proteomic analysis of abnormal intramyoplasmic aggregates in desminopathy. J Proteomics. 2013 Sep;90:14-27. PMID: 23639843. doi: 10.1016/j.jprot.2013.04.026.
131. Brooks D, Naeem F, Stetsiv M, Goetting SC, Bawa S, Green N, et al. Drosophila NUAK functions with Starvin/BAG3 in autophagic protein turnover. PLoS Genet. 2020 04;16(4):e1008700. PMID: 32320396. doi: 10.1371/journal.pgen.1008700.

Chapter 2 - A conserved STRIPAK complex is required for autophagy in muscle tissue

Yungui Guo[1], Qiling Zeng[1], David Brooks[1] and Erika R. Geisbrecht[1*]

[1]Department of Biochemistry and Molecular Biophysics, Kansas State University, Manhattan, KS 66506, USA

*Corresponding author

E-mail: geisbrechte@ksu.edu

Running title: STRIPAK and autophagy in muscle

Key Words: Muscle, STRIPAK, NUAK, autophagy, *D. melanogaster*

This chapter has been published as a journal article in *Molecular Biology of the Cell*.

Abstract

Autophagy is important for cellular homeostasis and to prevent the abnormal accumulation of proteins. While many proteins that comprise the canonical autophagy pathway have been characterized, the identification of new regulators may help understand tissue and/or stress-specific responses. Using an *in silico* approach, we identified Striatin interacting protein (Strip), MOB kinase activator 4 (Mob4), and Fibroblast growth factor receptor 1 oncogene partner 2 (Fgop2) as conserved mediators of muscle tissue maintenance. We performed affinity purification mass spectrometry (AP-MS) experiments with *Drosophila melanogaster* (*D. melanogaster)* Strip as a bait protein and co-purified additional Striatin Interacting Phosphatase and Kinase (STRIPAK) complex members from larval muscle tissue. NUAK and Starvin (Stv) also emerged as Strip-binding proteins and these physical interactions were verified in vivo using Proximity Ligation Assays (PLA). To understand the functional significance of the STRIPAK-NUAK-Stv complex, we employed a sensitized genetic assay combined with RNA interference (RNAi) to demonstrate that both *NUAK* and *stv* function in the same biological process with genes that encode for STRIPAK complex proteins. RNAi-directed knockdown of *Strip* in muscle tissue led to the accumulation of ubiquitinated cargo, p62, and Atg8a, consistent with a block in autophagy. Indeed, autophagic flux was decreased in *Strip RNAi* muscles, while lysosome biogenesis and activity were unaffected. Our results support a model whereby the STRIPAK-NUAK-Stv complex coordinately regulates autophagy in muscle tissue.

Introduction

Balancing protein synthesis and protein degradation is crucial to maintain normal cellular functions. In addition to the routine turnover of proteins, cells must have the ability to rapidly

respond to internal or external signals by modulating the dynamics of protein turnover or rerouting proteins through other degradation pathways. Autophagy is one such degradation pathway that degrades bulk cellular components in the lysosome [1, 2]. Activation of receptors at the cell surface, oxidative stress, and starvation can trigger endocytosis and autophagy to degrade cellular components for energy [3].

Multiple types of autophagy, each with its own subtleties, allow the cell to selectively or non-selectively degrade cellular material. Clearance of organelles or proteins generally occurs through macroautophagy, where a double-membraned structure called the phagophore forms de novo and sequesters cellular components within a closed autophagosome [4, 5]. During maturation, autophagosomes can merge with existing late endosomes (LEs)/multivesicular bodies (MVBs) to form a hybrid structure called the amphisome prior to fusion with lysosomes [3]. Selectivity in the degradation process occurs when autophagy receptors recruit and link particular cargo to the autophagy machinery. One example is chaperone-assisted selective autophagy (CASA), whereby recognition of the actin crosslinking protein Filamin by the Bcl-2–associated athanogene 3 (Bag3)-Heat-shock cognate 70 (Hsc70) complex recruits p62/Sequestosome-1 (SQSTM1) [6-9]. This adapter protein then binds to Autophagy-related 8a (Atg8a)/microtubule-associated protein 1 light chain 3 (MAP1LC3/LC3) to coordinate autophagosome formation and eventual lysosomal fusion [10-12].

Even though autophagy occurs in every cell, the importance of this process in muscle tissue is exemplified by the number of muscle disorders that are linked to mutations in genes that encode for autophagy components and/or the abnormal accumulation of autophagic or lysosomal vacuoles within diseased muscle tissue [2, 13-15]. For example, mutations in the lysosomal marker lysosomal Associated Membrane Protein 2 (LAMP2) cause Danon disease, characterized by the

accumulation of autophagic vacuoles [16-18]. Mutations in vacuolar ATPase Assembly Factor VMA21 (VMA21) result in excessive autophagy (XMA) and patients with Duchenne muscular dystrophy (DMD) exhibit lower levels of the Microtubule-associated protein 1A/1B-light chain 3-II (LC3 II) and excess p62 [19-21]. Moreover, mutations in human Filamin C and Bag3 result in Myofibrillar Myopathy (MFM), a progressive disease in which protein aggregates and muscle tissue disintegration are prevalent in biopsies [22-25]. Modeling of MFM diseases in zebrafish or mice show that autophagic activity is impaired, thus linking abnormal protein accumulation to a deficiency in protein turnover [24]. Identifying additional proteins that mediate autophagy will help understand the etiology and progression of diseases linked to this cellular process.

The striatin-interacting phosphatase and kinase (STRIPAK) multi-subunit signaling complex has emerged as a central component in the coordination of intertwined signaling networks in a wide variety of cellular processes [26-28]. Striatin is the founding member of this complex and acts as a scaffolding hub for other components, together which form one of the four families of regulatory subunits for Protein phosphatase 2A (PP2A) [29]. The core proteins that comprise the STRIPAK complex are evolutionarily conserved across diverse organisms. However, their varied subcellular distribution suggest that STRIPAK proteins may form sub-complexes that target distinct substrates in different intracellular pathways that ultimately influence cell growth, cell division, and actin cytoskeleton organization, among others. Recent papers have uncovered roles for STRIPAK complex proteins in myofibril assembly in zebrafish and in *D. melanogaster* adult flight muscles [30, 31], thus highlighting additional functions for these abundant, promiscuous proteins.

Here we uncover components of the STRIPAK complex that affect muscle development through an *in silico* screening approach in the flour beetle *Tribolium castaneum (T. castaneum)*.

Targeted RNAi against select STRIPAK proteins in *D. melanogaster* revealed morphological abnormalities in larval muscles. Affinity-purification and mass spectrometry (AP-MS) studies confirmed the presence of additional STRIPAK complex members in muscle tissue, including those implicated in autophagy. Detailed analysis of a core STRIPAK member, Striatin interacting protein (Strip), further revealed a role for the STRIPAK complex in the regulation of autophagic flux in muscle tissue.

Results

Taking advantage of the evolutionary conservation of genes essential for muscle development and maintenance, we screened iBeetle-Base, a database of *Tribolium castaneum* (*Tc*) RNAi phenotypes using the search term 'larval muscle irregular' to broadly identify genes that alter muscle morphology [32-34]. Out of the ~8500 individual protein-encoding genes targeted using dsRNA injections in the *pig-19* line expressing GFP in all larval somatic muscles [35], this *in silico* approach uncovered 592 genes with abnormal muscle phenotypes (Figure B.1). After eliminating genes that failed to form Cytoscape interaction networks, we focused on the remaining 55 candidates (Figure 2.1A). Analysis of representative images for each of these genes in iBeetle-Base revealed similar muscle phenotypes for RNAi knockdown of *TC010759* (*Tc-Strip*), *TC012571* (*Tc-Mob4*), and *TC007423* (*Tc-Fgop2*) (Figure 2.1B). These abnormalities were primarily characterized by gaps in the stereotypical embryonic muscle pattern, indicative of missing and/or detached muscles. Representative images in the iBeetle database were obtained from a first-pass screen without systematic repetitions [34]. Despite this limitation, the similarity in phenotypes for three different members of the STRIPAK complex, combined with physical

interactions identified by Search Tool for the Retrieval of Interacting Genes/Proteins (STRING) network analysis provided the rationale for further analysis.

To determine if these proteins play a conserved role in *D. melanogaster* muscle development, we induced mRNA knockdown of *Strip*, *MOB kinase activator 4* (*Mob4*), or *Fibroblast growth factor receptor 1 oncogene partner 2* (*Fgop2*) using previously published upstream activating sequence (UAS)-*RNAi* lines for each gene under control of the *Mef2*-Gal4 driver [36]. *Mef2>lacZ* controls showed an overall normal muscle pattern as visualized with Myosin heavy chain (Mhc)-GFP in the late third larval (L3) instar stage (Figure 2.2A). At this whole organismal level, missing muscles were occasionally present in *Strip RNAi* L3 larvae.

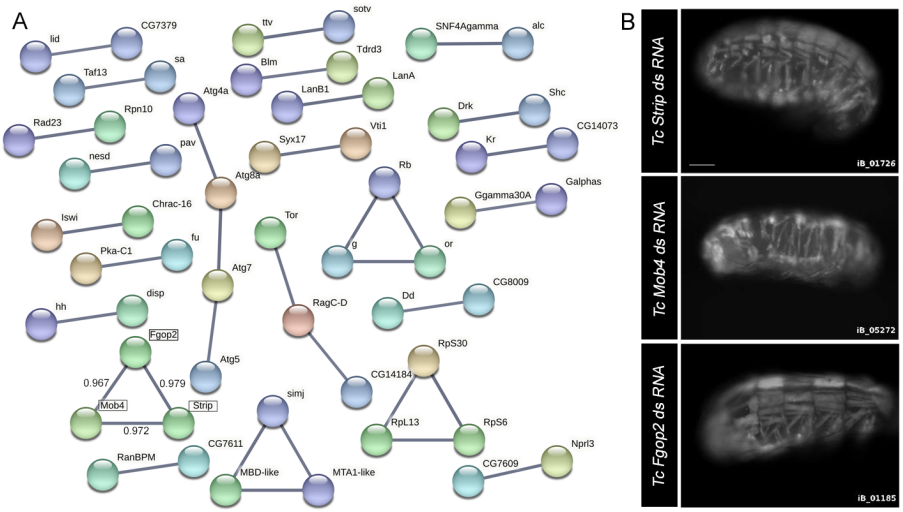


Figure 2.1. Network analysis uncovers interacting genes in *T.castaneum*.

(A) Cytoscape rendering of the 55 genes identified in the iBeetle-base *in silico* screen that exhibit one or more known interactions (see **Figure B.1**). (B) Representative images of muscle morphology defects in *T.castaneum* late-stage embryos visualized with GFP after injection of dsRNA for Strip, Mob4, or Fgop2 (https://ibeetle-base.uni-goettingen.de/). Scale bar, 50 µm.

However, a role for Strip in muscle function became more obvious during the L3 to pupal transition when body wall muscles contract to form a stereotypical pupal size. Induction of *Strip RNAi* using

two independent UAS-hairpin lines exhibited longer pupal cases (**Figure 2.2B**), whereby the pupal axial ration (length/width) was increased by ~30% compared to *Mef2>lacZ* controls (**Figure 2.2C**). To determine if obvious morphological differences may explain the failure of muscle contraction, we examined L3 muscles before the pupal stage. Phalloidin labeling of filleted *Mef2>lacZ* control larvae revealed a striated pattern of F-actin in the easily imaged ventral longitudinal 3 (VL3) and 4 (VL4) muscles (**Figure 2.2D**). Muscle-induced *Strip RNAi* disrupted this normal F-actin morphology, typified by a loss of the repeated sarcomere pattern and small regions that lacked phalloidin staining. Western blot analysis showed that Strip protein levels were reduced by ~60-70% in *Strip RNAi* muscle carcasses (**Figure 2.2E**).

Identification and functional characterization of muscle STRIPAK complex components

RNAi knockdown of *Mob4* or *Fgop2 mRNA* in muscle tissue resulted in stereotypical pupal case sizes and largely normal muscle morphology with occasional areas of hypercontraction (**Figure B.2 A-C**). Four possibilities, which are not mutually exclusive, may explain the absence of *Strip RNAi*-like phenotypes. While reduced transcript levels of *Mob4* or *Fgop2 mRNA* are evident by quantitative RT-PCR analysis (**Figure B.3**), we cannot rule out the possibility that Mob4 or Fgop2 protein levels are not decreased. Stage-specific and/or species-specific differences may explain the phenotypic variations between beetles and flies. At present, we cannot conclude if Mob4 or Fgop2 are required earlier in development since we did not analyze embryonic or early larval phenotypes. Recent comparisons between *T. castaneum* and *D. melanogaster* have revealed more divergence in gene function governing basic developmental processes, including myogenesis, than previously thought [37, 38]. Thus, species-specific differences may at least partially account

for a lack of phenotype in *Mob4* or *Fgop2 RNAi* L3 muscles. Finally, Strip may function independently of the STRIPAK complex in L3 muscle tissue.

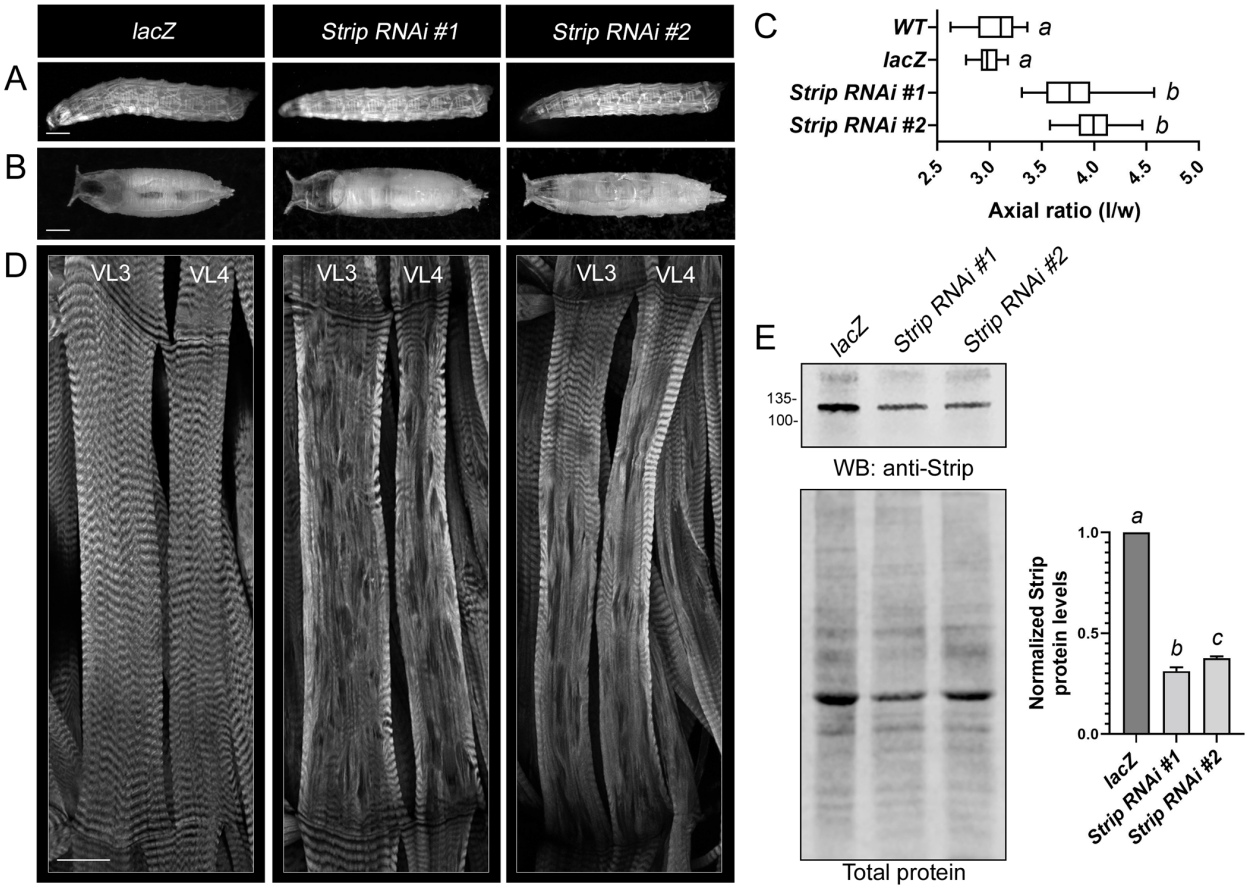


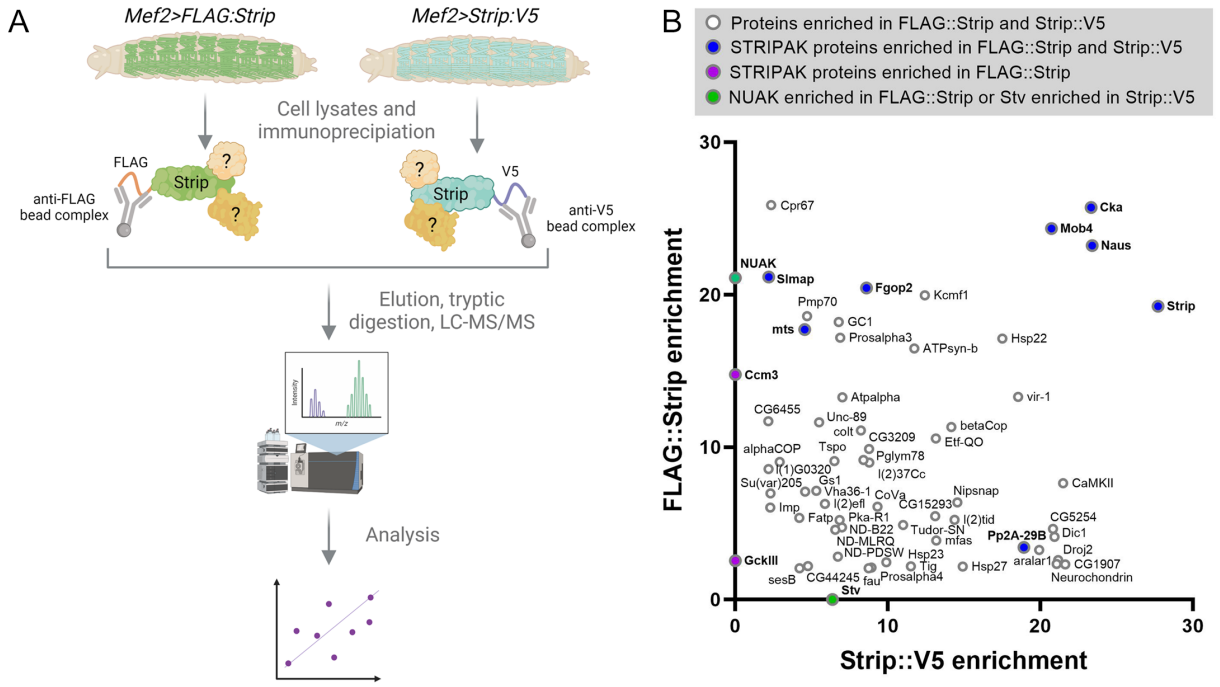
Figure 2.2. Induction of Strip RNAi in muscle tissue compromises muscle structure and function.

Mef2-Gal4 driven expression of UAS-*lacZ* control or two independent UAS-*Strip RNAi* lines. (A) Whole mount images of L3 larvae visualized with MHC-GFP reveal no obvious difference between the control and *Strip RNAi* muscle patterns. Anterior is to the left. (B) Images of stereotypical pupal cases representative of *Mef2>lacZ* controls or elongated pupal cases upon a reduction of Strip. Anterior is to the left. (C) Box and whiskers plot showing the relative axial ratio (length/width) of pupal case size in control vs *Strip RNAi* muscles. N≥20. Different letters indicate statistical significance between groups. (D) Phalloidin labeling for F-actin reveals normal, repeated sarcomeres in VL3 and VL4 control muscles (left panel). This striated pattern is disrupted in *Strip RNAi* muscles. All images are maximum intensity projections with anterior towards the top. (E) Representative Western blot of Strip protein levels upon induction of *Strip RNAi* in L3 muscles (top panel). Total protein loading control (bottom panel). Different letters indicate statistical significance between groups. Scale bars, 1 mm (panels A and B), 50 μm (panel D).

To identify proteins that physically interact with Strip in this context, we developed an affinity purification-mass spectrometry (AP-MS) approach (**Figure 2.3A**). N-terminally tagged FLAG::Strip or C-terminally tagged Strip::V5 were independently expressed in muscle under Gal4/UAS control and isolated from L3 larvae using affinity tag-specific beads. The resulting protein complexes were trypsin digested and subjected to MS analysis. Peptide coverage of the Strip bait proteins varied from 49.6% to 77% in three independent experiments. Enrichment was calculated by averaging the label-free quantification (LFQ) intensity values for each experimental group (Mef2>FLAG::Strip or Mef2>Strip::V5) minus the average values for control groups (Mef2>lacZ). Using a cut-off of 2.0 as the minimum enrichment value, a total of 195 proteins co-purified with FLAG::Strip and 336 proteins co-purified with Strip::V5.

We next plotted proteins that were present in both datasets based on their relative enrichment values (**Figure 2.3B**). Both Mob4 and Fgop2 had enrichment values >20 in the FLAG::Strip pulldowns or >9 in the Strip::V5 pulldowns, thus validating our AP-MS approach and STRING-Cytoscape interactions. We also confirmed the presence of five additional STRIPAK components, Connector of kinase to AP-1 (Cka), Nausicaa (Naus), Sarcolemma Associated Protein (Slmap), microtubule star (mts), and Protein phosphatase 2A at 29B (PP2A-29B) in both datasets. Two STRIPAK proteins, Cerebral cavernous malformation 3 (Ccm3) and Germinal centre kinase III (GckIII) emerged only in the FLAG::Strip pulldowns, possibly indicating that the C-terminal V5 tag interfered with binding to Strip. This data is summarized in **Figure 2.3C**.

Two additional proteins that caught our interest as possible Strip-binding proteins were NUAK and Stv. NUAK was enriched ~20x in the FLAG::Strip dataset, while Stv was present ~7x in our V5::Strip samples. Since we previously published a role for the NUAK-Stv complex in



C

Gene Symbol	Gene name	Human protein(s)	Strip::V5 enrichment	FLAG::Strip enrichment
Strip	Striatin interacting protein	STRIP1, STRIP 2	27.2	19.2
Naus	Nausica	CTTNBP2NL	23.4	23.2
Cka	Connector of kinase to AP-1	STRN, STRN3, STRN4	23.3	25.7
Mob4	MOB kinase activator 4	MOB4	20.7	24.3
Pp2A-29B	Protein phosphatase 2A at 29B	PPP2R1A	18.9	3.4
Fgop2	Fibroblast growth factor receptor 1 oncogene partner 2	FGFR1OP2	8.6	20.4
mts	microtubule star	PPP2CA	4.6	17.7
Slmap	Sarcolemma associated protein	SLMAP	2.2	21.2
Ccm3	Cerebral cavernous malformation 3	PDCD10	0.0	14.8
GckIII	Germinal centre kinase III	STK24	0.0	2.5

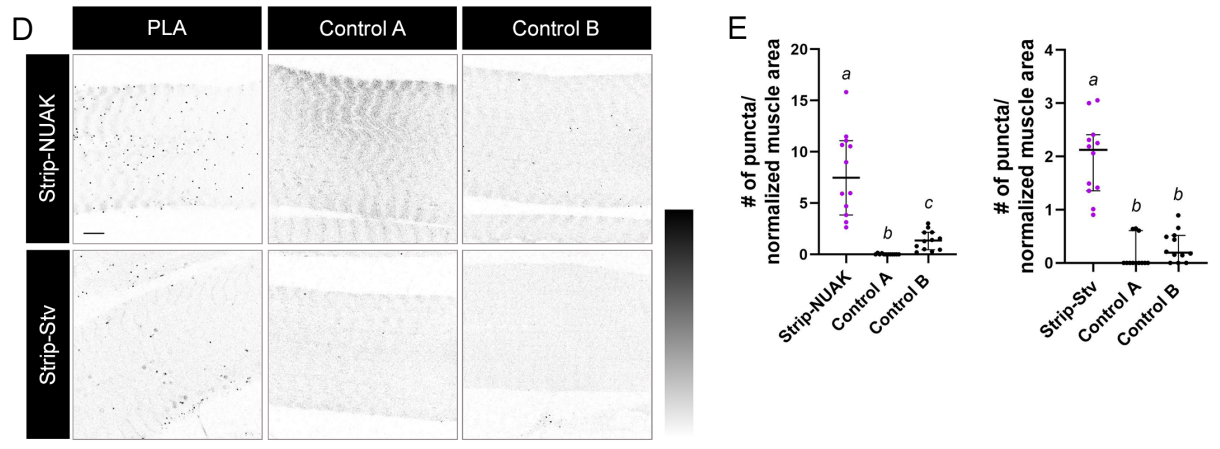


Figure 2.3. Co-purification of STRIPAK complex proteins from larval muscle tissue.

(A) Schematic of the AP-MS strategy. Either N-terminally tagged FLAG::Strip or C-terminally tagged Strip::V5 fusion proteins were expressed in larval body wall muscles with *Mef2*-Gal4. After the preparation of cell lysates and immunoprecipitation with either anti-FLAG or anti-V5 beads, the resulting protein complexes were subjected to MS/MS and quantitative peptide identification. *Mef2>lacZ* lysates were used for control pulldowns. Created with BioRender.com (B) Enrichment plot showing proteins that co-purified with FLAG::Strip vs lacZ (y-axis) or Strip::V5 vs lacZ (x-axis). The enrichment difference was calculated by subtracting the average peptide intensities for each protein in the tagged pulldown minus controls. (C) Canonical proteins of the STRIPAK complex that co-purified with the bait protein Strip from larval muscle tissue. The corresponding human proteins and relative abundance in MS experiments are listed. (D) Representative confocal single-plane images corresponding to PLA experiments characterizing physical interactions of complexes containing Strip-NUAK (top panels) or Strip-Stv (bottom panels) within VL3 muscles. The PLA experiments were performed on *Mef2>FLAG::Strip* muscles or *Mef2>Strip::V5* muscles. Control A includes no primary antibodies and only PLA reagents on either *Mef2>FLAG::Strip* muscles or *Mef2>Strip::V5* muscles. Control B includes both primary and PLA reagents on *WT* muscles. (E) Dot plot depicting the number of PLA puncta/normalized muscle areas in the indicated genotypes. N≥12. Genotypes with different letters are statistically different. Scale bars, 10 μm (panel D).

autophagy [39], we next verified the presence of Strip-NUAK or Strip-Stv complexes using the proximity ligation assay (PLA) approach. Rabbit antibodies raised against NUAK [40] or Stv [6, 41] were used in conjunction with commercially available anti-FLAG or anti-V5 antibodies generated in mice (**Figure 2.3D**). The number of puncta corresponding to a Strip-NUAK complex was increased in *Mef2>FLAG::Strip* muscles compared to two independent controls (**Figure 2.3E**). Control experiment A was performed on *Mef2>FLAG::Strip* muscles with no primary antibody and only PLA reagents. Control experiment B used both primary antibodies and PLA reagents on *WT* muscles lacking a FLAG-tagged version of Strip. Similar results were obtained for *Mef2>Strip::V5* muscles, whereby more puncta corresponding to a Strip-Stv complex were observed than in control experiments (**Figure 2.3E**). Together, our AP-MS and PLA results confirm that the STRIPAK complex, together with NUAK and Stv, is expressed in muscles and can be co-purified with Strip.

To determine if individual STRIPAK components function in NUAK and/or Stv-mediated processes, we utilized two separate assays that take advantage of sensitized genetic backgrounds and available RNAi lines. Stable fly stocks of the genotype *NUAK*^{K99R}*+/-, Mef2*-Gal4 and *stv*^{1}*+/-, Mef2*-Gal4 were mated with two independent UAS-*RNAi* lines for each STRIPAK complex protein (except *Pp2A-29B* as other RNAi lines were lethal before the L3 stage). First, we assessed muscle contraction during the larval to pupal transition as described earlier [39, 42, 43]. Heterozygous *NUAK*^{K99R}*+/-* or *stv*^{1}*+/-* larvae underwent normal muscle contraction and exhibited a pupal axial ratio comparable to *WT* and *Mef2>lacZ* controls (**Figure 2.2C**). Even though RNAi-directed knockdown of Strip alone showed decreased muscle contraction (**Figure 2.2C and Figure 2.4, A and B**), removal of a single copy of *NUAK* or *stv* enhanced this phenotype, demonstrating that Strip functions in the same biological process as the NUAK-Stv complex (**Figure 2.4, A and B**). The same results were obtained for the knockdown of *Cka* or *Naus,* whereby muscle contraction deficits of either gene alone were exacerbated in the sensitized *NUAK*^{K99R}*+/-* or *stv*^{1}*+/-* backgrounds. While all RNAi lines used in these experiments showed knockdown of *mRNA* transcripts (**Figure B.3**), some of the STRIPAK complex members exhibited milder and more variable results. All pair-wise combinations of RNAi lines (*e.g., Mef2>Strip RNAi #1* vs. *NUAK*^{K99R}*+/-, Mef2>Strip RNAi #1*) showed a statistically significant enhancement of muscle contraction defects upon removal of a single copy of *NUAK*^{K99R} (**Figure 2.4A**), but only a single RNAi line directed against *Fgop2* and *Slmap* and none against *GckIII* or *Pp2A-29B* reached significant values of $p<0.05$ (**Figure 2.4B**). Neither *Mob4 RNAi* line enhanced muscle contraction defects in the *stv*^{1}*/+* background.

Measurements of muscle contractility during the larval to pupal transition is a relatively stringent assay that relies on the failure of multiple muscles to contract. Thus, we also assessed the

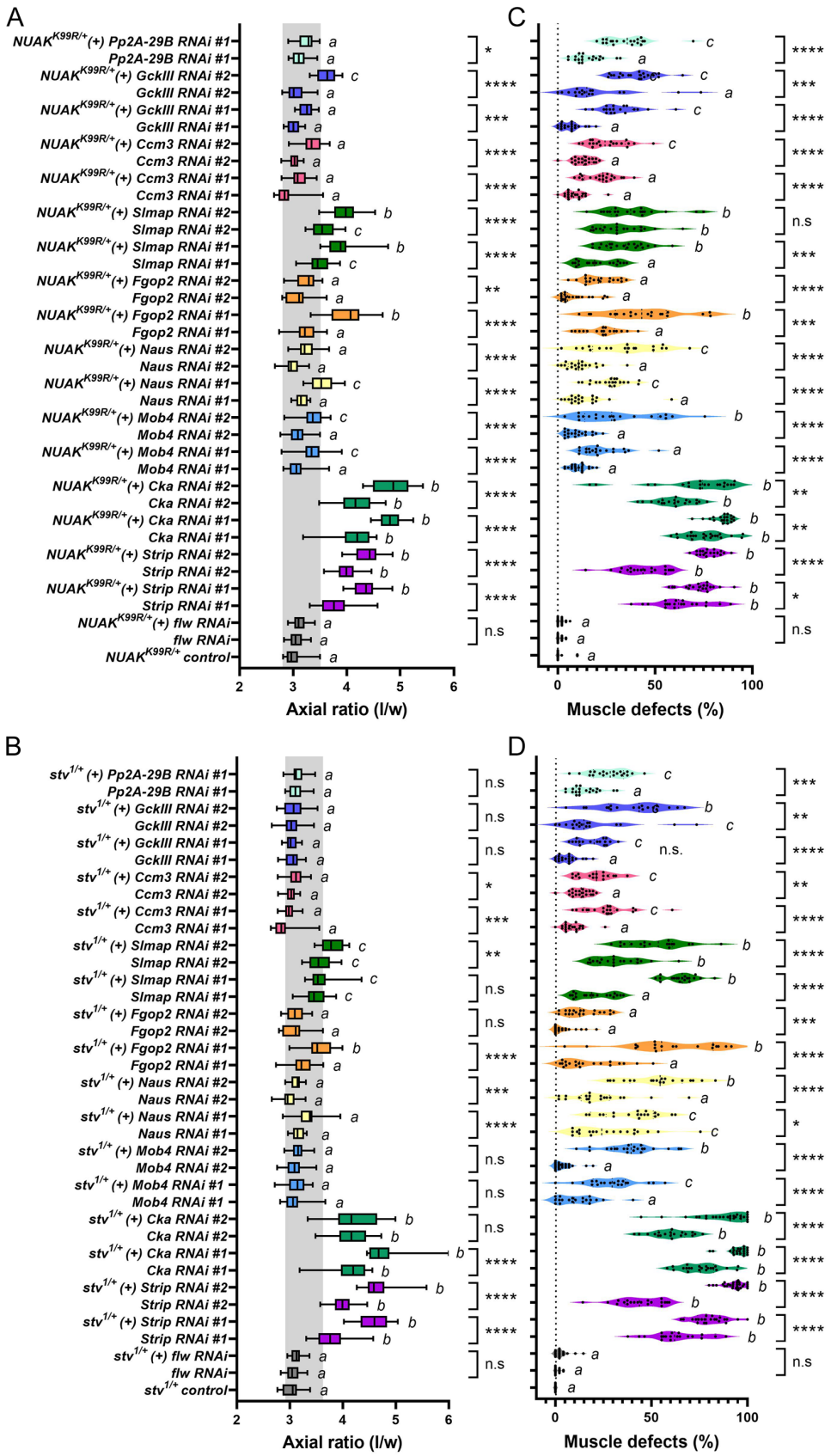

A
B
C
D
NUAK^K99R/+ (+) Pp2A-29B RNAi #1
Pp2A-29B RNAi #1
NUAK^K99R/+ (+) GckIII RNAi #2
GckIII RNAi #2
NUAK^K99R/+ (+) GckIII RNAi #1
GckIII RNAi #1
NUAK^K99R/+ (+) Ccm3 RNAi #2
Ccm3 RNAi #2
NUAK^K99R/+ (+) Ccm3 RNAi #1
Ccm3 RNAi #1
NUAK^K99R/+ (+) Slmap RNAi #2
Slmap RNAi #2
NUAK^K99R/+ (+) Slmap RNAi #1
Slmap RNAi #1
NUAK^K99R/+ (+) Fgop2 RNAi #2
Fgop2 RNAi #2
NUAK^K99R/+ (+) Fgop2 RNAi #1
Fgop2 RNAi #1
NUAK^K99R/+ (+) Naus RNAi #2
Naus RNAi #2
NUAK^K99R/+ (+) Naus RNAi #1
Naus RNAi #1
NUAK^K99R/+ (+) Mob4 RNAi #2
Mob4 RNAi #2
NUAK^K99R/+ (+) Mob4 RNAi #1
Mob4 RNAi #1
NUAK^K99R/+ (+) Cka RNAi #2
Cka RNAi #2
NUAK^K99R/+ (+) Cka RNAi #1
Cka RNAi #1
NUAK^K99R/+ (+) Strip RNAi #2
Strip RNAi #2
NUAK^K99R/+ (+) Strip RNAi #1
Strip RNAi #1
NUAK^K99R/+ (+) flw RNAi
flw RNAi
NUAK^K99R/+ control
stv^1/+ (+) Pp2A-29B RNAi #1
Pp2A-29B RNAi #1
stv^1/+ (+) GckIII RNAi #2
GckIII RNAi #2
stv^1/+ (+) GckIII RNAi #1
GckIII RNAi #1
stv^1/+ (+) Ccm3 RNAi #2
Ccm3 RNAi #2
stv^1/+ (+) Ccm3 RNAi #1
Ccm3 RNAi #1
stv^1/+ (+) Slmap RNAi #2
Slmap RNAi #2
stv^1/+ (+) Slmap RNAi #1
Slmap RNAi #1
stv^1/+ (+) Fgop2 RNAi #2
Fgop2 RNAi #2
stv^1/+ (+) Fgop2 RNAi #1
Fgop2 RNAi #1
stv^1/+ (+) Naus RNAi #2
Naus RNAi #2
stv^1/+ (+) Naus RNAi #1
Naus RNAi #1
stv^1/+ (+) Mob4 RNAi #2
Mob4 RNAi #2
stv^1/+ (+) Mob4 RNAi #1
Mob4 RNAi #1
stv^1/+ (+) Cka RNAi #2
Cka RNAi #2
stv^1/+ (+) Cka RNAi #1
Cka RNAi #1
stv^1/+ (+) Strip RNAi #2
Strip RNAi #2
stv^1/+ (+) Strip RNAi #1
Strip RNAi #1
stv^1/+ (+) flw RNAi
flw RNAi
stv^1/+ control
2 3 4 5 6
Axial ratio (l/w)
0 50 100
Muscle defects (%)
n.s
n.s.

Figure 2.4. Functional interactions between NUAK and stv with STRIPAK complex members.

(A-D) Each RNAi line was expressed alone in muscle tissue using *Mef2*-Gal4 or in a sensitized $NUAK^{K99R}$ (A,C) or stv^{1} (B,D) heterozygous background. Two RNAi lines were selected against each STRIPAK complex gene except for *PP2A-29B* as other *PP2A-29B RNAi* lines tested were lethal prior to the L3 stage. (A, B) Box and whisker plots of muscle contractility are depicted by the axial ratio (length/width) of individual pupae of the indicated genotypes. A shaded grey box indicates the min to max values for controls. (C,D) Scatter plots depicting muscle defects in L3 larvae (aberrant F-actin patterning, gaps between myofibrils, and detached muscles). Each data point presents the percentage of muscles with abnormal morphology in individual larvae. N≥20 for pupal case morphology and N≥18 for muscle morphology abnormalities. Genotypes with different letters are statistically different between groups ($p<0.05$). ****, $p<0.0001$; ***, $p<0.001$; **, $p<0.01$; * $p<0.05$; n.s, not significant.

morphology of individual L3 muscles with the rationale that minor structural defects may be present, but not severe enough to cause functional deficits in overall contractile ability. Each genotype displayed morphological abnormalities that were enhanced in the $NUAK^{K99R}$ or stv^{1} sensitized backgrounds, although there was some variability among RNAi lines (**Figure 2.4, C and D**). Aside from Strip, muscle-directed RNAi against either *Cka* line showed strong muscle contraction and sarcomere morphology phenotypes in our quantitative analysis. Indeed, F-actin patterning in *Cka RNAi* muscles phenocopies *Strip* phenotypes (**Figure B.4**). RNAi knockdown of the phosphatase *flapwing* (*flw)* did not exhibit a phenotype on its own or in combination with either the $NUAK^{K99R}$ or stv^{1} alleles, thus serving as a negative control for all experiments. These data together firmly demonstrate a requirement for the STRIPAK complex in muscle contraction and the maintenance of the integrity of muscle tissue in concert with the NUAK-Stv complex.

Markers associated with autophagy are increased in *Strip RNAi* muscles

Since the loss of NUAK or Stv impairs autophagy in muscle tissue [39], we next examined the relative distribution and levels of the autophagosome marker Atg8a upon induction of *Strip*

RNAi. In control *Mef2>lacZ* muscles, fluorescence corresponding to Atg8a puncta was visible at low levels (**Figure 2.5A**). RNAi-silencing of *Strip* with either RNAi line not only increased the overall number of puncta but also shifted the relative size of each Atg8a(+) puncta to greater than 3.75 μm^2 (**Figure 2.5B**). While some of these larger puncta were located near nuclei (see inset), a large proportion were broadly distributed throughout the cell in *Strip RNAi* muscles. The inability to visualize puncta corresponding to autophagosomes in *Atg8a RNAi* muscles confirmed the specificity of the anti-Atg8a antibody (**Figure 2.5A**).

Refractory to sigma P (ref(2)p)/p62 is an adapter protein that simultaneously interacts with ubiquitinated cargo and Atg8a to ensure the delivery of autophagic substrates to the autolysosome for degradation [10-12]. Thus, increased p62 protein would be predicted upon a decrease in Strip function. Indeed, the total number and relative size of p62-containing structures were increased in *Strip RNAi* muscles (**Figure B.5A**). Less than ten puncta corresponding to p62 were present within a single VL3 or VL4 muscle and the relative area of most puncta was between 3.75–7.50 μm^2 (**Figure B.5B**). RNAi-silencing of *Strip* induced abundant p62 signal within each muscle and a concomitant increase in the size of each puncta, of which a substantial proportion was also enlarged greater than 3.75 μm^2. To confirm this increase in p62, we also examined the quantity and relative size of p62-containing structures in control and *Strip* RNAi muscles using a p62-GFP fusion protein (**Figure B.5C**). Similar increases in puncta number and size were observed for p62-GFP, with a noticeable increase in the area of larger puncta (>7.5 μm^2) (**Figure B.5D**). Some of the larger, irregular p62-GFP structures (arrows) may correspond to aggregates of p62 due to overexpression [44].

If the clustering and delivery of ubiquitinated proteins to the autophagosome are dependent upon p62, then both Ub and Atg8a should overlap with p62 staining. To test this, we first

immunostained L3 muscles with anti-p62 and anti-Ub antibodies. Consistent with anti-p62 staining alone in Figure S5C, the number of p62(+)-puncta was increased in *Strip RNAi* muscles (**Figure 2.5C**). The total number of puncta that stained positive for both Ub and p62 increased ~5-fold in *Strip RNAi #1* and ~2.5-fold in *Strip RNAi #2* compared to controls (**Figure 2.5D**). When

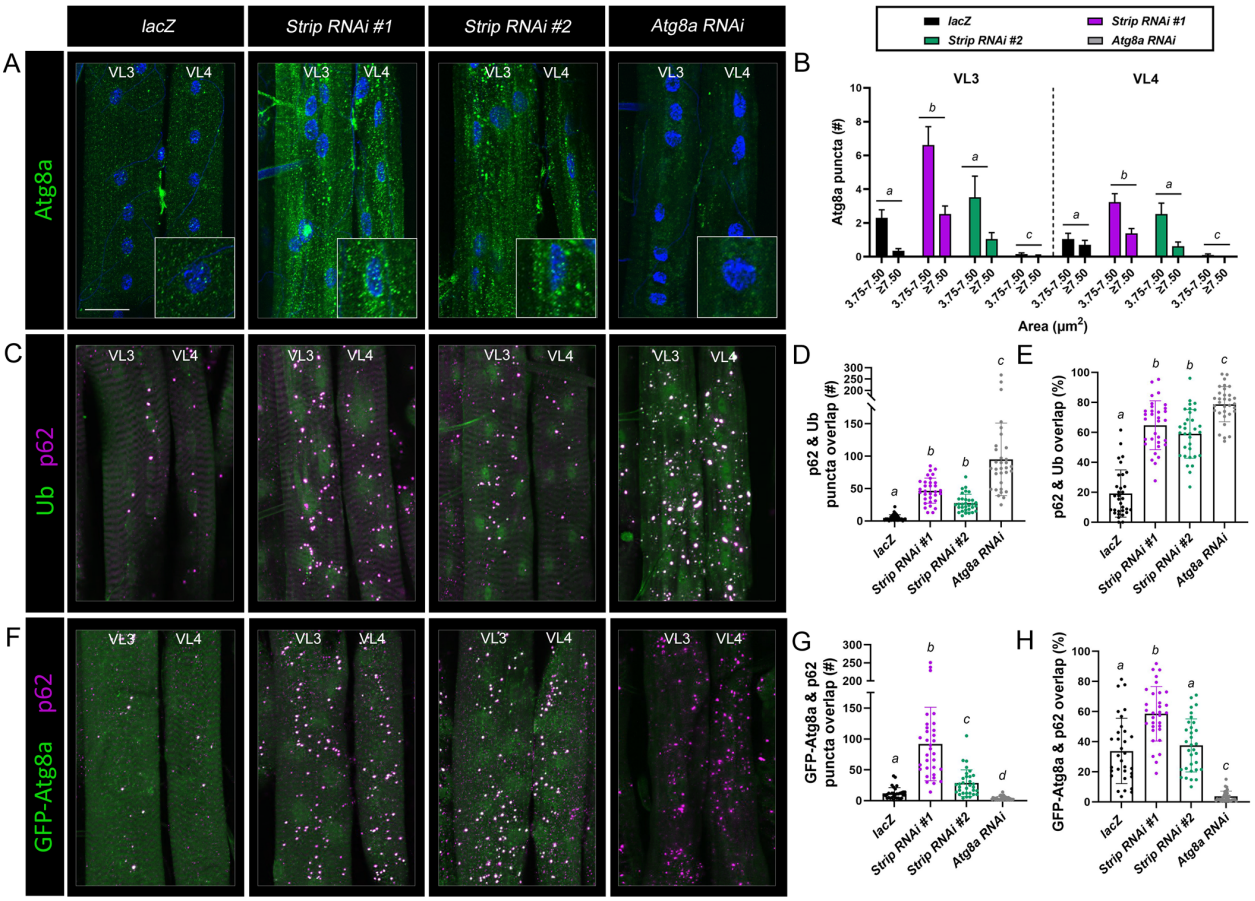


Figure 2.5. p62-Ub and p62-Atg8a complexes accumulate in Strip RNAi muscles.

(A) *Mef2-Gal4* flies were mated with *UAS-lacZ*, *UAS-Strip RNAi* #1, *UAS-Strip RNAi* #2 or *UAS-Atg8a RNAi* to assess the relative amount of Atg8a. Maximum intensity projection images of muscles VL3 and VL4 from L3 larvae reveal an increase in the size and number of Atg8a puncta (green). Inset depicts the area around a single nucleus. (B) Bar chart quantification shows an increase in the overall size and number of Atg8a(+) structures in *Strip RNAi* muscles compared to *lacZ* controls. N≥15. Genotypes with different letters are statistically different. (C) Maximum intensity projections of VL3 and VL4 muscles immunostained for p62 (magenta) and Ub (green) in *lacZ* control, *Strip RNAi* or *Atg8a RNAi* muscles. There is a clear increase in both p62 and Ub puncta upon knockdown of Strip or Atg8a. (D, E) Scatter bar graphs reveal an increase in the number of puncta (D) and the percentage of puncta (E) in VL3 and VL4 muscles that show overlap between p62 and Ub in *Strip* or *Atg8a RNAi* muscles compared to controls. N≥32. Genotypes with

different letters are statistically different. (F) VL3 or VL4 muscles from L3 larvae expressing GFP-Atg8a (green) and anti-p62 (magenta) in the indicated genotypes. There are more p62(+) puncta that show overlap with GFP-Atg8a in *Strip* knockdown muscles than in *lacZ* control muscles. *Atg8a RNAi* shows increased p62, but a loss of GFP-Atg8a staining. (G,H) Scatter bar plots of puncta in VL3 and VL3 muscles. There is an obvious increase in the number of puncta (G) and the percentage of puncta (H) that show overlap between p62 and GFP-Atg8a in *Strip RNAi* line #1 muscles compared to controls or *Atg8a RNAi*. N≥32. Genotypes with different letters are statistically different. Scale bars, 25 μm (panels A, C, F).

quantitated as percentage overlap, the ~20% observed in *lacZ* controls increased to ~60% upon a reduction in Strip (**Figure 2.5E**). This trend was even more pronounced upon loss of Atg8a whereby Ub-p62 conjugates form, but fail to recruit Atg8a thereby blocking delivery to the lysosome.

To examine the overall distribution of Ub-tagged proteins, soluble and insoluble fractions were prepared from L3 muscle tissue fillets followed by Western blotting with an anti-Ub antibody that recognizes both mono-and polyubiquitin, but not free ubiquitin. Elevated levels of ubiquitinated species were observed in both the soluble and insoluble fractions obtained from *Strip RNAi #1* and *Atg8a RNAi* muscles, with a mild increase in the insoluble portion in *Strip RNAi #2* muscles (**Figure B.6A**). Ubiquitin chain assembly on outer membrane proteins of damaged mitochondria recruits autophagic machinery for eventual lysosomal degradation [45, 46]. To assess if Strip influences mitochondrial turnover, we examined the colocalization of mitochondria and p62-GFP (**Figure B.6B**). Overall, mitochondrial morphology was similar in control and *Strip RNAi* muscles with no indication of swollen mitochondria that fail to undergo autophagic clearance due to their large size [47]. Moreover, mitochondria and p62-GFP staining did not overlap, as would be expected if ubiquitinated cargo on damaged organelles is tagged for destruction. Thus, it seems likely that the primary substrate of Ub and p62 targeting are not mitochondrial proteins.

We next examined the overlap between p62 and Atg8a. Since antibodies against each protein were generated in the same species and cannot effectively be used in double immunostaining experiments, we took advantage of the GFP-tagged Atg8a fusion protein (GFP-Atg8a). This protein faithfully recapitulates results obtained with anti-Atg8a antibody staining (**Figure 2.5, A and B**) as we observed an increase in the number and size of GFP-Atg8a (+) structures corresponding to autophagosomes (**Figure B.5 E and F**). Similar to the results for Ub-p62 conjugates, the total number and percentage of puncta that stained positive for p62 and GFP-Atg8a were more prominent in *Strip RNAi* muscles (**Figure 2.5F**). This result was most striking in *RNAi* line *#1,* where the number of puncta that showed overlap increased from an average of 10 puncta in *lacZ* control muscles to nearly 100 puncta in *Strip RNAi #1* (**Figure 2.5G**) and the percentage of puncta that overlapped in *Strip RNAi* was nearly doubled (**Figure 2.5H**). Together these data confirm that loss of Strip causes an accumulation in ubiquitinated substrates that get recognized by p62 and recruit Atg8a.

Loss of Strip disrupts autophagic flux

The coordinated increase in Ub, p62, and Atg8a suggests that the autophagy pathway is blocked. To examine autophagic flux, or the overall progression from the formation of an autophagosome to the degradation of cargo in the autolysosome, we next took advantage of the differential pH sensitivity of fluorescent tags in the GFP-mCherry (mCh)-Atg8a tandem fusion protein [48-50]. In autophagosomes, both tags emit fluorescent light resulting in co-fluorescence (white puncta) (**Figure 2.6A**). However, the fusion of autophagosomes with late endosomes or lysosomes exposes the fluorescent tags to an acidic environment where the GFP fluorescence

signal is quenched. mCh signal persists until all proteins within the autolysosome are degraded. Thus, the GFP signal labels the autophagosome prior to its fusion with the lysosome.

This GFP-mCh-Atg8a fusion protein was expressed in *lacZ* control or *Strip RNAi* muscles. The first observation was an increase in the overall number of GFP-Atg8a puncta corresponding to autophagosomes (**Figure 2.6B**). These results are consistent with the elevated numbers of autophagosomes marked by anti-Atg8a or GFP-Atg8a in **Figure 2.5A** and **Figure B4E**, respectively. Pearson's correlation coefficient (PCC) was used to quantitatively assess the overlap of GFP and mCh as a measure of autophagosomes (**Figure B.7**). PCC values for control muscles averaged ~0.3 but increased to ~0.5 in *Strip RNAi* muscles (**Figure 2.6C**). Next, both control and experimental L3 larvae expressing GFP-mCh-Atg8a were fed the lysosomal fusion inhibitor chloroquine (CQ) for 6 hours before analysis [51, 52]. As expected, the relative amount of autophagosomes (using PCC as a readout) was increased upon CQ feeding in *Mef2>lacZ* controls, demonstrating an efficient block of autophagosomal-lysosomal fusion. CQ treatment of *Mef2>Strip* RNAi larvae caused a similar accumulation of autophagosomes as observed in CQ-treated control muscles (**Figure 2.6C**). These results together demonstrate that decreasing Strip function impedes autophagy. The additional increase in PCC values upon further blocking the fusion between autophagosomes with lysosomes with CQ may be due to the perdurance of Strip protein in L3 muscles (**Figure 2.2E**).

Two additional assays were used to probe autophagic flux with isolated muscle carcasses to eliminate tissues (e.g., fat body) that exhibit high autophagic activity. First, we assessed the conversion of GFP-mCh-Atg8a to 'free' mCh to monitor autophagy-dependent delivery into the lysosome [48, 50]. When autophagy proceeds normally, the GFP-mCh-Atg8a reporter is cleaved within the lysosome and the free mCh tag can be visualized via Western blotting. Our results

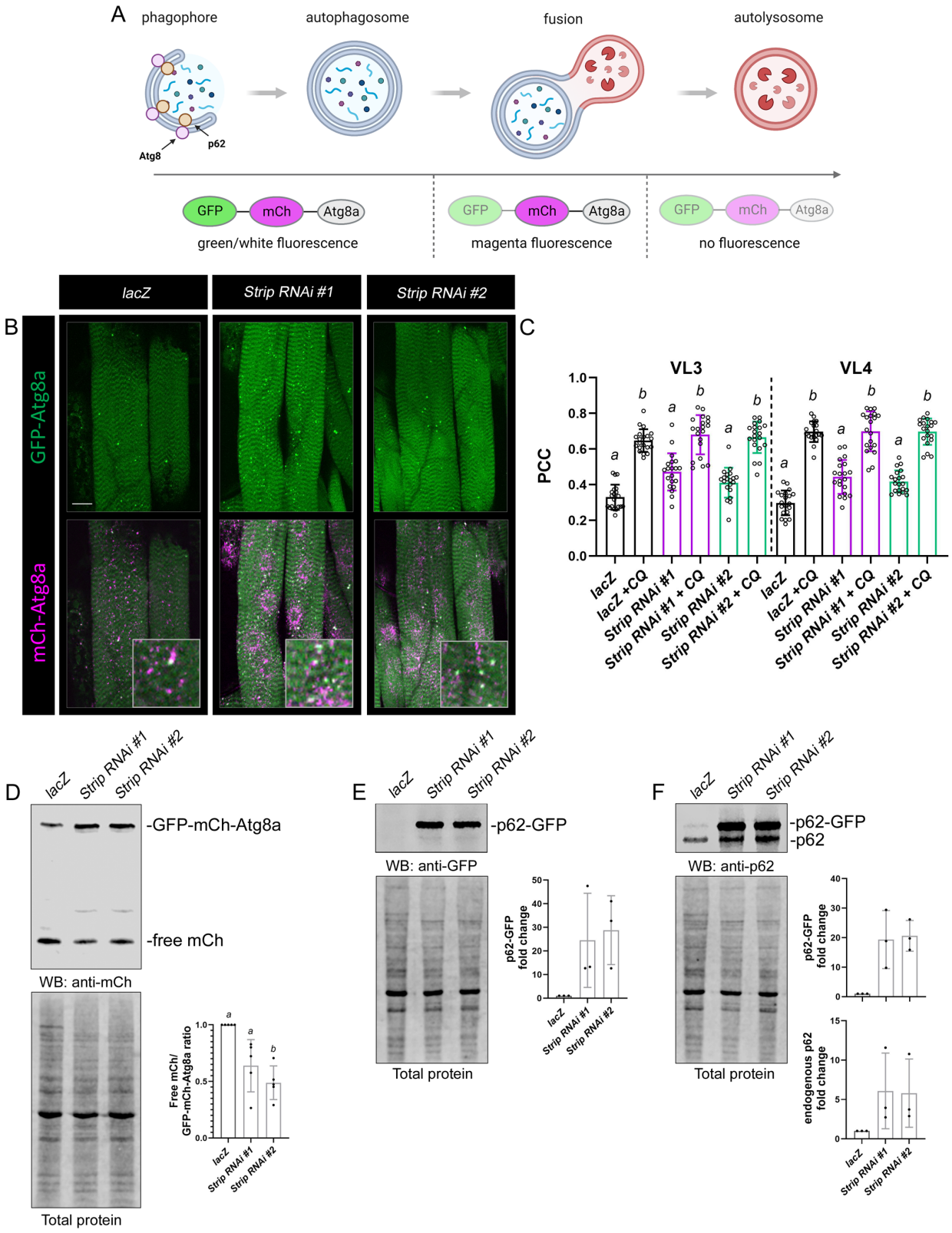


Figure 2.6. Knockdown of Strip impedes autophagic flux.

(A) Schematic showing how the pH-sensitive GFP-mCh-Atg8a tandem fusion protein is used to monitor autophagy. Created with BioRender.com. (B) Stacked confocal images of the GFP-mCh-Atg8a fusion protein in control or *Strip RNAi* muscles. Autophagosomes are marked by GFP-Atg8a (green or white puncta) and lysosomal compartments are labeled by mCh-Atg8a (magenta). Note the increase in autophagosomes upon a decrease in Strip. Inset shows the area around a single nucleus. (C) The scatter bar plot depicts the Pearson's correlation coefficient (PCC), or the amount of overlap between green and white signals corresponding to autophagosomes. N≥20. (D) mCh conversion assay assessed by Western blotting in muscles expressing *UAS-GFP-mCh-Atg8a*. Probing with an antibody against mCh shows a decrease in the amount of liberated mCh in *Strip RNAi* muscles (top panel). Loading control shows total protein levels (bottom panel). Bar scatter plot quantifying the ratio of free mCh-Atg8a/GFP-mCh-Atg8a normalized to total protein. N=3 biological replicates. (E,F) The overall level of p62 is increased in *Strip RNAi* muscles using two independent methods. Anti-GFP detects the p62-GFP fusion protein only (E), while an anti-p62 antibody detects both endogenous and GFP-tagged p62 (F). Total protein loading control (bottom panel). N=5 biological replicates for each experiment. Scale bars, 25 μm (panel A). Genotypes with different letters are statistically different ($p<0.05$).

showed an impairment in the amount of the full-length GFP-mCh-Atg8a fusion protein that is cleaved to produce the free tag in *Strip RNAi* knockdown muscles compared to control samples (**Figure 2.6D**). Since p62 itself is degraded in autolysosomes during normal autophagy, an increase or decrease in the amount of p62 serves as a marker of autophagic flux [48, 50, 53]. Expression of the p62-GFP fusion protein in *lacZ* control or *Strip RNAi* muscles by Western blotting allowed us to assess both tagged and endogenous p62 simultaneously. Using an antibody against GFP, there was a clear increase in the amount of the p62 fusion protein upon induction of *Strip RNAi* compared to *lacZ* alone (**Figure 2.6E**). Probing with an anti-p62 antibody detected the same increase in p62-GFP, but also showed elevated levels of endogenous p62 protein upon a loss of Strip (**Figure 2.6F**). Together, it is clear that autophagic flux is decreased in *Strip RNAi* muscles.

Lysosomal homeostasis is maintained in *Strip RNAi* muscles

Autophagosomal maturation involves a series of fusion events with endocytic compartments before gaining competency for lysosomal fusion [1]. Thus, the intersection between

the autophagy and endocytic pathways makes it difficult to distinguish between effects due to altered autophagic flux and/or dysfunction of the endolysosomal pathway. For example, Ras-related protein Rab7 (Rab7) is associated with late endosomes and lysosomes and plays a role in the fusion of autophagosomes to lysosomes [54-58]. To determine if Strip influences Rab7-dependent events, we first assessed Rab7 localization in control and *Strip RNAi* muscles. Rab7 was present as puncta throughout control muscles and accumulated in large, circular structures upon induction of *Strip RNAi* (**Figure 2.7A**). Next, we assessed the relationship between Rab7 and p62. Knockdown of Rab7 increased both endogenous p62 and p62-GFP protein levels (**Figure 2.7B**), thus supporting the functional link between the endocytic and autophagic pathways. Moreover, p62(+) puncta could be found associated with Rab7 structures in *Strip RNAi* muscles compared to controls (**Figure 2.7C**). These data together, bring up the possibility that flux through the endolysosomal and/or autolysosomal pathway may be affected.

Elevated numbers of autophagosomes and a corresponding reduction in autophagic flux could be due to decreased lysosome biogenesis and/or a block in the lysosomal turnover of cargo. First, we examined the relative amount of lysosomes using lysosomal-associated membrane protein 1 (Lamp1)-GFP as a marker for this organelle. In control muscles, lysosomes are generally distributed throughout the muscle, but tend to accumulate around the syncytial nuclei (**Figure 2.8A)**. Induction of *Strip RNAi* mildly altered this distribution pattern, whereby lysosomes appeared more clustered in the perinuclear region. As this feature obscured an accurate quantification of lysosomal number, we assessed if the expression of autophagosome and/or lysosome biogenesis markers is dependent on Strip. First, we verified the utility of the real-time PCR approach in muscle carcasses using the *Mef2*-Gal4 driver to induce *Strip RNAi*. Indeed, there

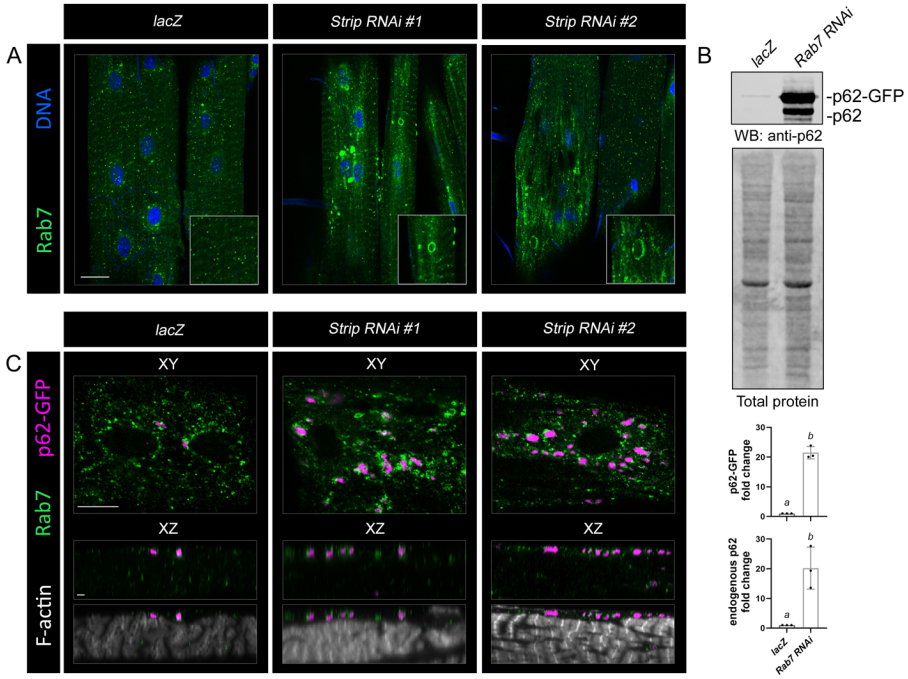


Figure 2.7. Endosome morphology is altered upon loss of Strip.

(A) VL3 or VL4 muscles of the indicated genotypes were immunostained with Rab7 to visualize late endosomes. Larger structures labeled with Rab7 were present in *Strip RNAi* muscles. (B) *Mef2*-driven *p62-GFP* was visualized by Western blotting in *lacZ* control or *Rab7 RNAi* muscles. Autophagic flux is impeded upon a reduction in Rab7 as visualized with anti-p62 that detects the p62-GFP fusion protein and endogenous p62. (C) High magnification images of L3 control or *Strip RNAi* muscles expressing UAS-*p62-GFP* and labeled with anti-Rab7 and phalloidin. Rab7 and p62 accumulate close to one another at the muscle surface. Scale bars, 50 µm (panels A and C), 10 µm (panel C, XY scans), 2 µm (panel C, XZ scans).

was a ~60% reduction in *Strip* transcript levels using qPCR (**Figure 2.8B**). Autophagy and lysosomal biogenesis is regulated by mammalian transcription factor EB (TFEB), or melanocyte-inducing transcription factor (Mitf) in *D. melanogaster* [59-61]. The relative abundance of *Mitf* transcripts, as well as its transcriptional targets *Autophagy-related 1* (*Atg1)*, *Autophagy-related 18 (Atg18a)*, and *Cysteine proteinase-1* (*Cp1)*, were not significantly changed in *Strip RNAi* muscles (**Figure 2.8B**). Thus, it seems unlikely that autophagosome biogenesis (Atg1, Atg18) or lysosomal biogenesis (Cp1) are altered as has been previously shown for *D. melanogaster* Myotubularin-

related phosphatase 6 (MTMR6) [62]. Levels of *p62* transcripts were also not appreciably changed in *Strip RNAi* muscles, further highlighting that the increase in p62 protein is indeed due to a block in autophagy rather than increased expression levels (**Figure 2.8B**).

To determine if Strip impairs the degradation of cargo, thus leading to autophagosome accumulation, we assayed for lysosomal function using an assay to measure Cathepsin-B activity. Cleavage of a fluorescent substrate by active cathepsins is a general indicator of lysosome function [63]. However, we observed no obvious difference in the relative number of puncta that stained positive for Cathepsin B activity (**Figure 2.8, C and D**). The Vacuolar H+-ATPase SFD subunit (VhaSFD)/V1H served as a negative control since lysosomal acidification does not occur upon RNAi depletion of V1H in fat body tissue RNAi [64]. These data together indicate that lysosome biogenesis and lysosome activity are not impaired in *Strip RNAi* muscles.

An alternative explanation for the increase in autophagosomes is the inability of this organelle to undergo fusion with lysosomes. Since Lysotracker labels lysosomes in live tissues, we co-labeled with p62-GFP to mark ubiquitinated cargo that could be captured by autophagosomes for degradation. In control *lacZ* muscles, ~60% of lysosomes were found to be associated with p62-GFP (**Figure 2.8E**). This value increased to ~85% in muscles that were expressing either *Strip RNAi* line, raising the possibility that impaired lysosomal fusion may be one contributing factor to explain the autophagic block observed in *Strip RNAi* muscles.

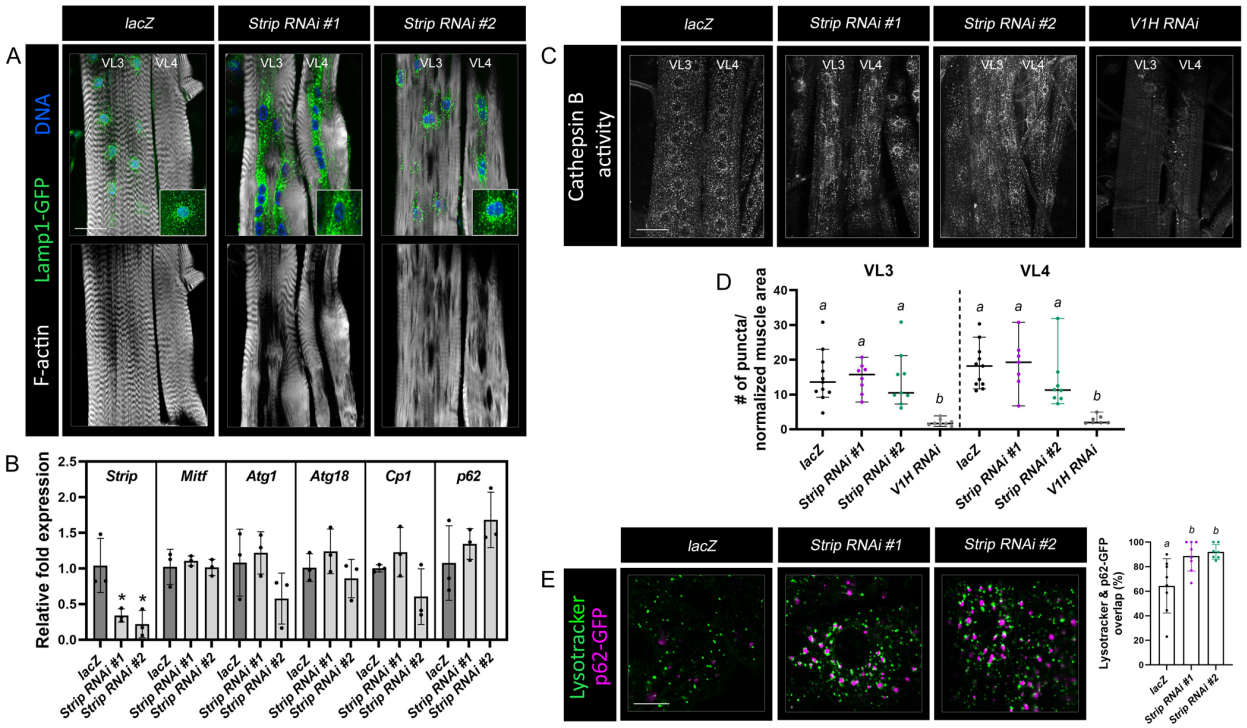


Figure 2.8. Lysosomal fusion appears partially blocked upon a reduction of Strip in muscles.

A) Labeling with Lamp1-GFP (green)shows no overt difference in the overall number of lysosomes between *lacZ* or *Strip RNAi* muscles, although the lysosomes appear clustered around nuclei in the latter. (B) mRNA transcripts implicated in autophagosome or lysosome biogenesis were analyzed by qPCR in muscle fillets from *lacZ* or *Strip RNAi* individuals. Primers corresponding to *Strip* were used as a positive control to assure the validity of RNAi knockdown. No statistically significant differences in transcript levels were observed for *Atg1*, *Atg18*, *Cp1*, *Mitf*, or *p62*. (C) Monitoring lysosomal activity by Cathepsin B staining reveals no appreciable difference in control muscles or muscles expressing ds hairpins against Strip. V1H RNAi was used as a positive control for a reduction in lysosomal activity (Mauvezin et, al 2015). (D) Quantitation of puncta stained with Cathepsin Red(+)/1ooo μm^2 represented in a scatter plot. N≥8. Genotypes with different letters are statistically different ($p<0.05$). (E) *Mef2-Gal4, p62-GFP* flies were mated with *UAS-lacZ* or *UAS-Strip RNAi* flies. Lysotracker was used to label lysosomes. Muscles deficient for Strip show close proximity between p62 and lysosomes compared to controls. Scale bars, 50 µm (panels A and C), 10 µm (panel E).

Discussion

Our efforts to understand how evolutionarily conserved proteins required for muscle development in *Tribolium* also function in *D. melanogaster* led us to explore how the STRIPAK

complex intersects with autophagy. Our previous studies defined a role for the NUAK-Stv complex in mediating the autophagic degradation of Filamin [39]. Here we functionally link the STRIPAK complex to NUAK and Stv and show that autophagy is blocked, possibly due to inefficient fusion with lysosomes. Although we did not observe alterations in autophagosome or lysosome biogenesis (assessed by qPCR) or lysosomal activity, we cannot rule out the possibility that yet unidentified factors affect endosomal or endolysosomal flux, thus overloading the pathway.

The search term 'larval muscle irregular' used to screen iBeetle-base RNAi phenotypes broadly describe muscles that are mispatterned, thinner, round, degenerative, and more. The descriptor terms primarily used for *Tc-strip dsRNA*, *Tc-Mob4 dsRNA*, and *Tc-Fgop2 dsRNA* larval musculature phenotypes were 'pattern irregular' and 'pattern not present.' Moreover, RNAi phenotypes for each of these gene products also affected other stages of the *Tribolium* lifecycle, including oogenesis, larval cuticle development, and elytra formation, just to name a few [34]. Thus, the STRIPAK complex has broad functions throughout development and likely even multiple functions within the same tissue, including muscle. Loss of Mob4 or Striatin-3 compromises myofibril assembly in zebrafish [30], while the STRIPAK complex family members Slmap, Cka, and Strip are essential for sarcomerogenesis in *D. melanogaster* indirect flight muscles (IFMs) [31]. Our identification of STRIPAK proteins co-purifying with Strip in muscle tissue combined with the functional involvement of Strip with the NUAK-Stv complex in autophagy demonstrates a role for STRIPAK complex members in both muscle development and maintenance.

One advantageous feature of model organisms is the presence of a single ortholog compared to higher organisms which may possess multiple protein family members. For example, the human genome encodes for two Strip proteins (Strip1/2) and three Striatin proteins

(STRN1/3/4), while *D. melanogaster* possesses one gene of each [27]. This feature allows for the unambiguous characterization of phenotypes through genetic analysis without complications of overlapping family members exhibiting compensatory roles. In larval body wall muscles, knockdown of Strip or Cka affected muscle architecture and muscle contraction to a greater extent than a reduction in other STRIPAK complex proteins. It is possible that inefficient protein knockdown of the selected RNAi lines in muscle tissue accounts for the weaker phenotypes. This seems unlikely since many of these RNAi lines, such as those directed against Mob4, were used to assess autophagosome transport defects in neurons [65]. Alternatively, if some members of the STRIPAK complex function coordinately with other pathways, Mob4 or Fgop2 phenotypes are only visible in the sensitized $NUAK^{K99R}$/+ or stv^{1}/+ background compared to expression of RNAi alone.

Autophagosome nucleation has been most extensively studied in yeast where phagophore assembly sites (PAS) are initiated in close proximity to the endoplasmic reticulum (ER) and may directly fuse with nearby vacuoles [66, 67]. Autophagosome biogenesis in higher eukaryotes can occur simultaneously at multiple locations, including the ER. In both yeast and mammalian cells, specialized subdomains of the ER, termed ER exit sites, serve as an organizing platform for autophagosome formation [68]. Since ER exit sites are dispersed throughout both mammalian and *D. melanogaster* multinucleated muscle cells [69, 70], it stands to reason that autophagosomes can also form at several locations before eventual fusion with endosomes and/or lysosomes. *D. melanogaster* Cka physically interacts with Dynein and directly binds Atg8a to facilitate the transport of autophagosomes and dense core vesicles within the axons of motoneurons [65]. This relatively long-range movement from the site of autophagosome initiation to the site of lysosomal fusion is not a major impediment in muscle cells where the accumulation of stalled

autophagosomes appears closer to their lysosomal targets. In Strip RNAi muscles, p62-marked autophagosomes were rarely observed far away from lysosomes, suggesting that transport in this genotype was largely unaffected in muscle tissue.

After the completion of autophagosome formation, additional fusion events with various endolysosomal compartments have been defined that are required before the final fate of degradation by autolysosomes. This process, referred to as autophagosome maturation, includes the fusion of multivesicular bodies or late endosomes with autophagosomes to form the intermediate or hybrid amphisome structure [1, 3]. While Rab5 is normally present on early endosomes, Rab 7 is predominant on late endosomes; this Rab5 to Rab 7 switch ensures endosome maturation [3, 54, 55]. Rab7/Ypt7 can also be recruited to autophagosomes by the Mon1-Ccz1 guanosine exchange factor (GEF) complex in starved yeast or larval fat cells [71, 72]. This nutrition-dependent switch in organelle localization diversifies possible functions of Rab7 but also merits caution in the interpretation of deciphering which step of autophagy may be affected. Roles for Rab7 have been delineated in the movement of late endosomes towards lysosomes as well as autophagosome maturation [1, 55]. Autophagosome accumulation in Ypt7-KO yeast or Rab7 knockdown in *D. melanogaster* cells indicates that the fusion step between autophagosomes and lysosomes is blocked [57, 58, 73]. However, CRISPR/Cas9-mediated KO of Rab7 in Madin-Darby canine kidney II (MDCK-II) cells showed an increase in structures positive for LC3 and the lysosome marker Lamp2, indicating that autophagosome fusion could proceed to generate autolysosomes [74]. More studies need to be performed to determine if this result is a general feature in mammalian cell types.

Deciphering the molecular role of STRIPAK complex components can be difficult due to subunit heterogeneity in different tissues and/or a functional requirement for core complex

members in different stages of the same biological process, such as autophagy. In *D. melanogaster*, some (Cka, Strip and Mob4), but not all (Ccm3, GckIII), of the core STRIPAK complex components tested were required for axonal autophagosome transport [65], while Strip and Cka (but not Fgop2, GckIII, Mob4, or Slmap) were required for spermatogenesis [75]. Since mammalian Ccm3 links Striatin and GckIII proteins [76], these data provide support for different STRIPAK subcomplexes dependent upon the biological context. Unc-51 like autophagy activating kinase (Ulk1) is well known for its role in autophagy initiation [66, 67, 77]. In a comprehensive set of experiments, Hu, et al. uncovered multiple phosphatase complexes as targets of Ulk1 kinase activity, one of these being Striatin [78]. Interestingly, many of these phosphorylated substrates are also required for autophagosome maturation and autophagosome-lysosome fusion, thus suggesting that intricate regulation and feedback loops regulate autophagy. Defining targets of STRIPAK complex activity during each step of autophagy would help clarify these intricate details.

Materials and methods

In silico screen

The search terms 'larval' and 'muscle' 'irregular' were queried using the search function in iBeetle-Base (https://ibeetle-base.uni-goettingen.de/) [33]. The retrieved *Tc* genes were converted to current Flybase IDs (Fbgn number) and analyzed using Cytoscape (https://cytoscape.org/) [79].

D. melanogaster genetics

All stocks were maintained on standard cornmeal-molasses-yeast-agar medium at 25 °C unless specified. Gal4/UAS crosses were set up at 25 ◦C and shifted to 31 ◦C at the beginning of the L1 stage. The following RNAi lines stocks were obtained from either the Bloomington *D.*

melanogaster Stock Center (BDSC, Bloomington, IN) or the Vienna *D. melanogaster* Resource Center (VDRC, Vienna, Austria): *UAS-Strip RNAi #1* (v16211); *UAS-Strip RNAi #2* (BL34657); *UAS-cka RNAi #1* (v106971); *UAS-cka RNAi #2* (BL28927); *UAS-Mob4 RNAi #1* (v110742); *UAS-Mob4 RNAi #2* (v40442); *UAS-Naus RNAi #1* (BL34879); *UAS-Naus RNAi #2* (v31375);; *UAS-Fgop2 RNAi #1* (v47389); *UAS-Fgop2 RNAi #2* (BL60065); *UAS-Slmap RNAi #1* (v8199); *UAS-Slmap RNAi #2* (BL32509); *UAS-Ccm3 RNAi #1* (v106841); *UAS-Ccm3 RNAi #2* (v109453); *UAS-GCKIII RNAi #1* (BL35339), *UAS-GCKIII RNAi #2* (BL57042); *UAS-PP2A-29B RNAi #1* (BL43283); *UAS-flw RNAi* (BL38336); *UAS-Atg8a RNAi* (V43097); *UAS-NUAK RNAi* (BL35194); *UAS-stv RNAi* (v34408), *UAS-Rab7 RNAi* (BL27051); and *UAS-V1H RNAi* (v47471). Additional fly stocks obtained from the BDSC include *Mef2-Gal4* (BL27390), *da-Gal4* (BL37291), *MHC-GFP* (BL38462), *UAS-lacZ* (BL3956), *UAS-GFP-Atg8a* (BL51656), and *UAS-GFP-mCh-Atg8a* (BL37749). The YFP::Lamp1^{CPTI001775} insertion (DGGR115240) is from the Kyoto *D. melanogaster* Stock Center (DGGR, Kyoto, Japan). Other stocks include the alleles *stv*^{1} [41] and *NUAK*^{K99R} (manuscript in preparation) in addition to the transgenic lines *UAS-FLAG::Strip* [80], *UAS-Strip::V5* [80]; and *UAS-p62-GFP* [81].

Muscle tissue visualization

Larval whole mounts. Wandering L3 larvae resulting from parents of the genotype *Mef2-Gal4, MHC-GFP* x *UAS-lacZ* or a *UAS-RNAi* line of interest were individually selected from the sides of a vial or bottle. Larvae were heat-killed and imaged on a Leica M165FC fluorescent stereoscope.

Muscle carcass dissections and immunostaining. Wandering L3 larvae were placed on a Sylgard plant, pinned near the mouth hooks at the anterior end, and the internal organs were removed. The resulting muscle carcasses were fixed in 4% formaldehyde and subjected to standard

immunostaining protocols with normal goat serum used as a blocking agent in PBT [39]. Tissues were stained with the following primary antibodies: rabbit anti-p62/ref(2)p (1:200, Abcam, Cambridge, MA), rabbit anti-Atg8a (1:200, Millipore, Burlington, MA), mouse anti-Rab7 (1:25, Developmental Studies Hybridoma Bank, Iowa City, IA) and rabbit anti-Filamin DZ00502 (1:200, Boster Bio, Pleasanton, CA). Fluorescence was detected using the following secondary antibodies: Alexa Fluor anti-rabbit or anti-mouse 488 or 594 (1:400, Invitrogen, Waltham, MA). F-actin was labeled with phalloidin 488 or 594 (1:400, Molecular Probes, Eugene, OR) and nuclei were stained with Hoechst dye (1:400, Invitrogen, Waltham, MA). Images were captured using a Zeiss 700 confocal microscope. Image processing and analysis were performed using a combination of Zen Black (Zeiss), ImageJ (NIH), and Adobe Photoshop. All images taken at 20x are displayed as maximum intensity projections. Data acquisition at 63x magnifications is presented as single plane confocal micrographs or maximum intensity projections as indicated in the figure legend. ***PLA.*** Wandering L3 larvae of the genotypes *Mef2>FLAG::Strip*, *Mef2>Strip::V5*, or w^{1118} were heat-killed, dissected, fixed in 4% formaldehyde and washed in PBT before following general instructions for the Duolink® In Situ Red Starter Kit Mouse/Rabbit (Sigma-Aldrich, St. Louis, MO). Tissues were blocked for 1 h at 37 °C in the Duolink® blocking solution, incubated with primary antibody diluted in the Duolink® antibody diluent overnight at 4 °C. Primary antibodies used were anti-FLAG F1804 (1:400, Sigma-Aldrich, St. Louis, MO), anti-NUAK DZ41105 (1:400, Boster Bio, Pleasanton, CA), anti-V5 R960-25 (1:400, Invitrogen, Waltham, MA), and rabbit anti-Stv (1:400) [6, 41]. Tissues were washed twice for 5 min in wash buffer A and then incubated in 40 µl PLA probe solution (8 µl PLUS probe, 8 µl MINUS probe, 24 µl antibody diluent) for 1 h at 37 °C. Tissues were washed twice for 5 min in wash buffer A and then incubated for 30 min at 37 °C in 40 µl ligation solution (8 µl ligation buffer, 31 µl ddH2O, 1 µl ligase). Tissues were

washed twice for 5 min in wash buffer A and incubated for 100 min at 37 °C in 40 µl amplification solution (8 µl amplification buffer, 31.5 µl ddH2O, 0.5 µl polymerase). Tissues were washed twice for 10 min in wash buffer B, then rinsed for 1 min with 0.01× wash buffer B and Phalloidin 488 to label F-actin (1:400, Molecular Probes, Eugene, OR). Tissues were mounted in PLA mounting medium. ***Lysosomal dyes***. For LysoTracker red staining, wandering L3 larvae were live dissected in Ca^{2+}-free HL3.1 buffer. After internal organs were removed, the muscle carcasses were incubated in 100nM LysoTracker™ Red DND-99 diluted in HL3.1 (Invitrogen, Waltham, MA) for 5 min at room temperature (wrapped in foil to avoid light) and imaged immediately. For Magic red staining, wandering L3 larvae were live dissected in HL3.1, the internal organs were removed, and muscle carcasses were incubated with Magic Red diluted in HL3.1 buffer (1:250, Magic Red Cathepsin B Assay, ImmunoChemistry, Davis, CA) for 20 min at 37 ºC (wrapped in foil to avoid light). After a quick wash in PBS, the samples were imaged immediately.

Immunoblot analysis

Dissected muscle carcasses were placed into SDS sample buffer, boiled at 95 °C for 3 min, homogenized, boiled for an additional 10 min at 95 °C, and centrifuged at 20,000 x g for 1 min to pellet debris. The resulting protein samples were separated by sodium dodecyl sulfate-polyacrylamide gel electrophoresis (SDS-PAGE) and transferred to the nitrocellulose blotting membrane (pore size 0.45 µm, Cytiva, Marlborough, MA) using the Trans-Blot® Turbo™ Transfer System (Bio-Rad, Hercules, CA). Membranes were probed with the following primary antibodies: rabbit anti-mCh ab167453 (1:5000, Abcam, Cambridge, UK), rabbit anti-GFP A-21311 (1:50o0, Thermo Fisher Scientific, Waltham, MA), rabbit anti-ref(2)p ab178440 (1:2000, Abcam, Cambridge, UK), and rabbit anti-Strip DZ41200 (1:2000, Boster Bio, Pleasanton, CA).

The rabbit anti-Strip antibody was generated against a recombinant protein that included amino acids 70-322 of the Strip-PB isoform and affinity-purified. IRDye 800CW secondary antibodies (LI-COR Biosciences, Lincoln, NE) were used at 1:10000 and Revert 700 Total Protein Stain (LI-COR Biosciences, Lincoln, NE) was used as a loading control. Membranes were developed using the LI-COR Odyssey XF and quantitation of relative protein levels was performed in Empiria Studio Software (LI-COR Biosciences, Lincoln, NE). ***Soluble/insoluble fraction preparation.*** Muscle carcasses from six dissected larvae were homogenized in 80 µL ice cold Triton X-100 soluble buffer (1% Triton X-100, and 1% Halt Protease Inhibitors Cocktail (ThermoFisher, Waltham, MA) in PBS. The homogenate was centrifuged at 21,000 x g for 10 minutes at 4 °C. The supernatant (Triton X-100 soluble sample) was collected as the soluble fraction. The pellet from the Triton X-100 soluble buffer homogenization was washed three times with 600µL ice cold Triton X-100 soluble buffer. 80 µL of room temperature insoluble buffer (4 M urea, 4% SDS, 10% 2-Mercaptoethanol, 125 mM Tris-HCl, pH 6.8, 50% glycerol, 0.2% (w/v) orange G) was added and the pellet was re-homogenized. The resulting mixture represented the insoluble fraction. All of the samples were boiled 10 minutes and centrifuged before loading to a SDS-PAGE gel. Western blotting was performed using rabbit anti-mono- and polyubiquitinylated conjugates monoclonal antibody FK2 (1:1000, Enzo Life Sciences, Farmingdale, NY).

Quantitative RT-PCR (qPCR)

Total RNA was collected from five wandering L3 larvae which were raised at 31ºC, dissected and purified using the RNeasy Mini Kit (Qiagen, Hilden, Germany). For **Figure 2.8B**, three RNA samples for each genotype were prepared. cDNA was synthesized from 350 ng of RNA using the qScript XLT cDNA SuperMix kit (Quanta Biosciences, Beverly, MA). For the qPCR reactions,

1:15 dilutions of the cDNA were combined with PowerUp SYBR Green Master Mix (ThermoFisher, Waltham, MA). The following primers were used at a final concentration of 1 μM for the assessment of autophagosome and lysosome biogenesis: *Strip* forward 5'- CGGAACTTCAAACGCTCCCT, reverse 5'- TGTTGGCATTATTTTGACCCTCG; *Atg1* forward 5'-GTCGGGGAATATGAATACAGCTC, reverse 5'- GCATGTGTTTCTTGCGATGAC; *Atg18a* forward 5'- GTGTTCGTCAACTTCAACCAGA, reverse 5'-TGTCCAGGGTCGAGTCCAC; *Cp1* forward 5'-TCAACTACACTCTGCACAAGC, reverse 5'-GCCAGTCCACAGATTTGGG; *Mitf* forward 5'- AGTATCGGAGTAGATGTGCCAC reverse 5'- CGCTGAGATATTGCCTCACTTG; *p62/ref(2)p* forward 5'- GCC CTC CCA GAA TTA CAC CA reverse 5'- GTT GGC CGA AGA ACC CTC T; *rp49* forward 5'-GCCCAAGGGTATCGACAACA, reverse 5'- GCGCTTGTTCGATCCGTAAC. For validation of RNAi knockdowns in **Figure B2.3**, eight RNA samples for each genotype were prepared, cDNA was synthesized from 150 ng of RNA, and a 1:10 dilution of cDNA was used for qRT-PCR. Primer sequences used are as follows: *Cka* forward 5'- CGCCCCAATACACAATACCG, reverse 5'- GGCGCGTCAAATCCGATTT; *Mob4* forward 5'- GGCCAGGCACAAAATCCAAG, reverse 5'- TACTTCCACACGCCCTCATC; *Naus* forward 5'- CGACAGTTCAGCGACGAC, reverse 5'- GATTCCAGCGCTCCGGAT; *Fgop2* forward 5'- ATGTCGAACCTATCCGTGGG, reverse 5'- GATTGTTGTTCTCCGCCTCC; *Slmap* forward 5'- ATGCACTGCGAAACGAGATT, reverse 5'- GAAGTATGCCGCACTCGTTT; *Ccm3* forward 5'- TCGTTCTGCCCGTCATACTG, reverse 5'- GGATTGTTCTGCTCCGACTTG; *GckIII* forward 5'- CAGCTGACCAACACCACATC, reverse 5'- CTTGGGGATGAGGAAGAGCA; *Pp2a-29B* forward 5'- AGGATGATGTAGAGCACCTGG, reverse 5'- GCACCAAGTCCACCCTAGTA.

All primers were synthesized at Integrated DNA Technologies (IDT, Stokie, IL). Quantitative transcript levels were obtained using a QuantStudio 3 instrument with QuantStudio Design and Analysis software (TheroFisher, Waltham, MA). Normalize fold change was calculated using the 2-ΔΔCt method and graphed as Mean +/- SEM using GraphPad 9.4.1.

AP-MS

Experiment. ~120 wandering L3 larvae resulting from parents of the genotype *Mef2*-Gal4 x UAS-*3xFLAG::Strip*, *Mef2*-Gal4 x UAS-*Strip::V5*, or *Mef2*-Gal4 x UAS-*lacZ* were selected from the sides of media bottles. In total, three biological replicates per genotype were collected. Larvae were gently washed using 0.7% NaCl + 0.04% Triton-100 solution to remove food debris, followed by a rinse with double-distilled water. The washed larvae were transferred to a dounce homogenizer with 1 mL lysis buffer (100mM NaCl, 50mM Tris-HCl pH 7.3, 1% NP-40, 1X Halt protease inhibitor cocktails, 1X Halt Phosphatase inhibitor cocktails, 10μM MG132). After homogenization with a pestle, the lysate was transferred to 1.5 ml microcentrifuge tubes. The supernatant was collected after centrifugation at 4°C for 5 minutes at 12,000 x g. Next, anti-FLAG® M2 Magnetic Beads m8823 (MilliporeSigma, Burlington, MA) or the anti-V5 mAb-Magnetic Beads (MBL, Woburn, MA) were incubated with the supernatant at 4 °C for 2 hours on a Barnstead Labquake Rotating Shaker. For the anti-FLAG immunoprecipitation, beads were washed three times in 400 µl cold wash buffer A (100mM NaCl, 50mM Tris-HCl pH 7.3, 0.05% NP-40) followed by two more times in 400 µl cold wash buffer B (100mM NaCl, 50mM Tris-HCl pH 7.3). The NaCl concentration was 150mM for wash and lysis buffers for the anti-V5 pulldown. All washed samples were flash frozen in liquid nitrogen and kept at -80 °C until they were sent to the Recombinant DNA/Protein Resource Facility at Oklahoma State University for MS analysis

where each biological replicate was performed in triplicate [82, 83]. ***Analysis.*** Peptides were identified and quantified by using MaxQuant v1.5.3.8 [84]. Data analysis and statistical analysis were carried out in the freely available Perseus software platform (https://maxquant.net/perseus/) [85]. Label-free quantification (LFQ) intensities were imported into Perseus and the raw data was filtered to remove potential contaminants or incorrect protein identifications. Expression values were converted to $\log_2$ for data normalization before statistical analysis [86]. For each biological replicate, proteins that passed the statistical threshold after being subjected to a two-sample t-test (Permutation-based FDR $p<0.05$) were kept for further analysis. Imputation was performed to replace missing values from a normal distribution. The values for each genotype across all experiments were averaged and the difference between experiments and controls was defined as the enrichment value.

Quantitation

Assessment of muscle contractility during the L3 to pupal transition. Pupae of the indicated genotypes were removed from vials, oriented dorsal side up, and attached to slides using a small drop of nail polish. Images were taken with a Leica M165 FC Stereomicroscope. Length and width measurements for each pupa was performed in ImageJ using the line and measure functions. Values were put into an Excel spreadsheet and the axial ratio (length/width) was calculated for each individual. The raw data were imported into Graphpad Prism 9.4.1 and graphed as a box and whiskers plot. N≥20 for each genotype. ***Muscle defect quantification.*** Embryos from parents of the genotype *Mef2*-Gal4 x UAS-*RNAi* at 25 °C were collected and transferred to 31 °C at the L1 stage. Wandering L3 larvae were dissected in PBS. The resulting muscle carcasses were fixed in 4% methanol-free formaldehyde (Polysciences) for 15 minutes at room temperature and washed

three times in PBST before incubating with phalloidin 488 (1:400) and Hoechst (1:400). For each individual larvae, seven distinct muscle fibers (VL1, VL2, VL3, VL4, LO1, LL1, and SBM) from eight randomly selected abdominal hemisegments were examined under the Zeiss 700 confocal microscope. The number of normal or defective muscles for each larvae was divided by the total number of muscles to calculate the percentage of muscle defects. N≥18 for each genotype. ***Puncta quantification.*** The Analyze-Particles function in ImageJ (NIH) was used to identify and measure GFP-Atg8a, p62-GFP, Atg8a, and p62 puncta. The colocalization between the GFP channel and the mCh channel using the GFP-mCh-Atg8a construct was determined using the Fiji/ImageJ Just Another Colocalization Plugin (JACoP) plugin. Quantitative analysis is represented by the Pearson correlation coefficient (PCC). N≥20 for each genotype. ***Statistical Analysis.*** Statistical analyses were performed in GraphPad 9.4.1. The unpaired student t-test was used to evaluate the significance between pairwise comparisons followed by the Mann-Whitney test. All other data sets that compared three or more unmatched groups that did not conform to a Gaussian distribution were subjected to one-way ANOVA analysis using the nonparametric Kruskal-Wallis test. For groups of data with the same letter (*e.g.,* a,b), the difference between the means is not statistically significant ($p>0.05$). Different letters indicate statistical significance between different data groups ($p<0.05$ – $p<0.001$). See **Table B.1** for a complete description of statistical tests and p-values.

Reference

1. Zhao YG, Zhang H. Autophagosome maturation: An epic journey from the ER to lysosomes. J Cell Biol. 2019 Mar 04;218(3):757-70. PMID: 30578282. doi: 10.1083/jcb.201810099.
2. Xia Q, Huang X, Huang J, Zheng Y, March ME, Li J, et al. The Role of Autophagy in Skeletal Muscle Diseases. Front Physiol. 2021;12:638983. PMID: 33841177. doi: 10.3389/fphys.2021.638983.
3. Ganesan D, Cai Q. Understanding amphisomes. Biochem J. 2021 May 28;478(10):1959-76. PMID: 34047789. doi: 10.1042/BCJ20200917.
4. Parzych KR, Klionsky DJ. An overview of autophagy: morphology, mechanism, and regulation. Antioxid Redox Signal. 2014 Jan 20;20(3):460-73. PMID: 23725295. doi: 10.1089/ars.2013.5371.
5. Hansen M, Rubinsztein DC, Walker DW. Autophagy as a promoter of longevity: insights from model organisms. Nat Rev Mol Cell Biol. 2018 Sep;19(9):579-93. PMID: 30006559. doi: 10.1038/s41580-018-0033-y.
6. Arndt V, Dick N, Tawo R, Dreiseidler M, Wenzel D, Hesse M, et al. Chaperone-assisted selective autophagy is essential for muscle maintenance. Curr Biol. 2010 Jan;20(2):143-8. PMID: 20060297. doi: 10.1016/j.cub.2009.11.022.
7. Kettern N, Dreiseidler M, Tawo R, Höhfeld J. Chaperone-assisted degradation: multiple paths to destruction. Biol Chem. 2010 May;391(5):481-9. PMID: 20302520. doi: 10.1515/BC.2010.058.
8. Ulbricht A, Arndt V, Höhfeld J. Chaperone-assisted proteostasis is essential for mechanotransduction in mammalian cells. Commun Integr Biol. 2013 Jul;6(4):e24925. PMID: 23986815. doi: 10.4161/cib.24925.
9. Höhfeld J, Benzing T, Bloch W, Fürst DO, Gehlert S, Hesse M, et al. Maintaining proteostasis under mechanical stress. EMBO Rep. 2021 Aug 04;22(8):e52507. PMID: 34309183. doi: 10.15252/embr.202152507.
10. Komatsu M, Waguri S, Koike M, Sou YS, Ueno T, Hara T, et al. Homeostatic levels of p62 control cytoplasmic inclusion body formation in autophagy-deficient mice. Cell. 2007 Dec 14;131(6):1149-63. PMID: 18083104. doi: 10.1016/j.cell.2007.10.035.
11. Pankiv S, Clausen TH, Lamark T, Brech A, Bruun JA, Outzen H, et al. p62/SQSTM1 binds directly to Atg8/LC3 to facilitate degradation of ubiquitinated protein aggregates by autophagy. J Biol Chem. 2007 Aug 17;282(33):24131-45. PMID: 17580304. doi: 10.1074/jbc.M702824200.
12. Bjørkøy G, Lamark T, Brech A, Outzen H, Perander M, Overvatn A, et al. p62/SQSTM1 forms protein aggregates degraded by autophagy and has a protective effect on huntingtin-induced cell death. J Cell Biol. 2005 Nov 21;171(4):603-14. PMID: 16286508. doi: 10.1083/jcb.200507002.
13. Castets P, Frank S, Sinnreich M, Rüegg MA. "Get the Balance Right": Pathological Significance of Autophagy Perturbation in Neuromuscular Disorders. J Neuromuscul Dis. 2016 May 27;3(2):127-55. PMID: 27854220. doi: 10.3233/JND-160153.
14. Franco-Romero A, Sandri M. Role of autophagy in muscle disease. Mol Aspects Med. 2021 Dec;82:101041. PMID: 34625292. doi: 10.1016/j.mam.2021.101041.
15. Margeta M. Autophagy Defects in Skeletal Myopathies. Annu Rev Pathol. 2020 Jan 24;15:261-85. PMID: 31594457. doi: 10.1146/annurev-pathmechdis-012419-032618.

16. Rowland TJ, Sweet ME, Mestroni L, Taylor MR. Danon disease - dysregulation of autophagy in a multisystem disorder with cardiomyopathy. J Cell Sci. 2016 Jun 01;129(11):2135-43. PMID: 27165304. doi: 10.1242/jcs.184770.
17. Kazuma S. Autophagic vacuolar myopathy: Danon disease and related myopathies. Neurol Clin Neurosci2021. p. 271-347.
18. Tanaka Y, Guhde G, Suter A, Eskelinen EL, Hartmann D, Lüllmann-Rauch R, et al. Accumulation of autophagic vacuoles and cardiomyopathy in LAMP-2-deficient mice. Nature. 2000 Aug 24;406(6798):902-6. PMID: 10972293. doi: 10.1038/35022595.
19. Ramachandran N, Munteanu I, Wang P, Ruggieri A, Rilstone JJ, Israelian N, et al. VMA21 deficiency prevents vacuolar ATPase assembly and causes autophagic vacuolar myopathy. Acta Neuropathol. 2013 Mar;125(3):439-57. PMID: 23315026. doi: 10.1007/s00401-012-1073-6.
20. De Palma C, Morisi F, Cheli S, Pambianco S, Cappello V, Vezzoli M, et al. Autophagy as a new therapeutic target in Duchenne muscular dystrophy. Cell Death Dis. 2012 Nov 15;3(11):e418. PMID: 23152054. doi: 10.1038/cddis.2012.159.
21. Munteanu I, Kalimo H, Saraste A, Nishino I, Minassian BA. Cardiac autophagic vacuolation in severe X-linked myopathy with excessive autophagy. Neuromuscul Disord. 2017 Feb;27(2):185-7. PMID: 27916343. doi: 10.1016/j.nmd.2016.10.007.
22. Fichna JP, Maruszak A, Żekanowski C. Myofibrillar myopathy in the genomic context. J Appl Genet. 2018 Nov;59(4):431-9. PMID: 30203143. doi: 10.1007/s13353-018-0463-4.
23. Luo YB, Peng Y, Lu Y, Li Q, Duan H, Bi F, et al. Expanding the Clinico-Genetic Spectrum of Myofibrillar Myopathy: Experience From a Chinese Neuromuscular Center. Front Neurol. 2020;11:1014. PMID: 33041974. doi: 10.3389/fneur.2020.01014.
24. Batonnet-Pichon S, Behin A, Cabet E, Delort F, Vicart P, Lilienbaum A. Myofibrillar Myopathies: New Perspectives from Animal Models to Potential Therapeutic Approaches. J Neuromuscul Dis. 2017;4(1):1-15. PMID: 28269794. doi: 10.3233/JND-160203.
25. Guglielmi V, Tomelleri G, Vattemi G. Myofibrillar myopathies through the microscope: From diagnosis to molecular pathogenesis. M icroscopie2018.
26. Hwang J, Pallas DC. STRIPAK complexes: structure, biological function, and involvement in human diseases. Int J Biochem Cell Biol. 2014 Feb;47:118-48. PMID: 24333164. doi: 10.1016/j.biocel.2013.11.021.
27. Kück U, Radchenko D, Teichert I. STRIPAK, a highly conserved signaling complex, controls multiple eukaryotic cellular and developmental processes and is linked with human diseases. Biol Chem. 2019 May 01. PMID: 31042639. doi: 10.1515/hsz-2019-0173.
28. Shi Z, Jiao S, Zhou Z. STRIPAK complexes in cell signaling and cancer. Oncogene. 2016 Sep 01;35(35):4549-57. PMID: 26876214. doi: 10.1038/onc.2016.9.
29. Sents W, Ivanova E, Lambrecht C, Haesen D, Janssens V. The biogenesis of active protein phosphatase 2A holoenzymes: a tightly regulated process creating phosphatase specificity. FEBS J. 2013 Jan;280(2):644-61. PMID: 22443683. doi: 10.1111/j.1742-4658.2012.08579.x.
30. Berger J, Berger S, Currie PD. Mob4-dependent STRIPAK involves the chaperonin TRiC to coordinate myofibril and microtubule network growth. PLoS Genet. 2022 Jun;18(6):e1010287. PMID: 35737712. doi: 10.1371/journal.pgen.1010287.
31. Kaya-Çopur A, Marchiano F, Hein MY, Alpern D, Russeil J, Luis NM, et al. The Hippo pathway controls myofibril assembly and muscle fiber growth by regulating sarcomeric gene expression. Elife. 2021 Jan 06;10. PMID: 33404503. doi: 10.7554/eLife.63726.
32. Dönitz J, Gerischer L, Hahnke S, Pfeiffer S, Bucher G. Expanded and updated data and a query pipeline for iBeetle-Base. Nucleic Acids Research; 2017. p. D831–D5.

33. Dönitz J, Schmitt-Engel C, Grossmann D, Gerischer L, Tech M, Schoppmeier M, et al. iBeetle-Base: a database for RNAi phenotypes in the red flour beetle Tribolium castaneum. Nucleic Acids Res. 2015 Jan;43(Database issue):D720-5. PMID: 25378303. doi: 10.1093/nar/gku1054.
34. Schmitt-Engel C, Schultheis D, Schwirz J, Ströhlein N, Troelenberg N, Majumdar U, et al. The iBeetle large-scale RNAi screen reveals gene functions for insect development and physiology. Nat Commun. 2015 Jul 28;6:7822. PMID: 26215380. doi: 10.1038/ncomms8822.
35. Schultheis D, Weißkopf M, Schaub C, Ansari S, Dao VA, Grossmann D, et al. A Large Scale Systemic RNAi Screen in the Red Flour Beetle. G3 (Bethesda). 2019 Apr 09;9(4):1009-26. PMID: 30733381. doi: 10.1534/g3.118.200995.
36. Brand AH, Perrimon N. Targeted gene expression as a means of altering cell fates and generating dominant phenotypes. Development. 1993 Jun;118(2):401-15. PMID: 8223268. doi: doi.org/10.1242/dev.118.2.401.
37. Hakeemi MS, Ansari S, Teuscher M, Weißkopf M, Großmann D, Kessel T, et al. Screens in fly and beetle reveal vastly divergent gene sets required for developmental processes. BMC Biol. 2022 Feb 08;20(1):38. PMID: 35135533. doi: 10.1186/s12915-022-01231-4.
38. Schultheis D, Weißkopf M, Schaub C, Ansari S, Dao VA, Grossmann D, et al. A Large Scale Systemic RNAi Screen in the Red Flour Beetle *Tribolium castaneum* Identifies Novel Genes Involved in Insect Muscle Development. G3 (Bethesda). 2019 Apr 09;9(4):1009-26. PMID: 30733381. doi: 10.1534/g3.118.200995.
39. Brooks D, Naeem F, Stetsiv M, Goetting SC, Bawa S, Green N, et al. Drosophila NUAK functions with Starvin/BAG3 in autophagic protein turnover. PLoS Genet. 2020 04;16(4):e1008700. PMID: 32320396. doi: 10.1371/journal.pgen.1008700.
40. Bawa S, Gameros S, Baumann K, Brooks DS, Kollhoff JA, Zolkiewski M, et al. Costameric Integrin and Sarcoglycan protein levels are altered in a. Mol Biol Cell. 2020 Dec:mbcE20070453. PMID: 33296226. doi: 10.1091/mbc.E20-07-0453.
41. Coulson M, Robert S, Saint R. Drosophila starvin encodes a tissue-specific BAG-domain protein required for larval food uptake. Genetics. 2005 Dec;171(4):1799-812. PMID: 16143622. doi: 10.1534/genetics.105.043265.
42. Green N, Odell N, Zych M, Clark C, Wang ZH, Biersmith B, et al. A Common Suite of Coagulation Proteins Function in Drosophila Muscle Attachment. Genetics. 2016 Aug. PMID: 27585844. doi: 10.1534/genetics.116.189787.
43. LaBeau-DiMenna EM, Clark KA, Bauman KD, Parker DS, Cripps RM, Geisbrecht ER. Thin, a Trim32 ortholog, is essential for myofibril stability and is required for the integrity of the costamere in Drosophila. Proc Natl Acad Sci U S A. 2012 Oct;109(44):17983-8. PMID: 23071324. doi: 10.1073/pnas.1208408109.
44. Pircs K, Nagy P, Varga A, Venkei Z, Erdi B, Hegedus K, et al. Advantages and limitations of different p62-based assays for estimating autophagic activity in Drosophila. PLoS One. 2012;7(8):e44214. PMID: 22952930. doi: 10.1371/journal.pone.0044214.
45. Onishi M, Yamano K, Sato M, Matsuda N, Okamoto K. Molecular mechanisms and physiological functions of mitophagy. EMBO J. 2021 Feb 01;40(3):e104705. PMID: 33438778. doi: 10.15252/embj.2020104705.
46. Palikaras K, Lionaki E, Tavernarakis N. Mechanisms of mitophagy in cellular homeostasis, physiology and pathology. Nat Cell Biol. 2018 Sep;20(9):1013-22. PMID: 30154567. doi: 10.1038/s41556-018-0176-2.

47. Wang ZH, Clark C, Geisbrecht ER. Drosophila Clueless is involved in Parkin-dependent mitophagy by promoting VCP-mediated Marf degradation. Hum Mol Genet. 2016 Feb. PMID: 26931463. doi: 10.1093/hmg/ddw067.
48. Lőrincz P, Mauvezin C, Juhász G. Exploring Autophagy in Drosophila. Cells. 2017 Jul 12;6(3). PMID: 28704946. doi: 10.3390/cells6030022.
49. Mauvezin C, Ayala C, Braden CR, Kim J, Neufeld TP. Assays to monitor autophagy in Drosophila. Methods. 2014 Jun;68(1):134-9. PMID: 24667416. doi: 10.1016/j.ymeth.2014.03.014.
50. Nagy P, Varga Á, Kovács AL, Takáts S, Juhász G. How and why to study autophagy in Drosophila: it's more than just a garbage chute. Methods. 2015 Mar;75:151-61. PMID: 25481477. doi: 10.1016/j.ymeth.2014.11.016.
51. Zirin J, Nieuwenhuis J, Perrimon N. Role of autophagy in glycogen breakdown and its relevance to chloroquine myopathy. PLoS Biol. 2013 Nov;11(11):e1001708. PMID: 24265594. doi: 10.1371/journal.pbio.1001708.
52. Zirin J, Nieuwenhuis J, Samsonova A, Tao R, Perrimon N. Regulators of autophagosome formation in Drosophila muscles. PLoS Genet. 2015 Feb;11(2):e1005006. PMID: 25692684. doi: 10.1371/journal.pgen.1005006.
53. Ding S, Hong Y. The fluorescence toolbox for visualizing autophagy. Chem Soc Rev. 2020 Nov 21;49(22):8354-89. PMID: 33156302. doi: 10.1039/d0cs00913j.
54. Hyttinen JM, Niittykoski M, Salminen A, Kaarniranta K. Maturation of autophagosomes and endosomes: a key role for Rab7. Biochim Biophys Acta. 2013 Mar;1833(3):503-10. PMID: 23220125. doi: 10.1016/j.bbamcr.2012.11.018.
55. Guerra F, Bucci C. Multiple Roles of the Small GTPase Rab7. Cells. 2016 Aug 18;5(3). PMID: 27548222. doi: 10.3390/cells5030034.
56. Kirisako T, Baba M, Ishihara N, Miyazawa K, Ohsumi M, Yoshimori T, et al. Formation process of autophagosome is traced with Apg8/Aut7p in yeast. J Cell Biol. 1999 Oct 18;147(2):435-46. PMID: 10525546. doi: 10.1083/jcb.147.2.435.
57. Fujita N, Huang W, Lin TH, Groulx JF, Jean S, Nguyen J, et al. Genetic screen in Drosophila muscle identifies autophagy-mediated T-tubule remodeling and a Rab2 role in autophagy. Elife. 2017 Jan 07;6. PMID: 28063257. doi: 10.7554/eLife.23367.
58. Lőrincz P, Tóth S, Benkő P, Lakatos Z, Boda A, Glatz G, et al. Rab2 promotes autophagic and endocytic lysosomal degradation. J Cell Biol. 2017 Jul 03;216(7):1937-47. PMID: 28483915. doi: 10.1083/jcb.201611027.
59. Bouché V, Espinosa AP, Leone L, Sardiello M, Ballabio A, Botas J. Drosophila Mitf regulates the V-ATPase and the lysosomal-autophagic pathway. Autophagy. 2016;12(3):484-98. PMID: 26761346. doi: 10.1080/15548627.2015.1134081.
60. Yang C, Wang X. Lysosome biogenesis: Regulation and functions. J Cell Biol. 2021 Jun 07;220(6). PMID: 33950241. doi: 10.1083/jcb.202102001.
61. Agostini F, Agostinis R, Medina DL, Bisaglia M, Greggio E, Plotegher N. The Regulation of MiTF/TFE Transcription Factors Across Model Organisms: from Brain Physiology to Implication for Neurodegeneration. Mol Neurobiol. 2022 Aug;59(8):5000-23. PMID: 35665902. doi: 10.1007/s12035-022-02895-3.
62. Allen EA, Amato C, Fortier TM, Velentzas P, Wood W, Baehrecke EH. A conserved myotubularin-related phosphatase regulates autophagy by maintaining autophagic flux. J Cell Biol. 2020 Nov 02;219(11). PMID: 32915229. doi: 10.1083/jcb.201909073.

63. Barral DC, Staiano L, Guimas Almeida C, Cutler DF, Eden ER, Futter CE, et al. Current methods to analyze lysosome morphology, positioning, motility and function. Traffic. 2022 May;23(5):238-69. PMID: 35343629. doi: 10.1111/tra.12839.
64. Mauvezin C, Nagy P, Juhász G, Neufeld TP. Autophagosome-lysosome fusion is independent of V-ATPase-mediated acidification. Nat Commun. 2015 May 11;6:7007. PMID: 25959678. doi: 10.1038/ncomms8007.
65. Neisch AL, Neufeld TP, Hays TS. A STRIPAK complex mediates axonal transport of autophagosomes and dense core vesicles through PP2A regulation. J Cell Biol. 2017 Feb;216(2):441-61. PMID: 28100687. doi: 10.1083/jcb.201606082.
66. Hollenstein DM, Kraft C. Autophagosomes are formed at a distinct cellular structure. Curr Opin Cell Biol. 2020 Aug;65:50-7. PMID: 32203894. doi: 10.1016/j.ceb.2020.02.012.
67. Zhao YG, Zhang H. Formation and maturation of autophagosomes in higher eukaryotes: a social network. Curr Opin Cell Biol. 2018 Aug;53:29-36. PMID: 29727743. doi: 10.1016/j.ceb.2018.04.003.
68. Graef M, Friedman JR, Graham C, Babu M, Nunnari J. ER exit sites are physical and functional core autophagosome biogenesis components. Mol Biol Cell. 2013 Sep;24(18):2918-31. PMID: 23904270. doi: 10.1091/mbc.E13-07-0381.
69. Ralston E, Ploug T, Kalhovde J, Lomo T. Golgi complex, endoplasmic reticulum exit sites, and microtubules in skeletal muscle fibers are organized by patterned activity. J Neurosci. 2001 Feb;21(3):875-83. PMID: 11157074.
70. Wang ZH, Rabouille C, Geisbrecht ER. Loss of a Clueless-dGRASP complex results in ER stress and blocks Integrin exit from the perinuclear endoplasmic reticulum in Drosophila larval muscle. Biol Open. 2015;4(5):636-48. PMID: 25862246. doi: 10.1242/bio.201511551.
71. Gao J, Langemeyer L, Kümmel D, Reggiori F, Ungermann C. Molecular mechanism to target the endosomal Mon1-Ccz1 GEF complex to the pre-autophagosomal structure. Elife. 2018 Feb 15;7. PMID: 29446751. doi: 10.7554/eLife.31145.
72. Hegedűs K, Takáts S, Boda A, Jipa A, Nagy P, Varga K, et al. The Ccz1-Mon1-Rab7 module and Rab5 control distinct steps of autophagy. Mol Biol Cell. 2016 Oct 15;27(20):3132-42. PMID: 27559127. doi: 10.1091/mbc.E16-03-0205.
73. Cong J, Fan T, Yang X, Squires JW, Cheng G, Zhang L, et al. Structural and functional changes in maternal left ventricle during pregnancy: a three-dimensional speckle-tracking echocardiography study. Cardiovasc Ultrasound. 2015 Jan;13:6. PMID: 25626356. doi: 10.1186/1476-7120-13-6.
74. Klionsky DJ, Abdelmohsen K, Abe A, Abedin MJ, Abeliovich H, Acevedo Arozena A, et al. Guidelines for the use and interpretation of assays for monitoring autophagy (3rd edition). Autophagy. 2016;12(1):1-222. PMID: 26799652. doi: 10.1080/15548627.2015.1100356.
75. La Marca JE, Diepstraten ST, Hodge AL, Wang H, Hart AH, Richardson HE, et al. S*trip* and C*ka* negatively regulate JNK signalling during D*rosophila* spermatogenesis. Development. 2019 Jun 28;146(13). PMID: 31164352. doi: 10.1242/dev.174292.
76. Kean MJ, Ceccarelli DF, Goudreault M, Sanches M, Tate S, Larsen B, et al. Structure-function analysis of core STRIPAK Proteins: a signaling complex implicated in Golgi polarization. J Biol Chem. 2011 Jul 15;286(28):25065-75. PMID: 21561862. doi: 10.1074/jbc.M110.214486.
77. Mercer TJ, Gubas A, Tooze SA. A molecular perspective of mammalian autophagosome biogenesis. J Biol Chem. 2018 Apr 13;293(15):5386-95. PMID: 29371398. doi: 10.1074/jbc.R117.810366.

78. Hu Z, Sankar DS, Vu B, Leytens A, Vionnet C, Wu W, et al. ULK1 phosphorylation of striatin activates protein phosphatase 2A and autophagy. Cell Rep. 2021 Sep 28;36(13):109762. PMID: 34592149. doi: 10.1016/j.celrep.2021.109762.
79. Shannon P, Markiel A, Ozier O, Baliga NS, Wang JT, Ramage D, et al. Cytoscape: a software environment for integrated models of biomolecular interaction networks. Genome Res. 2003 Nov;13(11):2498-504. PMID: 14597658. doi: 10.1101/gr.1239303.
80. Sakuma C, Kawauchi T, Haraguchi S, Shikanai M, Yamaguchi Y, Gelfand VI, et al. Drosophila Strip serves as a platform for early endosome organization during axon elongation. Nat Commun. 2014 Oct 14;5:5180. PMID: 25312435. doi: 10.1038/ncomms6180.
81. Chang YY, Neufeld TP. An Atg1/Atg13 complex with multiple roles in TOR-mediated autophagy regulation. Mol Biol Cell. 2009 Apr;20(7):2004-14. PMID: 19225150. doi: 10.1091/mbc.e08-12-1250.
82. Brooks DS, Vishal K, Bawa S, Alder A, Geisbrecht ER. Integration of proteomic and genetic approaches to assess developmental muscle atrophy. J Exp Biol. 2021 Nov 01;224(21). PMID: 34647571. doi: 10.1242/jeb.242698.
83. Kawakami J, Brooks D, Zalmai R, Hartson SD, Bouyain S, Geisbrecht ER. Complex protein interactions mediate Drosophila Lar function in muscle tissue. PLoS One. 2022;17(5):e0269037. PMID: 35622884. doi: 10.1371/journal.pone.0269037.
84. Cox J, Mann M. MaxQuant enables high peptide identification rates, individualized p.p.b.-range mass accuracies and proteome-wide protein quantification. Nat Biotechnol. 2008 Dec;26(12):1367-72. PMID: 19029910. doi: 10.1038/nbt.1511.
85. Tyanova S, Temu T, Sinitcyn P, Carlson A, Hein MY, Geiger T, et al. The Perseus computational platform for comprehensive analysis of (prote)omics data. Nat Methods. 2016 09;13(9):731-40. PMID: 27348712. doi: 10.1038/nmeth.3901.
86. Cox J, Hein MY, Luber CA, Paron I, Nagaraj N, Mann M. Accurate proteome-wide label-free quantification by delayed normalization and maximal peptide ratio extraction, termed MaxLFQ. Mol Cell Proteomics. 2014 Sep;13(9):2513-26. PMID: 24942700. doi: 10.1074/mcp.M113.031591.

Chapter 3 - Orchestration of autophagosome fusion by STRIPAK complex components in muscle tissue

Yungui Guo[a] and Erika R. Geisbrecht[a]

[a]Department of Biochemistry and Molecular Biophysics, Kansas State University, Manhattan, KS 66506, USA

This chapter has been published as a punctum in the journal *Autophagy Reports*.

Abstract

Autophagy is a central process responsible for the disposal of normal as well as damaged cellular proteins and organelles. Proper regulation of multiple steps – including initiation and the fusion between autophagosomes and lysosomes – is essential for the completion of cargo disposal. While the function of many proteins that mediate canonical autophagy has been characterized, the identification of new autophagy regulators may shed light on differences between tissues and/or responses to cellular stresses. In this punctum, we discuss our recent findings about how the Striatin-Interacting Phosphatase and Kinase (STRIPAK)-NUAK-Starvin (Stv) complex coordinately regulates autophagy in the muscle tissue of *Drosophila melanogaster*.

Keywords Autophagy; *Drosophila;* muscle; STRIPAK; Strip; NUAK

Abbreviations

Atg8a, autophagy-related 8a; BAG3, BCL2–associated athanogene 3; CASA, chaperone-assisted selective autophagy; Cp1, Cysteine proteinase-1; Fgop2, fibroblast growth factor receptor 1 oncogene partner 2; FLNC, Filamin C; HSC70, heat-shock cognate 70 complex; Mob4, MOB kinase activator 4; PLA, proximity ligation assay; Rab7, ras-related protein rab-7; RNAi, RNA interference; Strip, striatin-interacting protein; STRIPAK, striatin interacting phosphatase and kinase; Stv, starvin; SQSTM1, sequestosome 1; TFEB, transcription factor EB; Ub, ubiquitin.

Summary

Autophagy is a fundamental housekeeping mechanism that removes intracellular material by delivering into lysosomes. Cargo destined for lysosomal degradation may be normal cellular constituents that need to be recycled or are damaged and therefore have to be removed to prevent their accumulation. Selective autophagy broadly describes the degradation of specific cytoplasmic components that needs to be turned over. One example of a selective type of autophagy that is activated in response to mechanical tension is chaperone-assisted selective autophagy (CASA). The CASA BAG3 (BCL2–associated athanogene 3)-HSC70 (heat-shock cognate 70 complex) complex recognizes damaged client proteins, such as the actin-crosslinking protein FLNC (Filamin C). Ubiquitination of FLNC recruits the selective autophagy receptor p62/SQSTM1 (sequestosome 1) and subsequently Atg8a (autophagy-related 8a), triggering autophagosome formation and eventually leading to the lysosomal degradation of FLNC and associated components. The importance of CASA is exemplified by mutations in *BAG3* that result in childhood muscle dystrophy, cardiomyopathy, and respiratory deficiencies.

Drosophila melanogaster Stv (starvin), the ortholog of mammalian BAG3, biochemically and genetically interacts with the evolutionarily conserved NUAK kinase and the resulting NUAK-Stv complex plays an important role in the autophagic clearance of proteins in larval muscles. While many core components of the autophagy machinery are known, identifying additional regulators may elucidate mechanisms that underlie tissue and/or stress-specific responses that involve this pathway. Here we discuss how the NUAK-Stv complex coordinates with the striatin interacting phosphatase and kinase (STRIPAK) complex to regulate autophagy in *D. melanogaster* muscle tissues.

We first used an in silico approach to identify conserved mediators of muscle tissue maintenance [1]. Three of these candidates, Strip (striatin-interacting protein), Mob4 (MOB kinase activator 4), and Fgop2 (fibroblast growth factor receptor 1 oncogene partner 2) are part of the STRIPAK complex. Using Strip as a bait protein in *D. melanogaster* larval muscle tissue, we performed affinity purification-mass spectrometry (AP-MS) experiments and identified seven other known STRIPAK components. Interestingly, NUAK and Stv also co-purified with Strip and these physical interactions were verified in muscle tissue using the proximity ligation assay (PLA). We next employed genetic interaction assays using an RNA interference (RNAi) approach to confirm that STRIPAK complex members function with NUAK and Stv in the same biological process. These data led us to hypothesize that Strip and associated STRIPAK proteins may function in autophagy with the NUAK-Stv complex.

To assess changes in autophagy progression, we used immunostaining to detect ubiquitin (Ub), p62 and Atg8a upon RNAi knockdown of Strip in larval muscles. We observed an increased number of Ub-, p62-, or Atg8a-positive puncta in S*trip RNAi*-treated muscles compared to controls. Moreover, the percentage of puncta positive for both Ub and p62 (indicative of ubiquitinated cargo) or p62 and Atg8a (corresponding to autophagosomal precursors and autophagosomes) was also elevated in Strip knockdown muscles. This accumulation of autophagosomal intermediates suggested either increased biogenesis or a block in autophagosome turnover. We ruled out a role for Strip in the induction of autophagy as mRNA transcript levels corresponding to autophagosome (*Atg1, Atg18p,* and *p62*) or lysosome biogenesis *[TFEB transcription factor EB)* and *Cp1 (Cysteine proteinase-1)]* markers were not elevated in *Strip RNAi*-treated muscles. We next examined autophagic flux in tissue using the GFP-mCherry (mCh)-Atg8a tandem fusion protein. The GFP tag is acid-sensitive while the mCh tag is acid-insensitive. Therefore, both tags emit fluorescence

resulting in yellow puncta when in autophagosomal precursors and autophagosomes. In autolysosomes, however, the GFP signal is quenched and only the red fluorescence can be detected. The Pearson correlation coefficient (PCC) was used to quantitatively assess the overlap of GFP and/or mCh as a measure of autophagosome abundance and showed increased PCC values in *Strip RNAi* muscles compared to controls. Moreover, the addition of the lysosomal inhibitor chloroquine resulted in a higher number of autophagosomes in experimental as well as control larvae expressing GFP-mCh-Atg8a, further proving that decreasing Strip function inhibits autophagy.

Two additional assays were used to confirm decreased autophagic flux after induction of *Strip RNAi* in muscle tissues. First, the full-length GFP-mCh-Atg8a fusion protein is cleaved within the lysosome during normal autophagic turnover, and the free mCh tag can be detected by Western blotting. Indeed, we observed less free mCh in *Strip RNAi* muscles. Second, since p62 gets degraded in the lysosome along with selected cargo appended with Ub, p62 levels serve as an indirect marker to assess autophagic flux. Strip depletion resulted in elevated p62 levels, further supporting the notion that autophagic flux is decreased in *Strip RNAi* muscles.

Since degradation of either the tandem fusion protein or p62 was reduced upon Strip knockdown, it is possible that lysosomal function may be compromised. However, measurements of cathepsin B proteolytic activity showed no difference between control or experimental muscles. Instead, we observed enlarged p62-positive structures directly adjacent to lysosomes, suggesting an impairment in autophagosome-lysosome fusion as the cause of the autophagic flux block observed in *Strip RNAi* muscles.

An interesting observation was the presence of enlarged Rab7 (ras-related protein rab-7) -positive structures in muscles subjected to Strip knockdown. It is known that endosomes can fuse with autophagosomes to form an intermediate structure called an amphisome, before fusion with

lysosomes. Thus, maybe an additional role of Strip is to regulate amphisome production to ensure the complete activity of the autophagy pathway. Deciphering molecular targets of the STRIPAK complex will help solve this mystery.

Disclosure statement

The authors declare that they have no conflict of interest.

Funding

This work was supported by the National Institute of Arthritis and Musculoskeletal and Skin Diseases (NIAMS) of the National Institutes of Health (NIH) under award number RO1AR060788 to E.R.G. Thanks to the Kansas State University Johnson Cancer Research Center (JCRC) for travel funds to Y.G.

ORCID

Yungui Guo - https://orcid.org/0009-0001-1970-1806

Erika R. Geisbrecht - https://orcid.org/0000-0002-1450-7166

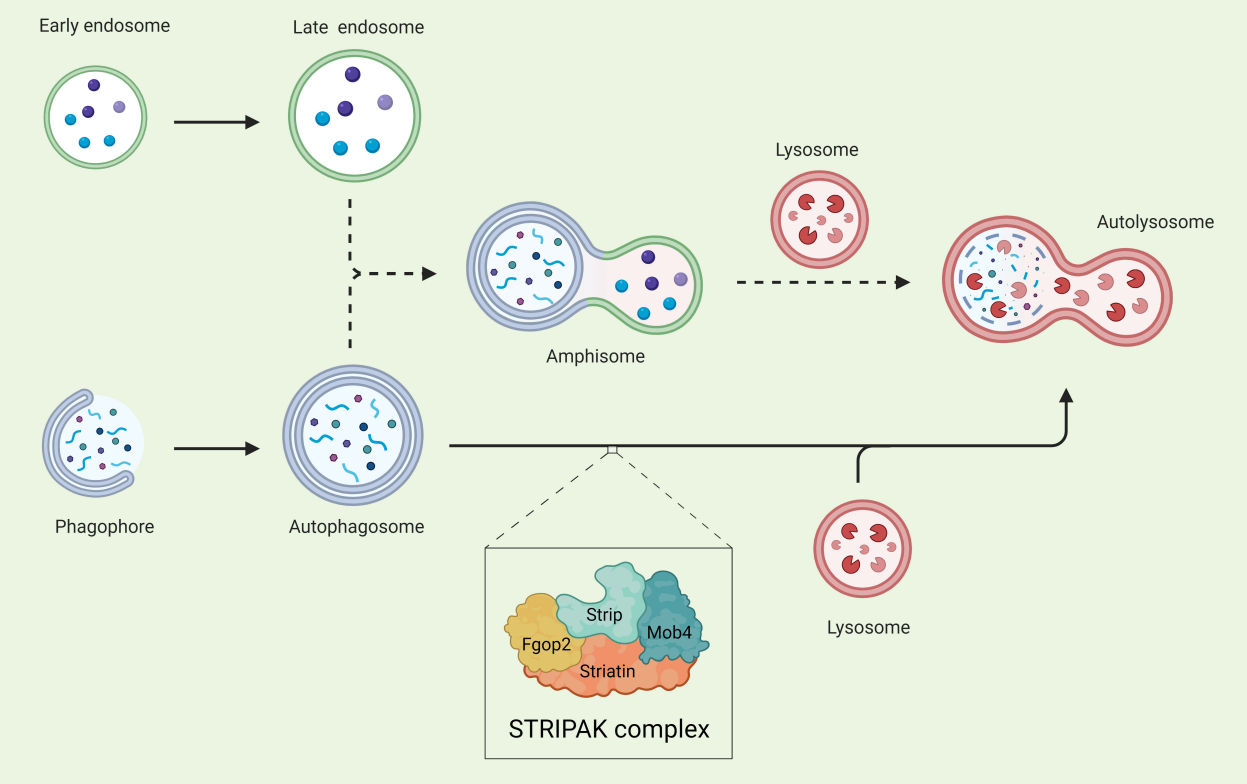


Figure 3.1. Model depicting possible degradation routes for Strip-mediated autophagosome turnover during autophagy in *D. melanogaster* muscles.

Phagophores expand into double-membrane autophagosomes and these complete autophagosomes can directly fuse with lysosomes (solid arrows). Endosomes can also fuse with autophagosomes to produce an intermediate amphisome structure before fusion with lysosomes and subsequent cargo degradation (dotted arrows). Created with Biorender.com

Reference

1. Guo Y, Zeng Q, Brooks D, Geisbrecht ER. A conserved STRIPAK complex is required for autophagy in muscle tissue. Mol Biol Cell. 2023 Aug 01;34(9). PMID: 37379167. doi: 10.1091/mbc.E23-01-0006.

Chapter 4 - Protocol for affinity purification-mass spectrometry interactome profiling in larvae of *Drosophila melanogaster*

Yungui Guo, [1,3,*] Steven D Hartson, [2] Janet Rogers, [2] Lillian Brooks-Kanost, [1] David Brooks, [1,3] and Erika R Geisbrecht[1,4,**]

[1]Department of Biochemistry and Molecular Biophysics, Kansas State University, Manhattan, KS 66503
[2]Department of Biochemistry and Molecular Biology, Oklahoma State University, Stillwater, OK 74078
[3]Technical contacts
[4]Lead contact

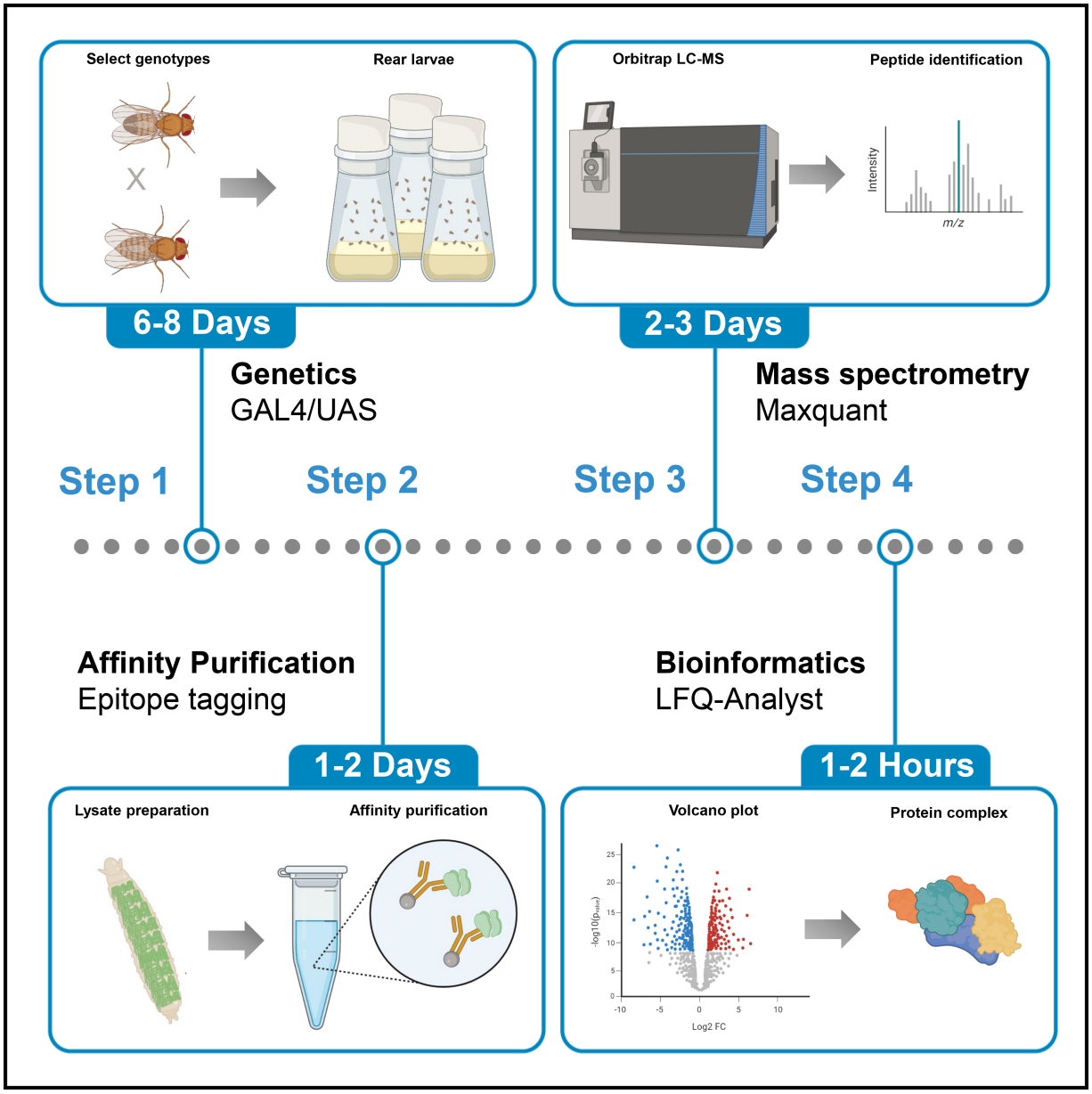
*Correspondence: yungui1@ksu.edu, dsbrooks@ksu.edu
**Correspondence: geisbrechte@ksu.edu

This chapter has been published as a journal article in *STAR Protocols*.

Summary
Many techniques exist for the identification of protein interaction networks. We present a protocol that relies on an affinity purification-mass spectrometry (AP-MS) approach to detect proteins that co-purify with a tagged bait of interest from *Drosophila melanogaster* (*D. melanogaster*) larval muscles using the GAL4/UAS expression system. We also describe steps for the isolation and identification of protein complexes, followed by streamlined bioinformatics analysis for rapid and reproducible results. This protocol can be extended to investigate protein interactions in other tissues.

For complete details on the use and execution of this protocol, please refer to Guo, *et al*.[1]

Graphical abstract



Before you begin

Multiple methods exist for assessing in vivo protein-protein interactions[2]. Assessing the composition of protein complexes within single cells or tissues at different times in development requires methods to enrich and/or isolate tagged proteins. The bipartite GAL4/UAS system in *Drosophila melanogaster* (*D. melanogaster*) provides an excellent platform for the spatial and

temporal control of protein expression[3]. Coupled with extensive options for epitope tagging proteins of interest, this versatility allows for the affinity purification of bait proteins and their associated binding partners from a specific tissue and/or cell type. Using this expression system, experiments can move from concept to scientific data in just a few weeks employing "label-free" mass spectrometry (MS) methods. These label-free approaches are ergonomic in the front-end design of experiments and there is a robust software pipeline for analyzing label-free MS data. Outlined below are multiple parameters to consider when selecting the best approach for AP-MS experiments.

Epitope-tagging, creation of transgenic flies, and validation of bait solubility

This section describes the planning and validation steps necessary for the successful enrichment of bait proteins from whole larvae.

Epitope tagging. Multiple methods exist to tag proteins of interest *in vivo*[4]. One main advantage of tagging an endogenous protein at its normal location in the genome is to avoid non-specific and/or spurious protein interactions due to overexpression. However, this approach is limited in assessing cell and/or tissue-specific interactions if the tagged protein is also expressed outside the tissue of interest. Binary expression systems, including GAL4/UAS, LexA-lexAop and QF-QUAS systems have been developed for routine use in *D. melanogaster* to express proteins of interest in different cell types or even in single cells of interest throughout development[3, 5, 6]. The GAL4/UAS system is widely used as thousands of GAL4 lines are available in individual research labs and/or reared at the Bloomington *Drosophila* Stock Center (https://bdsc.indiana.edu/index.html). Since the GAL4 protein binds to a specific nucleotide sequence referred to as the upstream activating sequence (UAS), expression of downstream epitope-tagged proteins is induced only in the expected cell types (**Figure 4.1A**). As mentioned

above, one downfall of this approach is the possibility of overexpression artifacts that can affect data interpretation. However, this limitation can be overcome through temperature modulation. Since the GAL4/UAS system is temperature-dependent, expression levels can be titrated by changing the temperature at which the flies are reared. Optimal temperature conditions can be determined through phenotype analysis (i.e., making sure that no overexpression artifacts are visible in the tissue of interest) and/or addition to Western blotting to assess protein levels.

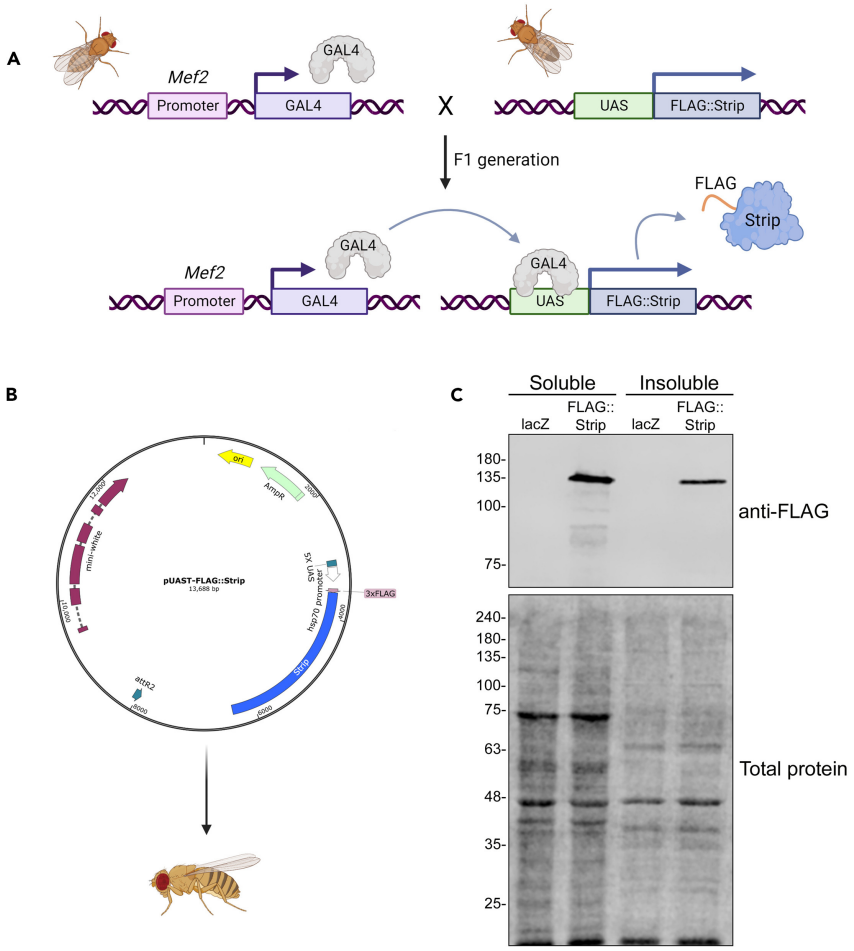


Figure 4.1. Strategy to determine the solubility of a tagged bait protein.

(A) Schematic illustration of the binary GAL4/UAS expression system. One fly line contains the GAL4 protein under the control of the *Mef2* promoter. The other fly stock possesses a UAS-based transgene containing the FLAG-tagged Strip protein. Mating of these two lines will produce progeny that express the GAL4 protein and the UAS element within the same cells. In this study, FLAG::Strip will be made in all cells that normally express the Mef2 protein. (B) Representation of the *Drosophila* pUAST transformation vector that was used to generate transgenic flies expressing FLAG::Strip. Note the vector also contains an ampicillin resistance gene for growth

in *E. coli* and a *white+ (w+)* gene for the selection of transformants by eye color. (C) Western blot validating the expression and solubility of the FLAG::Strip protein in larval muscle tissue (*Mef2>FLAG::Strip*). *Mef2>lacZ* was used as a negative control.

Epitope tags can be added in-frame at the N- or C-terminus. Two approaches are commonly used to assess if the location of the appended amino acids affects *in vivo* protein function[7]. The first is to express the tagged protein in a wild-type background to assay for dominant phenotypes. A second, or alternative method, is to determine whether or not the tagged protein can rescue mutant phenotypes due to loss of gene function[8]. The lack of an overexpression phenotype and the ability to compensate for the loss of the protein in mutant analysis provide strong evidence that the location of the epitope tag on either end of the protein does not overtly affect function. The most commonly used epitope tags are peptides that vary between 8-14 amino acids in length[7]. The efficiency of pulldowns can be improved through tandem repetition of epitope tags, the most common being 3xHA.

Creation of transgenic flies. After deciding on the type of epitope tag and the location of the tag on the N- or C-terminus, transgenic flies must be created to express the bait protein in the cell(s) of interest. In this study, a cDNA encoding for the Strip protein was fused in-frame with an N-terminal FLAG tag into a *Drosophila* expression vector and was injected into embryos using standard protocols to generate UAS-FLAG::Strip transgenic flies (**Figure 4.1B**)[9]. Multiple fee-for-service companies routinely perform this service to save research labs time and money.

Validation of bait solubility. To identify *in vivo* protein complexes, the bait of interest must be in the soluble fraction to ensure recovery from tissue lysates and subsequent analysis by MS. After expression of the bait protein using the GAL4/UAS system, soluble and insoluble lysates can be prepared from whole tissue samples followed by Western blotting to assess bait protein expression

and solubility. In this study, either control (UAS-lacZ) or bait protein (UAS-FLAG::Strip) lysates were prepared and assessed by Western blotting using an antibody against the FLAG epitope tag (**Figure 4.1C**). **Troubleshooting 1**

Fly crosses

Timing: 6-8 days

1. Collect 200-300 virgin females of the appropriate genotype.

   Note: In this study, we use virgin females that express GAL4 under the control of the *Mef2* promoter (*Mef2*-GAL4) for muscle expression[10].

2. In a bottle containing *Drosophila* media (**Table 4.1**), add ~100-150 virgin females and ~ 50 males.

   Note: In this study, we set up a control cross using UAS-lacZ males and an experimental cross with UAS-FLAG::Strip males.

Table 4.1. *Drosophila* media.

Reagent	Final concentration	Amount
Agar	5.3%	5.3 g
Yeast	1.6%	16 g
Cornmeal	6.7 %	67 g
Soy flour	9.2%	9.2 g
Corn syrup	7.0%	70 mL
Propionic Acid	0.44%	4.4 mL
10 % Tegosept	1.3%	1.3 mL
Water	N/A	up to 1L
Total		**1 L**

Store at 18°C for up to 1 month.
Note: This recipe makes 20 bottles with 50 mL of food each.

Critical: Propionic Acid can be hazardous and/or toxic. Institutional safety guidelines should be followed for safe use and disposal.

1. Incubate the bottles containing flies at 25°C for 2 days.

2. Transfer the parents to new bottles every 24 hr so the females will continue to lay fresh eggs.

   Note: Late wandering L3 larvae will begin to appear ~5-6 days after the initial mating cross is set up. **Troubleshooting 2**

Table 4.2. Key resources table.

REAGENT or RESOURCE	SOURCE	IDENTIFIER
Chemicals, peptides, and recombinant proteins		
Drosophila Agar	Genesee Scientific	Cat# 66-103
Inactive Dry Yeast	Genesee Scientific	Cat# 62-106
Flystuff Yellow Cornmeal	Genesee Scientific	Cat# 62-100
Light-Unsulphured Molasses	Sysco	Cat# 5370952
Propionic acid	Fisher Scientific	Cat# A258-500; CAS: 79-09-4
Tegosept	Genesee Scientific	Cat #: 20-258; CAS: 99-76-3
NaCl	Fisher Scientific	Cat# BP358-212 CAS: 7647-14-5
Triton X-100	Fisher Scientific	Cat# BP151-100 CAS: 9002-93-1
Tris Base	Fisher Scientific	Cat# BP152-5 CAS: 77-86-1
IGEPAL CA-630 (equivalent to Nonidet P-40)	ThermoFisher	Cat# J61055.AE CAS: 9002-93-1
Halt protease inhibitor cocktail, EDTA free (100X)	ThermoFisher Scientific	Cat# 78425
Halt phosphatase inhibitor cocktail	ThermoFisher Scientific	Cat# 78420
MG132	MilliporeSigma	Cat# 474790 CAS:133407-82-6
N-Phenylthiourea (PTU)	MilliporeSigma	Cat# P7629 CAS:103-85-5
FLAG M2 Magnetic beads	MilliporeSigma	Cat# M8823
Liquid Nitrogen	Matheson Tri-Gas, Inc	CAS: 7727-37-9
Urea	MilliporeSigma	Cat# U5128 CAS: 57-13-6

Tris (2-carboxyethyl) phosphine hydrochloride	MilliporeSigma	Cat# 646547 CAS: 51805-45-9
Iodoacetamide	MilliporeSigma	Cat# I6125 CAS: 144-48-9
Trypsin/LysC	Promega	Cat # V5072
Formic acid	MilliporeSigma	Cat# F0507 CAS: 64-18-6
Acetonitrile	MilliporeSigma	Cat# 34998 CAS: 75-05-8
Critical commercial assays		
BCA Protein Assay kit	ThermoFisher Scientific	Cat# 23227
Deposited data		
Proteomes - *Drosophila melanogaster*		https://www.uniprot.org/proteomes/UP000000803
Experimental models:		
P{Mef2-GAL4.247}	Bloomington *Drosophila* Stock Center	BDSC: 50742 FBti0152995
P{UAS-lacZ.NZ}J312	Bloomington *Drosophila* Stock Center	BDSC: 3956 FlyBase: FBti0012289
P{UAS-Strip.FLAG}	Sakuma, et al.[9]	FlyBase:FBtp0108464
Software and algorithms		
MaxQuant	Max-Planck-Institute of Biochemistry	https://maxquant.net/maxquant/ RRID:SCR_014485
Perseus	Max-Planck-Institute of Biochemistry	https://maxquant.net/perseus/ RRID:SCR_015753

LFQ Analyst	Monash Proteomics and Metabolomics Platform & Monash Bioinformatics Platform, Monash University	https://analyst-suite.monash-proteomics.cloud.edu.au/apps/lfq-analyst/
Python	Python Software Foundation	https://www.python.org/ RRID:SCR_008394
Anaconda	Anaconda Inc	https://www.anaconda.com/
Unipressed		https://multimeric.github.io/Unipressed/
Other		
6oz Square Bottom Drosophila Bottles	Genesee Scientific	Cat# 32-130
Flugs - Plastic Fly Bottles, Drosophila Closures	Genesee Scientific	Cat# 49-100
Fisherbrand Premium Microcentrifuge Tubes, 1.5mL	Fisher Scientific	Cat# 05-408-129
Eppendorf Centrifuge 5424 R	Fisher Scientific	Cat# 05-413-947PM RRID:SCR_019852
DynaMag - Spin Magnet	ThermoFisher	Cat# 12320D
Corning™ PYREX™ Dounce Homogenizer, 7mL	Fisher Scientific	Cat# 11-850-51
Thermo Scientific Labquake Tube Shaker/Rotator	Fisher Scientific	Cat# 13-687-12Q
Flystuff Embryo Collection Cage-Mini	Genesee Scientific	Cat# 59-105
Olympus Plastics 24-112, 200µl Round Gel Tip, 0.57mm Racked	Genesee Scientific	Cat# 24-112
BioPureSPN C18 spin column	The Nest Group	Cat# HMM S18R
Acclaim PepMap 100 C18 HPLC Column, 70mm, trap column	ThermoFisher	Cat# 164946
Acclaim PepMap 100 C18 HPLC Column, 500mm, Analytical Column	ThermoFisher	Cat# 164942
Orbitrap Fusion mass spectrometer	ThermoFisher	

Materials and equipment setup

Solutions to be prepared in advance

- 0.7% (w/v) NaCl /0.04% (v/v) Triton X-100: Dissolve 0.7 g NaCl and 0.04 mL Triton X-100 in 100 mL Milli-Q water.
- 5 M NaCl: Dissolve in Milli-Q water and store at 20°-22°C.
- 1 M Tris-HCl (pH = 7.3): Prepare in Milli-Q water and adjust the pH to 7.3 with HCl. Store at 20°-22°C.
- 10 % NP40 (v/v): Add 10 mL NP40 to 100 mL Milli-Q water. Store at 4°C.
- 10 mM MG132: Dissolve MG132 in DMSO. Aliquot and store at -20°C.

Table 4.3. FLAG lysis buffer.

Reagent	Final concentration	Volume
5 M NaCl	100 mM	1 mL
1 M Tris-HCl pH 7.3	50 mM	2.5 mL
10 % IGEPAL CA-630	1%	5 mL
Milli-Q water	n/a	41.5 mL
Total	**n/a**	**50 mL**

The solution can be stored at 4°C for up to 1 week.

***Alternative**:* The pH of the Tris-HCl may range from 7.3-7.6.

***Alternative**:* 10 % Nonidet P-40 (NP40) can be substituted for IGEPAL CA-630.

Solutions to be prepared on the day of the experiment

- Lysis buffer plus inhibitors
- Wash buffer A
- Wash buffer B

Table 4.4. FLAG lysis buffer plus inhibitors.

Reagent	Final concentration	Amount

FLAG lysis buffer	n/a	4.9 mL
Halt protease inhibitor cocktail (100x)	1x	50 µL
Halt phosphatase inhibitor cocktail (100x)	1x	50 µL
10 mM MG132	10 µM	5 µL
Total	**n/a**	**5 mL**

Table 4.5. Wash buffers.

	Reagent	**Final concentration**	**Amount**
Wash buffer A	5 M NaCl	100 mM	1 mL
	1 M Tris-HCl pH 7.3	50 mM	2.5 mL
	10% NP40	0.05%	0.25 mL
	Milli-Q water	n/a	46.25 mL
	Total	**n/a**	**50 mL**
Wash buffer B	5 M NaCl	100 mM	1 mL
	1 M Tris-HCl pH 7.3	50 mM	2.5 mL
	Milli-Q water	n/a	46.5 mL
	Total	**n/a**	**50 mL**

Step-by-step method details

Larval lysate preparation

Timing: 1-2 h

The steps below describe how to prepare lysates for subsequent pulldown experiments.

1. Isolation of larvae.
    a. Using a metal probe or wet paintbrush, gently transfer ~120 wandering L3 larvae (per genotype) from the sides of media bottles to an inverted embryo collection cage.

Critical: A minimum of 3 samples should be prepared per genotype (e.g., 3 controls and 3 experimental baits).

b. Wash 3 times with 0.7% (w/v) NaCl /0.04% (v/v) Triton X-100 to remove dirt and food debris.

c. Rinse larvae well with Milli-Q water.

d. Blot off excess water from the bottom of the embryo collection cage on a paper towel before proceeding.

Critical: Do not let the samples sit for more than 5 minutes before proceeding to the next step so the larvae do not desiccate. If multiple samples are being prepared, the embryo collection cage can be slightly submerged in water until needed.

2. Homogenization of larvae.

    a. Transfer the washed larvae to a pre-chilled glass Dounce homogenizer with 1 mL of cold FLAG lysis buffer plus inhibitors.

    b. Homogenize the larvae on ice until the lysate solution is turbid and no chunks of tissue are present. **Troubleshooting 3**

    c. Transfer the resulting lysate into a labeled 1.5 mL microcentrifuge tube and keep on ice until all samples are prepared.

3. Supernatant preparation

    a. Centrifuge the microcentrifuge tubes at 12000 x g for 10 min at 4°C.

    b. Use a gel loading pipette tip to transfer the supernatant to a new 1.5 mL microcentrifuge tube.

Optional: Protein concentration can be determined using the BCA Protein Assay. Typical yields after lysate preparation are ~10 mg/ml.

Optional: Gently invert the tube to mix thoroughly. Remove 40 µL of supernatant to a new 1.5 mL microcentrifuge tube to assess the amount of bait protein in input sample(s). Store at -80°C until a Western blot is performed.

Pause point*:* Samples can be stored at -80°C after this step before affinity purification.

Affinity purification

Timing: 4-6 h depending on the number of samples

The steps below describe the procedure to isolate an epitope-tagged bait protein of interest for mass spectrometry analysis.

4. Preparation of magnetic beads
    a. Gently invert the bottle of anti-FLAG® M2 magnetic beads to resuspend the resin before use.
    b. Remove 50 µL and transfer to a new 1.5 mL microcentrifuge tube.
    c. Equilibrate beads by resuspending in 1 mL FLAG lysis buffer (without inhibitors).
    d. Gently invert 3 times and place the tube in the DynaMag magnetic separator for ~ 1 min to retain the beads.
    e. Remove the supernatant and repeat the washes 2 more times.
    f. Use a gel loading tip to remove any residual liquid before proceeding.
5. Immunoprecipitation of tagged protein complexes.
    a. For each supernatant prepared in Step 3, add 1 mL to the microcentrifuge tube prepared in Step 4 that contains 50 µL of equilibrated beads.

Note: If the supernatant was frozen after Step 3, thaw on ice.

    b. Incubate on a rotating shaker for 2 h at 4°C.

c. Place the tube in the magnetic separator for ~ 1 min to collect the beads.

d. Remove the supernatant.

e. Wash with cold wash buffer A.

   i. Add 400 µL of cold Wash buffer A

   ii. Incubate on a rotating shaker for 5 min at 4°C.

   iii. Place the tube in the magnetic separator for ~ 1 min to retain the beads.

   iv. Remove the supernatant.

   v. Repeat the washes 2 more times.

f. Wash an additional 2 times with cold wash buffer B.

   i. Add 400 µL of cold Wash buffer B

   ii. Incubate on a rotating shaker for 5 min at 4°C.

   iii. Place the tube in the magnetic separator for ~ 1 min to retain the beads.

Optional: Remove 5µL of beads (10% of bead volume) to assess the amount of bait protein after pulldowns. Store at -80°C until a Western blot is performed.

   iv. Remove the supernatant.

   v. Repeat 1 more time.

Critical: It is critical that the last two wash steps exclude detergent for subsequent MS analysis.

g. Use a gel loading tip to remove all excess liquid from the beads.

Critical: Every bit of residual wash volume must be removed.

h. Flash freeze samples in liquid nitrogen and store at -80°C until MS analysis.

Pause point*:* Samples can be stored at -80°C for several months if multiple genotypes are being prepared.

Optional: Western blotting can be performed with the input sample (Step 3) and pulldown sample (Step 5f) to assess the amount of bait protein before and after pulldown. **Troubleshooting 4**

Optional: An SDS-PAGE gel from control and bait pulldown samples (Step 5f) can be run and stained by Coomassie or Silver staining to assess the background after pulldown. **Troubleshooting 5**

Elution and digestion of antibody-bound protein complexes

Timing: 18 - 24 h

The protocol below is to prepare affinity-purified complexes (i.e., the antibody chains are covalently bound to resin) before MS injection and fragmentation.

6. Elution of proteins from the antibody-bound protein complexes.
    a. Re-suspend the washed immunoresins in a 5:1 ratio of buffered 8M urea, 0.1 M Tris-HCl, pH 8.0/immunoresin pellet.

Critical: Solid urea and urea solutions can decompose to produce isocyanic acid, which will carbamylate protein N-termini, lysines, and other residues. Accordingly, urea solids should be less than 4 months old and urea solutions should be prepared fresh on the day of the antibody elutions.

    i. Incubate the suspension at room temperature (RT) for 1 hr by gently vortexing or stirring at 10 min intervals.
    ii. Centrifuge the samples at 10,000 x g at RT for 5 min.
    iii. Use a gel loading tip to carefully transfer 50 µL of supernatant to a new 1.5 ml microcentrifuge tube, while avoiding aspiration of immunoresin beads.

    b. Reduction and alkylation of samples.

i. Reduce the supernatants by adding 1/20th volume of 100 mM Tris (2-carboxyethyl) phosphine hydrochloride and incubate at RT for 30 min.

ii. Alkylate the samples by adding 1/10th volume of 100 mM iodoacetamide and incubating at RT in the dark for 30 min.

iv. Dilute the reactions to a total volume of 400 µL with Tris-HCl, pH 8.0 (100 mM final concentration of Tris-HCl).

Critical: This protocol omits reducing agents from the initial elution of the antibody resins so that the covalently bound IgG chains will be retained on the antibody beads. This is critical because reducing agents can elute IgG chains that will hinder the subsequent LC-MS analysis.

Critical: Tris (2-carboxyethyl) phosphine hydrochloride and Iodoacetamide can be hazardous and/or toxic. Institutional safety guidelines should be followed for safe use and disposal.

7. Peptide digestion.
    a. To each diluted reaction sample, add 2 µg of trypsin/LysC.
    b. Digest 12-18 hrs at 37°C.
    c. Desalt the reactions on a C18 spin column.
    d. Use vacuum centrifugation to dry the peptide eluates until just barely dry

Mass Spectrometry

Timing: ~3 hrs/sample

The following steps describe how to prepare peptides and how to run the samples for MS analysis.

8. Peptide reconstitution and separation
    a. Reconstitute the peptide mixture in 80 µL of 0.1% aqueous formic acid at RT.
        i. Dissolve for 7 min and vortex gently.

ii. Dissolve for an additional 7 min and vortex gently.

iii. Dissolve for an additional 7 min and vortex gently.

iv. Centrifuge at 10,000 x g at RT for 5 min to pellet any particulates that might clog the HPLC column.

v. Transfer 35 µL of the clarified supernatant to the autosampler vial.

vi. The sample is subjected to three sequential LC-MS analyses, each using a 10 µL injection.

Critical: Formic acid can be hazardous and/or toxic. Institutional safety guidelines should be followed for safe use and disposal.

9. LC-MS/MS analyses

a. We favor the routine use of commercial nanoscale HPLC columns 75 microns id x 50 cm length, packed with 2-micron particles of C18 (see Key Resources Table). But shorter columns and/or larger C18 particles should suffice for probing protein interactomes. Similarly, we favor 2-hr gradients for the chromatographic separation of peptides, but 1-hr gradients should suffice.

b. We favor data-dependent "shotgun" programming of the mass spectrometer, targeting the instrument's MS/MS efforts on ions that show peptide-like isotopic profiles, charge states +2 to +6, and using a dynamic exclusion "memory" to prevent redundant MS/MS targeting. In our Fusion mass spectrometer, we use the quadrupole to select parent peptide ions, the HCD cell for peptide fragmentation, and the ion trap for analysis of the peptide ion fragments (in MS jargon, a "high/low" mass accuracy approach). In our hands, and high/high approach using quadrupole selection, HCD dissociation, and Orbitrap analysis of both precursors and

fragments works equally well. As noted above, interactomics mass spectrometry does not require the depth and speed needed for complex proteomes, thus a wide variety of MS and MS/MS approaches could be used.

c. The informatics flow that we describe below utilizes the "LFQ protein intensity" outputs from the MaxQuant search application. At the time of this writing, MaxQuant is described as supporting data collected on instruments manufactured by Thermo Fisher Scientific, Bruker Daltonics, AB Sciex , and Agilent Technologies.

Note: It is beyond the scope of this protocol to exhaustively review options for the LC-MS/MS analyses. Here we describe our preferences and provide commentary.

MaxQuant peptide assignments

Timing: 3-4 hrs on a 2-processor, 30-thread workstation equipped with a solid-state drive

The following steps describe the use of the MaxQuant software[11] to identify and quantify peptides and proteins in the affinity-purified samples.

10. Use the MaxQuant proteomics software[11] to search a database of *D. melanogaster* reference protein sequences that can be downloaded from UniProt: https://www.uniprot.org/proteomes/UP000000803

Note: New versions of MaxQuant are updated regularly and can be freely downloaded from https://cox-labs.github.io/coxdocs/maxquant_instructions.html.

a. Supplementing three default parameters suggested by MaxQuant (LFQ without data normalization, Match Between Runs (MBR), and the 2-peptide LFQ rule), also

use the additional modification ‘pyroglutamate cyclization of N-terminal peptide Q residues.

Alternative: The 2-peptide LFQ rule increases rigor/stringency in the data by reducing potential false positives. A 1-peptide rule can be used for exploration and/or speculation of possible hits.

11. The resulting ProteinGroups.txt file contains unprocessed raw data from the MaxQuant software with quantitative information about peptides and proteins.
12. The LFQ-Analyst program (see Steps 13-15 below) accommodates a simplified input *.txt* file that must contain the columns listed in Table 2.

Table 4.6. Required columns for the LFQ_Analyst_MaxQuant.txt file.

Columns	**Description**
LFQ intensity (for each sample)	Label-free quantification intensities calculated by the MaxQuant software.
Only identified by site	When marked with '+', this protein group was identified only by a modification site.
Reverse	When marked with '+', this protein group contains no protein, made up of at least 50% of the peptides of the leading protein.
Potential contaminant	When marked with '+', this protein group was found to be a common contaminant.
Razor + unique peptides	The total number of razor (shared between protein groups) + unique (not shared with another protein group) peptides.
Protein IDs	Uniprot identifier (ID) numbers of protein(s) contained within the group.
Protein names	Name(s) of protein(s) contained within the group.
Gene names	Name(s) of the gene(s) associated with the identified protein(s).

Optional: Occasionally *s*ome Uniprot protein IDs are not assigned species-specific protein names and/or gene names. Two options exist. The protein IDs can be manually searched at https://www.uniprot.org/ or can be autofilled using the *Uniprot_Protein_match.py* program. Columns in the **.txt* file should be in the same order as **Table 4.6**. See **Method C4.1** for example. and instructions.

Recompilation of data using LFQ Analyst

Timing: 1-2 h per experiment

Each step below details the workflow for the analysis of label-free quantitative proteomic data generated using the MaxQuant search parameters outlined above in the user-friendly, interactive web-based program LFQ-Analyst[12].

13. Open a web browser and go to https://analyst-suites.org/apps/lfq-analyst-dev/
14. Click on 'Analysis' in the sidebar on the left side of the web page (**Figure 4.2A**).
    a. Upload the *LFQ_Analyst_MaxQuant.txt* file described in Step 12 in the appropriate location in the 'Analysis' tab.
    b. Upload the *LFQ_Analyst_experimental_design.txt* file in the appropriate location in the 'Analysis' tab.

Alternative: There is an Experimental design template that can be modified as an alternative to uploading an Experimental Design Matrix file.

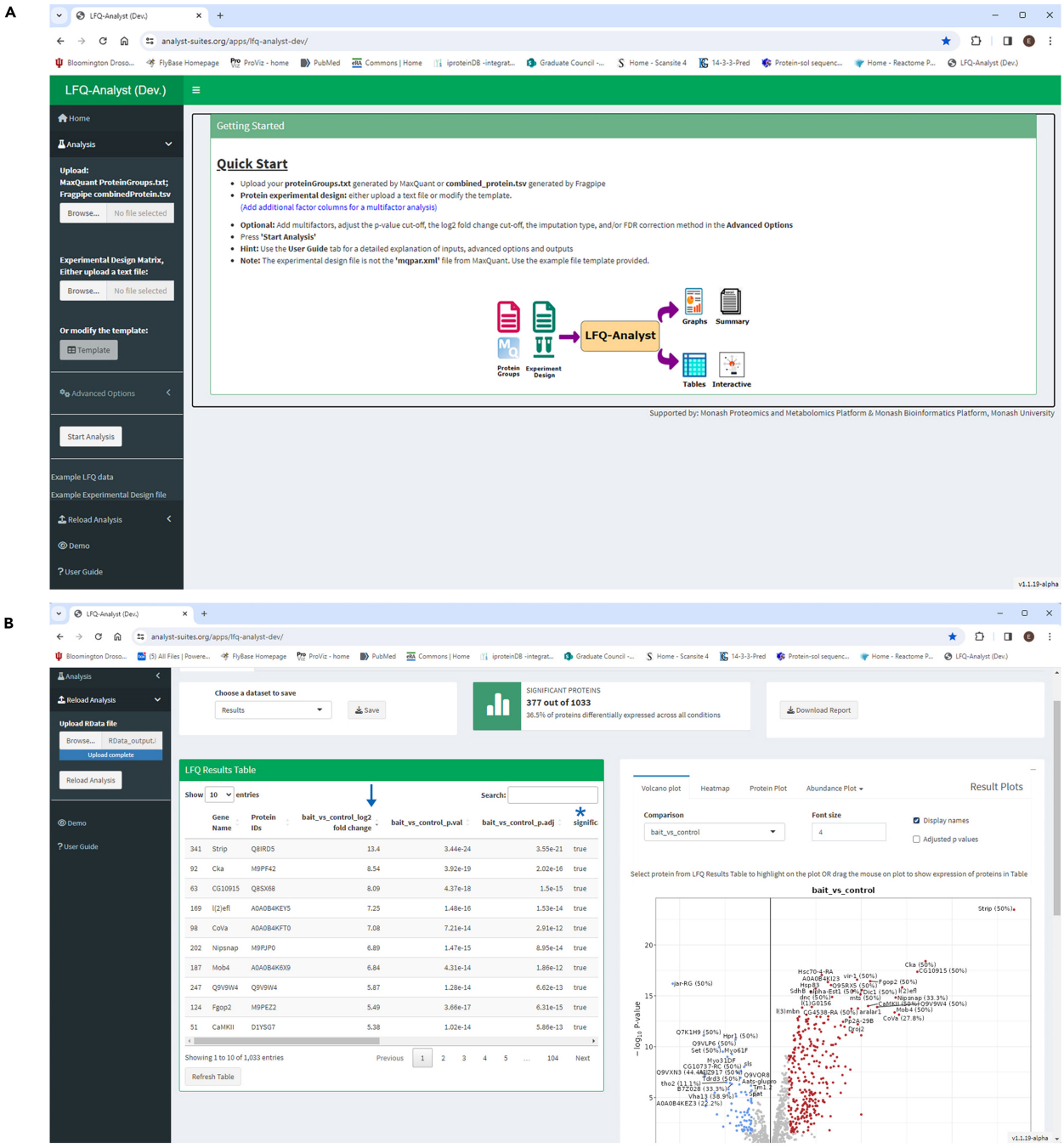


Figure 4.2. LFQ-Analyst interface.

(A) Screenshot of the LFQ-Analyst homepage. For data analysis, a *MaxQuant.txt* file or an *Experimental Design Matrix.txt* file is uploaded using the top or bottom 'Browse' buttons, respectively. (B) Screenshot of the Results page after LFQ-Analyst analysis.

Optional: Additional parameters, such as Multifactor Analysis, p-value cutoff, Log2 fold change cutoff, and type of FDR correction can also be adjusted. See the User Guide for more explanation of these variables.

c. Press the 'Start Analysis' button located in the 'Analysis' tab.

15. A Results window will appear after the analysis is complete (**Figure 4.2B**).

a. Save all datasets using the pulldown tab on the top left of the screen to save Results, Original_matrix, Imputed_matrix, Full_dataset, and Rdata.

Note: Rdata can be reloaded using the Browse tab for future analysis.

b. A full report containing a summary of Methods, Results, and Analysis plots can be downloaded using the 'Download Report' button at the top right of the screen. Individual plots for Results (Volcano plot, Heatmap, Protein plot, etc.), Quality control (PCA plot, Sample correlation, Imputation, etc.), or Enrichment (Gene ontology or Pathway enrichment) can also be saved for data analysis or publication.

Expected outcomes

Numerous proteomic applications have been developed to quantify proteins in biological studies. Both label-based and label-free quantification strategies are common [13], with the latter relying on the comparison of peptide signal intensities across different samples. Advantages of label-free approaches include lower costs since chemical and/or metabolic tags can be expensive, the elimination of labeling variability among samples, and reduced time for sample preparation. MaxQuant is a popular software suite that converts raw mass spectrometric data to provide quantitative information on peptides and proteins [11]. While many options exist to analyze MaxQuant output files, we have primarily relied on the Perseus software platform which provides

a multitude of statistical and visualization tools for data analysis [14]. Here we outline an alternative for the analysis of MaxQuant data using the LFQ-Analyst web platform. Note that a comprehensive description of the LFQ-Analyst program, including a detailed comparison of data analysis in LFQ-Analyst vs Perseus, is published [12]. Here we focus on output parameters directly relevant to assessing the success outcome of an AP-MS experiment.

The data processing workflow within LFQ-Analyst first removes contaminant proteins, reverse-sequence proteins, and proteins that are only identified by peptides that contain modified amino acids. All LFQ intensities in the MaxQuant-generated *protein.txt* files are next converted to a $\log_2$ scale and then all replicates (i.e., 3 biological and 3 technical replicates for each sample) are grouped accordingly into bait or control samples as specified in the *experimental_design.txt* file. Proteins that are significantly enriched have an adjusted p-value < 0.05 (using the Benjamini-Hochberg method) and an absolute fold change > 2. In our FLAG:::Strip vs. lacZ AP-MS data, the number of proteins that reached this threshold was ~36.5 % (377/1033) (blue box in **Figure 4.2B**), which includes both up- or down-regulated proteins. As described in Shah, et al, LFQ-Analyst outputs are divided into four primary categories: quality control (QC) plots, the LFQ results table, data results plots, and enrichment analysis [12]. The expected outcomes concerning QC and results visualization will be described further below (except expression analysis which will not be discussed further).

A systematic approach to assess data quality is essential to determine whether or not an epitope-tagged MS experiment is successful. First, it is important to assess reproducibility among replicates and between different samples. Multi-scatter plots display pairwise distributions that depict the degree of correlation between samples [15]. When this type of analysis is applied to experimental replicates of the bait protein, robust reproducibility between samples is observed

(**Figure 4.3A**). This duplicability is also quantified as a correlation value where the closer the value to 1, the higher the correlation between the two compared datasets. Another common tool is Principle Components Analysis (PCA), a method that reduces complex datasets and is a good assessment to determine abundance patterns across different samples [15]. In this study, replicates corresponding to either the FLAG::Strip pulldowns or control pulldowns were clustered together, demonstrating consistency among technical replicates as well as the contrast between experimental and control samples (**Figure 4.3B**).

After assuring that datasets pass the quality control tests described above, the next step is to assess the abundance of the bait protein relative to other identified proteins. By default, the interactive LFQ Results table displays protein names in alphabetical order. Clicking on the 'bait_vs_control_log_2 fold change column' (blue arrow in **Figure 4.2B**) sorts the data according to protein enrichment. Consistent with being a bait protein, Strip is the highest-ranked protein in terms of fold change for all proteins that reach statistical significance (asterisk in significance column in **Figure 4.2B**). Selecting the row that corresponds to Strip in the LFQ Results Table (**Figure 4.3C**) in combination with the Abundance Plot>Abundance comparison shows the mean abundance of Strip compared to all other bait or control proteins (**Figure 4.3D**). These analyses confirm the success of our AP-MS approach since Strip is most the abundant protein identified. Note that sequence coverage of Strip in each independent replicate was >60% [1].

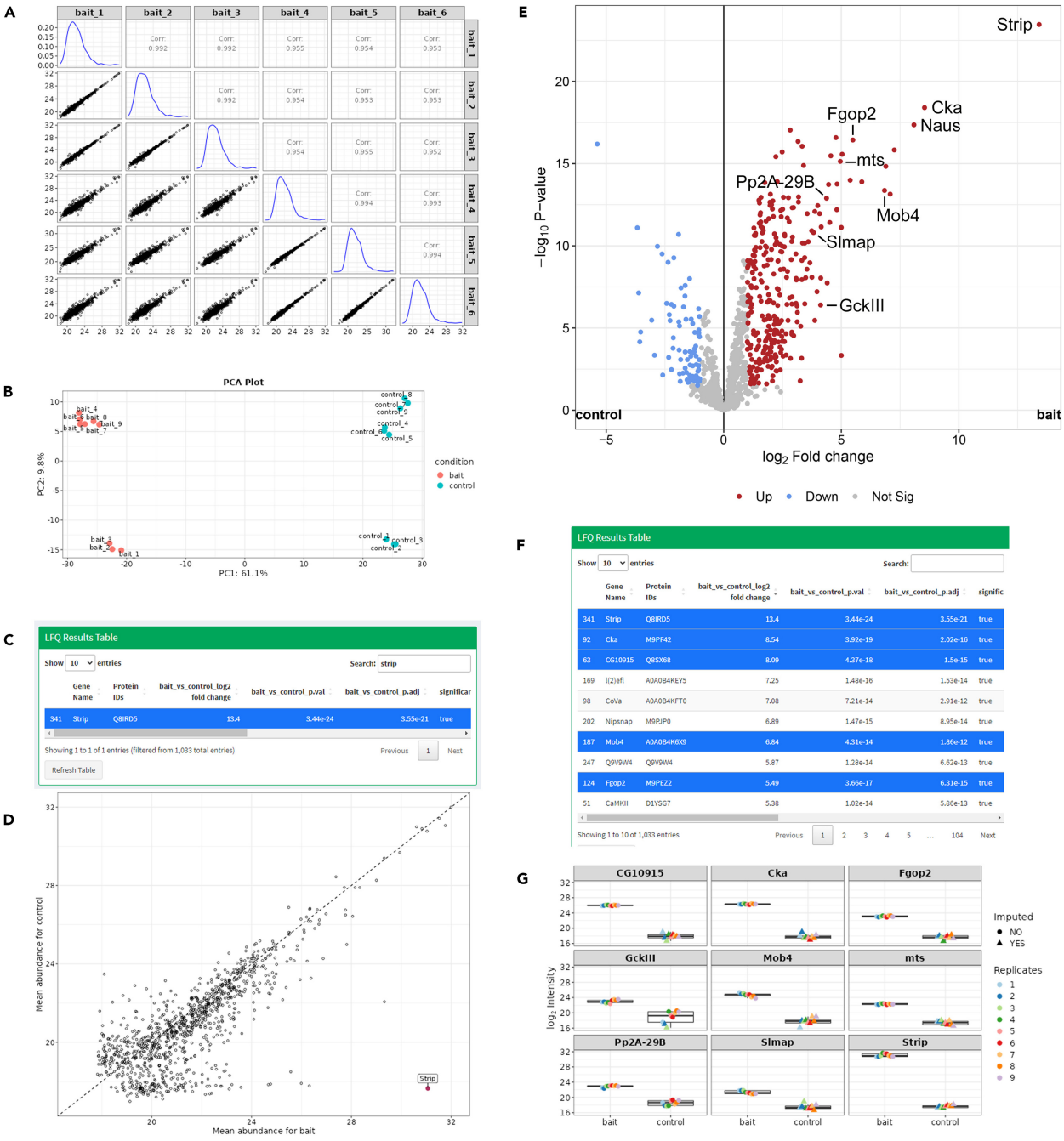


Figure 4.3. A sample of the quality control and analysis output available using LFQ-Analyst.

(A) Scatterplots of the selected bait pull-down samples showing correlation plots of individual data points and correlation values for each comparison. (B) PCA plot of AP-MS data demonstrate clustering among similar biological replicates, but separation between control (blue) and bait (pink) samples. PC1 is depicted on the x-axis and PC2 is depicted on the y-axis. (C) Individual proteins in the LFQ Results Table can be selected for additional examination. (D) One type of analysis is a scatterplot showing the mean abundance of Strip in bait and control samples compared to all other proteins. (E) Volcano plot depicting bait vs. control pull-downs. Log_2 fold changes are depicted in

the x-axis and with -$\log_{10}$ *p*-values on the y-axis. Proteins that are significantly upregulated in experimental pull-downs are shown in red and validated members of the STRIPAK complex are labeled. (F and G) Rows corresponding to proteins in the LFQ Results Table can be highlighted (F) and individual LFQ intensities can be visualized as a boxplot (G).

The primary goal of AP-MS experiments is to identify enriched proteins that physically interact with a bait protein of interest. Easy visualization of candidate binding proteins is achieved using the interactive Volcano plot function which displays '$\log_2$ fold changes' on the x-axis and '-$\log_{10}$ p-values' on the y-axis. Data points in red depict enriched proteins in Strip bait pulldowns vs lacZ control pulldowns and thus possible interactors (**Figure 4.3E**). Strip is already established as a member of the striatin-interacting phosphatase and kinase (STRIPAK) complex. Notably, multiple other proteins that comprise this multi-subunit signaling complex appear in the enriched fraction (see labeled proteins in **Figure 4.3E**). The selection of individual STRIPAK components in the LFQ Results Table allows for a comparison of protein abundance in either bait or control pulldown datasets (**Figure 4.3F**). Both physical and genetic interactions among STRIPAK complex members are well validated in multiple systems and across organisms[1, 16-21], thus demonstrating the robustness of our approach.

Since MS is a sensitive technique, hundreds to thousands of proteins may co-purify with a bait protein of interest and thus validation of putative protein-protein interactions that emerge from AP-MS experiments can be labor-intensive and costly. This challenge is often addressed using various approaches to enhance pull-down specificity. In contrast, here we use a different method, namely quantifying the proteins present in both control and experimental pulldowns, followed by a statistical approach toward validation of the proteins whose recovery is specific to the bait pulldowns. Two tactics have worked well in our experience to focus on the highest confidence candidates. The first is to increase the number of biological replicates beyond the minimum of n=3

for each genotype. In large-scale pulldowns of *Drosophila* Elmo from late-staged embryos, increasing the number of samples to n=8 allowed for the efficient identification of multiple proteins that functionally and genetically interact with this protein[22-24]. A second approach to narrow down the number of proteins for further analysis is to simultaneously perform the bait pulldowns with a different tag. We recently used this strategy to identify muscle-enriched proteins that function with Strip in the STRIPAK complex[1]. In addition to the FLAG-Strip pulldown experiments, we also performed AP-MS pulldowns using transgenic flies that express a V5 tag on the C-terminus of Strip (Strip-V5). Proteins common in both pulldowns, hence using a Venn diagram, were considered for further analysis. An additional advantage of performing duplicate pulldowns with tags on either the N- or the C-terminus is the ability to uncover proteins that may be missed if a single tag interferes with binding.

Limitations

Many of the limitations associated with this protocol can be overcome through careful experimental design. Overexpression of tagged proteins using the binary GAL4/UAS expression system may cause aberrant phenotypes leading to spurious protein interactions. Modulation of protein levels may be accomplished by decreasing the copy number of the GAL4 and/or UAS insertions or by lowering temperature. Protein solubility is a second issue that must be considered. Different buffer formulations can be used to maximize the amount of soluble protein present in lysates before immunoprecipitation.

Troubleshooting

Problem 1:

Tagged bait protein is not soluble or partially soluble (**before you begin**).

Potential solution:

- If the amount of soluble bait protein is low, the amount of starting material can be increased.
- A different lysis buffer can be used that may increase the amount of soluble protein.
- A different Gal4 driver may lower expression levels allowing for increased solubility.
- The type or location of the tag on the bait protein may help increase solubility.

Problem 2:

Limited starting material for experiments (**before you begin**)

Potential solution:

- Increase the numbers of males and females used to set up the initial cross.
- Overexpression of select tagged proteins may slow development. In this case, the experimental cross can be set up before the control cross.
- Overexpression of select tagged proteins may be lethal and/or partially lethal. Decrease the temperature at which the flies are reared, set up replicate crosses to increase the number of progeny or use a different Gal4 driver.

Problem 3:

Melanization after larval homogenization (**Step 2**).

Potential solution:

- Add N-Phenylthiourea (PTU) to a final concentration of 0.001% to inhibit melanization.

Problem 4:

Low yield of bait protein after pulldown (**Step 5**).

Potential solution:

- Increase the amount of starting material.
- Decrease the stringency of the wash buffer.

Problem 5:

Samples contain a high amount of background proteins after pulldown (**Step 5**).

Potential solution:

- Increase the stringency (higher salt concentration and/or increased detergent) of the wash buffer and/or wash additional times to decrease the background.
- Try a different brand of antibody-conjugated beads for pulldown experiments.
- After lysis preparation, spin the supernatant 2x to reduce additional components in the lysate that may cause background.
- Increase the number of biological and/or technical replicates.

Resource availability

Lead contact
Erika R. Geisbrecht (geisbrechte@ksu.edu)
Technical contacts
Yungui Guo (yungui1@ksu.edu), David Brooks (dsbrooks@ksu.edu)
Materials availability
This study did not generate new unique reagents.
Data and code availability
The published article includes all [datasets/code] generated or analysed during this study.
Acknowledgments
This work was supported by NIH grant RO1AR060788 to E.R.G. and a Johnson Center Cancer award to Y.G. Mass spectrometry analyses were conducted in the Mass Spectrometry and Proteomics Core Facility at Oklahoma State University.
Author contributions
Y.G., J.R., and S.H. performed the experiments. E.R.G. wrote the original draft of the manuscript and prepared the figures. Y.G., S.H., and D.B. edited the manuscript. L.B.K. wrote the python program. D.B. wrote the accompanying python program protocol and assisted with compiling the Key Resources table(**Table 4.2**).
Declaration of interests
The authors declare no competing interests.

Reference

1. Guo Y, Zeng Q, Brooks D, Geisbrecht ER. A conserved STRIPAK complex is required for autophagy in muscle tissue. Mol Biol Cell. 2023 Aug 01;34(9). PMID: 37379167. doi: 10.1091/mbc.E23-01-0006.
2. Elhabashy H, Merino F, Alva V, Kohlbacher O, Lupas AN. Exploring protein-protein interactions at the proteome level. Structure. 2022 Apr 07;30(4):462-75. PMID: 35219399. doi: 10.1016/j.str.2022.02.004.
3. Brand AH, Perrimon N. Targeted gene expression as a means of altering cell fates and generating dominant phenotypes. Development. 1993 Jun;118(2):401-15. PMID: 8223268. doi: doi.org/10.1242/dev.118.2.401.
4. Kimple ME, Brill AL, Pasker RL. Overview of affinity tags for protein purification. Curr Protoc Protein Sci. 2013 Sep 24;73:9..1-9..23. PMID: 24510596. doi: 10.1002/0471140864.ps0909s73.
5. Potter CJ, Tasic B, Russler EV, Liang L, Luo L. The Q system: a repressible binary system for transgene expression, lineage tracing, and mosaic analysis. Cell. 2010 Apr 30;141(3):536-48. PMID: 20434990. doi: 10.1016/j.cell.2010.02.025.
6. Lai SL, Lee T. Genetic mosaic with dual binary transcriptional systems in Drosophila. Nat Neurosci. 2006 May;9(5):703-9. PMID: 16582903. doi: 10.1038/nn1681.
7. Jarvik JW, Telmer CA. Epitope tagging. Annu Rev Genet. 1998;32:601-18. PMID: 9928493. doi: 10.1146/annurev.genet.32.1.601.
8. Duffy JB. GAL4 system in Drosophila: a fly geneticist's Swiss army knife. Genesis. 2002 2002 Sep-Oct;34(1-2):1-15. PMID: 12324939. doi: 10.1002/gene.10150.
9. Sakuma C, Kawauchi T, Haraguchi S, Shikanai M, Yamaguchi Y, Gelfand VI, et al. Drosophila Strip serves as a platform for early endosome organization during axon elongation. Nat Commun. 2014 Oct 14;5:5180. PMID: 25312435. doi: 10.1038/ncomms6180.
10. Ranganayakulu G, Elliott DA, Harvey RP, Olson EN. Divergent roles for NK-2 class homeobox genes in cardiogenesis in flies and mice. Development. 1998 Aug;125(16):3037-48. PMID: 9671578. doi: 10.1242/dev.125.16.3037.
11. Cox J, Mann M. MaxQuant enables high peptide identification rates, individualized p.p.b.-range mass accuracies and proteome-wide protein quantification. Nat Biotechnol. 2008 Dec;26(12):1367-72. PMID: 19029910. doi: 10.1038/nbt.1511.
12. Shah AD, Goode RJA, Huang C, Powell DR, Schittenhelm RB. LFQ-Analyst: An Easy-To-Use Interactive Web Platform To Analyze and Visualize Label-Free Proteomics Data Preprocessed with MaxQuant. J Proteome Res. 2020 Jan 03;19(1):204-11. PMID: 31657565. doi: 10.1021/acs.jproteome.9b00496.
13. Anand S, Samuel M, Ang CS, Keerthikumar S, Mathivanan S. Label-Based and Label-Free Strategies for Protein Quantitation. Methods Mol Biol. 2017;1549:31-43. PMID: 27975282. doi: 10.1007/978-1-4939-6740-7_4.
14. Tyanova S, Temu T, Sinitcyn P, Carlson A, Hein MY, Geiger T, et al. The Perseus computational platform for comprehensive analysis of (prote)omics data. Nat Methods. 2016 09;13(9):731-40. PMID: 27348712. doi: 10.1038/nmeth.3901.

15. Schessner JP, Voytik E, Bludau I. A practical guide to interpreting and generating bottom-up proteomics data visualizations. Proteomics. 2022 Apr;22(8):e2100103. PMID: 35107884. doi: 10.1002/pmic.202100103.
16. Berger J, Berger S, Currie PD. Mob4-dependent STRIPAK involves the chaperonin TRiC to coordinate myofibril and microtubule network growth. PLoS Genet. 2022 Jun;18(6):e1010287. PMID: 35737712. doi: 10.1371/journal.pgen.1010287.
17. Hwang J, Pallas DC. STRIPAK complexes: structure, biological function, and involvement in human diseases. Int J Biochem Cell Biol. 2014 Feb;47:118-48. PMID: 24333164. doi: 10.1016/j.biocel.2013.11.021.
18. Kück U, Radchenko D, Teichert I. STRIPAK, a highly conserved signaling complex, controls multiple eukaryotic cellular and developmental processes and is linked with human diseases. Biol Chem. 2019 May 01. PMID: 31042639. doi: 10.1515/hsz-2019-0173.
19. La Marca JE, Diepstraten ST, Hodge AL, Wang H, Hart AH, Richardson HE, et al. S*trip* and C*ka* negatively regulate JNK signalling during D*rosophila* spermatogenesis. Development. 2019 Jun 28;146(13). PMID: 31164352. doi: 10.1242/dev.174292.
20. Neisch AL, Neufeld TP, Hays TS. A STRIPAK complex mediates axonal transport of autophagosomes and dense core vesicles through PP2A regulation. J Cell Biol. 2017 Feb;216(2):441-61. PMID: 28100687. doi: 10.1083/jcb.201606082.
21. Shi Z, Jiao S, Zhou Z. STRIPAK complexes in cell signaling and cancer. Oncogene. 2016 Sep 01;35(35):4549-57. PMID: 26876214. doi: 10.1038/onc.2016.9.
22. Biersmith B, Liu ZC, Bauman K, Geisbrecht ER. The DOCK protein sponge binds to ELMO and functions in Drosophila embryonic CNS development. PLoS One. 2011 Jan;6(1):e16120. PMID: 21283588. doi: 10.1371/journal.pone.0016120.
23. Geisbrecht ER, Haralalka S, Swanson SK, Florens L, Washburn MP, Abmayr SM. Drosophila ELMO/CED-12 interacts with Myoblast city to direct myoblast fusion and ommatidial organization. Dev Biol. 2008 Feb;314(1):137-49. PMID: 18163987. doi: 10.1016/j.ydbio.2007.11.022.
24. Liu ZC, Geisbrecht ER. Moleskin is essential for the formation of the myotendinous junction in Drosophila. Dev Biol. 2011 Nov;359(2):176-89. PMID: 21925492. doi: 10.1016/j.ydbio.2011.08.028.

Chapter 5 - Pavarotti and Tumbleweed function in mitophagy initiation via blockage of nuclear envelope bud formation

Yungui Guo[1], David Brooks[1], Ziwei Zhao[1], Erica Biven[1], and Erika R. Geisbrecht[1*]

[1]Department of Biochemistry and Molecular Biophysics, Kansas State University, Manhattan, KS 66506, USA

This chapter was submitted to the journal *Autophagy Reports*.

*Corresponding author
E-mail: geisbrechte@ksu.edu

Abstract

Pavarotti (Pav) and its binding partner Tumbleweed (Tum) are well known for their evolutionarily conserved roles in microtubule-dependent movements during cytokinesis. In post-mitotic muscle cells, we unexpectedly observed the clustering of autophagosomes without an obvious disorganization of the microtubule network in *pav RNAi* muscles. These autophagosome clusters contained ubiquitin and p62 and colocalized with mitochondria. This Pav-Tum complex was enriched in muscle nuclei, consistent with roles for Pav and Tum in nuclear envelope budding, an alternative pathway for the export of large ribonucleoproteins. Consistent with *Marf mRNA* as a cargo of the NEB pathway in *Drosophila* muscles, we found a reduction of *Marf mRNA* in the myoplasm of *pav* or *tum RNAi* muscles. Moreover, knockdown of Marf or the NEB components Wash or Torsin also caused autophagosome clustering. These data together define a model whereby blocking NEB reduces mitochondrial activity and in turn recruits p62 and autophagosome components for a lysosomal fate.

Key Words: Muscle; autophagosome; mitochondria, mitophagy, *D. melanogaster*…

Abbreviations: Atg8a: Autophagy-related protein 8; ATP5α: ATP-Synthetase α; dFz2: *Drosophila* Wingless receptor dFz2; L3: third instar larva; megaRNP: mega ribonucleoproteins; MT: microtubule; Marf: Mitochondrial assembly regulatory factor; NMJ: neuromuscular junction; NE: nuclear envelope; Pav: Pavarotti; Tum: Tumbleweed; TMRM: tetramethylrhodamine methyl ester; Ub: Ubiquitin; Wash: Wiskott-Aldrich Syndrome protein

Introduction

Macroautophagy (hereafter referred to as autophagy) is generally considered a non-selective, bulk degradation system whereby portions of the cytoplasm and organelles are delivered to the lysosome for degradation and recycling [1, 2]. In contrast, damaged or harmful cargo are eliminated through a selective autophagy process that is dependent on ubiquitin-dependent autophagy receptors [3]. Both forms of autophagy require phagophore formation, expansion, and closure, resulting in double-membraned autophagosomes that undergo eventual fusion with the lysosome.

GTPases of the dynamin family mediate dynamic mitochondrial fission and fusion, with fission dividing mitochondria into two and fusion uniting mitochondria. Mitochondrial assembly regulatory factor (Marf) is responsible for mediating outer mitochondrial fusion, while Dynamin-related protein 1 (Drp1) catalyzes the constriction of this organelle towards fission [4]. These dynamics are crucial for the regulation of mitochondrial quality. Fragmented or nonfunctional organelles are continually removed by basal mitophagy, while other factors, including aging, oxidative stress, or mutations, promote mitochondrial damage and trigger increased mitochondrial turnover [5, 6]. Mitophagy is one form of selective autophagy that prevents the accumulation of damaged mitochondria [7]. The ability of mitochondria to undergo dynamic fusion and fission

further highlights the need for a selective removal process as the fusion of impaired mitochondria with their healthy counterparts can drastically affect mitochondrial, and therefore cellular, energy outputs.

Nuclear envelope (NE) budding is a recently discovered alternative pathway for cargo that is too big to traverse through nuclear pores [8, 9]. Originally characterized as a route for herpesvirus export from the nucleus [10], it is now clear that NE budding is an endogenous mechanism of nuclear transport across multiple species, including *Saccharomyces cerevisiae*, *Drosophila melanogaster,* and *Homo sapiens*. Studies in *D. melanogaster* have largely focused on the requirement for NE budding in the transport of large ribonucleoprotein (megaRNP) complexes during larval neuromuscular junction (NMJ) development and for mitochondrial integrity in the adult indirect flight muscles (IFMs) [11-13]. For example, *par6* transcripts are found at foci corresponding to NE buds as well as the postsynaptic larval NMJ [11]. Additionally, mRNAs for *Marf* and other mitochondria-associated transcripts are present in NE bud foci in larval muscles [12].

Pavarotti (Pav)/kinesin family member 23 (KIF23) and its binding partner Tumbleweed (Tum)/RacGAP1 comprise the centralspindlin complex, which organizes microtubule (MT) arrays at the mitotic spindle during cytokinesis [13]. Recently, these two proteins were also shown to be enriched in NE bud foci and required for the nuclear budding process through physical interactions with Wiskott-Aldrich Syndrome protein (WASH) [13]. Here we present new data that knockdown of Pav or Tum in larval muscles results in the aggregation of autophagosomes that colocalize with mitochondria. *pav RNAi* muscle nuclei show fewer NE buds and reduced *Marf mRNA* in the myoplasm. Moreover, the aggregation of mitochondria and autophagosomes are phenocopied in

Marf RNAi muscles. We propose that loss of *Marf*, and possibly other transcripts, reduce mitochondrial integrity which in turn recruits ubiquitin and p62 for autophagosome formation.

Results

Loss of Pav results in elevated p62 puncta in larval bodywall muscles

To discover new autophagy regulators, we performed a mini RNAi screen that targeted proteins with microtubule or trafficking-related functions using *Drosophila* larval muscles as a cell biological model. UAS-RNAi lines were crossed with the *Mef2-GAL4* driver to selectively knock down target transcripts in muscle tissue. The selected RNAi genes were classified into four groups based upon predicted functions of the targeted proteins - dynein-related, kinesin-related, spindle-associated, and other (**Figure 5.1A**). Wandering third instar larva (L3) were filleted and the muscle carcasses were immunostained with an antibody generated against Ref(2)p/p62. p62 is an autophagy receptor that binds to ubiquitinated cargo and it's abundance reflects the state of autophagy in the cell [14, 15]. Quantitation was performed using the Analyze Particles function in ImageJ and the results reported reflect the total number of p62(+) puncta in the ventral longitudinal 3 (VL3) and ventral longitudinal 4 (VL4) muscles. In comparison to the negative control *Mef2>lacZ*, we observed a significant increase ($p<0.01$) in the number of p62(+) puncta in 9 out of the 12 RNAi lines tested. Knockdown of Pav/Kif23 resulted in the strongest phenotype compared to other RNAi lines, with approximately 3.6 fold more p62(+) puncta than the *lacZ* muscles (**Figure 5.1B and Figure D5.1B**). In some instances these p62-marker puncta were clustered together (**Figure 5.1B,** yellow triangle). While we have analyzed other muscle mutants with elevated p62, this clustering phenotype had not been observed previously [16, 17].

Since Pav belongs to the kinesin superfamily and is a MT motor protein [18], we next immunostained for MTs in *pav RNAi* muscles. The overall MT pattern was similar in *pav RNAi*

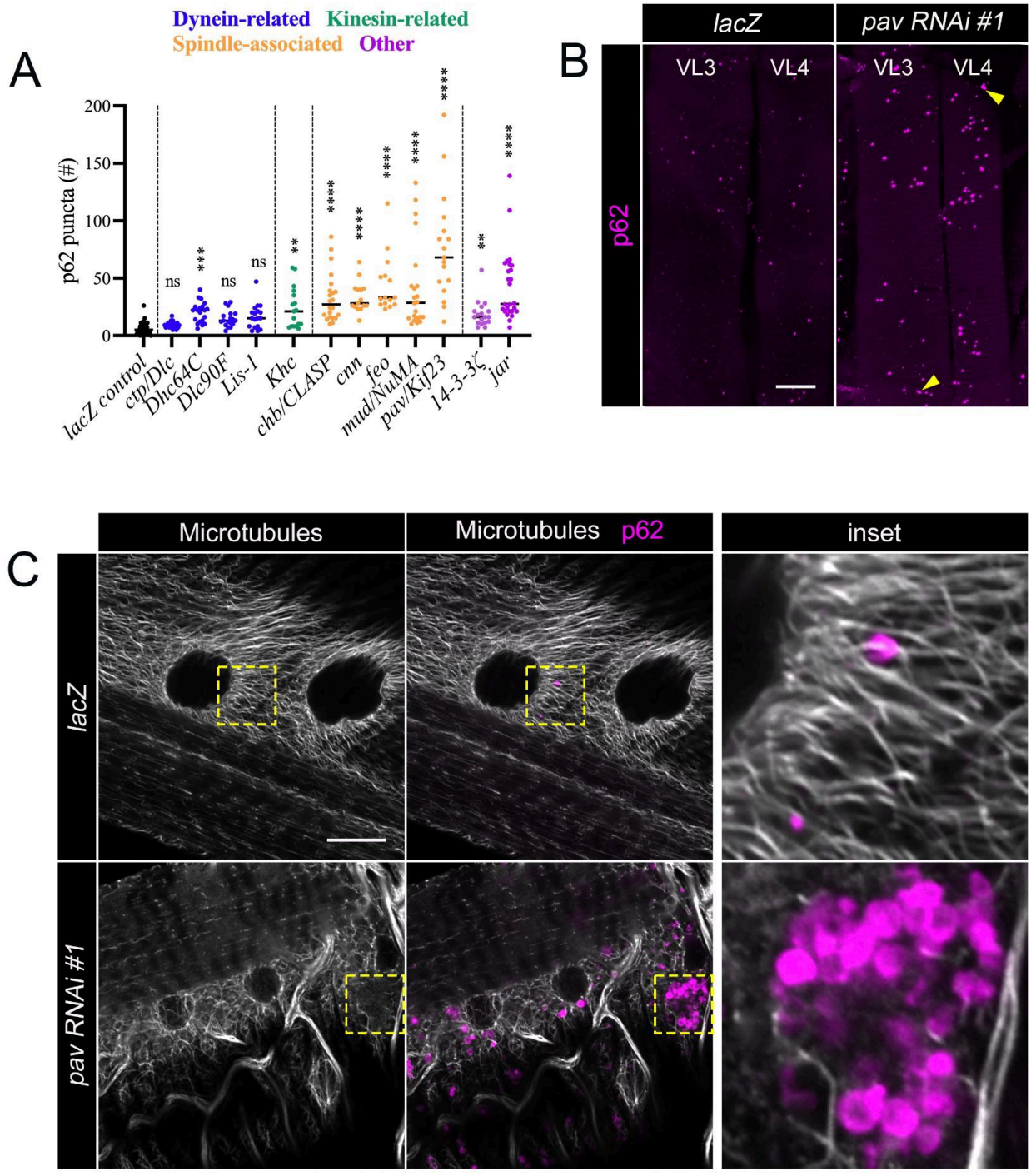


Figure 5.1. Genetic screen reveals Pav as new regulator of autophagic activity.

(A) Scatter bar plot shows the quantification of p62 puncta for *Mef2*-Gal4 driven expression of UAS-*lacZ* control or UAS-*candidate RNAi* lines. Each data point represents the total number of p62 puncta in VL3 or VL4 muscles of L3 larvae. N ≥ 15. (B) Maximum intensity projections of VL3 and VL4 muscles immunostained for p62 in *lacZ* control or *pav RNAi #1* muscles from L3 larvae reveal an increase in the number of p62 puncta (magenta). p62 clusters are indicated by the yellow triangle. (C) High magnification single plane images of control or *pav RNAi #1* VL3 muscles co-immunostained with anti-p62 (magenta) and anti-α-tubulin (gray). Inset depicts the area of the yellow dashed box. P values: ns, not significant; **, p<0.01; ***, p<0.01; ****, p<0.0001. Error bars indicate standard error of the mean (SEM). Statistics: Kruskal-Wallis test. Scale bars, 40 μm (panel B), 15 μm (panel C).

and *lacZ* muscles (**Figure 5.1C and Figure D5.1C**), indicating that a reduction in Pav function does not grossly alter MT organization. From high magnification images where the MTs and p62 were co-stained, we observed p62(+) puncta associated with microtubules in *lacZ* muscles (**Figure 5.1C**). However, in *pav RNAi* muscles, the MT staining was fainter and appeared to be excluded from the aggregated p62 structures. We analyzed a second, independent *pav RNAi* line and indeed, the number of p62(+) puncta in VL3/VL4 muscles was increased ~2 fold compared to *lacZ* controls and contained p62 clusters (**Figure D5.1A**, yellow triangles **and Figure D5.1B**).

Autophagosomes accumulate in *pav RNAi* and *tum RNAi* muscles.

D. melanogaster Tum is a binding partner of Pav during cytokinesis and NEB [13, 19], but Pav and Tum also have independent roles in embryo wound repair and oogenesis [20]. Therefore, we tested whether Tum is required to prevent the aggregation of p62(+) structures. p62 immunostaining of VL3/VL4 muscles in two different *tum RNAi* lines replicated both p62 phenotypes seen in *pav RNAi* muscles (**Figure D5.1A and D5.1B**). The total number of p62(+) puncta was increased ~2.6-fold in *tum RNAi #1* and ~4.6-fold for *tum RNAi#2* compared to *lacZ* control muscles. We also observed p62 clusters in *tum RNAi* muscles (**Figure D5.1A**, yellow triangle). Verification of RNAi knockdown in our original *pav* and *tum RNAi* lines was performed

using qPCR. Indeed, *pav mRNA* levels were reduced ~70% in the *pav RNAi* line compared to the control (**Figure D5.1D**) and *tum* transcripts were reduced ~60% in the *tum RNAi* line (**Figure D5.1E**). This data confirm the functionality of the *pav* and *tum RNAi* lines and demonstrate that both components of the centralspindlin complex have similar roles in preventing the formation of p62 clusters.

Ubiquitin (Ubi) chains appended to proteins and/or organelles confer a degradation signal directed to the proteasome (typically K48-linked chains) or the lysosome (typically K63-linked chains) [21]. In the latter case, the Ubi receptor p62 recognizes K63-linked Ubi chains and directly recruits Autophagy-related protein 8 (Atg8a)/Microtubule-associated protein 1A/1B-light chain 3 (LC3) to form the autophagosome [22]. If p62 is indicative of the autophagosome, then we would expect colocalization of p62 with both Ubi and Atg8a immunostaining in VL3/VL4 larval muscles. As expected since p62 binds to Ubi, the number of structures that showed positive staining for both p62 and Ubi was increased in *pav* and *tum RNAi* muscles compared with controls (**Figure 5.2A**). The total number of puncta marked by p62 and Ubi was increased ~4-fold in *pav RNAi* muscles and ~2.8-fold in *tum RNAi* muscles over that of *lacZ* (**Figure 5.2C**). These data are consistent with the fold increases seen in p62 immunostaining alone (**Figure D5.1B**). High magnification images in *lacZ* muscles showed a near perfect overlap of Ubi and p62 (**Figure 5.2E**). However, in muscles with *pav* or *tum* knockdown, there were clusters where Ubi staining was present, but the p62 signal was absent (**Figure 5.2E**, yellow triangles). These data highlight the dynamic process of p62 recognition of Ubi chains. Regions with Ubi signal that lack p62 likely represent Ubi-tagged proteins and/or organelles that have not yet recruited p62. Note areas lacking p62 are found on the outside or edges of Ubi clusters, suggesting that p62 may be key for initiating or promoting aggregation.

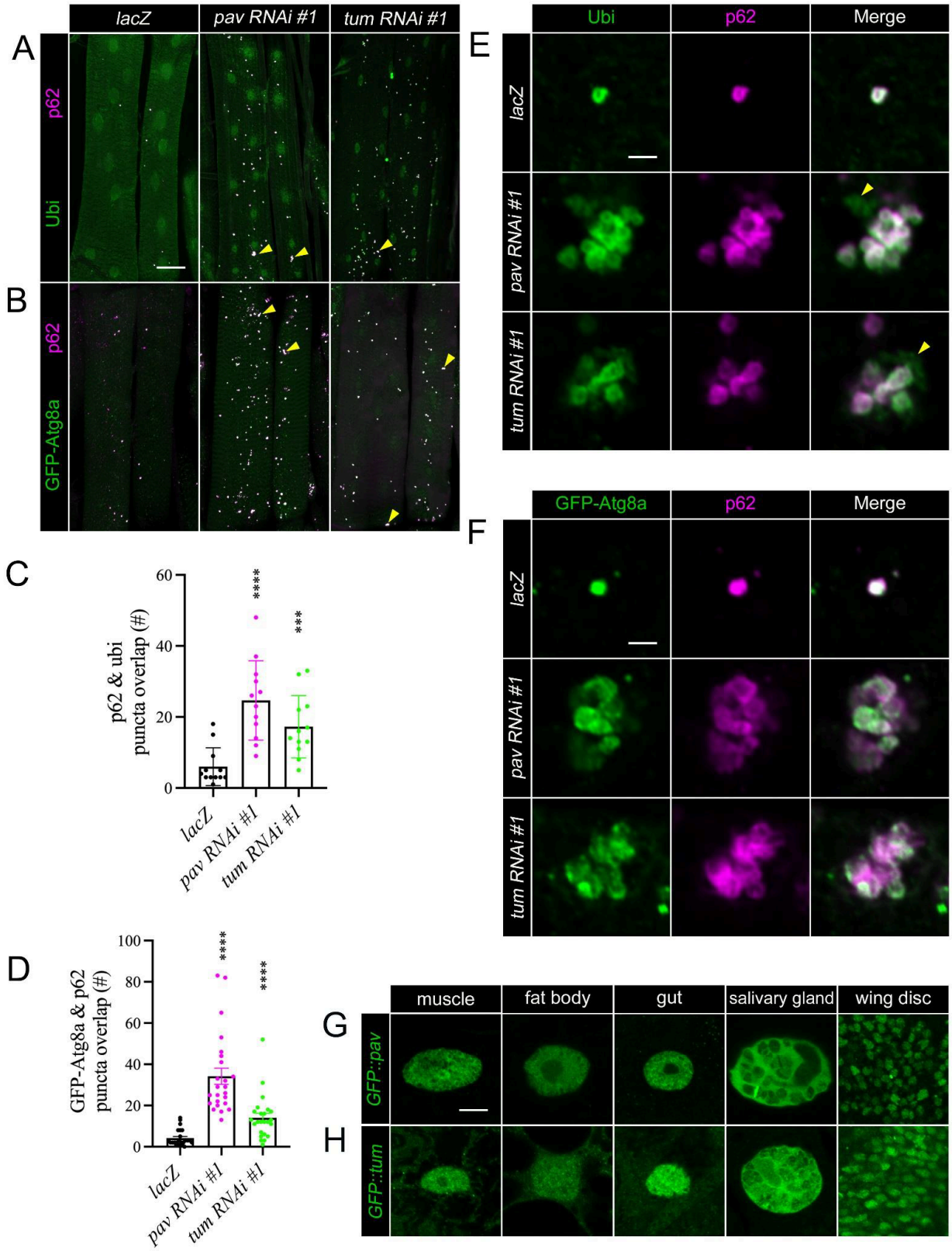

A
lacZ
pav RNAi #1
tum RNAi #1
p62
Ubi
B
p62
GFP-Atg8a
C
p62 & ubi puncta overlap (#)
60
40
20
0
****
***
lacZ
pav RNAi #1
tum RNAi #1
D
GFP-Atg8a & p62 puncta overlap (#)
100
80
60
40
20
0
****
****
lacZ
pav RNAi #1
tum RNAi #1
E
Ubi
p62
Merge
lacZ
pav RNAi #1
tum RNAi #1
F
GFP-Atg8a
p62
Merge
lacZ
pav RNAi #1
tum RNAi #1
G
H
muscle
fat body
gut
salivary gland
wing disc
GFP::pav
GFP::tum

Figure 5.2. p62-Ubi and p62-Atg8a complexes accumulate in pav and tum RNAi muscles.

(A and B) Maximum intensity projections of VL3 and VL4 muscles in *lacZ* control, *pav RNAi*, or *tum RNAi* muscles driven by *Mef2*-Gal4. (A) Following Pav or Tum knockdown, there is an appreciable increase in Ubi (green) and p62 (magenta). p62(+) and Ubi(+) clusters are present in *pav* and *tum RNAi* muscles (yellow triangles). (B) Muscles expressing GFP-Atg8a (green) and labeled with anti-p62 (magenta) have elevated numbers in *pav RNAi* or *tum RNAi* muscles compared to *lacZ* controls. Clusters marked by p62 and GFP-Atg8a are denoted by yellow triangles. (C and D) Scatter bar graphs reveal an increase in the number of puncta in VL3 and VL4 muscles that show overlap between p62 and Ubi (C) or p62 and GFP-Atg8a (D) in *pav* or *tum RNAi* muscles compared with controls. N =12 for C and N=24 for D. (E) Single plane, high magnification images of individual p62-Ubi puncta in *lacZ* muscles or p62-Ubi clusters in *pav* and *tum RNAi* muscles. The yellow triangle shows regions where Ubi (green) is not recognized by p62 (magenta). (F) High magnification, single plane confocal micrographs of L3 larvae muscles stained with antibodies against p62 and GFP. In *lacZ* muscles, p62 staining overlaps with GFP-Atg8a signal in a single mitochondria, whereas the overlap appears as clusters in *pav* and *tum RNAi* muscles. (G and H) Endogenous expression of GFP-tagged Pav (G) or Tum (H). show an enrichment inside the nuclei of the muscle, fat body, gut, salivary gland, and wing disc tissues. P values: ***, $p<0.01$; ****, $p<0.0001$. Error bars indicate standard error of the mean (SEM). Statistics: Student's t-test. Scale bars, 40 μm (panel A), 2 μm (panels E and F), 4 μm (panel G).

To verify whether the Ubi-p62 complexes recruit Atg8a, we next assessed p62 and Atg8a colocalization in *pav* and *tum RNAi* muscles. We were unable to perform double labeling using anti-p62 and anti-Atg8a because both antibodies were generated in the same species. Therefore, we took advantage of a GFP-tagged Atg8a fusion protein (GFP-Atg8a) and used an anti-GFP antibody to enhance Atg8a signal. Autophagosomes marked by Atg8a were indeed positive for p62 signal. Moreover, the total number of autophagosomes was increased in *pav RNAi* or *tum RNAi* muscles compared with control muscles (**Figure 5.2B and 5.2F**). The average number of autophagosomes in each *lacZ* set of VL3/VL4 muscles was ~4, but increased ~8-fold or ~4-fold in *pav RNAi* or *tum RNAi* muscles, respectively (**Figure 5.2D**). Additional analysis showed consistent overlap of p62 and GFP-Atg8a in clusters upon knockdown of Pav or Tum (**Figure 5.2B**; yellow triangle and **Figure 5.2F**). Here we conclude that the Ubi-p62 clustered aggregates correspond to autophagosomes.

To investigate if altered autophagosome and/or lysosome biogenesis explains the increase in autophagosome numbers, we examined the transcript levels of key genes required for the production of these organelles in control (*y,w* and *mCherry RNAi*) or *pav RNAi* larvae. The mammalian transcription factor EB (TFEB), or melanocyte-inducing transcription factor (Mitf) in *D. melanogaster*, is a master gene for autophagosoml and lysosomal biogenesis. The *Mitf mRNA*, as well as its transcriptional targets *Autophagy-related1 (Atg1)*, *Autophagy-related 18 (Atg18a)*, and *Cysteine proteinase-1 (Cp1)*, were not significantly changed in *pav RNAi* muscles (**Figure D5.2A**). There was also no increase in *p62* transcript levels compared to controls. This data together show that knockdown Pav does not enhance autophagosome (Atg1, Atg18) or lysosomal biogenesis (Cp1) via a transcriptional mechanism.

Pav and Tum function in the nucleus

Autophagosomes clearly accumulate in the myoplasm of *pav* or *tum*-deficient muscles. Thus, we were curious if the subcellular distribution of Pav and Tum are associated with these p62-Ubi autophagosomes. Despite trying different immunostaining methods, we failed to detect signal in muscle tissue using available anti-Pav and anti-Tum antibodies [13]. Therefore, we took advantage of GFP-tagged fusion proteins for Pav (Ubi-GFP-Pav) or Tum (sqh-Tum-GFP) and enhanced the signal using an anti-GFP antibody. While no signal was observed in the myoplasm, strong signal for GFP-Pav (**Figure 5.2G and Figure S5.2B**) and GFP-Tum (**Figure 5.2H and Figure D5.2B**) were observed in the nuclei of numerous larval tissues, including muscle, fat body, gut, salivary gland, and the wing disc. Our finding was consistent with previous reports in other tissues, such as *Drosophila* embryonic epidermis and ovary [23, 24]. This subcellular localization of Pav and Tum point towards a role for the centralspindlin complex in the nucleus.

A recent study described new functions for Pav and Tum in the formation of NE buds [13]. To visualize these structures in larval muscle nuclei, we immunostained using the only two markers available - the C-terminal fragment of the *Drosophila* Wingless receptor dFz2 (dFz2C) and Lamins [11-13, 25, 26]. Thus, colocalization with both anti-dFz2C and anti-Lamin B were used as criteria for counting the number of NE foci/nucleus (**Figure 5.3A**, yellow triangle). We identified 30 NE buds distributed among 102 nuclei (0.29 foci/nucleus) in w^{1118} muscles and 11 NE buds present in 105 nuclei (0.10 foci/nucleus) in *lacZ* muscles (**Figure 5.3B**). In contrast, only1-2 instances of NE bud visualization was observed in muscle nuclei after RNAi knockdown for Pav (0.01 foci/nucleus), Tum (0.01 foci/nucleus), and Wash (0.01 foci/nucleus) (**Figure 5.3A**). The persistence of NE buds is likely attributed to incomplete knockdown using the RNAi approach as we know there is remaining *pav* and *tum* transcripts via RT-PCR (**Figure D5.1D and Figure D5.1E**).

Nuclear roles for Pav and Tum influence mitochondrial and autophagosome clustering

Autophagosomes can engulf various intracellular items, including pathogens, impaired proteins, and organelles, before being conveyed to lysosomes for degradation [1, 7]. To determine the type of cargo inside the autophagosome clusters in *pav* and *tum RNAi* muscles, we performed colabeling experiments for p62 and candidate protein targets using available antibodies in our laboratory. Eventually we found that anti-p62 staining overlapped with weak anti-ATP5α signal (**Figure 5.3C**). The mitochondrial marker ATP-Synthetase α (ATP5α) is a biomarker used to measure mitochondrial content in humans [27]. This is consistent with the statement that faint staining of ATP5α indicates a reduction in mitochondrial activity [13] and supports using anti-ATP5α to monitor a sign of damaged mitochondria.

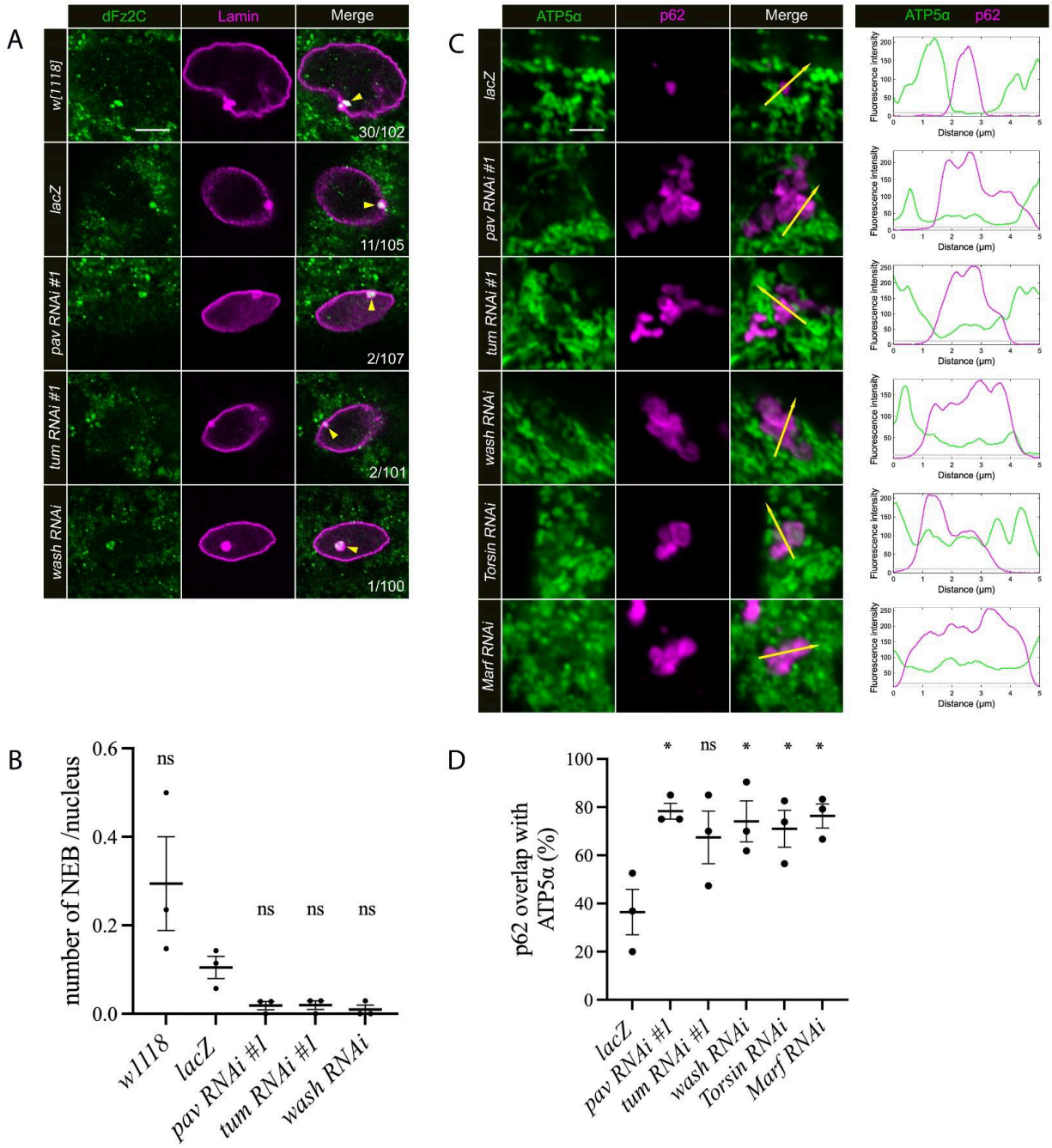


Figure 5.3. Knockdown of Pav or Tum decreases the formation of NE buds resulting in p62 clusters that overlap with faint ATP5α signal.

(A) The progeny from *Mef2-Gal4* flies mated with UAS-*lacZ*, UAS-*pav RNAi #1*, UAS-*tum RNAi #1*, or UAS-*wash RNAi* are analyzed here. *W[1118]* are used as a control. Representative nuclei from VL3 or VL4 muscles of the specified genotypes were stained with anti-Lamin and anti-dFz2C antibodies. NE buds correspond to foci that stain positive for both Lamin (magenta) and dFz2C

(green) and are indicated by the yellow triangles. The number of buds that stain positive for Lamin/dFz2C out of the total number of nuclei counted are shown in each panel. (B) Scatter plot quantifying the number of NE buds per nucleus. Each dot represents one group, and each group contains nuclei ≥33. (C) Confocal projections of muscles co-stained with anti-p62 (magenta) and anti-ATP5α (green) of the indicated genotypes. The corresponding fluorescence plots were produced using the ImageJ Plot Profile function which quantifies the fluorescence intensity across the trajectory of the yellow arrow. (D) Scatter plot quantifying the percentage of p62(+) puncta that overlaps with faint anti-ATP5α staining in the indicated genotypes. Every dot corresponds to a single group, and each group consists of p62 puncta ≥19. P values: ns, not significant; *, $p<0.05$. Error bars indicate the standard error of the means (SEM). Statistics: One-Way ANOVA (panels B and D). Scale bars, 6 μm (panel A), 3 μm (panel C).

Since the aggregated mitochondria stain weaker than the surrounding organelles, we used ImageJ to quantitate the intensity of green fluorescence (anti-ATP5α) and magenta fluorescence (anti-p62) as a measure of overlap (yellow arrow in the merged images in **Figure 5.3C**) in multiple RNAi genotypes that block the formation of NE buds. The anti-p62 staining did not overlap with the anti-ATP5α staining in *lacZ* muscles, but provided intensity levels for background (~5, dotted gray line) or maximal fluorescence (~200). Using this method, we confirmed that faint anti-ATP5α staining overlapped with p62 clusters in *pav RNAi, tum RNAi* and *wash RNAi* muscles (fluorescent intensity ~50). Only ~36% anti-p62 staining overlapped with faint anti-ATP5α staining in *lacZ* muscles, and this value was increased to ~78% in *pav RNAi* muscle, ~67% in *tum RNAi* muscles, and ~74% in *wash RNAi* muscles (**Figure 5.3D**). Previous research has shown that TorsinA is involved in the formation of NE buds in mouse neuronal nuclei [28]. Since *Drosophila* Torsin also mediates the transport of megaRNPs via NE budding [25], we also examined the consequences of *Torsin RNAi* in larval muscles. Similar to the RNAi phenotypes in Pav, Tum, or Wash muscles, we found that p62 overlapped with ~71% of faint anti-ATP5α staining upon the induction of *Torsin RNAi* (**Figure 5.3C,D**).

In all NE budding genotypes that exhibited p62 overlap with faint, clustered mitochondria, the majority of surrounding mitochondria retained ATP5α staining (**Figure D5.3A**). To confirm

that mitochondria with weak anti-ATP5α staining have reduced activity, we treated *lacZ* control and *pav RNAi* muscles with tetramethylrhodamine methyl ester (TMRM) and MitoTracker as an internal control (**Figure D5.3B**). The accumulation of TMRM in mitochondria with intact membrane potentials yields strong fluorescence. When mitochondrial membrane potential drops, TMRM signal declines or disappears. In randomly selected regions of muscles, we used ImageJ to measure the fluorescence intensities of MitoTracker and TMRM signal to calculate an intensity ratio. There was no overall difference in the TMRM/MitoTracker ratio between *pav RNAi* or *lacZ* muscles (**Figure D5.3C**), suggesting that the overall mitochondrial activity was unaffected in *pav RNAi* muscles. However, the TMRM signal was absent in areas where the MitoTracker staining was weak or faint in *pav RNAi* muscles (**Figure D5.3B**). This faint MitoTracker staining further validates the use of ATP5α as a marker for damaged, aggregated mitochondria.

Thus far our data provide strong evidence that blocking NE bud formation causes clustered autophagosomes (marked by p62) that overlap with mitochondria (denoted by weak ATP5α signal). Next, we wanted to ascertain why restricting NE bud development might result in this particular autophagosome phenotype. The mitochondrial morphology in the weakly staining ATP5α clusters resembles the smaller, spherical mitochondria upon RNAi knockdown of *Drosophila* Marf in either larval or adult indirect flight muscles [29, 30]. Therefore, we performed anti-p62 and anti-ATP5α colabeling in *Marf RNAi* muscles and indeed observed the same unique clustered autophagosome phenotype present in *pav*, *tum*, *wash*, or *Torsin RNAi* muscles (**Figure 5.3C**). The ratio of p62 signal that overlapped with faint anti-ATP5α staining was also elevated in *Marf RNAi* muscles, consistent with other genotypes (**Figure 5.3D**).

Marf mRNA is a known cargo of NE buds [12]. Since suppression of NE buds in *pav* or *tum* RNAi shows a mitochondrial clustering phenotype consistent with the knockdown of *Marf*

expression, we postulated that the export of *Marf* transcript from the nucleus to the myoplasm may be compromised upon a reduction in Pav function. Therefore, we conducted fluorescence in situ hybridization (FISH) to validate our hypothesis. FISH employs fluorescent probes to precisely determine the intracellular location of labeled nucleic acids within a cell. We generated an anti-sense probe to detect *Marf mRNA* and a sense probe to serve as a non-specific control. As expected, we detected *Marf* transcript in NE buds. In *lacZ* muscles treated with the anti-sense probe, *Marf mRNA* (magenta) co-localized with NE buds marked by Lamin (**Figure 5.4A**, yellow triangle). In contrast, there was low signal and no detected overlap between the sense *Marf* probe and NE buds in *lacZ* muscles. These data demonstrate the specificity of the anti-sense *Marf* probe.

We next quantitated foci corresponding to *Marf* probe in the myoplasm of control or *pav RNAi* muscles and observed a ~30% reduction in anti-sense *Marf mRNA* in comparison to *lacZ* muscles (**Figure 5.4B** and **Figure S5.3D**). Very little probe signal was seen in *lacZ* muscles treated with the sense probe (**Figure 5.4B** and **Figure D5.3D**), further confirming the probe's specificity. qPCR was also used to determine *Marf* transcript levels in *pav RNAi* muscles. Consistent with a decrease in *Marf mRNA* foci, there was ~40% decrease in *Marf mRNA* levels upon induction of *pav RNAi* compared to controls (**Figure 5.4C**). Note that knockdown of *Marf* transcript using this same method was stronger in *Marf RNAi* compared to *pav RNAi* (**Figure D5.3E**). Maybe the presence of an occasional NE budding event in *pav RNAi* muscles allows for the detection of *Marf mRNA* or maybe the cell has an additional and/or alternate route for the nuclear export of *Marf*. However, overall our data argue that loss of Pav reduces the presence of *Marf* transcript in muscles, resulting in mitochondrial abnormalities.

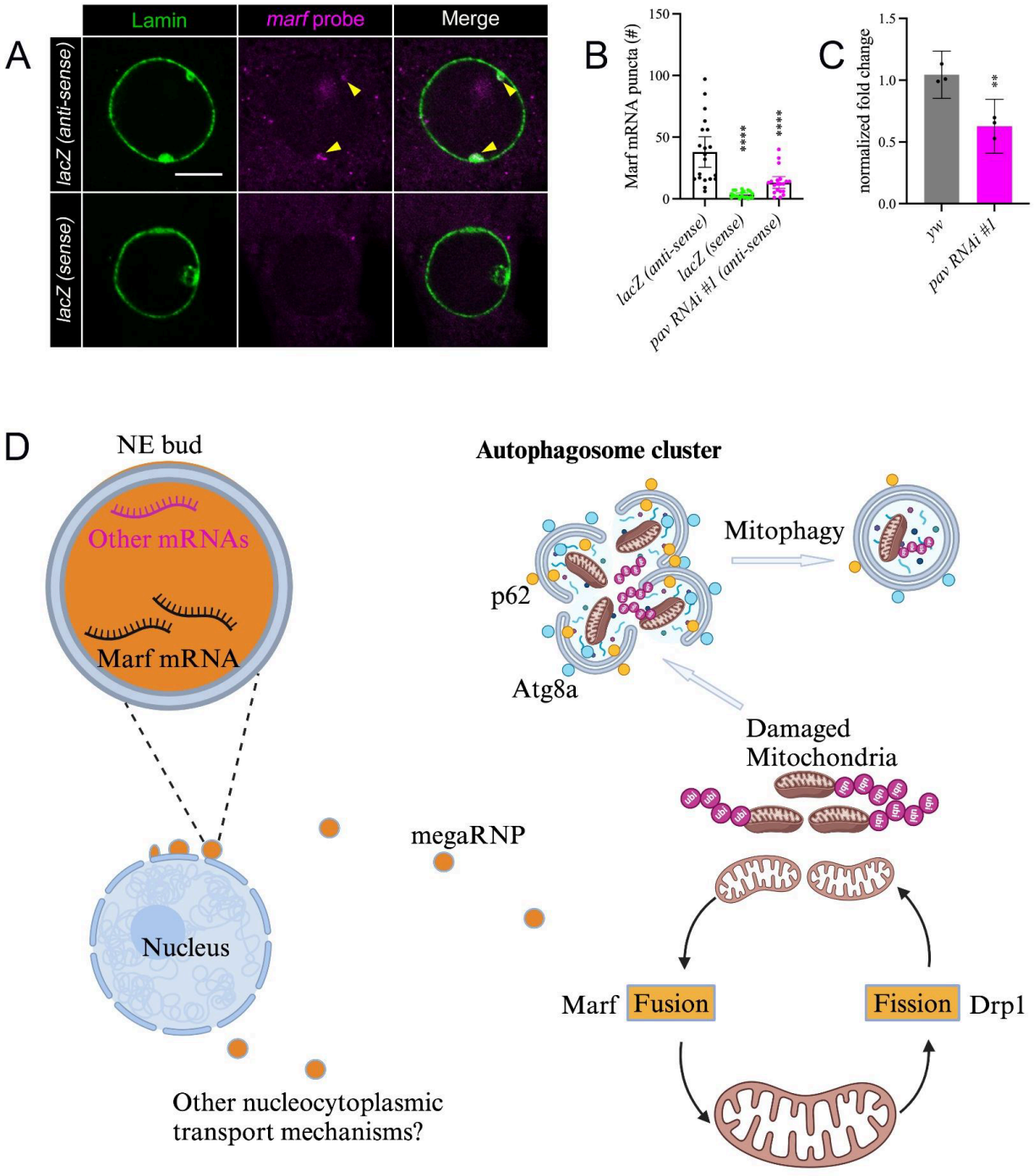


Figure 5.4. FISH and qPCR experiments demonstrate a reduction in Marf mRNA export and transcript levels in pav RNAi muscles.

(A) Confocal images of *lacZ* muscles incubated with the *Marf* anti-sense probe and stained with Lamin shows colocalization of *Marf mRNA* (magenta) with budding foci at the NE (green) as indicated by the yellow triangle. (B) Scatter bar graph shows that the number of foci corresponding to *Marf mRNA* in *lacZ* control muscles is greater than in *pav RNAi* muscles. N=20. (C) qPCR

shows that *Marf* transcript levels are significantly reduced in *pav RNAi* compared with controls. N= 3 biological replicates. (D) A proposed model for *Marf mRNA* export from NE buds to regulate mitochondrial morphology and health. P values: **, p<0.01; ****, p<0.0001. Error bars indicate standard error of the mean (SEM). Statistics: Student's t-test. Scale bars, 6μm.

Discussion

Using a screening approach to identify genes that influence the abundance of p62-linked cargo, we uncovered the spindle-associated protein Pav. Pav and Tum together comprise the centralspindlin protein complex with well-established roles in spindle formation via MT bundling during cytokinesis [19]. Autophagosomes marked by p62 and Atg8a were increased in number upon knockdown of Pav or Tum in larval muscles using RNAi approaches. Further characterization revealed three unexpected results. First, a portion of the increased autophagosome population formed clusters throughout the myoplasm. This clustering phenotype is not observed in other muscle mutants that also have elevated numbers of autophagosomes [16, 17]. Second, we were not able to visualize Pav or Tum protein in or near the aggregated autophagosomes using available antibodies or GFP-tagged versions of Pav or Tum. Instead, we observed an enrichment of Pav or Tum protein in the nucleus, seemingly inconsistent with a role for these proteins in the myoplasm. Third, the autophagosomes colabeled with weakly stained mitochondria, suggesting that a loss of mitochondrial content and/or activity, is sufficient to recruit autophagosomal machinery (Ubi, p62, and Atg8a) for eventual lysosomal turnover.

Our compiled data now integrates these initial findings and together provides a functional model explaining how the knockdown of Pav results in the formation of autophagosome clusters (**Figure 5.4D**). Pav participates in the formation of NE buds and *Marf mRNA* is one such cargo that is present at budding foci being exported from muscle nuclei [12, 13]. Insufficient transport

of *Marf mRNA* to the site of Marf protein synthesis decreases the ability of mitochondria to undergo fusion. Likewise, ablation of *Mitofusin 2*, the human homolog of *Drosophila* Marf, in mammalian hearts causes insufficient mitophagy, resulting in the buildup of defective mitochondria [31]. Although the trigger for the addition of Ubi to mitochondria is not yet clear, polyUbi recruits p62 and Atg8a to form autophagosomes. p62 has been shown to mediate the clustering of dysfunctional mitochondria in HeLa cells via its PB1 domain [32]. A similar mechanism may be functioning in muscle to polymerize defective mitochondria into dense clusters as a protective mechanism or because the aggregates are too large for lysosomal transfer and/or degradation.

Pav participates in the formation of NE buds in at least two larval tissues - salivary glands and bodywall muscle - to export megaRNPs from nuclei [11-13, 25]. Established cargo of these RNPs in larval muscles includes *par6* and *magi*, which encode for scaffolding proteins required at the postsynaptic NMJ [11]. It is hypothesized that specific transcripts are transported to and locally translated at the NMJ during expansion of these structures in larval development. Since mitochondria have a broader distribution throughout muscle cells [29], the final destination of *Marf* transcripts developing at foci corresponding to NE buds is not clear. FISH analysis of mRNAs present in megaRNPs reveal that a subset of NMJ-associated or mitochondrial-associated transcripts can be detected. Are select transcripts exported in different populations of megaRNPs that have different cellular targets? In the case of mitochondrial-associated mRNAs (such as *Marf*), is the final destination for each megaRNP random or are they targeted to mitochondria in regions of the cell that require more ATP or increased mitochondrial dynamics?

In addition to the weakly stained mitochondria that were marked with p62, we also observed ring-shaped mitochondria in *pav*, *tum*, *wash*, and *Torsin RNAi*, but not *lacZ* muscles (**Figure D5.3A**). However, these hollow, circular mitochondria did not overlap with anti-p62.

Ring-shaped mitochondria are also observed in mouse embryonic fibroblasts (MEFs) and HeLa cells after exposure to the protonophore carbonyl cyanide m-chlorophenyl hydrazine (CCCP) for 10 min [33]. This transition from a tubular to globular shape is independent of fission or fusion and may be an intermediate morphology before mitochondrial collapse. Alternatively, additional transcripts that mediate mitochondrial dynamics may also be transported by mega RNPs. Indeed, FISH analysis reveal low levels of *Drp1 mRNA* at NE foci [12].

We are the first to study how blocking NE budding causes mitochondrial dysfunction and recruitment of the autophagosome machinery in larval muscles as prior studies focused on the consequences of age-dependent mitochondrial defects in the *Drosophila* indirect flight muscles (IFMs) [12, 13]. The observation that four proteins required for NE bud formation (Pav, Tum, Wash, Torsin) all result in similar mitochondrial morphology defects strongly argues that the transport of mitochondrial-associated mRNAs is crucial for continued mitochondrial health. Moreover, the autophagosome clusters are a unique phenotype and is easily examined through immunostaining and microscopy. We believe that our results may provide a simple and rapid method for identifying new proteins that contribute to defects in NE bud development and/or transport in larval muscles.

Materials and Methods

Drosophila genetics and strains

All stocks were maintained on standard Bloomington *Drosophila* Stock Center (BDSC) cornmeal media at 25°C. Gal4/UAS crosses were set up at 25°C and embryos were collected for 6 hr periods before shifting to 31°C for maximal Gal4/UAS expression. UAS-RNAi lines were obtained from either the BDSC (Bloomington, IN) or the Vienna *Drosophila* Resource Center (VDRC, Vienna,

Austria) as indicated: UAS-*mCherry RNAi* (BL35785); UAS-*pav RNAi #1* (v46137); UAS-*pav RNAi #2* (v110330); UAS-*tum RNAi* (BL6439); UAS-*tum RNAi #2* (BL67923); UAS-*wash RNAi* (BL62866); UAS-*Torsin RNAi* (BL50620); UAS-*Marf RNAi* (v-40478); UAS-*ctp RNAi* (BL44044); UAS-*Dhc64C RNAi* (BL36698); UAS-*Dlc90F RNAi* (BL65189); UAS-*Lis1 RNAi* (BL35043); UAS-*Khc RNAi* (v44338); UAS-*chb RNAi* (BL34669); UAS-*cnn RNAi* (BL35761); UAS-*feo RNAi* (BL28926); UAS-*mud RNAi* (BL35044); UAS-*14-3-3ζ RNAi* (v48724); UAS-*jar RNAi* (BL28064). Additional fly stocks obtained from the BDSC include *Mef2-Gal4* (BL27390), *da-Gal4* (BL37291), UAS-*lacZ* (BL3956), *Ubi-p63E-GFP-pav* (BL81651), *sqh-sfGFP-tum* (BL76264). The *y,w* control is maintained in our lab.

Muscle fillets and immunostaining

Muscle carcass dissections were performed as described previously ([17]). Tissues were stained with the following primary antibodies: rabbit anti-p62/ref(2)p (1:200, ab178440, Abcam, Cambridge, MA), mouse anti-mono- and polyubiquitinylated conjugates recombinant monoclonal antibody UBCJ2 (1:1000, ENZ-ABS840, Enzo Life Sciences, Farmingdale, NY), mouse anti-GFP (1:25, 12E6, Developmental Studies Hybridoma Bank, Iowa City, IA), mouse anti-Lamin B (1:200, ADL67.10, Developmental Studies Hybridoma Bank, Iowa City, IA), mouse anti-ATP5α/blw (1:200, ab14748, Abcam, Cambridge, MA), mouse anti-α-Tubulin (1:1000, T5168, Sigma-Aldrich, St. Louis, MO), and guinea pig anti-dFz2C (1:2500) [26]. Fluorescence was detected using the following secondary antibodies: Alexa Fluor anti-rabbit, anti-mouse or anti-guinea pig 488 or 594 (1:400, Invitrogen, Waltham, MA). Images were captured using a Zeiss 700 confocal microscope. Image processing and analysis were performed using a combination of Zen Black (Zeiss), ImageJ (NIH), and Adobe Photoshop.

TMRM and MitoTracker

Wandering L3 larvae were dissected live in Ca^{2+}-free HL3.1 buffer. The muscle carcasses were incubated in 100-nM Tetramethylrhodamine ethyl ester perchlorate (TMRM) (HY-D0985A, MCE, Monmouth Junction, NJ) and 1-µM MitoTracker Green FM (M7514, Invitrogen) diluted in HL3.1 for 5 min at room temperature (kept inside a drawer to avoid light) and imaged immediately. Confocal microscopy parameters were kept the same while images were acquired for different samples.

Fluorescence In Situ Hybridization (FISH) probe synthesis

Digoxigenin (DIG) labeling sense and anti-sense RNA probes was an adaptation from Wilk et al, 2010 [34]. Briefly, 5 µg Marf plasmid (RE04414, Stock 9809, *Drosophila* Genomics Resource Center, Bloomington, IN) was linearized by treating with KasI restriction enzyme (R0544S, NEB, Ipswich, MA) in a 37˚C water bath for 1 hr. A 1% DNA agarose gel was used to check the digestion quality. The linearized DNA was recovered using the QIAprep Spin Miniprep Kit (#27106, QIAGEN, Hilden, Germany). After DNA recovery, the DNA concentration was measured using a NanoDrop Microvolume Spectrophotometer (Thermo Fisher Scientific, Waltham, MA). For DIG Labeling of the RNA probe, the following were added to an RNase-free 1.5 mL microcentrifuge tube on ice: 1µg linearized DNA with 2 µl 10x DIG-RNA-Labeling-Mix (11277073910, MilliporeSigma, Burlington, MA), 2 µl 10x RNAPol Reaction Buffer (B9012, NEB, Ipswich, MA), 1 µl SUPERase·In™ RNase Inhibitor (AM2694, Invitrogen, Waltham, MA), 2 µl T7 RNA Polymerase (for sense RNA probe synthesis) (M0251S, NEB, Ipswich, MA) or 2 µl T3 RNA Polymerase (for anti-sense RNA probe synthesis) (M0378S, NEB, Ipswich, MA), and RNase-free

water to a final volume of 20 µl. The contents were vortexed, spun briefly, and incubated at 37˚C for 3 hrs. The volume was then brought to 50 µl using RNase-free water and precipitated by adding 1 µg RNase-free glycogen (R0551, Invitrogen, Waltham, MA), 0.1 vol of 3 M sodium acetate, pH 5.2, and 2.5 vol of cold 100% ethanol. Each sample was vortexed and kept at -80˚C overnight. The following day the microcentrifuge tube was spun for 20 min at 4˚C at 12,000 x g and the supernatant was discarded. The pellet was washed with 500 µl cold 70% ethanol and microcentrifuged for 10 minutes at 4˚C at 12,000 x g. The pellet was allowed to air dry and resuspended in 50 µl RNase-free water. The samples were run on a 1% agarose gel to verify integrity. The probes were stored at -80˚C until needed.

Drosophila larvae muscle *Marf mRNA* detection

We used an established protocol for FISH with minor adaptations [34]. Wandering L3 larvae were live dissected in HL3.1 buffer and fixed in 1x phosphate-buffered saline + 0.1% Tween-20 plus 4% formaldehyde for 20 min. We used Fast Red TR/Naphthol AS-MX(F4648, MilliporeSigma) for the detection of hybridization signals. To do so, we dissolved the Trizma® tablet in 1 mL of distilled water, then added the Fast Red TR/Naphthol AS-MX tablet Vortex until dissolved. The solution was added to the sample at room temperature for 30 min and kept on the dark to develop the fluorescent signal.

Quantitative RT-PCR

qPCR samples were prepared as follows. The ubiquitous *da-Gal4* driver was used to knockdown gene expression in all tissues. *yw* was the control. Total RNA was harvested from three whole wondering L3 larvae which were raised at 31°C. RNA was purified using QuantaBio Extracta Plus

RNA kit (Quanta Biosciences, Beverly, MA). Three RNA samples for each genotype were prepared. cDNA was synthesized from 600ng or 1000ng of RNA using the qScript XLT cDNA SuperMix kit (Quanta Biosciences, Beverly, MA). For the qPCR reactions, 1:10 or 1:15 dilutions of the cDNA were combined with PowerUp SYBR Green Master Mix (ThermoFisher, Waltham, MA) and the appropriate primers. qPCR was performed with a QuantStudio 3 instrument and related software (ThermoFisher, Waltham, MA). All primers were used at a final concentration of 1 μM. Primers used to assess autophagosomes and lysosome biogenesis (**Figure D5.2A**): *Atg1* forward 5′-GTCGGGGAATATGAATACAGCTC, *Atg1* reverse 5′-GCATGTGTTTCTTGCGATGAC; *Atg18a* forward 5′-GTGTTCGTCAACTTCAACCAGA, *Atg18a* reverse 5'-TGTCCAGGGTCGAGTCCAC; *Cp1* forward 5′-TCAACTACACTCTGCACAAGC, *Cp1*reverse 5′-GCCAGTCCACAGATTTGGG; *Mitf* forward 5′-AGTATCGGAGTAGATGTGCC AC, *Mitf* reverse 5′-CGCTGAGATATTGCCTCACTTG; *p62* forward 5′-GCCCTCCCAGA ATTACACCA, *p62* reverse 5′-GTTGGCCGAAGAACCCTCT; and *rp49* forward 5′-GCCCAAGG GTATCGACAACA, *rp49* reverse 5′-GCGCTTGTTCGATCCGTAAC. Primers used to validate RNAi knockdowns (**Figure D5.1D and D5.1E**): *pav* forward 5'-ATGAAGGCAGTACCCAGGAC; *pav* reverse 5'-CGACA GAACACATTCACTGGA; *tum* forward 5'-TCGATGATCTGCGACGCT; *tum* reverse 5'-CTCGTTTTGTATCCTGGCCG. To determine *Marf mRNA* levels in *pav RNAi* muscles or *Marf RNAi* muscles, the following primers were used: *Marf* forward 5′-AGCCGAACATCT TCATCCTGA; *Marf* reverse 5′-TCCTTCTCGTTGCTCACCTT. Larvae were raised at 18°C for the *Marf RNAi* qPCR since they were lethal at higher temperatures (**Figure D5.3E**).

Quantification of Ubi, p62, or Atg8a puncta

The Analyze-Particles function in ImageJ was used to identify and measure the total number of puncta in VL3/VL4 muscles combined. The ROI-Manager function was used to measure the overlap between p62-Ubi or p62-GFP-Atg8a. The Plot-Profile function was used to assess colocalization of p62-ATP5α. The ROI-Manager-Measure function was used to quantitate TMRM and MitoTracker intensity.

NEB quantification

NEB were counted in muscles VL3 and VL4 from abdominal segments A2 and A3 of wandering L3 larvae. ≥100 nuclei were counted per genotype. Only foci that stained positive for both Lamin B and dFz2C staining were counted as a NEB. Since NEBs were not detected in all nuclei [8], the number of NEBs within each genotype was randomly separated into three groups using the random function in Excel. Image acquisition and NEB number quantification were both performed using Double-Blind strategies.

Statistical analysis

Statistical analyses were performed in Prism 10.1.2. The unpaired student t-test was used to determine the significance between pairwise comparisons followed by the Mann-Whitney test. Additional data sets that compared three or more unmatched groups that did not fit into a Gaussian distribution were analyzed using the nonparametric Kruskal-Wallis test using one-way ANOVA.

Acknowledgements

We are grateful to Susan Parkhurst for sharing the anti-dFz2C antibody. Stocks obtained from the BDSC are supported by a grant from the Office of the Director of the National Institutes of Health under Award Number P40OD018537. Other transgenic RNAi stocks was obtained from the VDRC (www.vdrc.at). Thanks to the Kansas State University Johnson Cancer Research Center

(JCRC) for travel funds to Y.G. and Z.Z. This study was supported by the National Institute of Arthritis and Musculoskeletal and Skin Diseases (NIAMS) of the National Institutes of Health (NIH) under award number RO1AR060788 to E.R.G.

References

1. Yamamoto H, Zhang S, Mizushima N. Autophagy genes in biology and disease. Nat Rev Genet. 2023 Jun;24(6):382-400. PMID: 36635405. doi: 10.1038/s41576-022-00562-w.
2. Aman Y, Schmauck-Medina T, Hansen M, Morimoto RI, Simon AK, Bjedov I, et al. Autophagy in healthy aging and disease. Nat Aging. 2021 Aug;1(8):634-50. PMID: 34901876. doi: 10.1038/s43587-021-00098-4.
3. Lamark T, Johansen T. Mechanisms of Selective Autophagy. Annu Rev Cell Dev Biol. 2021 Oct 06;37:143-69. PMID: 34152791. doi: 10.1146/annurev-cellbio-120219-035530.
4. Adebayo M, Singh S, Singh AP, Dasgupta S. Mitochondrial fusion and fission: The fine-tune balance for cellular homeostasis. FASEB J. 2021 Jun;35(6):e21620. PMID: 34048084. doi: 10.1096/fj.202100067R.
5. Palikaras K, Lionaki E, Tavernarakis N. Mechanisms of mitophagy in cellular homeostasis, physiology and pathology. Nat Cell Biol. 2018 Sep;20(9):1013-22. PMID: 30154567. doi: 10.1038/s41556-018-0176-2.
6. Onishi M, Yamano K, Sato M, Matsuda N, Okamoto K. Molecular mechanisms and physiological functions of mitophagy. EMBO J. 2021 Feb 01;40(3):e104705. PMID: 33438778. doi: 10.15252/embj.2020104705.
7. Vargas JNS, Hamasaki M, Kawabata T, Youle RJ, Yoshimori T. The mechanisms and roles of selective autophagy in mammals. Nat Rev Mol Cell Biol. 2023 Mar;24(3):167-85. PMID: 36302887. doi: 10.1038/s41580-022-00542-2.
8. Parchure A, Munson M, Budnik V. Getting mRNA-Containing Ribonucleoprotein Granules Out of a Nuclear Back Door. Neuron. 2017 Nov 01;96(3):604-15. PMID: 29096075. doi: 10.1016/j.neuron.2017.10.020.
9. Keuenhof KS, Kohler V, Broeskamp F, Panagaki D, Speese SD, Büttner S, et al. Nuclear envelope budding and its cellular functions. Nucleus. 2023 Dec;14(1):2178184. PMID: 36814098. doi: 10.1080/19491034.2023.2178184.
10. T H, L P, KS S, BG K, TC M. Nuclear egress of herpesviruses: the prototypic vesicular nucleocytoplasmic transport. Adv. Virus Res2016. p. 81-140.
11. Speese SD, Ashley J, Jokhi V, Nunnari J, Barria R, Li Y, et al. Nuclear envelope budding enables large ribonucleoprotein particle export during synaptic Wnt signaling. Cell. 2012 May 11;149(4):832-46. PMID: 22579286. doi: 10.1016/j.cell.2012.03.032.
12. Li Y, Hassinger L, Thomson T, Ding B, Ashley J, Hassinger W, et al. Lamin Mutations Accelerate Aging via Defective Export of Mitochondrial mRNAs through Nuclear Envelope Budding. Curr Biol. 2016 Aug 08;26(15):2052-9. PMID: 27451905. doi: 10.1016/j.cub.2016.06.007.
13. Davidson KA, Nakamura M, Verboon JM, Parkhurst SM. Centralspindlin proteins Pavarotti and Tumbleweed along with WASH regulate nuclear envelope budding. J Cell Biol. 2023 Aug 07;222(8). PMID: 37163553. doi: 10.1083/jcb.202211074.
14. Lőrincz P, Mauvezin C, Juhász G. Exploring Autophagy in Drosophila. Cells. 2017 Jul 12;6(3). PMID: 28704946. doi: 10.3390/cells6030022.
15. Liu WJ, Ye L, Huang WF, Guo LJ, Xu ZG, Wu HL, et al. p62 links the autophagy pathway and the ubiqutin-proteasome system upon ubiquitinated protein degradation. Cell Mol Biol Lett. 2016;21:29. PMID: 28536631. doi: 10.1186/s11658-016-0031-z.
16. Brooks D, Naeem F, Stetsiv M, Goetting SC, Bawa S, Green N, et al. Drosophila NUAK functions with Starvin/BAG3 in autophagic protein turnover. PLoS Genet. 2020 04;16(4):e1008700. PMID: 32320396. doi: 10.1371/journal.pgen.1008700.

17. Guo Y, Zeng Q, Brooks D, Geisbrecht ER. A conserved STRIPAK complex is required for autophagy in muscle tissue. Mol Biol Cell. 2023 Aug 01;34(9). PMID: 37379167. doi: 10.1091/mbc.E23-01-0006.
18. Lu W, Gelfand VI. Moonlighting Motors: Kinesin, Dynein, and Cell Polarity. Trends Cell Biol. 2017 Jul;27(7):505-14. PMID: 28284467. doi: 10.1016/j.tcb.2017.02.005.
19. White EA, Glotzer M. Centralspindlin: at the heart of cytokinesis. Cytoskeleton (Hoboken). 2012 Nov;69(11):882-92. PMID: 22927365. doi: 10.1002/cm.21065.
20. Nakamura M, Verboon JM, Prentiss CL, Parkhurst SM. The kinesin-like protein Pavarotti functions noncanonically to regulate actin dynamics. J Cell Biol. 2020 Sep 07;219(9). PMID: 32673395. doi: 10.1083/jcb.201912117.
21. Dikic I. Proteasomal and Autophagic Degradation Systems. Annu Rev Biochem. 2017 06;86:193-224. PMID: 28460188. doi: 10.1146/annurev-biochem-061516-044908.
22. Dósa A, Csizmadia T. The role of K63-linked polyubiquitin in several types of autophagy. Biol Futur. 2022 Jun;73(2):137-48. PMID: 35501575. doi: 10.1007/s42977-022-00117-4.
23. Jones WM, Chao AT, Zavortink M, Saint R, Bejsovec A. Cytokinesis proteins Tum and Pav have a nuclear role in Wnt regulation. J Cell Sci. 2010 Jul 01;123(Pt 13):2179-89. PMID: 20516152. doi: 10.1242/jcs.067868.
24. Minestrini G, Máthé E, Glover DM. Domains of the Pavarotti kinesin-like protein that direct its subcellular distribution: effects of mislocalisation on the tubulin and actin cytoskeleton during Drosophila oogenesis. J Cell Sci. 2002 Feb 15;115(Pt 4):725-36. PMID: 11865028. doi: 10.1242/jcs.115.4.725.
25. Jokhi V, Ashley J, Nunnari J, Noma A, Ito N, Wakabayashi-Ito N, et al. Torsin mediates primary envelopment of large ribonucleoprotein granules at the nuclear envelope. Cell Rep. 2013 Apr 25;3(4):988-95. PMID: 23583177. doi: 10.1016/j.celrep.2013.03.015.
26. Verboon JM, Nakamura M, Davidson KA, Decker JR, Nandakumar V, Parkhurst SM. Wash and the Wash regulatory complex function in nuclear envelope budding. J Cell Sci. 2020 Jul 08;133(13). PMID: 32503943. doi: 10.1242/jcs.243576.
27. Larsen S, Nielsen J, Hansen CN, Nielsen LB, Wibrand F, Stride N, et al. Biomarkers of mitochondrial content in skeletal muscle of healthy young human subjects. J Physiol. 2012 Jul 15;590(14):3349-60. PMID: 22586215. doi: 10.1113/jphysiol.2012.230185.
28. Tanabe LM, Liang CC, Dauer WT. Neuronal Nuclear Membrane Budding Occurs during a Developmental Window Modulated by Torsin Paralogs. Cell Rep. 2016 Sep 20;16(12):3322-33. PMID: 27653693. doi: 10.1016/j.celrep.2016.08.044.
29. Wang ZH, Clark C, Geisbrecht ER. Analysis of mitochondrial structure and function in the Drosophila larval musculature. Mitochondrion. 2016 Jan;26:33-42. PMID: 26611999. doi: 10.1016/j.mito.2015.11.005.
30. Wang ZH, Clark C, Geisbrecht ER. Drosophila Clueless is involved in Parkin-dependent mitophagy by promoting VCP-mediated Marf degradation. Hum Mol Genet. 2016 Feb. PMID: 26931463. doi: 10.1093/hmg/ddw067.
31. Dorn GW. Mitofusin 2 Dysfunction and Disease in Mice and Men. Front Physiol. 2020;11:782. PMID: 32733278. doi: 10.3389/fphys.2020.00782.
32. Narendra D, Kane LA, Hauser DN, Fearnley IM, Youle RJ. p62/SQSTM1 is required for Parkin-induced mitochondrial clustering but not mitophagy; VDAC1 is dispensable for both. Autophagy. 2010 Nov;6(8):1090-106. PMID: 20890124. doi: 10.4161/auto.6.8.13426.
33. Miyazono Y, Hirashima S, Ishihara N, Kusukawa J, Nakamura KI, Ohta K. Uncoupled mitochondria quickly shorten along their long axis to form indented spheroids, instead of rings, in

a fission-independent manner. Sci Rep. 2018 Jan 10;8(1):350. PMID: 29321618. doi: 10.1038/s41598-017-18582-6.
34. R W, M S, H Y, H K. In Situ Hybridization: Fruit Fly Embryos and Tissues. 2010. p. 9.3.1-9.3.26.

Chapter 6 - NUAK function in maintain normal muscle function.

6.1, Introduction

Approximately 1.71 billion individuals globally are affected by muscle-related disorders [1]. The identification of novel targets for maintaining normal muscle function is crucial for developing specific pharmaceutical interventions and treatment strategies. NUAK plays a vital role in preserving skeletal muscle function. Our research has uncovered novel functions of NUAK in muscle development, the degradation of damaged proteins, and sarcomere remodeling. Here I summarize my contribution to two additional projects. I advanced these projects by designing experimental protocols and providing technical assistance in experimental execution. My experimental contributions are shown in **Figures 6.1** and **6.2**.

6.2, Independent pathways control muscle tissue size and sarcomere remodeling

Cell growth and proliferation must be tightly controlled in multicellular organisms for normal tissue development and maintenance. Multi-organ communication to govern systemic growth is a complicated process and mechanisms that control it is still not fully understood.

NUAK is an evolutionarily conserved serine/threonine kinase expressed in multiple tissues of *Drosophila*, including neurons, muscles, and the fat body. We found that pupal and adult body size, including internal organs, was reduced when NUAK was specifically overexpressed in muscle tissues, and this phenotype was not due to inadequate feeding [2]. To determine why NUAK overexpression (OE) in muscles reduced organismal size, we performed RNA-seq to analyze gene expression changes between NUAK OE and control larvae. We found that NUAK OE in muscles changed the expression level of insulin pathway targets. *FOXO* and *PTEN*, both

negative regulators of the insulin pathway, also reduced organismal size when overexpressed. This result is consistent with previous studies, showing that systemic growth is regulated by insulin-like peptides activating insulin receptors in multiple target tissues [3-5]. This suggests NUAK acts as a negative regulator of the insulin pathway in muscle tissue. We also identified *methuselah-like 8 (mthl8)* as a novel target of both NUAK and insulin signaling.

The sarcomere is the essential unit of muscular contraction in striated muscles, composed of thick myosin filaments and thin actin filaments [6]. The growth of skeletal muscle is largely characterized by the incorporation of proteins into repeated sarcomeres [7, 8]. Further analysis revealed that NUAK OE or reduced insulin signaling led to fewer sarcomeres in muscle fibers. However, the protein synthesis was not affected in the NUAK OE or NUAK RNAi larvae muscles (**Figure 6.1**) [2]. We also discovered that muscle size reduction and sarcomere remodeling could be uncoupled. *Drosophila* Lasp protein is known for its role in regulating thin filament length and the relative spacing between filaments [9]. Therefore, we further analyzed Lasp protein location in muscles that exhibited variations in sarcomere size and found that the normal Lasp pattern was altered in NUAK OE, FOXO OE, or PTEN OE compared with control muscles. This result indicated that the abnormal localization of Lasp, caused by NUAK or reduced insulin signaling, may contribute to sarcomere remodeling.

Our work demonstrated that NUAK plays a crucial role in regulating muscle growth through modulation of insulin signaling. We also highlight the complex relationship between muscle growth and sarcomere remodeling, suggesting the existence of independent regulatory pathways for these processes. This work provides new insights into the molecular mechanisms controlling muscle size and structure, with potential implications for understanding muscle development and disease.

6.3, Identification of CryAB as a target of NUAK kinase activity in *Drosophila* muscle tissue.

Phosphorylation reactions, catalyzed by protein kinases, are one of the most prevalent and well-studied post-translational modifications in cells. Phosphorylation can change protein activity and interactions, thus playing significant roles in the regulation of various cellular processes. *Drosophila* NUAK contains a kinase domain and a C-terminal region. Our lab has demonstrated that the architecture of skeletal muscle was disrupted upon the knockdown of NUAK in muscle cells. However, it is not clear whether the NUAK kinase domain is responsible for maintaining normal muscle structure. Moreover, identifying more targets for the NUAK kinase will further our understanding of NUAK's function in maintaining normal muscle function.

To study the NUAK function, we created a kinase-dead form ($NUAK^{K99R}$) of NUAK by mutating a conserved lysine residue required for catalytic activity using CRISPR/Cas9 [10]. In this work, we found that about 60% of $NUAK^{K99R}$/ $NUAK^{K99R}$ embryos failed to hatch and the rest all died before pupation [11]. This embryonic lethality was not due to abnormal myogenesis and sarcomere formation, suggesting that muscle development still proceeded normally during embryogenesis. In our lab, the muscle morphology analysis uses L3-stage larvae, but almost all homozygous $NUAK^{K99R}$/$NUAK^{K99R}$ larvae died before this stage. To overcome this, we took advantage of the spatial and temporal UAS/Gal4 system to control expression. We designed transgenic flies containing mutations in the kinase domain. We created a UAS-controlled $NUAK^{K99R}$ transgenic fly. Previously, we generated a *UAS-*$NUAK^{E197K}$ fly line, the conserved glutamic acid at position 197(within the kinase domain) was mutated to lysine to mimic a missense mutation. In *C. elegans*, the *unc-82* (NUAK) E197K mutation disrupted muscle architecture [12]. The NUAK protein could be phosphorylated by upstream kinases, to study if the NUAK protein's

phosphorylation is necessary for its function, we mutated a conserved threonine located at position 226 to alanine [13, 14]. Indeed, we found that normal muscle structure was disrupted in the transgenic larvae overexpressing each of these kinase domain mutations. Furthermore, the overexpression of human kinase-dead NUAK1 (*UAS-hNUAK1 K84R*) in larval muscle, unlike human kinase-dead NUAK2 (*UAS-hNUAK2 K81R*), resulted in the disruption of normal muscle architecture and aberrant accumulation of CryAB (**Figure 6.2**) [11].These data confirm that NUAK kinase function is essential for maintaining normal muscle structure during larval muscle growth and human NUAK1 has a similar function to fly NUAK in muscle structure maintenance.

Previously, we performed a yeast two-hybrid (Y2H) experiment to identify potential binding partners of NUAK and uncovered l(2)efl/CryAB as a high-confidence interacting protein [10]. We further verified the NUAK-CryAB physical interaction through proximity ligation assay (PLA). We also found that CryAB abnormally accumulated within the muscle of NUAK kinase domain mutations (K99R, E197K, or T226A). To ascertain if CryAB may undergo phosphorylation by NUAK, we initially conducted an anti-CryAB western blot analysis. A band indicative of phosphorylated CryAB was seen in the wild-type NUAK OE sample but was not present in the kinase domain mutant samples. Our MS results also showed that CryAB was phosphorylated more under the NUAK OE background compared to the control. Moreover, we identified two novel phosphorylation sites on CryAB: serine 68 and serine 70. Mutation of these serine residues to alanine abolished CryAB phosphorylation, confirming their importance in the CryAB phosphorylation process.

In conclusion, we proved that NUAK kinase activity is essential for preventing muscle degeneration and maintaining normal structure. We demonstrated a physical interaction between NUAK and CryAB and showed that NUAK promotes the phosphorylation of CryAB. We also

identified two novel sites in CryAB that could be phosphorylated. Since CryAB mutations are associated with MFM, our data enhance our understanding of NUAK function in muscle development, protein turnover, and disease prevention.

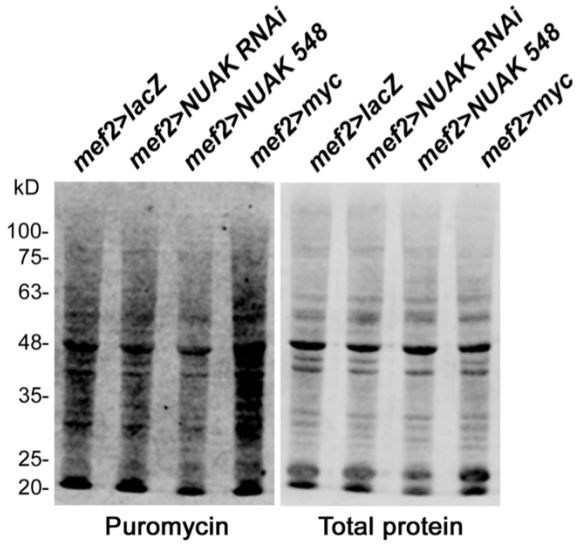


Figure 6.1. New protein synthesis is not altered in NUAK mutant muscles.

Western blot using antipuromycin to detect newly synthesized proteins (left panel) or staining for total protein (right panel) upon loss or overexpression of NUAK [2].

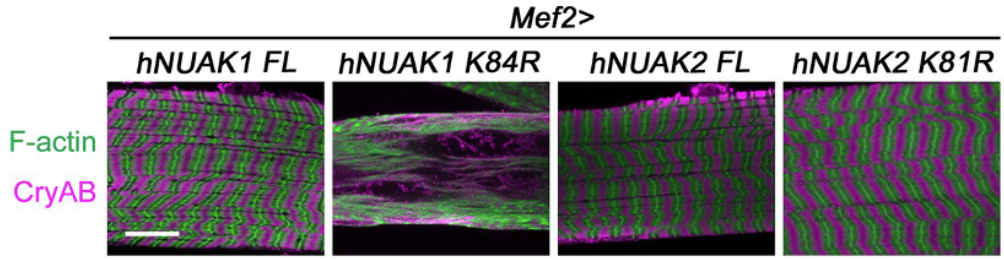


Figure 6.2. human NUAK1 and fly NUAK have similar functions in muscle structure maintenance.

L3 muscles stained for F-actin or anti-CryAB. Overexpression of kinase-dead hNUAK1 (*Mef2* > *hNUAK1 K84R*), but not hNUAK2 (*Mef2* > *hNUAK2 K81R*), disrupts muscle morphology and causes CryAB accumulation. Scale bar, 25 μm [11].

References

1. Alarcos Cieza and Kate Causey and Kaloyan Kamenov and Sarah Wulf Hanson and Somnath Chatterji and Theo V. Global estimates of the need for rehabilitation based on the Global Burden of Disease study 2019: a systematic analysis for the Global Burden of Disease Study 2019. The Lancet. 2020;396(10267):2006-17. doi: https://doi.org/10.1016/S0140-6736(20)32340-0.
2. Brooks D, Bawa S, Bontrager A, Stetsiv M, Guo Y, Geisbrecht ER. Independent pathways control muscle tissue size and sarcomere remodeling. Dev Biol. 2022 Jun 24;490:1-12. PMID: 35760368. doi: 10.1016/j.ydbio.2022.06.014.
3. Koyama T, Mendes CC, Mirth CK. Mechanisms regulating nutrition-dependent developmental plasticity through organ-specific effects in insects. Front Physiol. 2013 Sep 26;4:263. PMID: 24133450. doi: 10.3389/fphys.2013.00263.
4. Texada MJ, Koyama T, Rewitz K. Regulation of Body Size and Growth Control. Genetics. 2020 Oct;216(2):269-313. PMID: 33023929. doi: 10.1534/genetics.120.303095.
5. Mirth CK, Shingleton AW. Integrating body and organ size in Drosophila: recent advances and outstanding problems. Front Endocrinol (Lausanne). 2012;3:49. PMID: 22654869. doi: 10.3389/fendo.2012.00049.
6. Sweeney HL, Hammers DW. Muscle Contraction. Cold Spring Harb Perspect Biol. 2018 Feb 01;10(2). PMID: 29419405. doi: 10.1101/cshperspect.a023200.
7. Gautel M, Djinović-Carugo K. The sarcomeric cytoskeleton: from molecules to motion. J Exp Biol. 2016 Jan;219(Pt 2):135-45. PMID: 26792323. doi: 10.1242/jeb.124941.
8. Jorgenson KW, Phillips SM, Hornberger TA. Identifying the Structural Adaptations that Drive the Mechanical Load-Induced Growth of Skeletal Muscle: A Scoping Review. Cells. 2020 Jul 09;9(7). PMID: 32660165. doi: 10.3390/cells9071658.
9. Fernandes I, Schöck F. The nebulin repeat protein Lasp regulates I-band architecture and filament spacing in myofibrils. J Cell Biol. 2014 Aug 18;206(4):559-72. PMID: 25113030. doi: 10.1083/jcb.201401094.
10. Brooks D, Naeem F, Stetsiv M, Goetting SC, Bawa S, Green N, et al. Drosophila NUAK functions with Starvin/BAG3 in autophagic protein turnover. PLoS Genet. 2020 04;16(4):e1008700. PMID: 32320396. doi: 10.1371/journal.pgen.1008700.
11. Zhao Z, Brooks D, Guo Y, Geisbrecht ER. Identification of CryAB as a target of NUAK kinase activity in Drosophila muscle tissue. Genetics. 2023 Nov 01;225(3). PMID: 37713608. doi: 10.1093/genetics/iyad167.
12. Hoppe PE, Chau J, Flanagan KA, Reedy AR, Schriefer LA. Caenorhabditis elegans unc-82 encodes a serine/threonine kinase important for myosin filament organization in muscle during growth. Genetics. 2010 Jan;184(1):79-90. PMID: 19901071. doi: 10.1534/genetics.109.110189.
13. Sun X, Gao L, Chien HY, Li WC, Zhao J. The regulation and function of the NUAK family. J Mol Endocrinol. 2013 Oct;51(2):R15-22. PMID: 23873311. doi: 10.1530/JME-13-0063.
14. Yeh YY, Wrasman K, Herman PK. Autophosphorylation within the Atg1 activation loop is required for both kinase activity and the induction of autophagy in Saccharomyces cerevisiae. Genetics. 2010 Jul;185(3):871-82. PMID: 20439775. doi: 10.1534/genetics.110.116566.

Chapter 7 - Conclusions and Future Directions

Conclusions

BAG3/Stv mutations are associated with myofibrillar myopathy (MFM) [1-5]. Identifying additional regulators involved in the BAG3/Stv-mediated pathway can enhance our understanding of the relationship between BAG3/Stv and muscle diseases. Our work identified the Striatin-interacting phosphatase and kinase (STRIPAK) complex physically and genetically interacting with the NUAK-Stv complex in *Drosophila* larval muscles [6]. The NUAK-Stv-mediated chaperone-assisted selective autophagy (CASA) pathway is critical for maintaining muscle homeostasis, as it can selectively degrade damaged proteins [7]

We found that Strip knockdown in muscle cells resulted in the accumulation of ubiquitinated cargo, p62, and Atg8a, indicating a block in autophagy. This accumulation of autophagosomes was not due to altered autophagosome and lysosome biogenesis or lysosomal activity. Using a tandem GFP-mCherry-Atg8a fusion protein combined with chloroquine feeding, we demonstrated that autophagosome-lysosome fusion was partially impaired in Strip loss-of-function muscle cells. Our findings reveal that the STRIPAK complex plays a crucial role in maintaining normal muscle structure and regulating autophagy. Moreover, our work provides new insights into the molecular mechanisms governing CASA in muscle tissue and may have implications for understanding muscle-related disorders associated with autophagy dysfunction.

Previously, we performed RNA-seq experiments to compare gene expression levels in NUAK mutant and control larvae. The results identified a large group of downregulated genes related to microtubule transport in NUAK mutant larvae. We further analyzed candidate genes using a genetic screening approach to identify those functioning in the autophagy pathway. We found that Pavarotti (Pav) and its binding partner Tumbleweed (Tum) influenced autophagy.

Knockdown of Pav or Tum in muscle cells using RNAi formed autophagosome clusters, a unique phenotype not previously observed in our lab [6, 7]. Further analysis revealed that these autophagosomes had engulfed damaged mitochondria.

A recent study has shown that Pav and Tum proteins function in the formation of the nuclear envelope budding (NEB) [8], consistent with our finding that Pav and Tum proteins are enriched in the nucleus rather than the myoplasm. We demonstrated that Pav and Tum knockdown in muscle cells affects NEB formation, thus reducing *Marf mRNA* transport from nuclei to myoplasm. The reduction of *Marf mRNA* levels in the myoplasm impairs the mitochondrial fusion process, generating damaged mitochondria and triggering mitophagy. Consequently, p62 and Atg8a are recruited to the damaged mitochondria, forming autophagosome clusters.

Previously, researchers used dFz2C and Lamin B antibody co-immunostaining and counted the number of NEBs per nucleus to identify regulators controlling NEB formation [8, 9]. This approach is time-consuming and limited by reagent availability, as dFz2C antibody is not commercially available. Our work provides novel insights into how NEB formation links with mitophagy. Furthermore, we have developed a convenient biochemical method for rapid screening of genes involved in NEB formation.

Future Directions

To determine which human Strip orthologs are essential for autophagy.

As mentioned in Chapter 2, we found that Strip functions with the Stv-NUAK complex in muscle to regulate autophagy. *D. melanogaster* Strip and the human STRIP1 and STRIP2 orthologs share high identity and similarity and conserved domains (**Figure 7.1)**). Multiple studies indicate that the two human STRIP proteins have different functions [10]. In multiple cancer cell types, STRIP1 and STRIP2 knockdown lead to distinct phenotypes [10]. Moreover, STRIP2 but

not STRIP1 knockdown in zebrafish causes heart defects [11]. However, it is unknown which human Strip ortholog functions in muscle autophagy.

We recently obtained two published *Strip* alleles, a null allele named *doubled glomeruli* (*Strip*^{dogi}) [12] and a hypomorphic allele called *jam packed* (*strip*^{jam}), the latter of which survives through larval development to assess contractile muscles [13]. We hypothesize that *Strip*$^{jam/dogi}$ larvae have impaired autophagy similar to *Strip RNAi* muscles, thus providing a platform to test which human Strip protein is also required for protein turnover.

To test our hypothesis, cDNA sequences corresponding to human *STRIP1(FAM40A)* or *STRIP2(FAM40B)* will be synthesized by GenScript using codons optimized for expression in *D. melanogaster.* Each sequence will be tagged at the N-terminus with a FLAG tag or at the C-terminus with a V5 tag since previous studies showed that tagged Strip can rescue other *Strip*$^{jam/jam}$ phenotypes [13]. These DNA sequences will be cloned into the pUAST transformation vector and sent to Rainbow Transgenics for the creation of transgenic flies. These humanized transgenic lines will first be recombined with the appropriate *Strip* allele. Next they will be crossed to flies containing *Mef2*-Gal4 in the background of a different *Strip* allele. Immunostaining with anti-Ub, anti-p62, and anti-Atg8a will be performed on the genotypes listed in **Table 7.1**. Phalloidin will be added to label muscle.

We expect to see that expression of human STRIP1 or STRIP2 will rescue the *strip*$^{jam/dogi}$ muscle morphology and autophagy defects. If we do not observe rescue, we can also express the human STRIP proteins in other tissues, such as the nervous system, in case there are non-autonomous effects. If *strip*$^{jam/dogi}$ larvae do not have the same autophagy defects as S*trip RNAi* muscles, an alternative strategy will be to express these alleles in the *Strip RNAi* background to assess rescue.

To determine if Strip functions alone or requires the integrity of the STRIPAK complex to sustain autophagic flux.

STRIP and STRIPAK complex proteins have multiple roles in signaling, vascular development, and cardiac function [14]. Multiple members of the STRIPAK complex are associated with cardiac disease. Striatin (*D. melanogaster* Cka) is the scaffold of the STRIPAK complex. An association has been found between a variant of Striatin and salt sensitivity of blood pressure (SSBP) [15]. In dogs, an 8-bp deletion in the *Striatin* gene is the cause of arrhythmogenic right ventricular cardiomyopathy(ref) and dilated cardiomyopathy [16]. Sarcolemma-associated protein (SLMAP) is another STRIPAK complex member and certain mutations are associated with Brugada syndrome [17]. These data support the hypothesis that additional proteins may function with Strip.

A recent cryo-EM structure of Strip and other STRIPAK complex components revealed interface binding sites that when mutated, reduce the affinity between Strip and associated proteins [18]. The essential amino acids for binding are conserved between *Drosophila* and mammalian Strip. Therefore, in this aim will determine if Strip operates alone or if the integrity of the STRIPAK complex is also required for autophagy.

We will disrupt the assembly of the *D. melanogaster* STRIPAK complex by mutating the amino acids required for the Strip-Cka interaction (**Figure 7.2**) using two methods. First, flies containing either the Strip D474K or Strip R513A single point mutations with an N-terminal FLAG tag will be created via CRISPR/Cas9 platform (WellGenetics). Note we will also create the FLAG:Strip WT knock-in as a control. Second, we will create transgenic flies overexpressing either mutation (UAS-FLAG::Strip D474K or UAS-FLAG::Strip R513A) as we already have UAS-FLAG::Strip.

To check the effects of the desired mutations on the formation of the STRIPAK complex, we will prepare extracts of FLAG-tagged WT or FLAG-tagged mutant larvae and perform pulldowns using anti-FLAG M2 resin followed by Western blotting with anti-Cka antibodies. The IPs for either the endogenous Strip mutants or UAS-based constructs will be performed in triplicate and the resulting band intensities will be quantified using a LI-COR imaging system.

We expect to see significantly reduced binding of Cka in the FLAG-tagged Strip mutants compared to WT. If the CRISPR/Cas9 FLAG-Strip mutants are lethal prior to the larval stage, we will scale up and perform these experiments during late embryogenesis after muscles have formed or in a *Strip RNAi* background.

Table 7.1. Experimental design.

Negative control	*Mef2*-Gal4; *strip*^{dogi} x UAS-*GFP*; *strip*^{jam}
Positive control	*Mef2*-Gal4; *strip*^{dogi} x UAS-*FLAG::Strip*; *strip*^{jam}
	Mef2-Gal4; *strip*^{dogi} x UAS-*Strip::V5*; *strip*^{jam}
Experiment Group	*Mef2*-Gal4; *strip*^{dogi} x UAS-*FLAG::STRIP1*; *strip*^{jam}
	Mef2-Gal4; *strip*^{dogi} x UAS-*STRIP1::V5*; *strip*^{jam}
	Mef2-Gal4; *strip*^{dogi} x UAS-*FLAG::STRIP2*; *strip*^{jam}
	Mef2-Gal4; *strip*^{dogi} x UAS-*STRIP2::V5*; *strip*^{jam}



Figure 7.1. Strip protein schematics.

Both fly Strip and human STRIP proteins have conserved domains and amino acid sequences. The identity and similarity scores for STRIP1 and STRIP2 are compared to the fly protein.

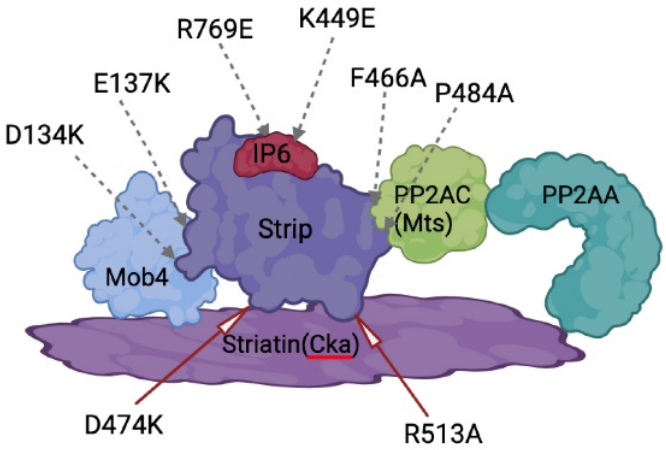


Figure 7.2. Schematic of Strip mutations that will disrupt the interaction between Strip and other STRIPAK members.

The Strip-Cka interaction will be tested in this proposal and other interactions (gray dotted lines) will be tested in the future or if time allows.

References

1. Béhin A, Salort-Campana E, Wahbi K, Richard P, Carlier RY, Carlier P, et al. Myofibrillar myopathies: State of the art, present and future challenges. Rev Neurol (Paris). 2015 Oct;171(10):715-29. PMID: 26342832. doi: 10.1016/j.neurol.2015.06.002.
2. Behl C. BAG3 and friends: co-chaperones in selective autophagy during aging and disease. Autophagy. 2011 Jul;7(7):795-8. PMID: 21681022. doi: 10.4161/auto.7.7.15844.
3. Fang X, Bogomolovas J, Wu T, Zhang W, Liu C, Veevers J, et al. Loss-of-function mutations in co-chaperone BAG3 destabilize small HSPs and cause cardiomyopathy. J Clin Invest. 2017 Aug;127(8):3189-200. PMID: 28737513. doi: 10.1172/JCI94310.
4. McCollum AK, Casagrande G, Kohn EC. Caught in the middle: the role of Bag3 in disease. Biochem J. 2009 Dec 14;425(1):e1-3. PMID: 20001957. doi: 10.1042/BJ20091739.
5. Meister-Broekema M, Freilich R, Jagadeesan C, Rauch JN, Bengoechea R, Motley WW, et al. Myopathy associated BAG3 mutations lead to protein aggregation by stalling Hsp70 networks. Nature communications. 2018;9(1):5342.
6. Guo Y, Zeng Q, Brooks D, Geisbrecht ER. A conserved STRIPAK complex is required for autophagy in muscle tissue. Mol Biol Cell. 2023 Aug 01;34(9). PMID: 37379167. doi: 10.1091/mbc.E23-01-0006.
7. Brooks D, Naeem F, Stetsiv M, Goetting SC, Bawa S, Green N, et al. Drosophila NUAK functions with Starvin/BAG3 in autophagic protein turnover. PLoS Genet. 2020 04;16(4):e1008700. PMID: 32320396. doi: 10.1371/journal.pgen.1008700.
8. Davidson KA, Nakamura M, Verboon JM, Parkhurst SM. Centralspindlin proteins Pavarotti and Tumbleweed along with WASH regulate nuclear envelope budding. Journal of Cell Biology. 2023;222(8):e202211074.
9. Speese SD, Ashley J, Jokhi V, Nunnari J, Barria R, Li Y, et al. Nuclear envelope budding enables large ribonucleoprotein particle export during synaptic Wnt signaling. Cell. 2012;149(4):832-46.
10. Suryavanshi N, Furmston J, Ridley AJ. The STRIPAK complex components FAM40A and FAM40B regulate endothelial cell contractility via ROCKs. BMC cell biology. 2018;19:1-13.
11. Wagh V, Doss M, Sabour D, Niemann R, Meganathan K, Jagtap S, et al. Fam40b is required for lineage commitment of murine embryonic stem cells. Cell Death & Disease. 2014;5(7):e1320-e.
12. Sakuma C, Kawauchi T, Haraguchi S, Shikanai M, Yamaguchi Y, Gelfand VI, et al. Drosophila Strip serves as a platform for early endosome organization during axon elongation. Nature communications. 2014;5(1):5180.
13. La Marca JE, Diepstraten ST, Hodge AL, Wang H, Hart AH, Richardson HE, et al. S*trip* and C*ka* negatively regulate JNK signalling during D*rosophila* spermatogenesis. Development. 2019 Jun 28;146(13). PMID: 31164352. doi: 10.1242/dev.174292.
14. Hwang J, Pallas DC. STRIPAK complexes: structure, biological function, and involvement in human diseases. The international journal of biochemistry & cell biology. 2014;47:118-48.
15. Gupta T, Connors M, Tan JW, Manosroi W, Ahmed N, Ting PY, et al. Striatin gene polymorphic variants are associated with salt sensitive blood pressure in normotensives and hypertensives. American Journal of Hypertension. 2018;31(1):124-31.
16. Meurs KM, Stern J, Sisson D, Kittleson M, Cunningham S, Ames M, et al. Association of dilated cardiomyopathy with the striatin mutation genotype in boxer dogs. Journal of Veterinary Internal Medicine. 2013;27(6):1437-40.

17. Ishikawa T, Sato A, Marcou CA, Tester DJ, Ackerman MJ, Crotti L, et al. A novel disease gene for brugada syndrome: sarcolemmal membrane–associated protein gene mutations impair intracellular trafficking of hnav1. 5. Circulation: Arrhythmia and Electrophysiology. 2012;5(6):1098-107.
18. Jeong B-C, Bae SJ, Ni L, Zhang X, Bai X-c, Luo X. Cryo-EM structure of the Hippo signaling integrator human STRIPAK. Nature structural & molecular biology. 2021;28(3):290-9.

Appendix A - Copyright Permissions

This appendix contains the copyright licenses for the work compiled in this dissertation.

Published Work Chapter 2- (Guo *et al.* 2023)[1].

Molecular Biology of the Cell Copyright Policy: the authors retain copyright under the License and Publishing Agreement (LPA) agreement.

Published Work Chapter 3- (Guo *et al.* 2023)[2].

Autophagy Reports Copyright Policy: under the terms of the Creative Commons CC BY license, which permits unrestricted use, distribution, reproduction in any medium, provided the original work is properly cited.

Published Work Chapter 4- (Guo *et al.* 2024)[3].

STAR Protocols Copyright Policy: Authors do not need to ask our permission to use images or information that you have previously published in a Cell Press journal; we ask only that you cite the original publication.

Work Chapter 5- (Guo *et al.* 2024).

This work was submitted to the Autophagy Reports but not published.

Other images

Figure 6.1[4], under Elsevier Policies: Author can Re-use their own material in new works without permission or payment (with full acknowledgment of the original article).

Figure 6.2[5].

OXFORD UNIVERSITY PRESS LICENSE TERMS AND CONDITIONS

Oct 10, 2024

This Agreement between Yungui Guo/Kansas State University ("You") and Oxford University Press ("Oxford University Press") consists of your license details and the terms and conditions provided by Oxford University Press and Copyright Clearance Center.

License Number	5885440166390
License date	Oct 10, 2024
Licensed Content Publisher	Oxford University Press
Licensed Content Publication	Genetics
Licensed Content Title	Identification of CryAB as a target of NUAK kinase activity in *Drosophila* muscle tissue
Licensed Content Author	Zhao, Ziwei; Brooks, David
Licensed Content Date	Sep 15, 2023
Type of Use	Thesis/Dissertation
Institution name	
Title of your work	Analysis of additional regulators necessary for autophagy in Drosophila muscle tissue
Publisher of your work	Kansas State University
Expected publication date	Oct 2024
Permissions cost	0.00 USD
Value added tax	0.00 USD
Total	**0.00 USD**
Title of new work	Analysis of additional regulators necessary for autophagy in Drosophila muscle tissue
Institution name	Kansas State University
Expected presentation date	Oct 2024
Order reference number	123456
Portions	Fig. 7d
The Requesting Person / Organization to Appear on the License	Yungui Guo/Kansas State University
Requestor Location	Kansas State University 141 Chalmers Hall, 1711 Claflin Rd. MANHATTAN, KS 66506 United States Attn: Kansas State University
Publisher Tax ID	GB125506730
Billing Type	Invoice
Billing Address	Kansas State University 141 Chalmers Hall, 1711 Claflin Rd. MANHATTAN, KS 66506 United States Attn: Kansas State University
Total	**0.00 USD**

Terms and Conditions

STANDARD TERMS AND CONDITIONS FOR REPRODUCTION OF MATERIAL FROM AN OXFORD UNIVERSITY PRESS JOURNAL

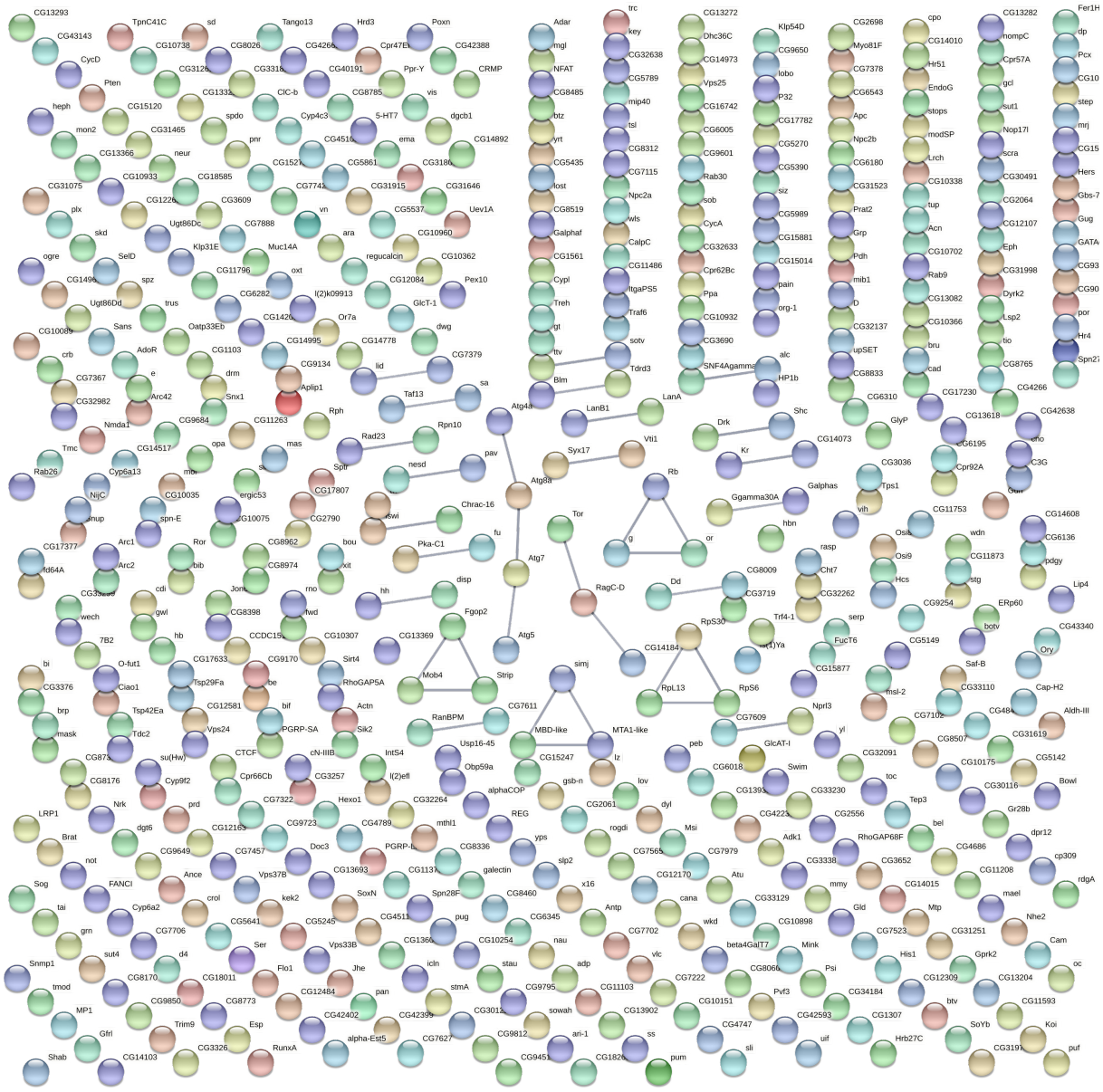
1. Use of the material is restricted to the type of use specified in your order details.
2. This permission covers the use of the material in the **English** language in the following territory: *world*. If you have requested additional permission to translate this material, the terms and conditions of this reuse will be set out in clause 12.
3. This permission is limited to the particular use authorized in (1) above and does not allow you to sanction its use elsewhere in any other format other than specified above, nor does it apply to quotations, images, artistic works etc that have been reproduced from other sources which may be part of the material to be used.
4. No alteration, omission or addition is made to the material without our written consent. Permission **must** be re-cleared with Oxford University Press if/when you decide to reprint.
5. The following credit line appears wherever the material is used: author, title, journal, year, volume, issue number, pagination, by permission of Oxford University Press or the sponsoring society if the journal is a society journal. Where a journal is being published on behalf of a learned society, the details of that society **must** be included in the credit line.
6. For the reproduction of a full article from an Oxford University Press journal for whatever purpose, the corresponding author of the material concerned should be informed of the proposed use. Contact details for the corresponding authors of all Oxford University Press journal contact can be found alongside either the abstract or full text of the article concerned, accessible from www.oxfordjournals.org Should there be a problem clearing these rights, please contact journals.permissions@oup.com
7. If the credit line or acknowledgement in our publication indicates that any of the figures, images or photos was reproduced, drawn or modified from an earlier source it will be necessary for you to clear this permission with the original publisher as well. If this permission has not been obtained, please note that this material cannot be included in your publication/photocopies.
8. While you may exercise the rights licensed immediately upon issuance of the license at the end of the licensing process for the transaction, provided that you have disclosed complete and accurate details of your proposed use, no license is finally effective unless and until full payment is received from you (either by Oxford University Press or by Copyright Clearance Center (CCC)) as provided in CCC's Billing and Payment terms and conditions. If full payment is not received on a timely basis, then any license preliminarily granted shall be deemed automatically revoked and shall be void as if never granted. Further, in the event that you breach any of these terms and conditions or any of CCC's Billing and Payment terms and conditions, the license is automatically revoked and shall be void as if never granted. Use of materials as described in a revoked license, as well as any use of the materials beyond the scope of an unrevoked license, may constitute copyright infringement and Oxford University Press reserves the right to take any and all action to protect its copyright in the materials.
9. This license is personal to you and may not be sublicensed, assigned or transferred by you to any other person without Oxford University Press's written permission.
10. Oxford University Press reserves all rights not specifically granted in the combination of (i) the license details provided by you and accepted in the course of this licensing transaction, (ii) these terms and conditions and (iii) CCC's Billing and Payment terms and conditions.
11. You hereby indemnify and agree to hold harmless Oxford University Press and CCC, and their respective officers, directors, employs and agents, from and against any and all claims arising out of your use of the licensed material other than as specifically authorized pursuant to this license.
12. Unless otherwise specified, inclusion under a Creative Commons license or any other Open Access license allowing onward reuse is prohibited.
13. Where permission to translate has been agreed, the credit line and any copyright/disclaimer notices provided by OUP shall be included on the same page as the Material, translated into the language of the new work, except for trademark names: Translated and reproduced by permission of Oxford University Press on behalf of the <Society Name>. Translation Disclaimer: OUP and the <Society Name> are not responsible or in any way liable for the accuracy of the translation. The Licensee is solely responsible for the translation in this publication/reprint.
14. Other Terms and Conditions:
v1.5

Questions? E-mail us at customercare@copyright.com.

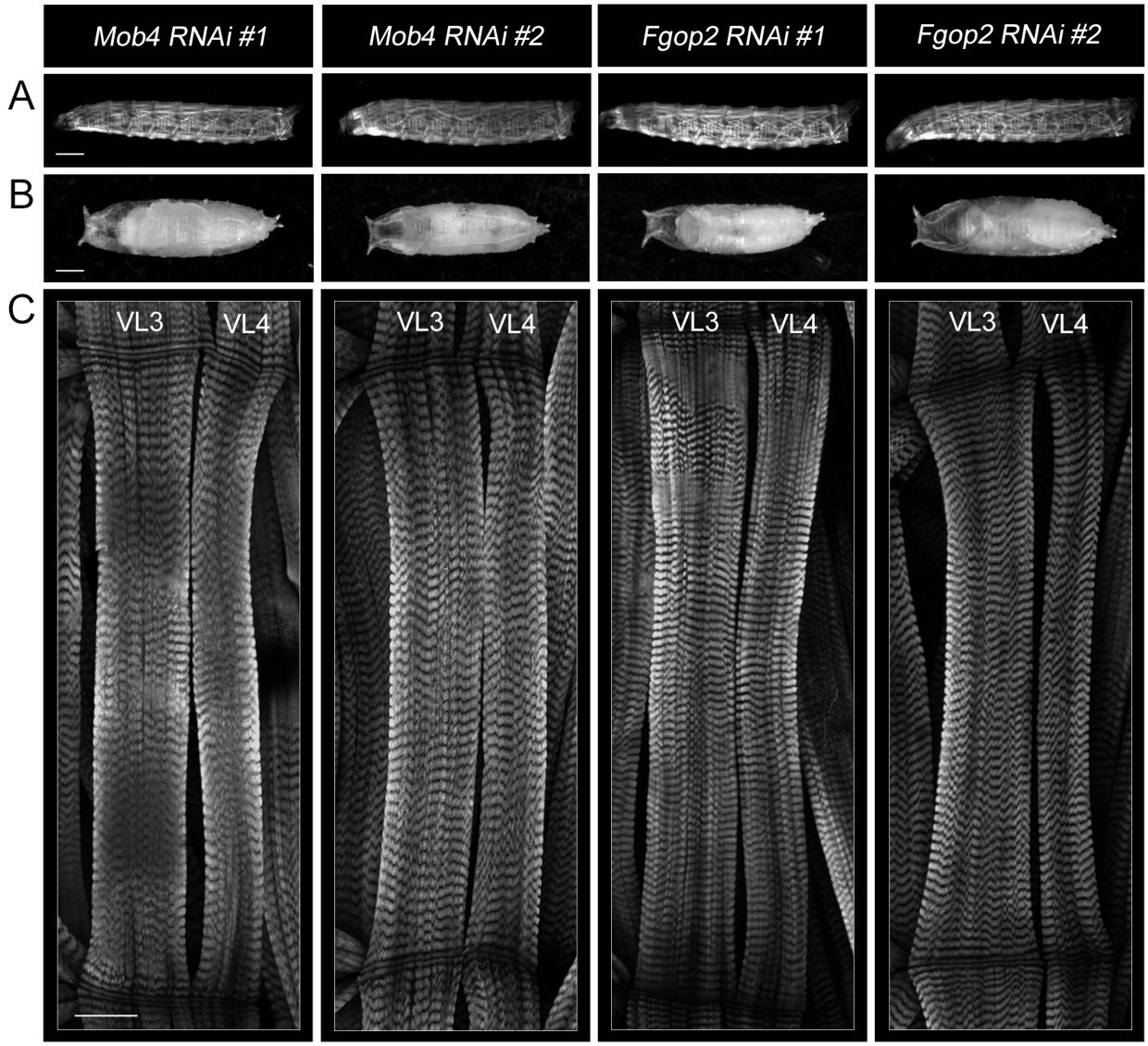
References

1. Guo Y, Zeng Q, Brooks D, Geisbrecht ER. A conserved STRIPAK complex is required for autophagy in muscle tissue. Mol Biol Cell. 2023 Aug 01;34(9). PMID: 37379167. doi: 10.1091/mbc.E23-01-0006.
2. Guo Y, Geisbrecht ER. Orchestration of autophagosome fusion by STRIPAK complex components in muscle tissue. Autophagy Rep. 2023;2(1). PMID: 37810188. doi: 10.1080/27694127.2023.2260670.
3. Guo Y, Hartson SD, Rogers J, Brooks-Kanost L, Brooks D, Geisbrecht ER. Protocol for affinity purification-mass spectrometry interactome profiling in larvae of Drosophila melanogaster. STAR Protoc. 2024 Jun 21;5(2):103064. PMID: 38743568. doi: 10.1016/j.xpro.2024.103064.
4. Brooks D, Bawa S, Bontrager A, Stetsiv M, Guo Y, Geisbrecht ER. Independent pathways control muscle tissue size and sarcomere remodeling. Dev Biol. 2022 Jun 24;490:1-12. PMID: 35760368. doi: 10.1016/j.ydbio.2022.06.014.
5. Zhao Z, Brooks D, Guo Y, Geisbrecht ER. Identification of CryAB as a target of NUAK kinase activity in Drosophila muscle tissue. Genetics. 2023 Nov 01;225(3). PMID: 37713608. doi: 10.1093/genetics/iyad167.

Appendix B - Chapter 2 Supplemental Materials

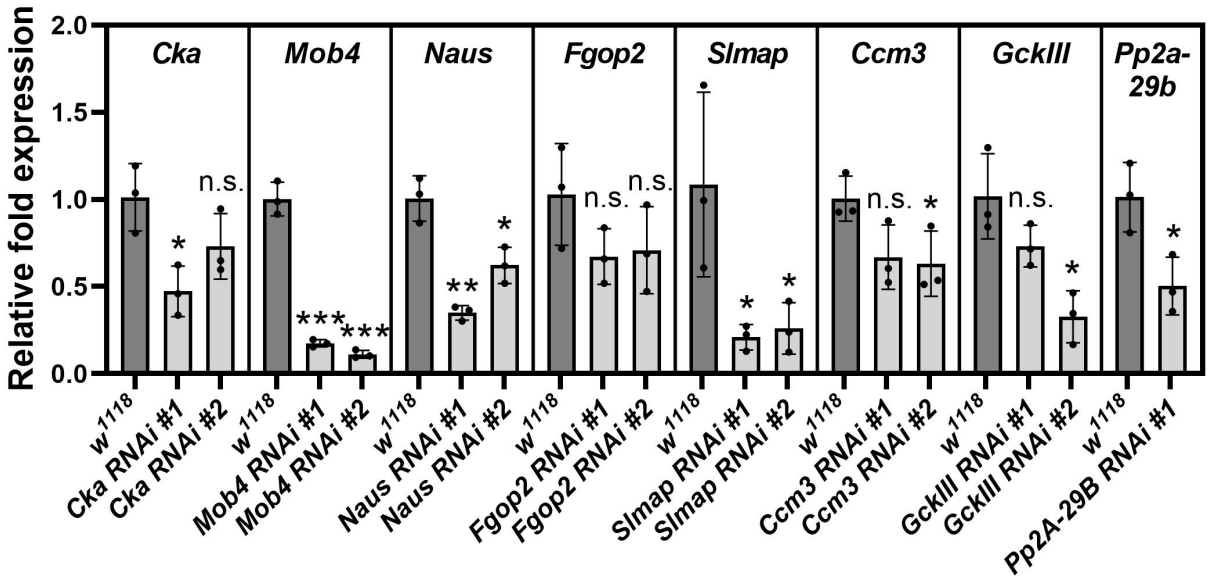


Appendix Figure B.1. Full panel of the 592 genes depicted by Cytoscape nodes that emerged from the in silico muscle morphology screen in T. castaneum.

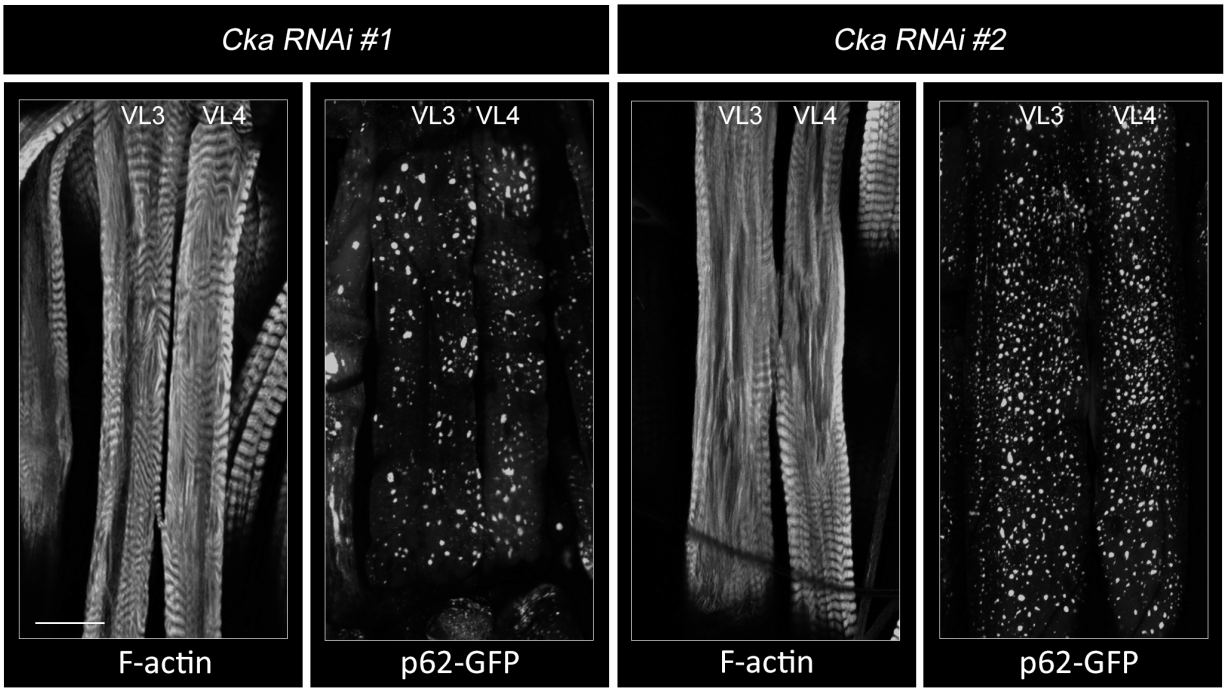


Appendix Figure B.2. No obvious functional or morphological phenotypes in *Mob4* or *Fgop2 RNAi* muscles.

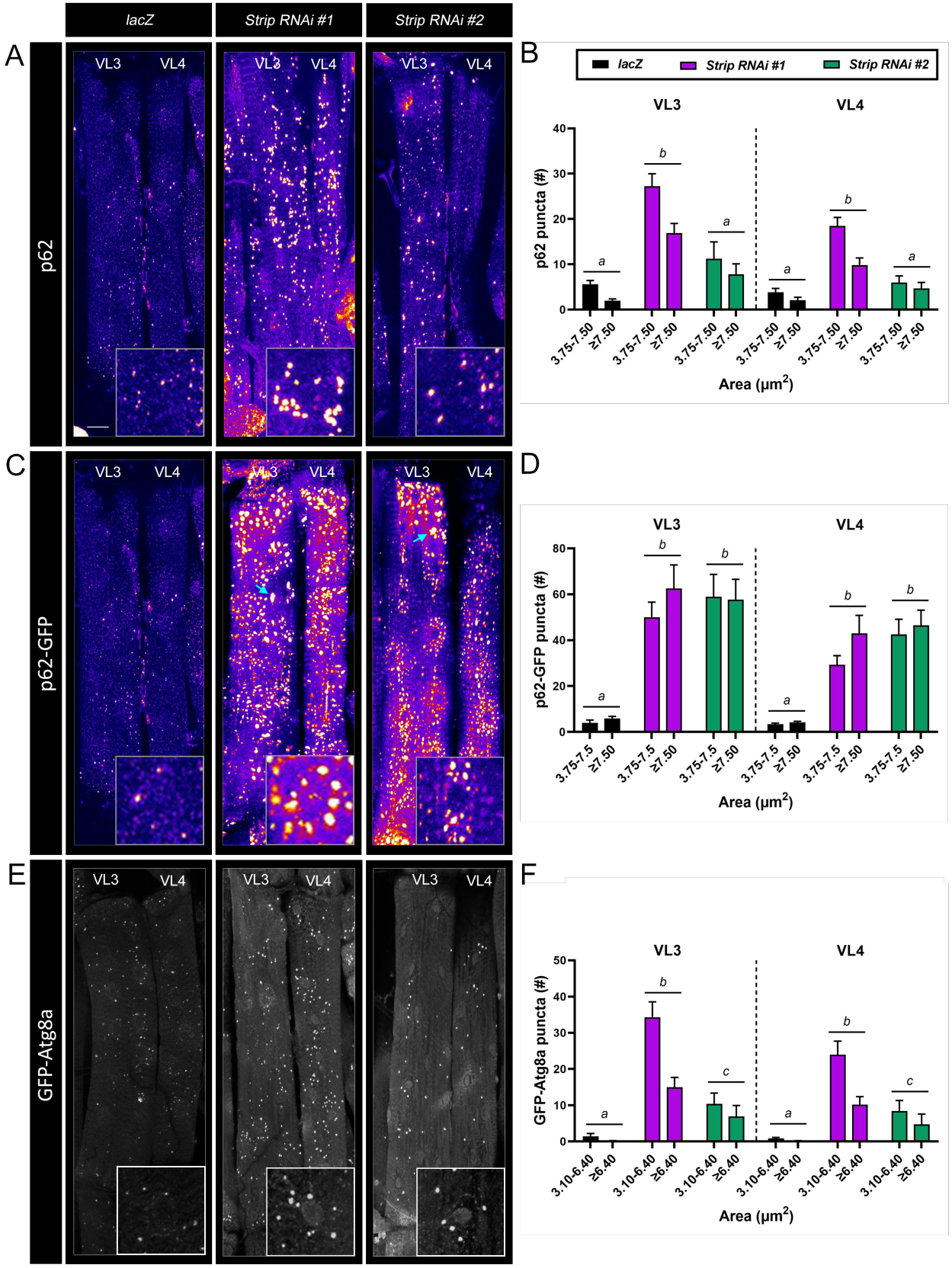
(A) Whole mount larvae expressing MHC-GFP to visualize the L3 muscle pattern. (B) Normal pupal case size is observed for all genotypes examined. (C) Overall muscle size, muscle attachments, and F-actin striated sarcomere pattern appear similar to *lacZ* control muscles (see **Figure 2.2**). Scale bars, 1 mm (panels A and B), 50 μm (panel C).



Appendix Figure B.3. Verification of RNAi knockdown for STRIPAK complex components. qRT-PCR was used to quantify the relative amount of mRNA for each of the indicated transcripts in muscle fillets of control (w^{1118}) or *Mef2*-mediated knockdown of the genotypes shown. *rp49* was used as a normalization control. N= 3 biological replicates. ***, p<0.001; **, p<0.01; *, p<0.05; n.s, not significant.

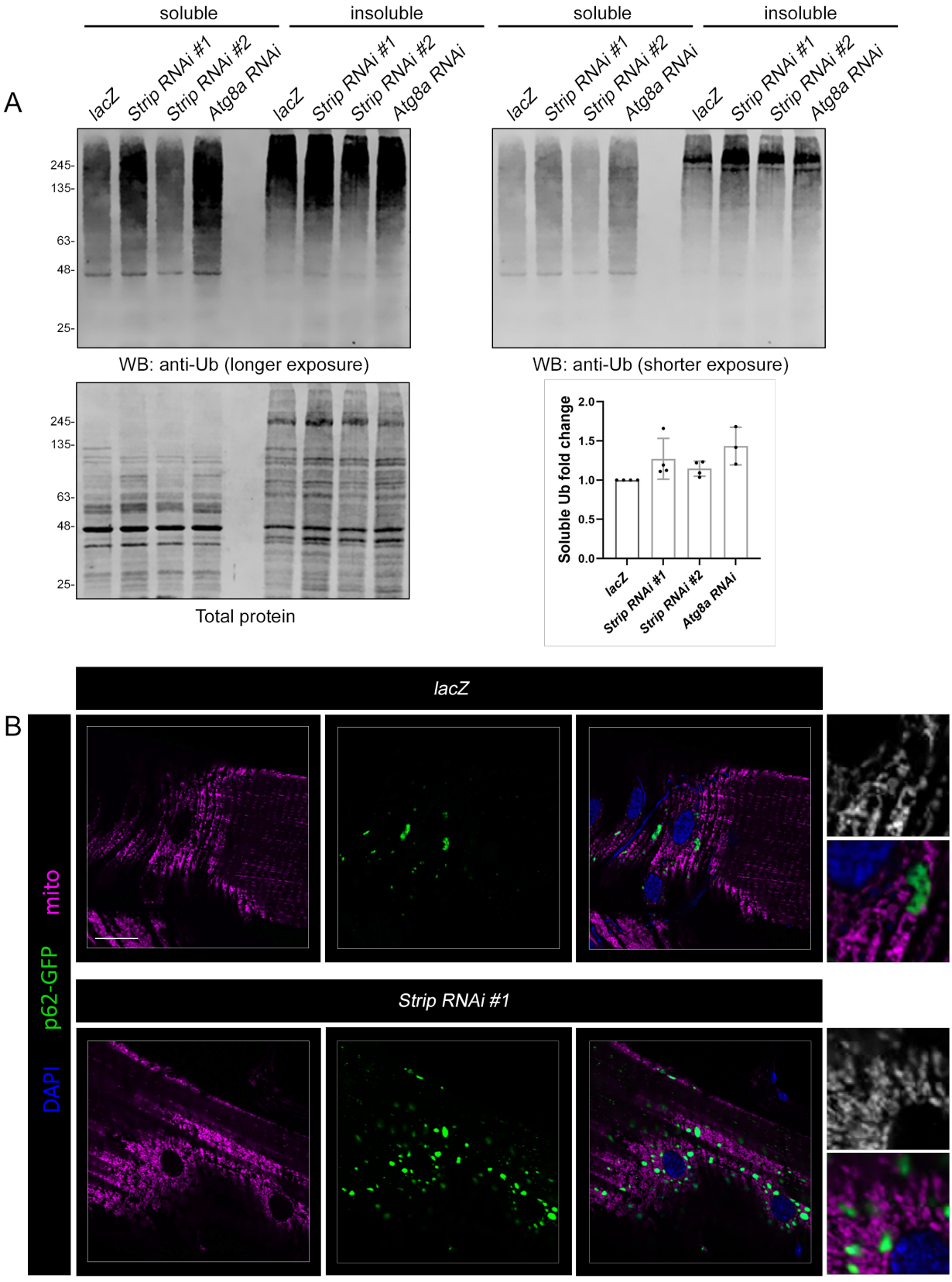


Appendix Figure B.4. Abnormal F-actin patterning and increased p62-GFP are prominent in *Cka RNAi* muscles.
Phalloidin staining to visualize F-actin in VL3 and VL4 muscles from *Mef2>Cka RNAi* larvae (left panels). P62-GFP is expressed in the background of *Mef2>Cka RNAi* muscles and is increased over *lacZ* controls in **Figure B.5**. Scale bar, 100 μm.

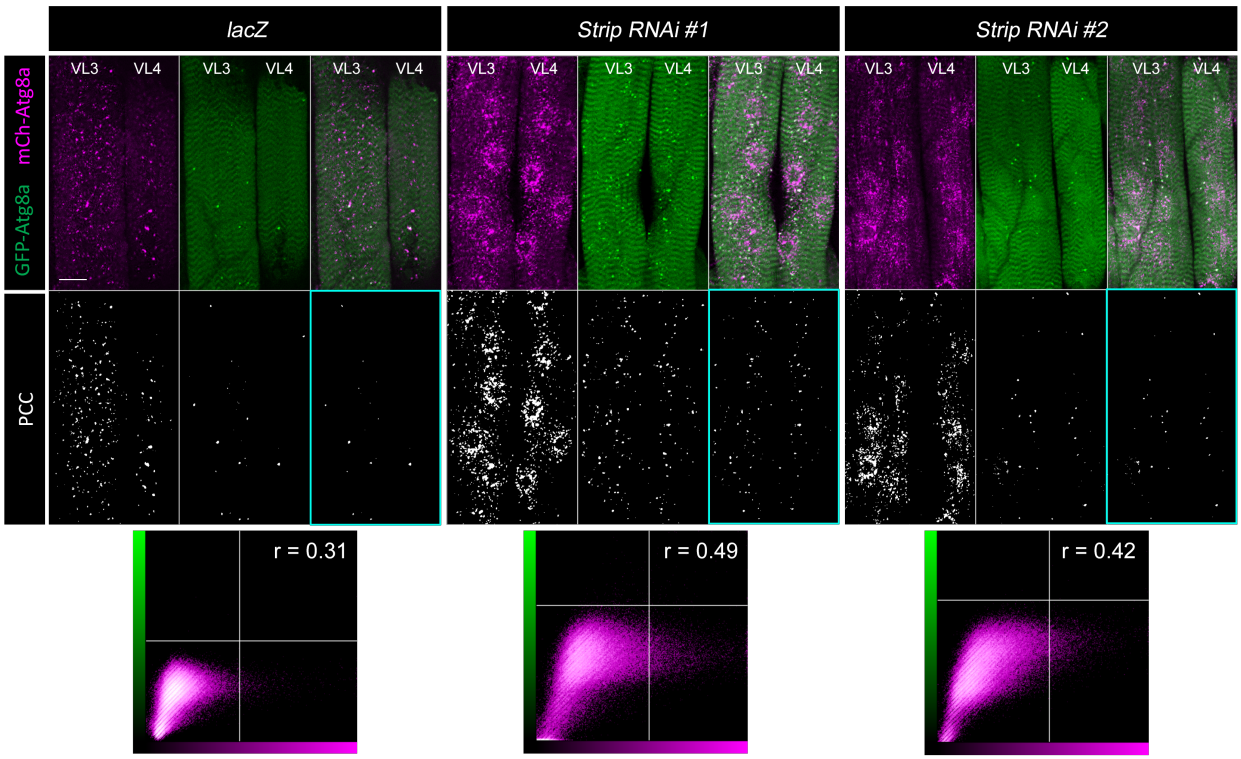


Appendix Figure B.5. Elevated p62, p62-GFP, and Atg8a-GFP upon induction of *Strip RNAi*.

All images are maximum intensity projections of muscles VL3 and VL4 from L3 larvae. (A) Anti-p62 signal (fire overlay) is increased in *Strip RNAi* muscles. Inset shows area around a single nucleus. (B) Bar graph shows the increase in the number and size of p62(+) puncta. (C) *Mef2-Gal4* was used to express *UAS-p62-GFP* in *lacZ* control or *Strip RNAi* muscles and representative images are presented as maximum intensity projections using the fire overlay to visualize intensity. There is a clear increase in p62-GFP(+) signal upon a decrease in Strip. Inset shows area around a single nucleus. (D) Bar graph shows a trend of larger and more numerous p62-GFP (+) puncta in *Strip RNAi* muscles. (E) L3 progeny from M*ef2-Gal4, UAS-GFP-Atg8a* flies mated with *UAS-lacZ* or *UAS-Strip RNAi* lines #1 or #2 show an increase in the size and number of GFP-Atg8a puncta. Inset depicts the area around a single nucleus. (B) Bar chart quantification shows an increase in the overall size and number of GFP-Atg8a(+) in *Strip RNAi* muscles compared to *lacZ* controls. $N \geq 20$ for each genotype. Genotypes with different letters are statistically different ($p<0.05$). Scale bar, 50 μm.


A
soluble
insoluble
soluble
insoluble
lacZ
Strip RNAi #1
Strip RNAi #2
Atg8a RNAi
245-
135-
63-
48-
25-
WB: anti-Ub (longer exposure)
WB: anti-Ub (shorter exposure)
Total protein
Soluble Ub fold change
2.0
1.5
1.0
0.5
0.0
B
lacZ
Strip RNAi #1
mito
p62-GFP
DAPI

Appendix Figure B.6. Ubiquitinated proteins are increased in Strip RNAi muscles with no obvious alteration in mitochondria.
(A) Western blot of soluble and insoluble proteins from controls or knockdown of Strip or Atg8a. Anti-Ub blots with longer (left panel) or shorter (right panel) exposure times show a general increase in Strip RNAi or Atga RNAi muscles. Total protein is shown as a loading control. Scatter bar graph shows a trend of increased proteins in the soluble fractions upon loss of Strip or Atg8a. N=4 biological replicates. (B) *Mef2-Gal4* was used to express *UAS-p62-GFP* (green) in *lacZ* control or *Strip RNAi* muscles and stained with anti-ATP5α to visualize mitochondria (magenta) or DAPI to label nuclei (blue). No obvious alterations in mitochondrial morphology or overlap with p62 is obvious. Scale bar, 10 µm.



Appendix Figure B.7. Determination of the Pearson correlation coefficient (PCC).
VL3 and VL4 Larval muscles expressing *GFP-mCh-Atg8a* in control or *Strip RNAi* muscles. (Top panel) The signal corresponding to mCh-Atg8a or GFP-Atg8a are in magenta or green, respectively. (Middle panel) Representative images of PCC overlays as determined by the ImageJ JACoP plugin is shown in white pixels on a black background. Note the amount of colocalization for mCh-Atg8a or GFP-Atg8a (cyan box). (Bottom panels) Representative graphs showing the Pearson correlation coefficient (r) for each genotype. Each axis ranges from 0 to 1 where the x-axis corresponds to mCh-Atg8a signal (magneta) and the y-axis representsGFP-Atg8a (green) signal. Scale bar, 50 µm.

Appendix Table B.1. Raw data and statistics summary.

Panel	Graph type	N value	Statistical test used	Precision	p-value[1]
Fig. 2C	Box and whisker plot	N≥20 for each genotype	One-way ANOVA Kruskal-Wallis test	Min to max	a vs. b (p<0.0001)
Fig. 2E	Column bar graph	N=3 biological replicates	One-way ANOVA Kruskal-Wallis test	Mean +/- SD	a vs. b, a vs. c (p<0.0001) b vs. c (p<0.001)
Fig. 3E	Scatter plots	N≥12 for each genotype	One-way ANOVA Kruskal-Wallis test	Mean +/- SD	a vs. b (p<0.001) a vs. c (p<0.05)
Figs. 4A,B	Box and whisker plot	N≥20 for each genotype	One-way ANOVA Kruskal-Wallis test t-test followed by Mann-Whitney for pair-wise comparisons	Mean +/- SD	a vs. b, b vs. c, a vs. c (p<0.05) ****, p<0.0001; ***, p<0.001; **, p<0.01; *, p<0.05; n.s, not significant
Figs. 4C,D	Violin plot	N≥18 for each genotype	One-way ANOVA Kruskal-Wallis test t-test followed by Mann-Whitney for pair-wise comparisons	Show all points	a vs. b, b vs. c, a vs. c (p<0.05) ****, p<0.0001; ***, p<0.001; **, p<0.01; *, p<0.05; n.s, not significant
Fig. 5B	Column bar graph	N≥15 for each genotype	Tukey's multiple comparisons test	Mean +/- SEM	a vs. b (p<0.001) a vs. c (p<0.05)
Fig. 5D	Scatter bar graph	N≥32 for each genotype	One-way ANOVA Kruskal-Wallis test	Mean +/- SD	a vs. b (p<0.001) a vs. c (p<0.0001) b vs. c (p<0.05)
Fig. 5E	Scatter bar graph	N≥32 for each genotype	One-way ANOVA Kruskal-Wallis test	Mean +/- SD	a vs. b, a vs. c (p<0.0001) b vs. c (p<0.05)
Fig. 5G	Scatter bar graph	N≥32 for each genotype	One-way ANOVA Kruskal-Wallis test	Mean +/- SD	a vs. b, b vs. d, c vs. d (p<0.0001) b vs. c (p<0.005) a vs. c, a vs. d (p<0.05)
Fig. 5H	Scatter bar graph	N≥32 for each genotype	One-way ANOVA Kruskal-Wallis test	Mean +/- SD	a vs. b (p<0.005) a vs. c, b vs. c (p<0.0001)
Fig. 6B	Scatter bar graph	N=20 for each genotype	One-way ANOVA Kruskal-Wallis test	Mean +/- SD	a vs. b (p<0.05)
Fig. 6C	Scatter bar graph	N=5 biological replicates	One-way ANOVA Kruskal-Wallis test	Mean +/- SD	a vs. b (p<0.05)

Fig. 6D	Scatter bar graph	N=3 biological replicates	One-way ANOVA Kruskal-Wallis test	Mean +/- SD	n.s. across all groups
Fig. 6E	Scatter bar graphs	N=3 biological replicates	One-way ANOVA Kruskal-Wallis test	Mean +/- SD	n.s. across all groups
Fig. 7B	Scatter bar graph	N=3 biological replicates	One-way ANOVA Kruskal-Wallis test	Mean +/- SD	n.s. across all groups
Fig. 8B	Scatter bar graph	N=3 biological replicates	Unpaired t-test	Mean +/- SD	*, p<0.05; n.s. across all groups
Fig. 8D	Scatter plot	N≥7 for each genotype	One-way ANOVA Kruskal-Wallis test	Median with 95% CI	a vs. b (p<0.05)
Fig. 8E	Scatter bar graph	N≥7 for each genotype	One-way ANOVA Kruskal-Wallis test	Mean +/- SD	a vs. b (p<0.05)
Panel	**Graph type**	**N value**	**Statistical test used**	**Precision**	**p-value**
Fig. S3	Column bar graph	N=3 biological replicates	Unpaired t-test	Mean +/- SD	***, p<0.001; **, p<0.01; *, p<0.05; n.s, not significant
Fig. S5B	Column bar graph	N≥20 for each genotype	Tukey's multiple comparisons test	Mean +/- SEM	a vs. b (p<0.0001)
Fig. S5D	Column bar graph	N≥20 for each genotype	Tukey's multiple comparisons test	Mean +/- SEM	a vs. b (p<0.0001)
Fig. S5F	Column bar graph	N≥20 for each genotype	Tukey's multiple comparisons test	Mean +/- SEM	a vs. b (p<0.0001) a vs. c,b vs. c (p<0.005)
Fig. S6A	Scatter bar graph	N=4 biological replicates	One-way ANOVA Kruskal-Wallis test	Mean +/- SD	n.s. across all groups

Appendix C - Chapter 4 Method C4.1

1. Download Anaconda from: https://www.anaconda.com/download

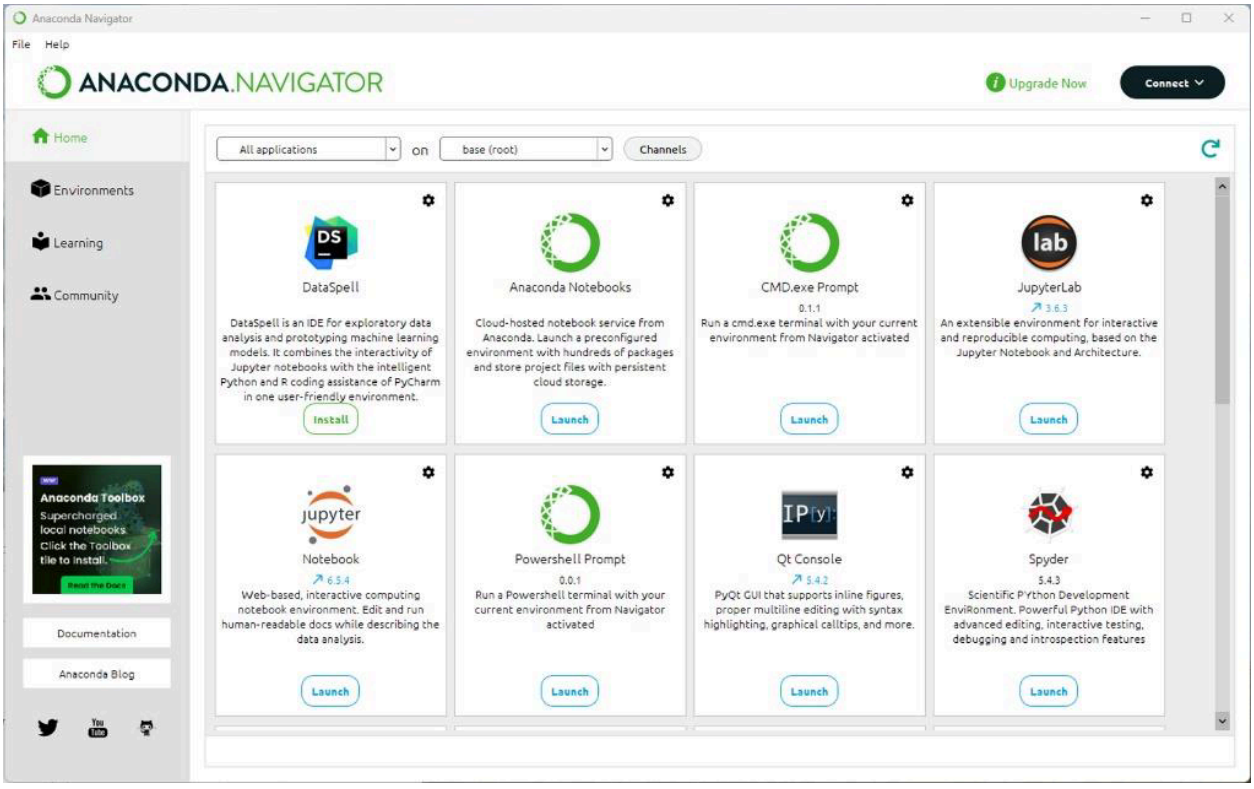
For this protocol, we created a folder C:\Python and downloaded Anaconda to it

Note: Select the box that will launch the Anaconda.Navigator home page after installation.

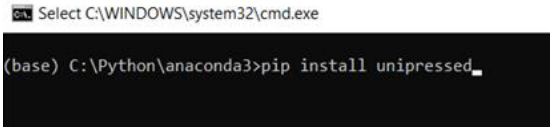
2. Move the "File S4. Uniprot_Protein_match" and the "*.txt" data file to be analyzed into the 'Scripts' folder located in the 'Anaconda3' folder (e.g., C:\Python\Anaconda3\Scripts).

3. Install Uniprot REST (Unipressed), a Python-based application programming interface (API) for querying protein names in the Uniprot protein database.

a. From the ANACONDA.NAVIGATOR home page, launch the 'CMD.exe Prompt'



b. In the command line, type: pip install unipressed

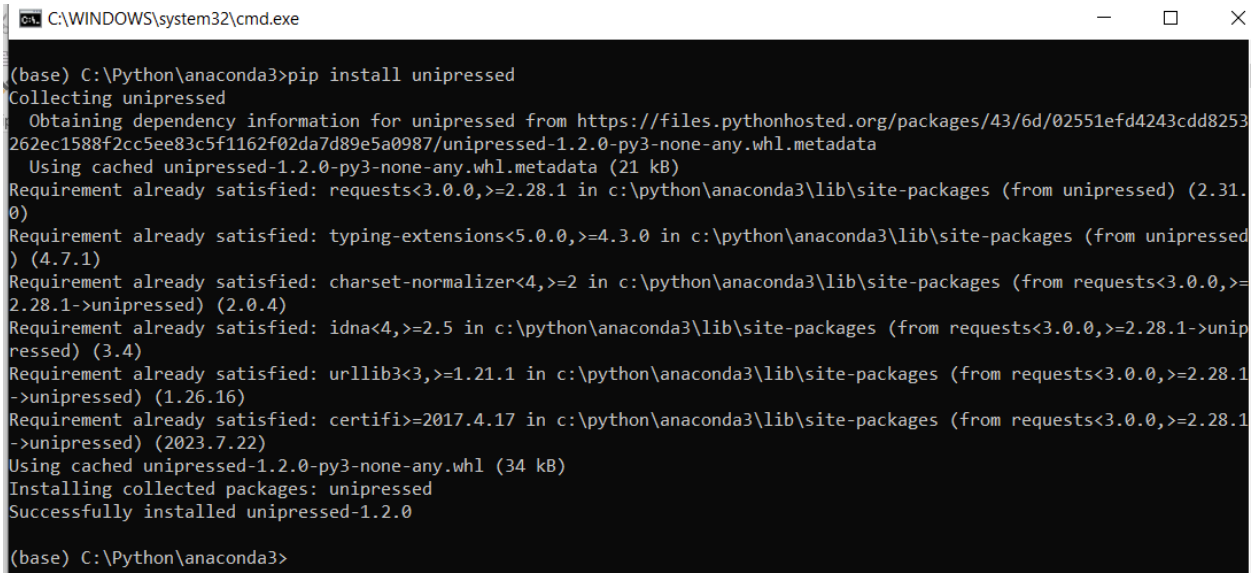


Note: If the location of the Anaconda3 folder is not in C:\Python, the directory can be changed:

cd = change directory: c:\Python>cd anaconda3 □ _c:\Python\anaconda3

cd.. = change directory to the pervious folder: c:\Python\anaconda3>cd.. □ _c:\Python\

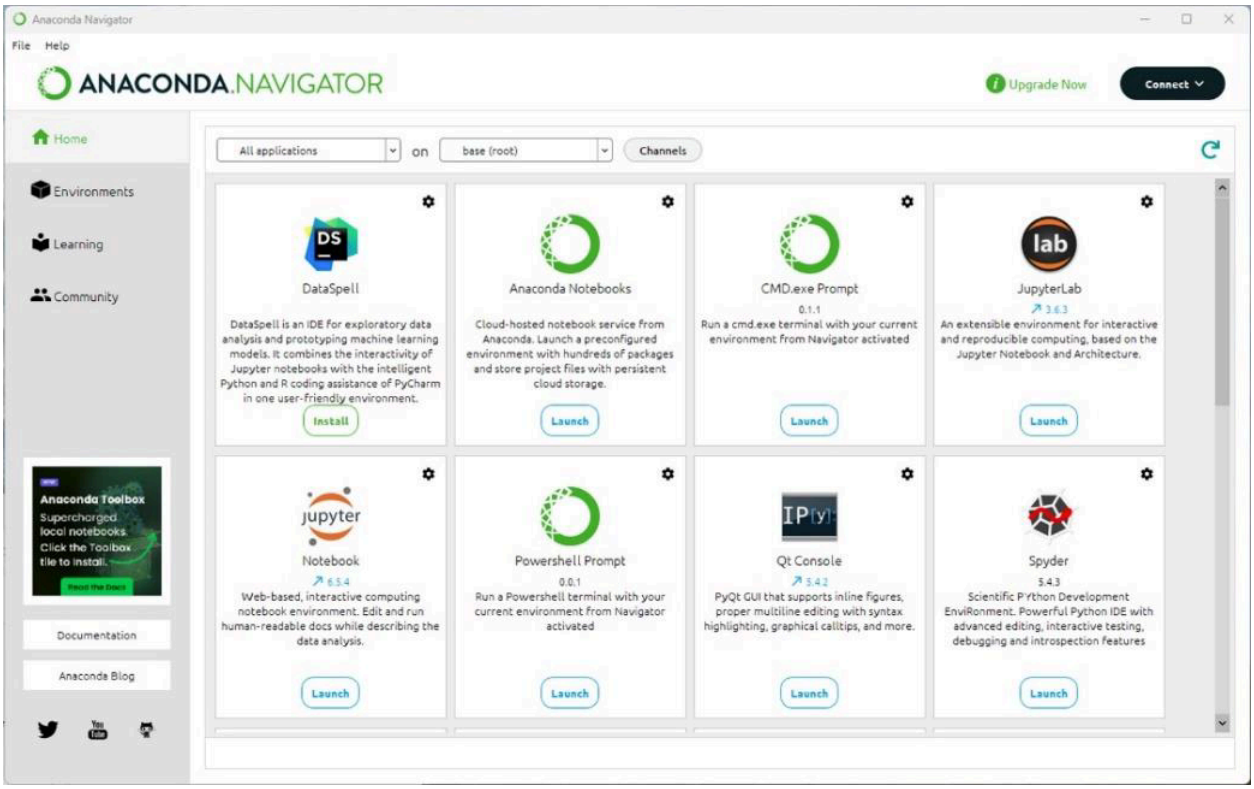
c. Proper installation of Unipressed should appear as follows:



d. Close the terminal by clicking “X” in the upper right corner.

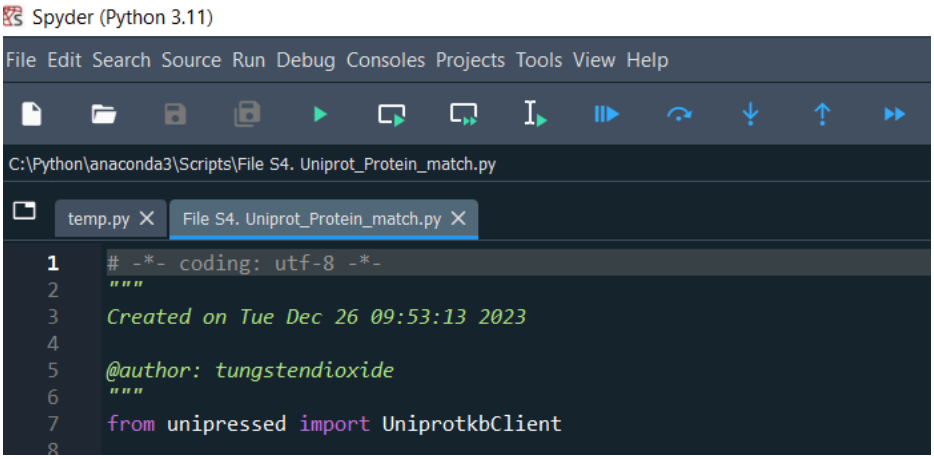
Note: Step 3 only needs to be completed one time after downloading Anaconda. Each new analysis using the File S4. Uniprot_Protein_match.py code can start at Step 4.

4. From the ANACONDA.NAVIGATOR home page, launch ‘Spyder,’ an interactive development environment to run Python programs.

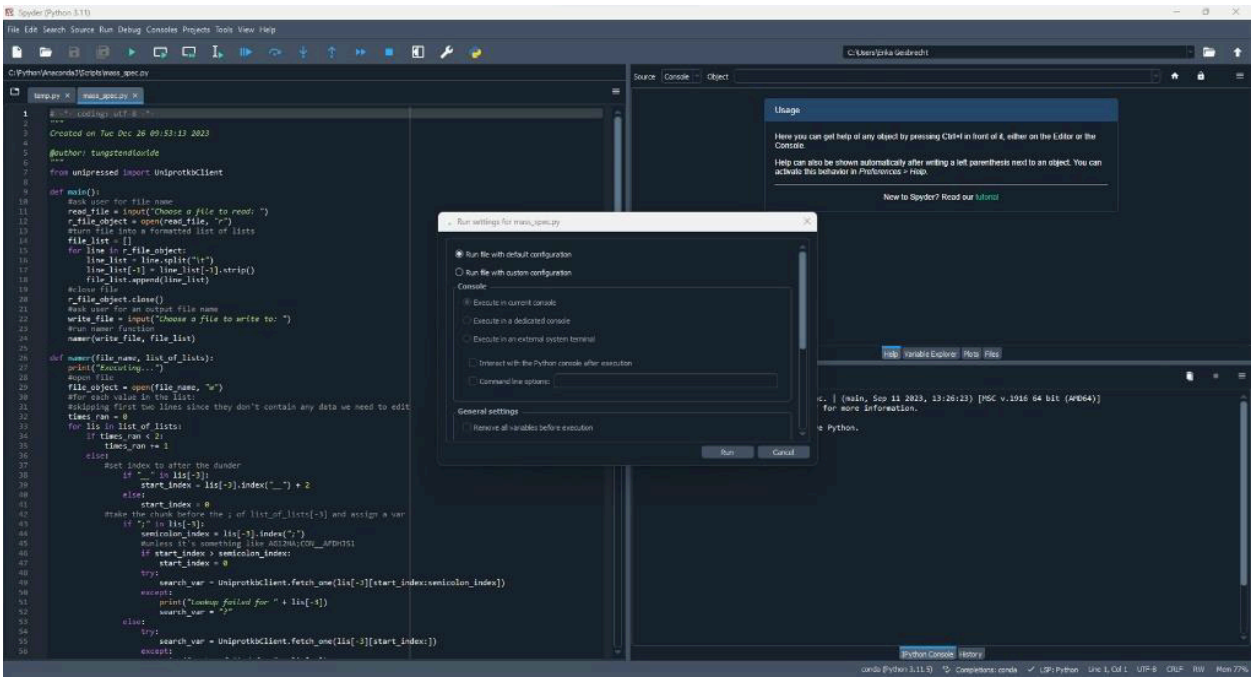


5. Open ‘File S4. Uniprot_Protein_match.py’ in Spyder: File>Open> File S4. Uniprot_Protein_match.py

a. Run the program by clicking the ‘play’ button.



b. A window may pop up entitled ‘Run settings for mass _spec.py’

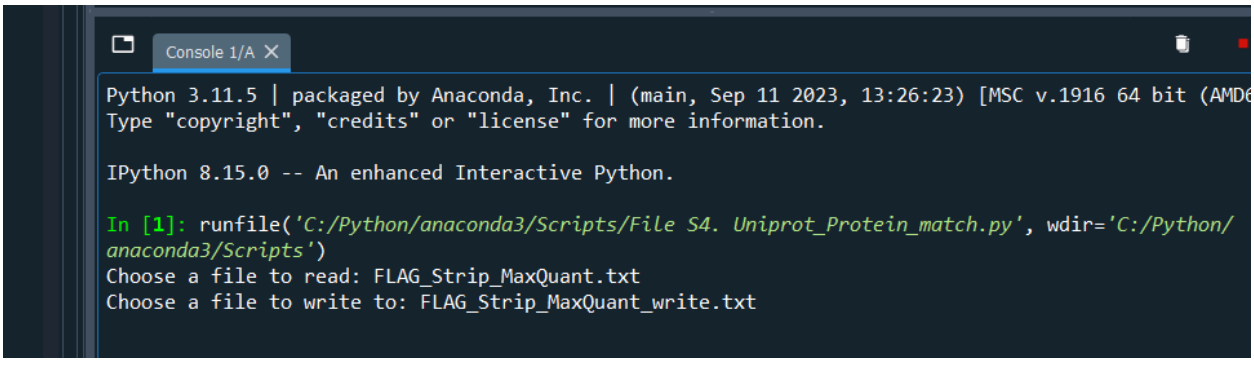


Choose ‘Run file with default configuration’ and press ‘Run’ (cyan arrow below)

c. In the lower right panel (“Console1/A” – yellow dotted rectangle above), type the name of the .txt file to be read (e.g., FLAG_Strip_MaxQuant.txt) and press the ‘Enter’ key.

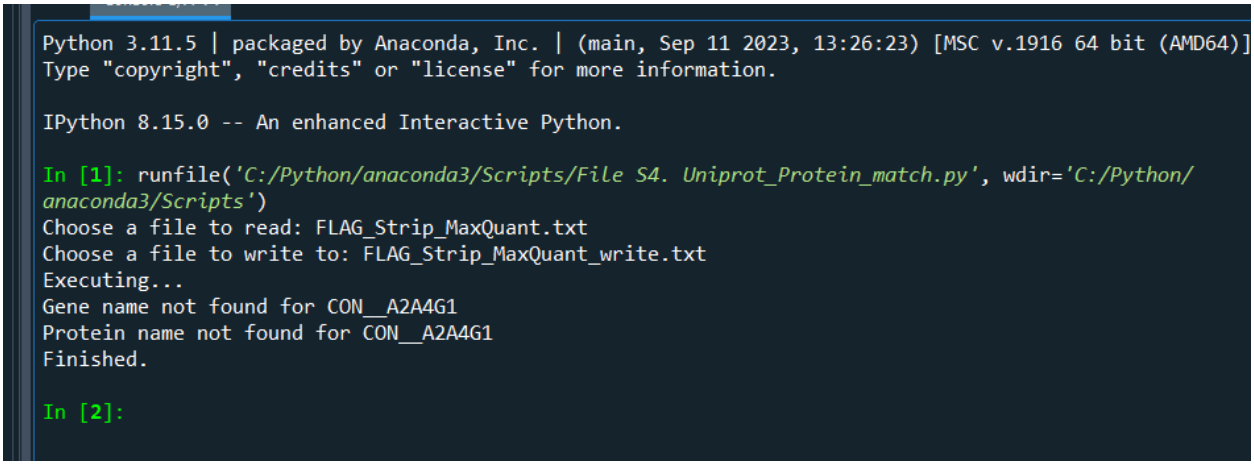
d. Choose the name of file to write to (e.g., FLAG_Strip_MaxQuant_write.txt) and press the ‘Enter’ key.

Note: The “write” file should have a different name than the “read” file. Also, the write file does not have to be created before running the program.



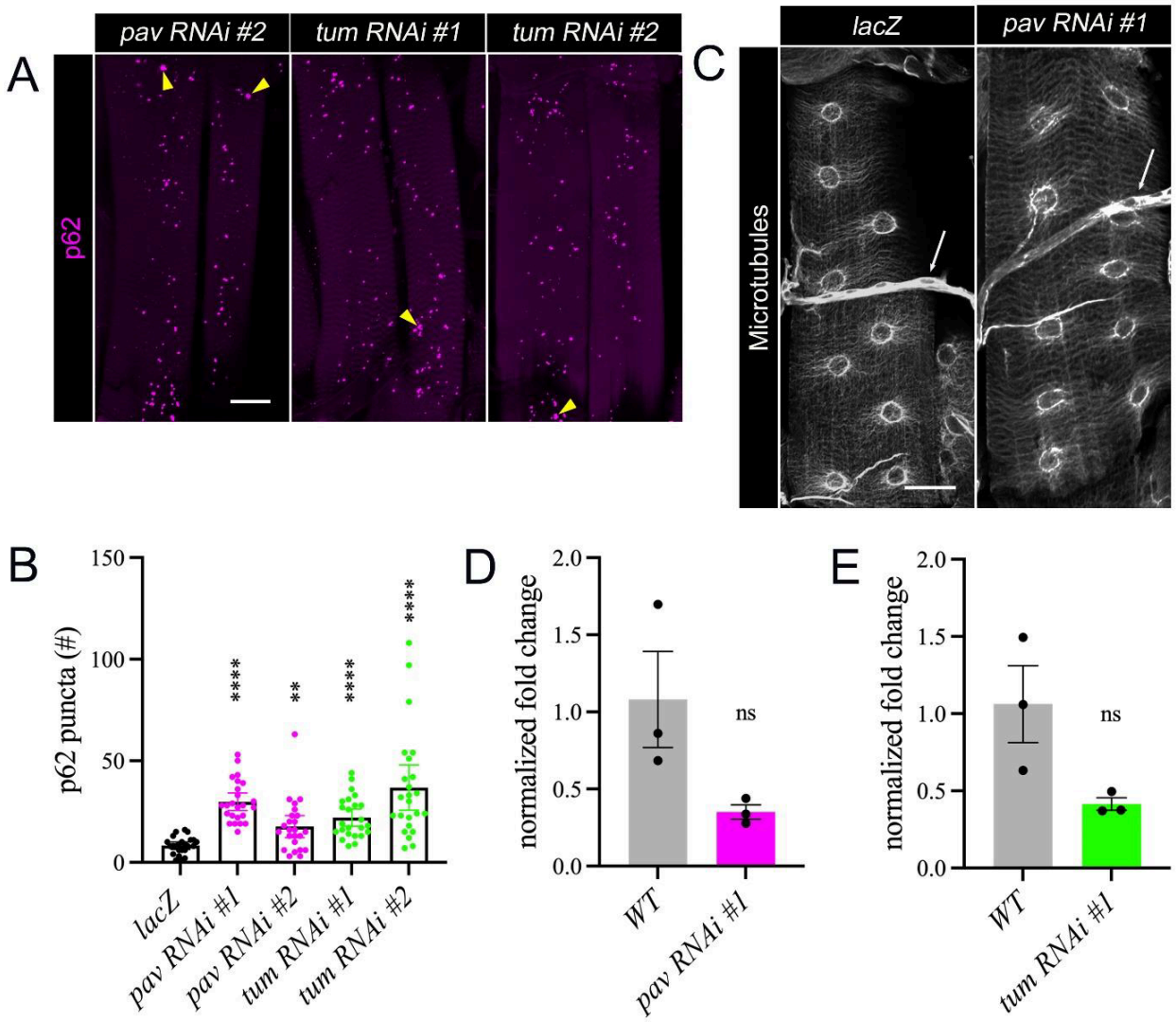
e. The program will execute until it is completed.

Note: If there are any errors (i.e., non-matching gene or protein names) they will be displayed as shown. These can be looked up manually for correction.

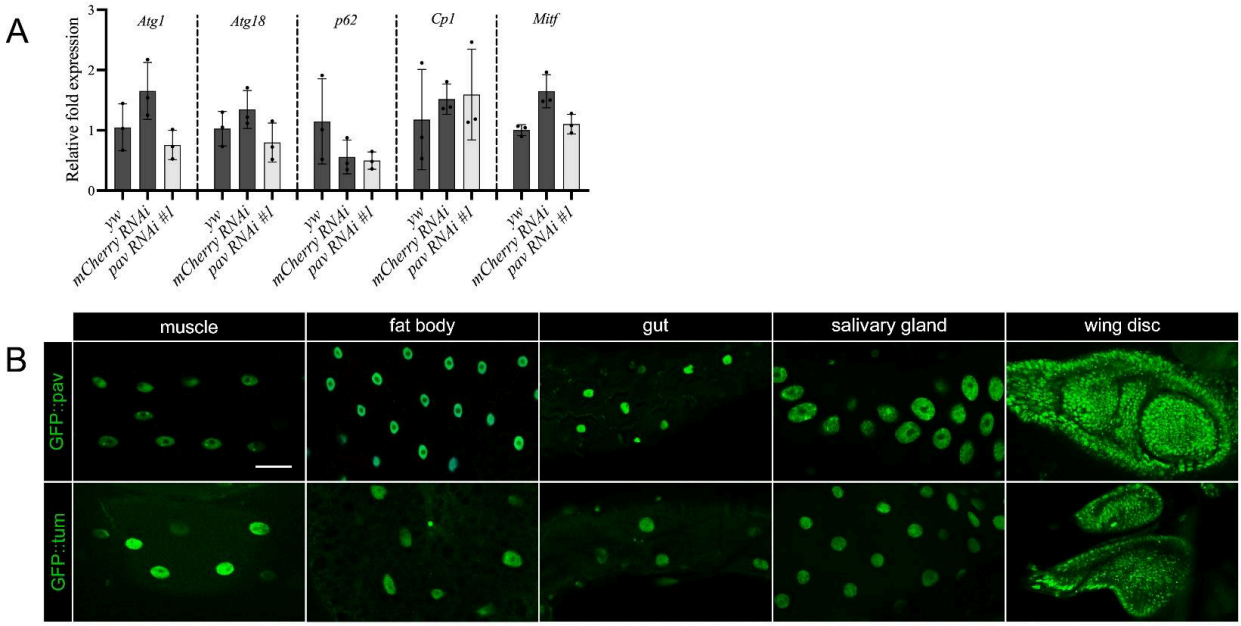


6. The corrected/amended file after executing the program (FLAG_Strip_MaxQuant.txt) can be found in the Anaconda3>Scripts folder (e.g., C:\Users\dsbrooks\anaconda3\Scripts).

Appendix D - Chapter 5 Supplemental Materials

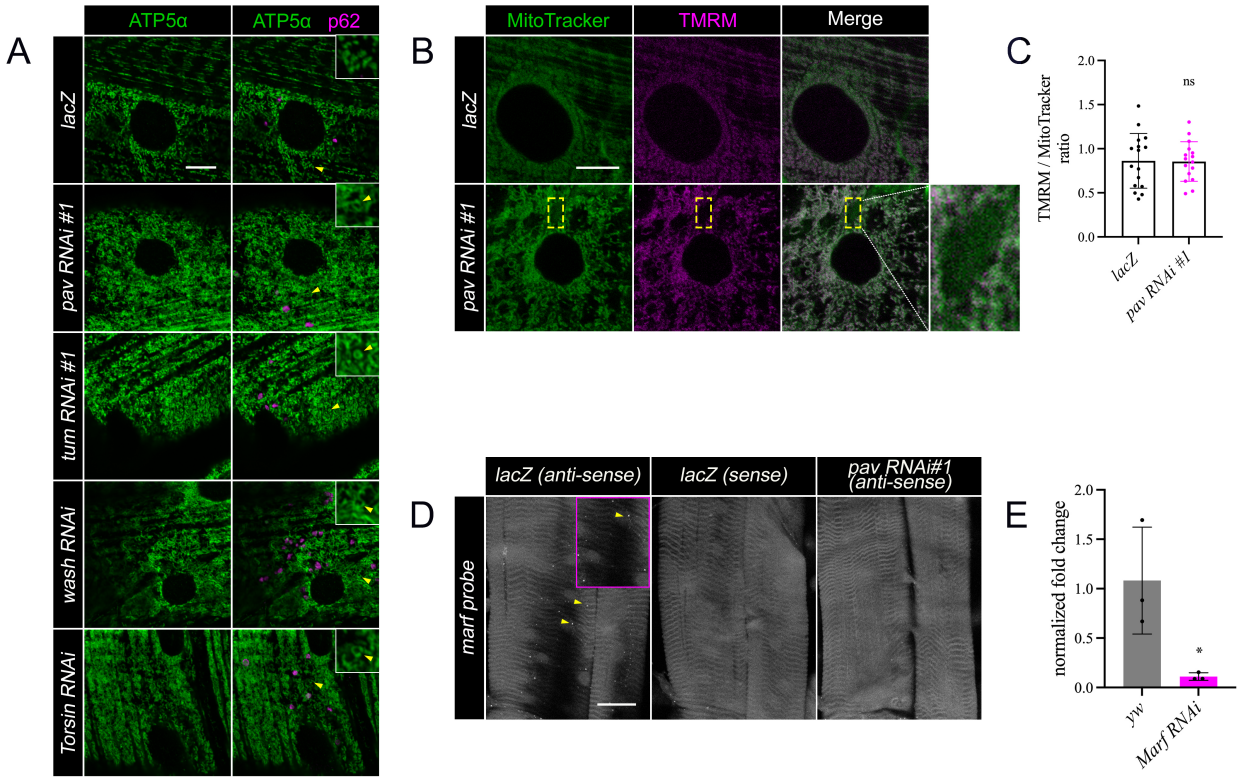


Appendix Figure D.1. *tum RNAi* muscles show a p62 phenotype similar to *pav RNAi* muscles. (A) Expression of UAS-*pav RNAi #2* or UAS-*tum RNAi #1* and *#2* using the *Mef2-Gal4* driver. VL3 and VL4 muscles of L3 larvae immunostained with anti-p62 (magenta). p62 clusters (yellow triangle) are observed in both *Mef2>pav RNAi #2* muscles and two independent lines expressing *Mef2>tum RNAi* in muscles. (B) Scatter bar graph shows an elevated number of p62 puncta in the *pav* or *tum RNAi* VL3/VL4 muscles compared to controls. Every data point corresponds to the count of p62 puncta in each VL3/VL4 pair. N=24. (C) Maximum intensity projections of the overall microtubule (gray) pattern in larval somatic body wall muscles. The stained structure indicated by the white arrow is trachea. (D and E) qRT-PCR was used to quantify the relative amount of *mRNA* for *pav* or *tum* in whole larvae of control (*y,w*) or *da-Gal4* driven knockdown. *rp49* is used as a normalization control. N= 3 biological replicates. P values: ns, not significant; **, $p<0.01$; ****, $p<0.0001$. Error bars indicate standard error of the mean (SEM). Statistics: Student's t-test. Scale bars, 40 µm (panels A, and C).



Appendix Figure D.2. Autophagosome or lysosome biogenesis are not affected upon Pav knockdown.

(A) *mRNA* transcripts necessary for autophagosome or lysosome biogenesis are analyzed by qPCR in whole larvae from *y,w* (control), *Mef2>mCherry RNAi* (control), or *Mef2>pav RNAi*. No statistically significant differences in transcript levels are observed for *Atg1*, *Atg18*, *Cp1*, *Mitf*, or *p62*. N= 3 biological replicates. (B and C) Low magnification confocal projections to visualize GFP-tagged Pav (B) or GFP-tagged Tum (C) in various tissues of L3 larvae. Scale bars, 40 μm.



Appendix Figure D.3. Mitochondrial integrity, membrane potential, and *marf RNAi* controls.

(A) Muscles from control or NE budding mutants stained with anti-p62 (magenta) and anti-ATP5α (green). Mitochondria that adopt ring-like structures (yellow triangle and inset) are detected in *pav RNAi #1, tum RNAi #1*, *wash RNAi*, and *Torsin RNAi* muscles but not in control *lacZ* muscles. (B) Confocal images of VL3 or VL4 muscles stained with TMRM (indicator of mitochondrial membrane potential) and MitoTracker (indication of mitochondrial mass). The inset shows a zoom of the yellow rectangular dashed box where weakly stained mitochondria have decreased membrane potential in *pav RNAi* muscles. (C) The ratio of TMRM to MitoTracker intensity was calculated in ImageJ from images similar to those in panel B and plotted as a scatter bar graph. No significant difference is detected in *pav RNAi #1* compared with *lacZ* controls. N=16. (D) FISH experiments on L3 *lacZ* or *pav RNAi* muscles treated with either anti-sense or sense (control) *marf* probes as indicated. Puncta corresponding to *marf* transcripts (yellow triangle), are prevalent in lacZ muscles, but reduced in *pav RNAi* muscles. (E) qPCR was used to validate the *marf RNAi* knockdown. N =3 biological replicates. Larvae were raised at 18ºC. P values: ns, not significant; *, $p<0.05$. Error bars indicate standard error of the mean (SEM). Statistics: Student's t-test. (panels B and D). Scale bars, 10 µm (panels A and B), 40 µm (panel D).